Dynamic Stall Modeling for Wind Turbines

M. A. Khan

Dynamic Stall Modeling for Wind Turbines

by

M. A. Khan

to obtain the degree of Master of Science
at the Delft University of Technology,
to be defended publicly on Tuesday August 7, 2018

Student number:	4473612	
Project duration:	November 1, 2017 – July 31, 2018	
Supervisors:	Dr. G. J. Schepers,	ECN
	Dr. C. J. Simao Ferreira,	TU Delft
	Prof. N. N. Sorensen,	DTU Wind Energy

An electronic version of this thesis is available at `http://repository.tudelft.nl/`.

TU Delft

Acknowledgments

The European Wind Energy Master program has been a wonderful experience for me. I have learned a lot and have made new friends and colleagues during this journey. All of them have proved instrumental in making me strive for improving myself in an intellectual and social capacity.

I would like to express my gratitude to Dr. Gerard Schepers. He has been an exceptional supervisor and mentor. This work wouldn't have been possible without his support and critical feedback. In addition, his team at ECN, especially Koen Boorsma and Marco Caboni, have been very helpful and kind in lending out information and technical assistance. I would also like to thank Assoc. Prof. Carlos S. Ferreira and Prof. Niels N. Sørensen for their valuable guidance despite of long distance communication.

Finally, I cannot neglect the fact that all my achievements in life always have had and will have a significant contribution from my parents and aunt. I thank my parents, aunt, and brothers for their endless moral and financial support to help me reach where I am today.

M.A. Khan
Delft, July 2018

Abstract

Modern wind turbines frequently operate at off-design conditions during their life cycle. They undergo dynamic loads characterized by unsteady aerodynamics. Predicting these unsteady aerodynamic loads has been very difficult due to the non-linear nature of unsteady aerodynamics. Especially when operating near the stall region, these turbine are prone to increased loads because of dynamic stall. Dynamic stall is typically observed when there is a turbulent inflow, yaw misalignment, or severe wind shear causing periodic variations in angle of attack. Nonetheless, the nature of dynamic stall phenomenon is still a topic under investigation.

The aim of this research was to investigate the performance of dynamic stall models in yawed and standstill conditions by using current state-of-the-art engineering models and validating the results with the New MEXICO (Model Rotor Experiments under Controlled Conditions) measurement campaigns. The first part of the research dealt with a detailed analysis of the New MEXICO experiments in standstill and yawed flow conditions. This part also encompassed extracting 3D polars from pressure measurements and a spectral analysis to characterize any vortex shedding phenomenon in standstill conditions. The second part of the research was concerned with validating dynamic stall models implemented in ECN's in-house aeroelastic tool Aero-Module. Three different dynamic stall models namely: Snel, ONERA, and Beddoes Leishman model, were extensively validated and improved using New MEXICO measurements in standstill and yawed flow conditions. Finally, a case study was performed on the AVATAR rotor, using afore-mentioned dynamic stall models, to access their effect on aerodynamic damping and, consequently, in predicting the onset of aeroelastic instabilities.

The research was able to shed light on our current understanding of dynamic stall phenomenon and the way we model it, hoping to improve the dynamic stall modeling capabilities in the future.

Contents

List of Figures

List of Tables

Nomenclature

Abbreviations

2D	Two dimensional
3D	Three dimensional
AoA	Angle of attack
ARE	Average Relative Error
AVATAR	Advanced aerodynamic tools for large rotors
AWSM	Aerodynamic Windturbine Simulation Module
B-L	Beddoes-Lieshman
BEM	Blade element momentum theory
BET	Blade element theory
CFD	Computational fluid dynamics
DES	Detached eddy simulation
DLC	Design load case
DNW	German-Dutch Wind Tunnel
DOF	Degree of freedom
DP	Data point (New MEXICO)
DS	Dynamic stall
ECN	Energy Research Centre of the Netherlands
EU	European Union
i.e.	that is
INNWIND.EU	Innovative wind conversion systems (10-20MW) project for offshore wind power
LES	Large eddy simulation
LEV	Leading edge vortex
LHS	Left hand side
MEXICO	Model rotor experiments under controlled conditions
MT	Momentum theory
NREL	National Renewable Energy Laboratory
ONERA	National Office for Aerospace Studies and Research
PIV	Particle image velocimetry

PSD	Power spectral density
RANS	Reynolds averaged Navier-Stokes equations
RHS	Right hand side
SST	Shear stress transport
TSR	Tip speed ratio
UAE	Unsteady aerodynamic experiment

Symbols

α	Angle of attack
α_0	Zero lift angle of attack
β	Yaw angle
∇	Divergence operator
δ	Logarithmic decrement
Γ	Circulation
λ	Tip speed ratio
μ	Dynamic viscosity of air
Ω	Rotational velocity of the rotor
ω_d	Damped natural frequency or modal frequency
ω_n	Natural frequency
ϕ	Flow angle
ψ	Azimuthal angle
ρ	Density of air
Θ	Larsen's separation parameter
θ	Pitch angle
θ_{cf}	Cross-flow angle of incoming velocity with respect to the blade quarter chord line
ζ	Damping ratio
a	axial induction
a'	Tangential induction factor
c	Airfoil chord length
C_d	Drag coefficient
C_l	Lift coefficient
C_M	Moment coefficient
C_n	Normal force coefficient of a blade section
C_p	Pressure coefficient

C_T	Thrust force coefficient
C_t	Tangential force coefficient of a blade section
C_{l_α}	Lift curve slope
$C_{l_{pot}}$	Potential lift coefficient
$C_{l_{sep}}$	Fully separated lift coefficient
f	Separation point location w.r.t chord lenght
F_n	Normal force of a blade section
F_t	Tangential force of a blade section
f_{C_l}	Rotational augmentation correction factor
k	Reduced frequency
St	Strouhal number
U_∞	Free-stream wind velocity
W	Resultant velocity
$w_{\frac{3}{4}}$	Downwash at three-quarter chord location

1 Introduction

In modern times, sustainable energy resources like wind power might be the answer to global warming and air pollution. However, they need to contend against conventional fossil fuel based energy systems on an economical front. Meaning that the levelized cost of wind energy needs to be lowered. Realizing this goal solicits a trend in developing larger wind turbines. Development of larger wind turbines require improved aeroelastic tools that can accurately predict the complex aerodynamics, elastic deformations, and inertial dynamics, which is representative for these behemoth structures. This thesis will touch upon dynamic stall, which is one of the many complex aerodynamic problems that still lack a complete understanding.

1.1. Motivation

Dynamic stall has been an important driver in predicting the large dynamic loads a wind turbine undergoes during its lift cycle. An accurate prediction of dynamic loads prevents over-designing a wind turbine; thus, effectively bringing down the cost of energy. Predicting these dynamic loads, occurring due to dynamic stall, requires low fidelity advanced engineering models or high fidelity CFD models. High fidelity CFD models being more accurate have the downside of being computationally expensive; therefore, they have limited use in design and load certification. On the contrary, low fidelity engineering models require much less computational resources, but at the expense of increased uncertainty in load prediction. Hence, improving upon these engineering models could greatly reduce the costs and lead to a better wind turbine design. The low fidelity dynamic stall models are used in conjunction with other advanced engineering models, which are based on Blade-element Momentum theory or the Lifting Line theory. The current research mainly focuses on engineering models to model dynamic stall in wind turbines.

The engineering models are a computationally efficient alternative to CFD codes; however, they need extensive validation from test measurements for calibration. These test measurements could be from Field Tests or Wind Tunnel Tests. Validating the engineering models with Field Test data is extremely difficult due to the stochastic nature of the wind environment. In that respect, wind tunnel measurements offer a much better alternative for validation due to the extremely controlled environment, with low levels of turbulence, as was also pointed out by H. Snel [84]. Therefore, isolating the effect of extremely important aerodynamic phenomenon, like dynamic stall and rotational augmentation, is feasible. The current study would be utilizing data from the New MEXICO experiments for validation. As mentioned above, dynamic stall models need calibration to accurately predict dynamic loads and to quantify any associated uncertainties in the model. This study aims to compare different dynamic stall models with experiments to access their performance and quantify the uncertainties, which could eventually help in developing cost effective wind turbine designs.

1.2. Aims and Objectives

The research is aimed at exploring the performance of dynamic stall models for wind turbines operating in yawed and standstill conditions by using different dynamic stall models and the New MEXICO experimental data for validation. Whereby, performance of the models will be determined based on the accuracy with which unsteady loads are predicted. The research will strengthen our understanding of dynamic stall phenomenon; and it will improve upon the current models to reduce load prediction uncertainties. Hence, bringing down the cost of wind turbines and, consequently, the cost of energy.

1.3. Research Questions

Formally, the main research research question is phrased as:

What is the performance of different dynamic stall models in predicting the dynamic loads on a wind turbine in yawed and standstill conditions?

The following is the list of important research questions that are derived from the main research question and are sub-divided further. Thus, forming a complete conceptual model of the research.

- *Which measurements in the New MEXICO data-base are representative for dynamic stall in yawed and standstill conditions?*
  - What is the measurement quality of the data, are there any kinks in pressure measurements?
  - How to establish credibility of standstill measurements?
  - Is dynamic stall observed in the experiments?
  - Is dynamic stall of self-excited nature observed in standstill measurements?
- *Which are the main assumptions and limitations of different dynamic stall models?*
  - What parameters lead to the optimum performance of dynamic stall models?
  - Validity of standalone dynamic stall models in light dynamic stall and deep dynamic stall regime?
- *How will the BEM code be used in conjunction with dynamic stall models?*
  - What other engineering models will be used as add-ons?
  - What are the limitations from BEM assumptions on the performance of dynamic stall models?
- What is the accuracy of the dynamic stall models in predicting unsteady loads on the New MEXICO turbine in yawed and standstill conditions?
  - Which statistical measure is used for determining model performance?
  - How sensitive are the results to degree of yaw in the turbine?
  - Which model is capturing or not capturing the experimental trends accurately, and why?
  - Validity of cross-flow principle in standstill conditions with spanwise flow?
  - Performance of dynamic stall models in aeroelastic simulation of standstill condition for AVATAR turbine?

1.4. Methodology

The focus of this research was to evaluate the load predicting capabilities of three different dynamic stall models, used as an add-on in a BEM based aerodynamic model. The three different dynamic stall models, namely, the Beddoes-Lieshman (B-L) model, Snel's model, and the ONERA model were evaluated in a coherent and quantitative fashion. Before running the dynamic stall models in a BEM code, the model tunning parameters were selected. In case of non-availability of unsteady experimental data for respective airfoil sections, parameters in the literature were used.

The first phase of the research was concerned with processing of the new MEXICO experimental database. A preliminary evaluation of data quality was undertaken, followed by selecting cases representative of conditions conducive for dynamic stall at large AoA. Second phase of the research started with learning the computational tool, which is ECN's in-house code called Aero-Module[1], and interfacing it with MATLAB environment to automate the generation of input files and execution of 'ECNAero.exe' file. The output files were also read through MATLAB environment. In the third phase, 3D airfoil polars were extracted from all standstill measurements in the New MEXICO database and compared with 2D airfoil polars to establish credibility of New MEXICO standstill measurements. Simulations of standstill conditions on the New MEXICO rotor were performed with different dynamic stall models. The simulated trends were compared with measurements

[1] Aero-module is ECN's aerodynamic solver having both a BEM model and a free vortex wake model.

and an error analysis was performed. In the fourth phase, the yawed conditions were simulated using different dynamic stall models and their quantitative and qualitative performance was evaluated. Finally, an aeroelastic case study on the AVATAR blade was carried out to establish the effect of dynamic stall models on damping of edgewise instabilities.

The afore-mentioned dynamic stall models were included in ECN's Aero-module code, which was extensively used during the course of this research. Validation of load predictions from these models was performed with the New MEXICO measurements for the respective operating conditions, which were representative of dynamic stall. Complex interactions between structure and the aerodynamics was not modeled in this research. The purpose was to study the dynamic stall phenomenon in isolation from structural influences, so that any complex aeroelastic interactions are excluded unless otherwise stated. A self-explanatory depiction of the research framework is presented in figure 1.1.

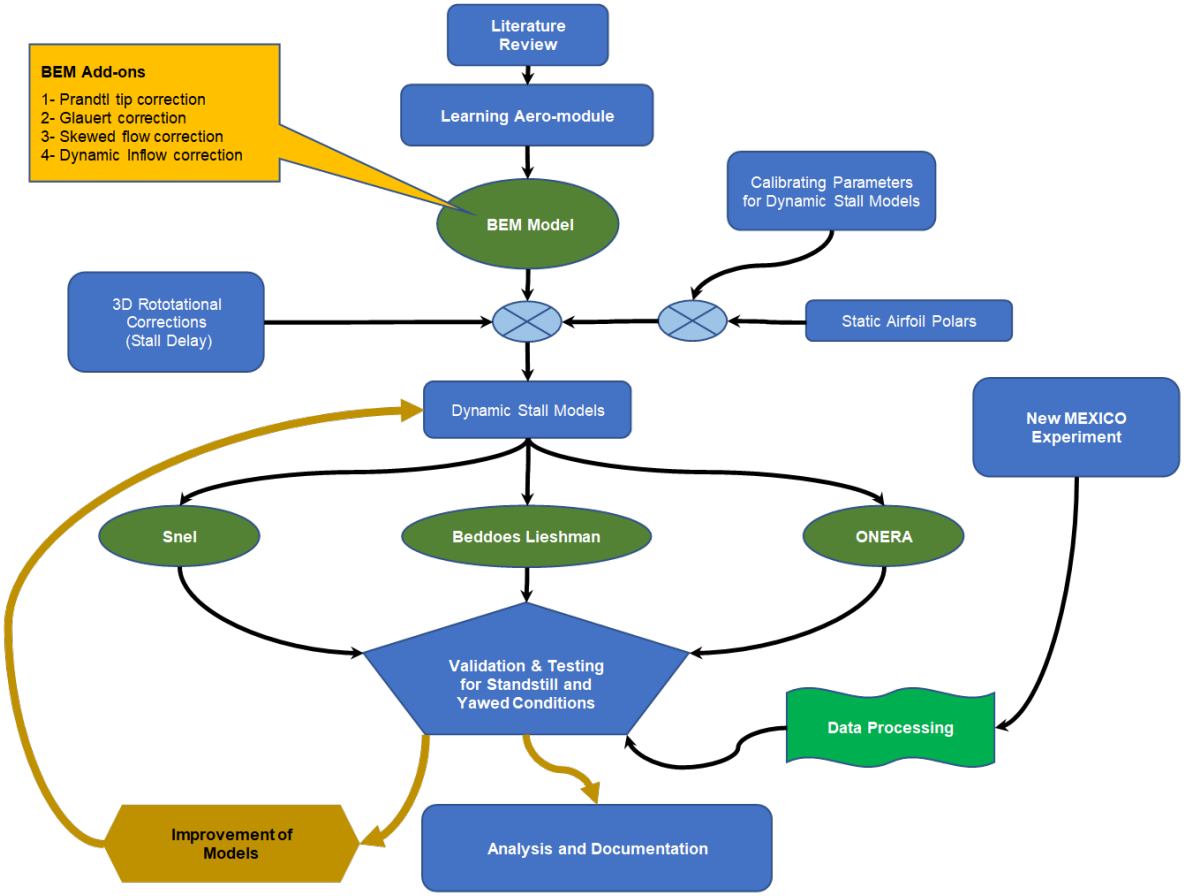

Figure 1.1: Research framework

1.5. Outline

The report starts with a brief introduction of theoretical background of the thesis and then moves on to discuss the work that has been done in the literature in Chapter 2. Chapter 3 discusses the New MEXICO database in detail along with analysis of pressure sensor data. Chapter 4 introduces the computational tool and presents a few validation results of standalone dynamics stall models and BEM simulations. Chapter 5 begins with analysis of New MEXICO standstill conditions and validates dynamic stall models. Improvements to Beddoes Leishman and ONERA model are also proposed at the end of this chapter. Chapter 6 investigates the effect of dynamic stall models on aerodynamic damping and the onset of edgewise instability on the AVATAR blade. Chapter 7 discusses the performance of dynamic stall in yawed conditions on the New MEXICO rotor. Finally, conclusions and recommendation are presented in Chapter 8.

2

Literature Review

This chapter provides an overview of the theoretical framework of this project and the research that has been done in the past on dynamic stall modeling. It starts with a brief overview of the unsteady aerodynamic environment of the wind turbine rotor. Followed by an introduction of the most common dynamic stall models being used in the industry and academia. In the subsequent section, an outline of the extent of experimental analysis on dynamic stall is presented. Lastly, the chapter emphasizes where the current research picks on.

2.1. Unsteady Aerodynamics of Wind Turbines

Rotating blades pose a serious challenge to aerodynamicists for predicting loads on a wind turbine. Mainly, because of the highly unsteady and three dimensional nature of such a flow field, which is still not fully understood [31, 48, 77, 84]. A host of different flow variables like: atmospheric turbulence, wind shear, wind veer, yawed flow, wind gusts, blade vibrations, and tower shadow effects add to the complexity of the flow over a wind turbine rotor, as shown in figure 2.1. Dynamic stall is one such complex flow phenomenon. In order to quantify the amount of flow unsteadiness, a non-dimensional parameter called reduced frequency is used. The reduced frequency (k) is defined as:

$$k = \frac{\omega c}{2U} \tag{2.1}$$

Where, ω is the characteristic frequency of the flow, c is the characteristic length, and U is the mean flow velocity. According to Leishman [44], for $0 < k < 0.05$ the flow is considered quasi-steady, $k > 0.05$ is treated as unsteady flow while $k > 0.2$ is characterized as a highly unsteady flow regime. However, Ricardo et al. [66] mentioned, in wind energy $k > 0.02$ is considered as an unsteady flow regime.

The stochastic nature of the wind coupled with the low rotational speed of wind turbines solicits that these machines will operate in a highly unsteady aerodynamic environment during their lifetime. Most common sources of unsteady aerodynamic effects on wind turbines are:

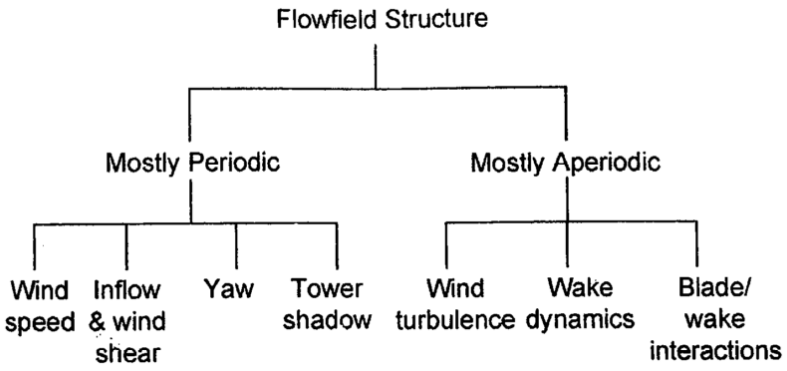

Figure 2.1: A schematic of the sources of unsteady aerodynamics on a wind turbine. Taken from Leishman [44].

1. **Wind sheer**: It is the vertical gradient in the wind velocity developed because of the friction with the ground. The wind sheer produces a vertical non-uniform velocity profile at the rotor disk, with higher velocities at the top and lower velocities at the bottom of the disk. Consequently, resulting in a skewed wake (the upper part of the wake convects faster than the lower part) and periodic variations in AoA.

2. **Yaw misalignment**: It happens when the wind turbine is facing out of the incoming wind direction. It commonly occurs on wind turbines because the yaw system is not fast enough to respond to sudden changes in wind direction. Therefore, the turbine has to operate for some time in yawed flow. Other causes could be a lack of accuracy in the yaw system to align with the incoming wind direction. In yawed flow a turbine experiences two main effects, as identified by Schepers [74]:

   (a) Advancing and retreating blade effect: Yaw misalignment leads to a component of incoming velocity in the rotor plane, which results in this effect along with constituting a skewed wake. This effect can be easily derived from the blade section velocity triangles at various azimuthal positions. For a positive yaw angle (β), a blade section will experience high AoA at the 12 o' clock azimuthal position and a low AoA at 6 o' clock azimuthal position of the blade, as shown in figure 2.2a. This high AoA at the top and low angle of attack at the bottom of rotor disc results in a tilting moment on the turbine rotor (because the velocity triangles are symmetric about a line from top to bottom of the rotor disc). However, in reality, it has been observed that a wind turbine experiences a restoring yawing moment when it is yawed. The reason for it can be explained through the skewed wake effect. It is to be noted, the advancing and retreating blade effect is most significant when the component of wind in the rotor plane ($U_\infty sin(\beta)$) is large enough to make a considerable difference between the AoA at the retreating and advancing side of the rotor disc. Alternatively, a lower angular velocity could also bring about this effect. Mathematically, meaning that this advancing and retreating blade effect is more likely to happen for lower tip speed ratios, where tip speed ratio (λ) is defined as:
   $$\lambda = \frac{R\Omega}{U_\infty}$$

   (b) Skewed wake effect: The wake of the rotor directly influences the induction at the rotor disc. Therefore, an un-symmetric or skewed wake, produced during yawed flow, would cast an imbalance in induction on the rotor disc. This imbalance is such that the upwind side of the disc has lower induction as compared to the downwind side of the rotor disc, as seen in figure 2.2b. Subsequently, a higher AoA at the upwind side and a lower AoA at the downside side results in creating the restoring yawing moment. As this effect has to do with induction at the rotor disc; therefore, it is most significant at higher tip speed ratios when the induction is high. Initially, Glauert [25] proposed a function that varies sinusoidally to model this phenomenon through induction at the rotor:
   $$a = \bar{a}\left(1 + K\frac{r}{R}\sin\psi\right) \tag{2.2}$$
   where, $\bar{a}$ is the average induction over the rotor disk, ψ is the azimuthal angle and K is a function of yaw angle. Since then, numerous attempts have been made in the literature to determine the function K. A summary of those various studies is presented by Micallef [57]. A slightly more accurate approach, although based on Glauert's theory, was determined by Schepers [73] using experimental data and based on a second order Fourier fit.

3. **Local sweep effects**: This effect arises when the local incident flow velocity is not normal to the blade section. Hence, eliciting a radial component of velocity along the blade span, as seen in figure 2.2a for a yawed rotor. It is seen from the figure that the sweep angle is maximum at the 3 o' clock and 9 o' clock azimuthal position while it is zero at the 12 o' clock and 6 o' clock azimuthal position. The radial component of flow from sweep angle complicates the aerodynamics further and a simple 2D blade section analysis where each section is assumed independent is no longer a valid assumption. This radial velocity has a direct influence on the boundary layer over the blade; therefore, directly effecting the onset of stall [44].

4. **Tower shadow**: This periodic effect happens whenever a blade crosses in front of the tower for an upwind turbine, or vice versa for a downwind turbine. However, the tower shadow effect is more pronounced for downwind turbines because of the larger velocity deficit and shed vorticity in the wake of the tower.

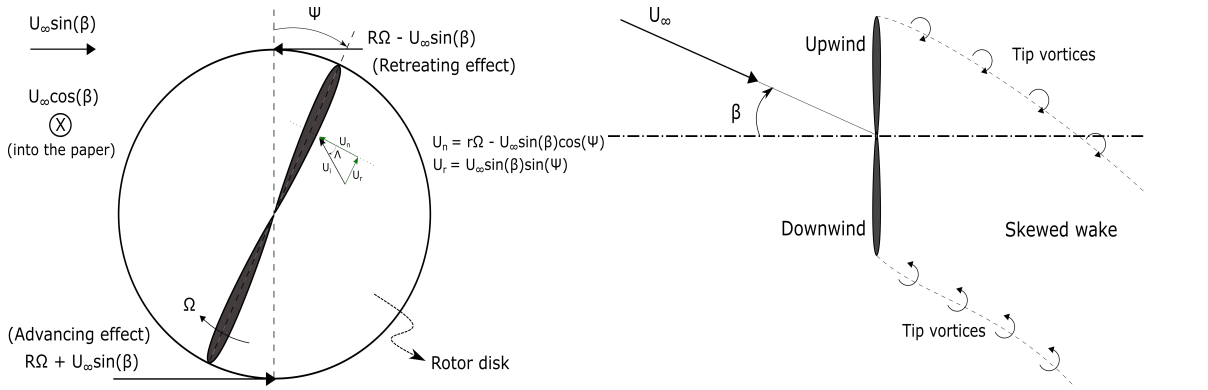

(a) Front view of the wind turbine rotor illustrating the advancing and retreating blade effect.

(b) Top view of the wind turbine rotor depicting the skewed wake effect.

Figure 2.2: A pictorial representation of a wind turbine in yawed flow with the accompanying effects. Ω is the rotational velocity of the rotor, ψ is the azimuthal angle, β is the yaw angle, U_∞ is the free-stream velocity, whereas U_i, U_n, and U_r are the local incident, normal, and radial velocity with sweep angle Λ.

Snel et al. [85] divided the non-stationary effects on a wind turbine into two parts: unsteady airfoil aerodynamics and dynamic inflow. These effects have completely different magnitudes of time scales; hence, as a simplification, can be analyzed separately. Dynamic stall is an unsteady viscous effect that falls under the umbrella of unsteady airfoil aerodynamics, along with Theodorsen's effect which is of non-viscous nature. While dynamic inflow describes the lag in the inflow velocity at the rotor plane due to trailing vorticity in the wake. Nonetheless, Leishman [48] advocates a different perspective. He is of the view that dynamic stall effects cannot be studied in isolation; a better understanding of the phenomenon needs just treatment of the wake vorticity. Because the trailing vorticity in the wake creates a non-uniform inflow velocity profile at the rotor plane; thus, exhibiting a non-uniform angle of attack (AoA) distribution.

In the subsequent sub-sections, some of the above mentioned unsteady aerodynamic effects on wind turbines will be discussed in detail.

2.1.1. Dynamic Inflow

From momentum theory, the axial induction at the rotor depends on the axial force exerted by the rotor on the wind. Whenever this axial loading is changed, a subsequent change in induction at the rotor is expected. However, due to the large mass of air passing through the rotor, the flow cannot respond to these changes instantaneously. Hence, there is a lag in the development of new induction at the rotor. This phenomena is termed as dynamic inflow or dynamic induction [77]. Dynamic inflow is closely associated with the trailing vorticity in the wake, and it can be easily explained through lifting line theory. For example, a sudden change in axial loading, through a step in pitch angle, changes bound circulation on the blade and trailing vorticity. The new strength trailing vorticity is convected slowly in the wake with a local velocity. Consequently, the wake is dominated by the old strength trailing vorticity which is still influencing induction at the rotor. As a result, induction at the rotor changes gradually as the new vorticity is convected downstream. It reaches a steady state once the new trailing vorticity has traveled 2-4 rotor diameters. At this stage, the effect of the old trailing vorticity is minimalistic. Dynamic inflow is typically modeled with a first order differential equation 2.3, as mentioned in Schepers [77]. Where, τ is a time constant directly proportional to the rotor size, u_i is the induced velocity at the rotor, and C_T is the axial thrust force coefficient.

$$\tau \frac{du_i}{dt} + 4u_i(1-u_i) = U_\infty C_T \tag{2.3}$$

Apart from a step change in pitch angle, change in rotor speed and wind speed can also change the induced velocity through changing axial loading on the rotor; thus, exhibiting dynamic inflow. However, Schepers [77] mentioned that a change in wind speed does not produce dynamic inflow effects like changes in rotor speed or pitch angle. The reason being, changes in wind speed do not change induced velocity at the rotor but, instead, they change ratio of induced velocity to free-stream velocity, called the axial induction factor a.

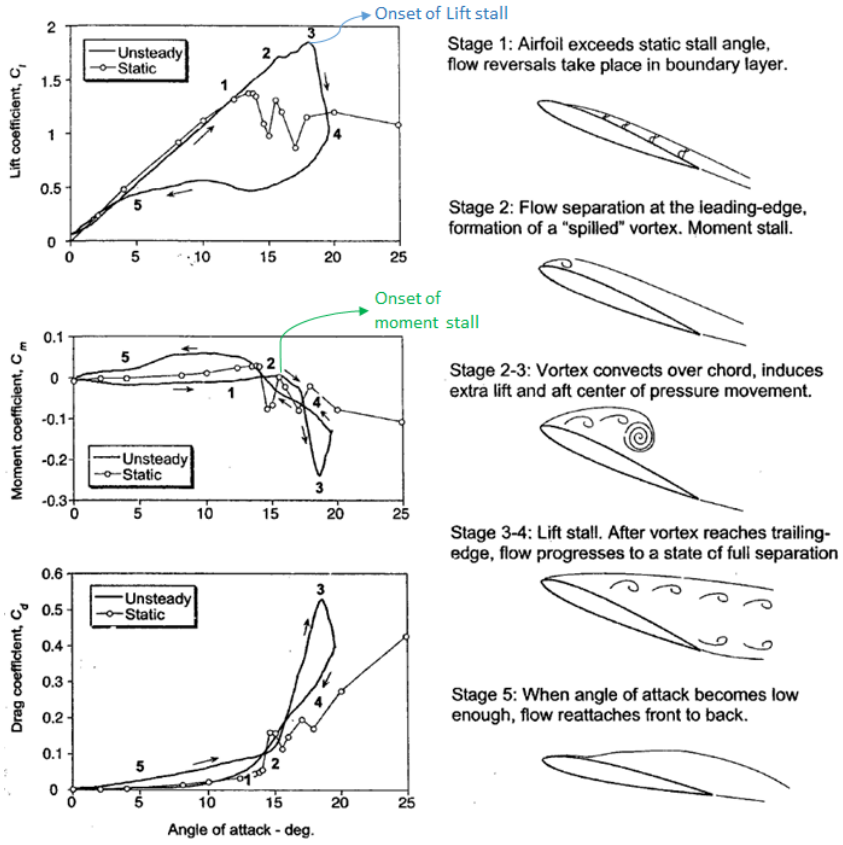

Figure 2.3: An illustration showing the different stages of flow development in a dynamic stall hysteresis loop on a 2D oscillating airfoil. Adapted from Leishman [44].

2.1.2. Dynamic Stall

Wind turbines typically operate at low rotational speeds; therefore, the inboard sections of the blades can experience large fluctuations in AoA due to variations in inflow velocity. Dynamic stall occurs on a wind turbine airfoil section due to these rapid changes in AoA, around the static stall AoA, which results in delaying the onset of stall to a much higher AoA than static stall [54]. Thus, leading to higher loads than predicted by the airfoil static polars. Dynamic stall not only delays the onset of stall, but also delays the re-attachment of flow after stall. Furthermore, dynamic stall is characterized by the formation of a large vortex near the leading edge. This leading edge vortex (LEV), once detached, moves over the upper surface to give additional lift increment till it crosses the trailing edge. The increase in maximum lift due to dynamic stall maybe beneficial in some circumstances; however, the violent vortex breakdown can result in strong oscillations on the structure of the blades, exhibiting a potential for catastrophic failure [59]. Moreover, dynamic stall greatly effects the aerodynamic damping of the blade section. According to McCroskey [54], stall-induced negative damping can materialize into single degree of freedom flutter (non-classical flutter) for pitching and plunging oscillations in an airfoil.

The flow over an airfoil in dynamic stall can be classified into five sequential stages, as identified by Leishman [44] and re-iterated, recently, by Mulleners and Raffel [59]. An illustration of these five stages is shown in figure 2.3. During the first stage, as the AoA increases from minimum value to the static stall angle, the lift also increases while closely following the static trend and the flow remains attached throughout. However, once the static stall angle is exceeded, recirculation starts appearing in the boundary layer near the trailing edge. But, this does not, yet, result in loss of lift due to increasing leading edge suction peak and the development of a LEV in stage two. After stage two, The LEV convects over the suction side, and as it convects the center of pressure[1] moves downstream along the chord with it. This results in a large nose-down pitching

[1] Center of pressure moves with the LEV because the LEV creates a region of low pressure at its core. As it moves along the suction side of airfoil, it distorts the pressure coefficient (C_p) distribution by increasing suction over the region where it passes. Effectively, shifting the center of pressure rearward as it moves over the airfoil surface.

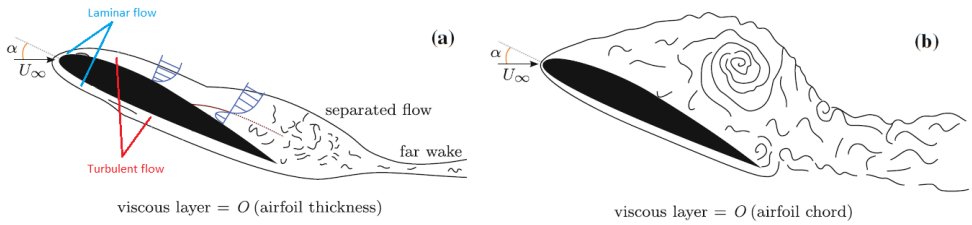

Figure 2.4: Depiction of flow topology difference between light stall and deep stall. Adapted from Mullener and Raffel [59].

moment, called moment "break" or moment stall, which is near point three in figure 2.3. It is to be noted that the onset of moment "break" occurs when the LEV starts convecting downstream or, correspondingly, when the leading edge suction peak reaches its maximum. After the LEV crosses the trailing edge, the lift coefficient abruptly decreases, called lift stall, due to the airfoil undergoing complete flow separation. The reattachment of the flow is delayed and occurs at a very low AoA.

Mulleners and Raffel [59] are of the view that complete understanding of the dynamic stall phenomenon is still lacking. Especially, the knowledge about the formation of the LEV and what induces its detachment from the airfoil is still a topic under hot debate. Therefore, they conducted elaborate experiments on an oscillating OA209 airfoil using pressure sensors and stereoscopic PIV. It was observed that the LEV induces small counter-rotating vortices, generated at the trailing edge, to move towards the leading edge. Eventually, being forced to detach because of this vortex-induced separation.

In subsonic flow, typical for wind turbines, dynamic stall can be classified into two different regimes. McCroskey [54] classified dynamic stall based on the extent of flow separation (The amount of flow separation is proportional to the maximum AoA for oscillating airfoils), whereas Mulleners and Raffel [59] presented a differentiation between light and deep dynamic stall based on occurrence of stall onset. In view of both these definitions, an explanation of light and deep dynamic stall is presented below:

Light Stall
Light stall is characterized by a viscous zone which has a thickness on the order of airfoil thickness, as shown in figure 2.4. In light stall, the dynamic stall onset angle is higher than the maximum AoA of the oscillation; therefore, forcing the separation of the dynamic stall vortex at the end of upstroke (first half of oscillation cycle). Light stall is effected by airfoil geometry and thickness, reduced frequency, maximum AoA, 3D effects, and the type of motion. Also, light stall is more prone to negative aerodynamic damping because of periodically moving in and out of stall.

Deep Stall
Deep stall has a larger viscous layer compared to light stall, which occurs during vortex-shedding. Vortex shedding is dominant in this stall regime; it produces high values of airloads when the vortex passes over the suction side of the airfoil. In deep stall the stall onset angle is reached ahead of the maximum AoA of the oscillation, as seen in figure 2.5. Deep stall has a lower tendency of producing negative aerodynamic damping, because of the large negative moment from the convecting vortex and the onset of moment stall before lift stall.

2.1.3. Three Dimensional Effects

The flow over a rotating blade is highly three dimensional and, in many instances, can be attributed to three dimensional boundary layer development over the blade [48]. In such a flow, centrifugal and Coriolis effects are prominent in influencing the boundary layer. According to Lindenburg [51], the Coriolis force, acting in the chordwise direction, in association with 'centrifugal pumping' stabilizes the boundary layer and pushes the separation point near the trailing edge. Effectively, increasing the suction on the airfoil's upper surface and delaying stall. 'Centrifugal pumping' mainly facilitates an outward spanwise flow, from root to tip, which tends to increase suction on the upper surface. On the other hand, Coriolis force acts on the spanwise moving flow in chordwise direction, as shown in figure 2.6. Consequently, mitigating effects of flow separation and pushing the separation point towards the trailing edge. Three dimensional corrections to the two dimensional airfoil data have been proposed in the literature to model these effects [51, 82]. A simplified model proposed by Snel [82] is expressed below:

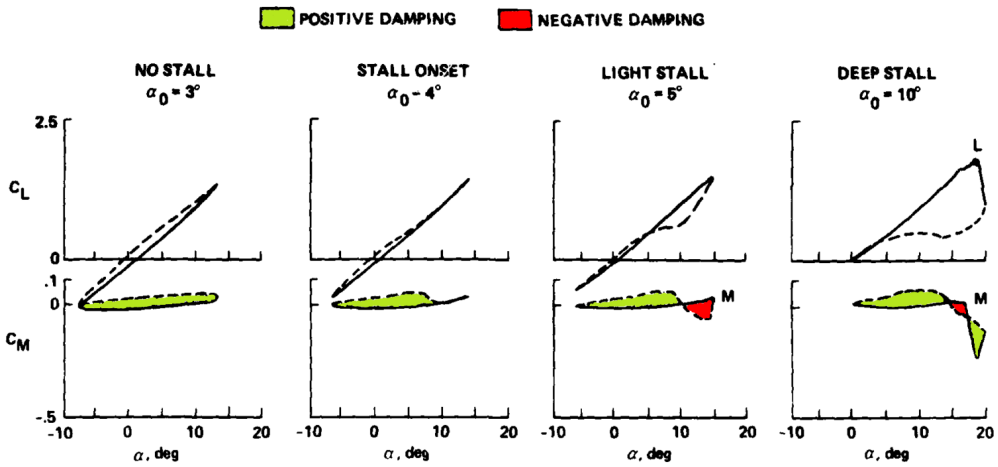

Figure 2.5: Different flow regimes for a pitching NACA 0012 airfoil. The pitch oscillation is prescribed, about the quarter chord point, according to the function (in degrees): $\alpha = \alpha_0 + 10sin(\omega t)$, with $k = 0.1$. The solid lines show upstroke motion while dashed lines show downstroke motion. The area enclosed by the moment curves represent the average cycle damping or the net work done on the fluid by the body, defined as $W_{net} = -\oint C_M d\alpha$. Reproduced from McCroskey [54].

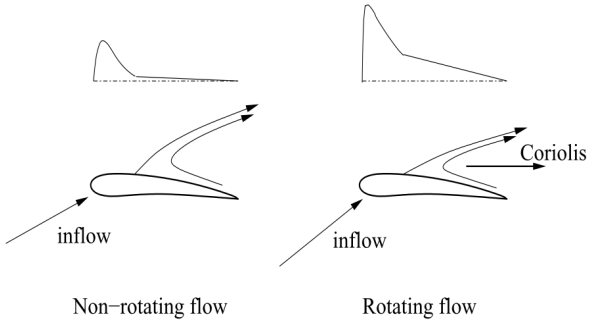

Figure 2.6: A comparison between flow across a rotating and non-ration airfoil section. Above each airfoil section, a rough representation of the respective suction pressure distribution along the chord is presented. Courtesy of Lindenburg [51].

$$C_{l,3D} = C_{l,2D} + 3.1(\frac{c}{r})^2 (C_{l,pot} - C_{l,2D}) \tag{2.4}$$

$$C_{l,pot} = C_{l_0} + 2\pi\alpha \tag{2.5}$$

Where, $C_{l,3D}$ is the corrected lift coefficient for three dimensional effects and $C_{l,2D}$ is the lift coefficient from 2D airfoil data. This correction is only applicable till 80 percent radial position and a maximum AoA of 30 degrees. After 30 degrees, the lift correction has to linearly decrease to zero at 50 degree AoA. Another often overlooked three dimensional effect is that of local sweep angle on a rotating blade section [48]; however, strong evidence of this effect on wind turbines is still lacking. Dynamic stall with sweep was observed to increase the maximum and mean lift coefficient while delaying stall to a higher AoA in comparison to dynamic stall with zero sweep. Moreover, Leishman suggested that sweep causes a lower convection velocity for the shed leading edge vortex; hence, delaying the dynamic lift to a higher AoA. He also made modification to the original Beddoes-Leishman model to incorporate these effect [45], documenting an improved prediction of unsteady loads.

2.2. Aerodynamic Models

Generally, three different types of modeling approaches are used to model the aerodynamics of a wind turbine. These include Blade-Element Momentum model, Lifting Line model, and CFD. CFD has the most computational head and accuracy among the other approaches. CFD relies on solving the Navier-Stokes equations to model the flow around a wind turbine rotor in a discretized computational domain. Due to the large

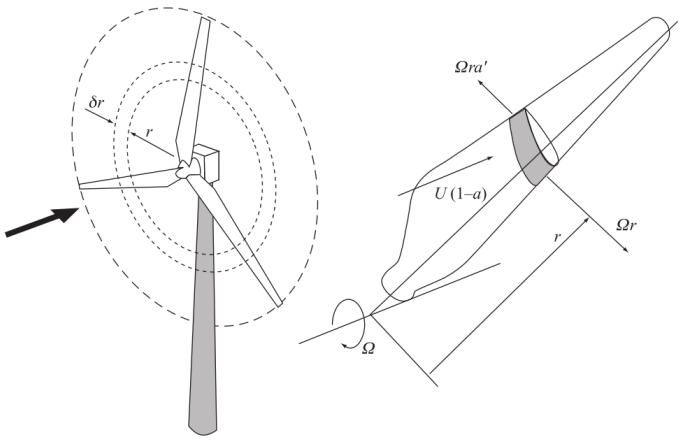

Figure 2.7: Diagram showing the discretization of a wind turbine rotor disk into annular elements. Reproduced from [13].

computational resources required by CFD, it is seldom used in an iterative design process or load certification analysis. Lifting line models are less computationally expensive than CFD because instead of discretization of a volume in space they discretize bound circulation on the blade and circulation in the wake (in the form of trailing and shed vortices). Nonetheless, they are still computational expensive as compared to BEM model as it only solves for forces and moments at the blade without solving the complete flow field around the blade. In the subsequent sections BEM model and Lifting Line or Vortex Wake model will be discussed in further detail.

2.2.1. Blade-Element Momentum Model

The BEM model has its foundation on momentum theory (MT) and strip theory or blade element theory. The momentum part deals with modeling the induction aerodynamics while the blade element part models blade aerodynamics [77]. The rotor is discretized into annular elements with radius r and length δr, as shown in figure 2.7. These annular elements exert axial and tangential force on the air passing through the rotor disk; thus, changing its axial and angular momentum, respectively. By virtue of the third law of motion, the air exerts an equal force on each annulus. These forces on the annulus are, effectively, exerted on the blade sections. According to strip theory, the loads on blade sections can be computed from the steady 2D airfoil characteristics.

Momentum Theory

The purpose of a wind turbine is to extract kinetic energy from the wind. In doing so, the rotor slows down the incoming wind and creates a pressure drop at the rotor disc. This process can be seen in figure 2.8 through a energy extracting streamtube. The rotor acts as a permeable actuator disc. The incoming flow slows down upstream of the actuator disc and static pressure increases. At the actuator disc the flow experiences a sudden drop in pressure while the velocity keeps on decreasing. In the far wake, the pressure is restored to its free stream value yet the velocity is less than the free-stream velocity. It is to be noted that, according to conservation of mass, the mass flow rate across the streamtube would remain constant that is

$$\dot{m} = \rho A_\infty U_\infty = \rho A_D U_D = \rho A_W U_W \tag{2.6}$$

It is assumed that the actuator disc retards the free-stream velocity by an axial induction factor a as

$$U_D = U_\infty(1-a) \tag{2.7}$$

The actuator disc imparts a change in momentum to the flow passing through the streamtube by decreasing the flow velocity. This change in momentum is equal to the pressure force across the actuator disc.

$$(p_D^+ - p_D^-)A_D = (U_\infty - U_w)\dot{m} \tag{2.8}$$

The right hand side of the above equation represents the rate of change of axial momentum while the left hand side represents the pressure force across the actuator disc. On applying Bernoulli's, equation to the

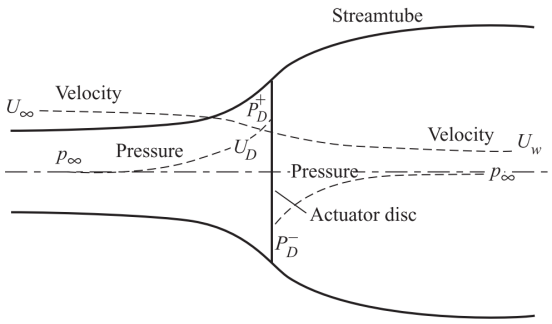

Figure 2.8: Energy extraction from the incoming flow by an actuator disc. From [13].

upstream and downstream of the streamtube separately the following relation can be derived between the axial induction factor and the velocity in the far wake.

$$U_D = U_\infty(1-2a) \tag{2.9}$$

The power extracted from the wind can be expressed as the product of thrust force times velocity at the actuator disc (that is the work done per unit time):

$$T = (p_D^+ - p_D^-)A_D = 2\rho A_D U_\infty^2 a(1-a) \tag{2.10}$$

$$P = TU_D = 2\rho A_D U_\infty^3 a(1-a)^2 \tag{2.11}$$

where, T is the thrust force and P is the power extracted from the wind. They can be expressed in non-dimensional form as thrust and power coefficient, respectively.

$$C_T = \frac{T}{\frac{1}{2}\rho U_\infty^2 A_D} = 4a(1-a) \tag{2.12}$$

$$C_P = \frac{P}{\frac{1}{2}\rho U_\infty^3 A_D} = 4a(1-a)^2 \tag{2.13}$$

From equation 2.10, the incremental thrust produced by an annular element can be expressed as

$$\delta T = 4\rho\pi r U_\infty^2 a(1-a)\delta r \tag{2.14}$$

The actuator disc not only retards the axial flow velocity but also imparts a tangential velocity component to the flow. The direction of this tangential component is opposite to the direction of rotor rotation and is expressed through a tangential induction factor a' as $r\Omega a'$ at the rotor disk and $2r\Omega a'$ in the far-wake. This tangential velocity is imparted to the flow because of the aerodynamic torque on the rotor. The rotor exerts an equal and opposite torque (tangential force) on the flow which changes the angular momentum of the flow. Hence, the aerodynamic torque is equal to the rate of change of angular momentum of the flow.

$$\delta Q = r\delta\dot{m}(2r\Omega a') = 4\rho\pi r^3 U_\infty a'(1-a)\Omega\delta r \tag{2.15}$$

where δQ is an incremental torque on an annular element.

Blade Element Theory

The blade element theory (BET) discretizes the blade into airfoil cross-sections of span δr and chord c at a radial location r, as depicted in figure 2.7. The forces on these discrete elemental airfoil cross-sections is calculated through the steady 2D airfoil polars. The AoA at each cross-section is computed through a velocity triangle as shown in figure 2.9(a). From the velocity triangle, the resultant relative velocity seen by the blade element is given by

$$W = \sqrt{(U_\infty(1-a))^2 + (r\Omega(1+a'))^2} \tag{2.16}$$

while the AoA is computed as

$$\alpha = \phi - \theta \tag{2.17}$$

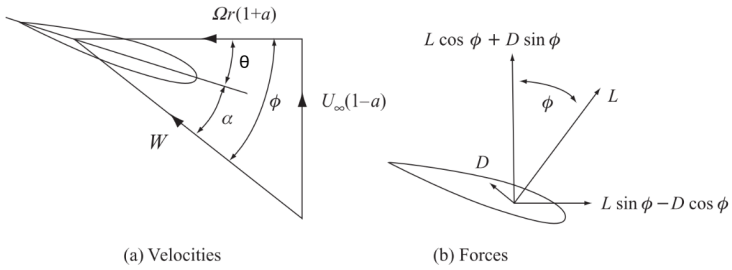

Figure 2.9: Velocity triangles and forces at a blade cross-section. θ and ϕ denote pitch and flow angle, respectively. From [13].

where, θ is the local pitch angle at the blade element and is the sum of aerodynamic twist and global pitch angle. With the AoA, lift and drag force can easily be computed. The lift and drag force contribute to the axial and tangential force component depending on the flow angle, as seen in figure 2.9(b).

$$\delta T = \frac{1}{2}\rho W^2 Bc(C_l \cos\phi + C_d \sin\phi)\delta r \tag{2.18}$$

$$\delta Q = \frac{1}{2}\rho W^2 Bcr(C_l \sin\phi - C_d \cos\phi)\delta r \tag{2.19}$$

where B is the number of rotor blades.

One of the main underlying assumption of BEM theory is that the change in momentum of the air passing through an annulus of the rotor disc is only brought about by forces from the blade element in that annulus [13]. This assumption leads to combining the thrust equations 2.18 with 2.14 and the torque equations 2.19 with 2.15 to give the following set of equations

$$\frac{W^2}{U_\infty^2} B\frac{c}{R} C_x = 8\pi a(1-a)\mu \tag{2.20}$$

$$\frac{W^2}{U_\infty^2} B\frac{c}{R} C_y = 8\pi\lambda a'(1-a)\mu^2 \tag{2.21}$$

where, $\mu = \frac{r}{R}$, C_x is the axial force coefficient, and C_y is the tangential force coefficient. The above two equation are solved in an iterative fashion to arrive at a converged solution.

Assumptions and Limitations
The classical BEM theory is limited to steady, uniform, axially aligned flow. The momentum theory break downs for a heavily loaded rotor (i.e. $a > \frac{1}{2}$) as it gives reverse flow in the far wake. The actuator disc model in the BEM theory assumes an infinite number of blades and neglects tip losses. 2D steady airfoil data is used to determine the lift and drag characteristics of airfoil sections while in reality the flow is highly unsteady and three dimensional. Therefore, various engineering add-ons are required to correct the BEM model for more complicated flow regimes, like Glauert's correction for heavily loaded rotor and Prandtl's tip loss correction, a summary of engineering corrections is presented in table 2.1 . Even with these corrections, certain intrinsic limitations of the BEM code still exist. Most important of all are the assumptions that each annular blade element is independent and absence of spanwise flow and radial induction. However, this is not true for a rotating blade which has a highly three dimensional flow with every blade cross-section inducing the flow over the entire blade [48].

2.2.2. Vortex Wake Models

These type of models are based on potential flow theory. A linearized potential flow (irrotational flow) solution is obtained to calculate the velocities and pressures at any point in the domain using superposition of elementary flow solutions. Using this principle any complex flow field can be determined. These model rely heavily on Biot-Savart law [42]. According to this law, velocity induced $\vec{v}_i$ at any point P in space, as seen in figure 2.10a, due to a vortex filament of strength $\vec{\zeta}$ (vorticity) can be computed using the relation:

$$\vec{v}_i = \frac{\Gamma}{4\pi}\int \frac{d\vec{l}(\vec{r}_0 - \vec{r}_1)}{|\,\vec{r}_0 - \vec{r}_1\,|^3} \tag{2.22}$$

Table 2.1: Summary of engineering add-ons or corrections used in a BEM model.

Assumptions/Limitations	Engineering Add-ons/Corrections
lightly loaded rotor (wind mill state)	Glauert's correction for heavily loaded rotor
Infinite number of blade (actuator disc)	Prandtl's tip loss correction
Axially aligned flow	Glauert's correction for yawed flow
Steady flow	Dynamic inflow
Spanwise flow neglected	Stall delay or rotational augmentation
Steady, uniform, axial flow	Dynamic stall
Infinite blade span	3D correction

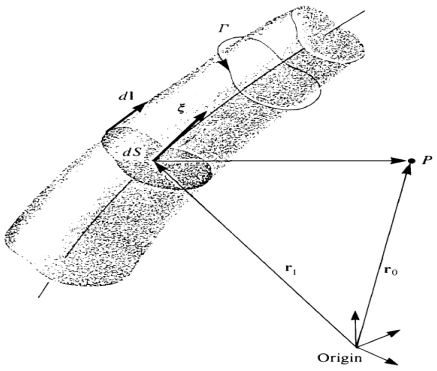

(a) Velocity induced at point P by a vortex segment.

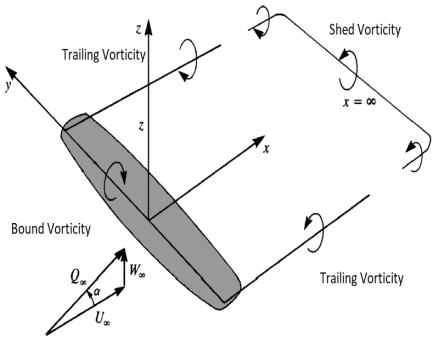

(b) Representation of a finite wing using a far field horseshoe model.

Figure 2.10: Adapted from [42].

where, Γ is circulation and is defined as the line integral about a closed curve C in a velocity field $\vec{v}$. Or, according to Stokes theorem, as the surface integral of the vorticity normal to the surface enclosed by the closed curve C.

$$\Gamma = \oint_C \vec{v} \cdot d\vec{l} = \int_S \vec{\zeta} \cdot \vec{n} dS \tag{2.23}$$

The vorticity is measure of flow rotation. It is defined as twice the angular velocity $\vec{\omega}$ of fluid element or the curl of velocity field.

$$\vec{\zeta} = 2\vec{\omega} = \nabla \times \vec{v} \tag{2.24}$$

In vortex wake models, the blade of a wind turbine is modeled with a lifting line or a lifting surface representing bound vorticity on the blade. The lifting line is discretized into vortex line filaments. According to Helmholtz theorem, these vortex filaments cannot end or start in space and their strength is assumed constant. As a result, they have to form a loop that is closed by trailing and shed vorticity of the same strength, as shown in figure 2.10b for the case of a finite wing modeled with a single vortex filament of strength Γ as an example. The trailing and shed vorticity together model wake of the blade. Using Biot-Savart law, the induced velocity at the blade due to all vortex filaments is computed as a linear summation, which gives the AoA at the blade sections. The AoA can then be used to determine lift and drag coefficients from static airfoil polar. Subsequently, lift can be used to find the bound circulation on a blade section conforming to Kutta–Joukowski theorem.

$$L' = \rho V \Gamma \tag{2.25}$$

L' is the lift per unit span at a particular blade section while V represents the incoming flow velocity. The new value of circulation is compared with the initial value (guess) to quantify the difference and reach a converged solution in an iterative fashion.

The vortex wake methods are broadly classified into two categories, namely, frozen wake models and free wake model. In frozen wake model, the geometry of the wake is prescribed as a priori based on the rotor geometry and undisturbed flow. Hence, there is no deformation of the wake. On the other hand, in case of a free wake model, the induction on the wake due to bound circulation on blade and wake self-induction is

taken into account resulting in deformation of the wake. The latter also requires more computational time in comparison to the former.

Assumption and Limitations
In contrast to BEM model, vortex wake model is able to model radial induction, tip losses, yawed flow, turbulent wake state, and dynamic inflow in an intrinsic manner [34]. However, like BEM model, it needs engineering methods to correct for stall delay and dynamic stall. A main drawback of these methods is the relatively large computational requirements in comparison to BEM model.

2.2.3. CFD Models

Computational fluid dynamic models are the most advanced and complicated models for simulating aerodynamic flow around a wind turbine. There are different types of CFD models but they all make use of the same set of governing equation of fluid flow. These governing equation are commonly known as the Navier-Stokes equations and are based on conservation laws such as mass, momentum, and energy conservation. For purposes of simulating flow around wind turbine mass conservation and momentum conservation equations are more relevant. A simplified representation of these equations is presented below:

$$\frac{\partial \rho}{\partial t} + \nabla \cdot (\rho \boldsymbol{u}) = 0 \tag{2.26}$$

$$\frac{\partial \boldsymbol{u}}{\partial t} + (\boldsymbol{u} \cdot \nabla)\boldsymbol{u} = -\frac{1}{\rho}\nabla p + \boldsymbol{F} + \frac{\mu}{\rho}\nabla^2 \boldsymbol{u} \tag{2.27}$$

equation 2.26 represents conservation of mass while equation 2.27 represents conservation of momentum. Where, $\boldsymbol{u}$ is velocity vector, p is pressure, and $\boldsymbol{F}$ represents body forces. Reynolds Averaged Navier-Stokes (RANS) equations are the most widely used CFD approach. They use time averaged Navier-Stokes equations to solve the flow field along with turbulence models to obtain closure of numerical solution. A far more superior approach is called Large Eddy Simulation (LES). LES uses spatial averaging instead of time averaging to resolve large scale coherent structures in the flow field while small turbulent structures are modeled. This approach has gained a lot of momentum in recent years due to increasing computational power of computers. Finally, Direct Numerical Simulation (DNS) is the most computationally expensive approach to CFD. Instead of leaving small scale turbulent structures to modeling, it resolves turbulence on all scales. Ranging from forcing scale, where large turbulent structures are created, to Kolmogorov scale where turbulent energy is dissipated into heat. DNS has the most computational head in comparison to LES and RANS; therefore, its use in practical problems is close to non-existent.

2.3. Dynamic Stall Models

An important aspect in simulating dynamic stall on a wind turbine is the dynamic stall model itself. A multitude of engineering models are being used in the industry and academia to predict dynamic stall. Initially, most of the dynamic stall models were developed for helicopter aerodynamics, for example, the Beddoes-Lieshmann [46] and ONERA model [93]. Nonetheless, there are dynamics stall models specifically tailored for wind turbine applications, like, DTU Risø model [33], Larsen's model [43], Snel's model [81], and Øye's model [60]. One of the main difference between helicopter aerodynamics and wind turbines aerodynamics is the absence of compressibility effects in the latter. Moreover, another main difference, is the use of thicker airfoils on wind turbine rotors. These differences require modifications in the dynamic stall models which are based on helicopter aerodynamics, to adapt them for wind turbine applications. Typically, dynamic stall models try to model the physical mechanisms governing dynamic stall with the help of differential equations. On the other hand, there are some dynamic stall models largely based on mathematical reasoning to reproduce dynamic stall effects. Nonetheless, majority of these different types of dynamics stall models rely on a steady airfoil polar as a backbone curve. As a result, they are called semi-empirical dynamic stall models. An in-depth overview of three most commonly used dynamic stall models, the ONERA, Snel, and B-L model, is presented in the subsequent sub-sections.

The ONERA, Snel, and B-L model rely on the steady airfoil polars; hence, their performance is limited by the quality of this data. Furthermore, each model has its own specific limitation. ONERA model is based on a linearizion assumption that the change is angle of attack is small, which is definitely not common on a wind turbine in yaw [40]. Snel's model mainly relies on mathematical modeling to reproduce the lift hysteresis around a steady polar, with limited flow physics modeling. It was originally tuned and tested for a limited

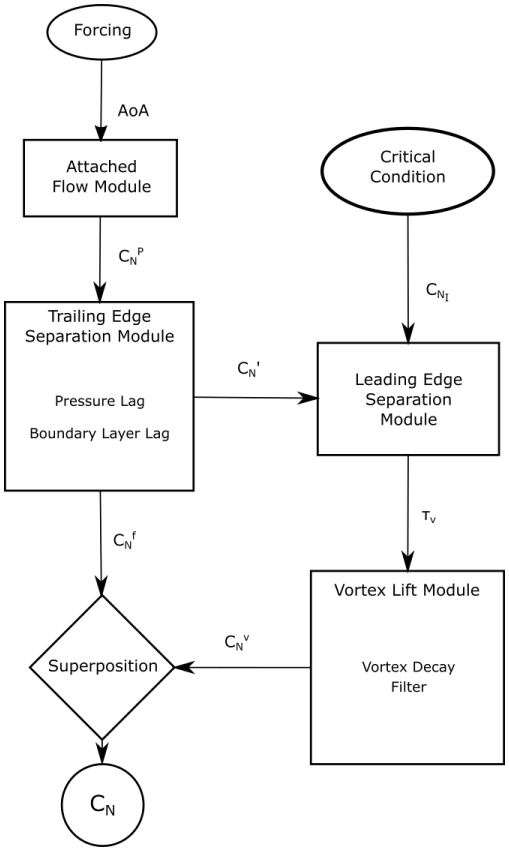

Figure 2.11: A flow diagram showing the various modules of the B-L model and their inputs and outputs.

number of airfoils. On the contrary, B-L model tries to model the physical process governing dynamic stall; nonetheless, it has no provision for modeling high frequency flow dynamics of self-excited nature [81] and effects of time-varying free-stream velocity are also ignored [33]. While Snel's model has a special provision in the form of a second order non-linear differential equation to model the high frequency dynamics without any external forcing.

2.3.1. Beddoes-Leishman Model

The B-L model is the most widely used and extensively tested dynamic stall model in the literature. B-L model primarily tries to simulate the physical mechanisms governing the phenomenon of dynamic stall mentioned in 2.1.2. These flow mechanisms are simulated by mathematically delaying the lift coefficient of attached flow, delaying the development of flow separation, and augmenting the lift coefficient through a convecting leading edge vortex. B-L model was originally developed by Beddoes and Leishman [46] for helicopter applications. Gupta and Leishman [30] adapted this model to make it suitable for wind turbine applications and tested it on a S809 airfoil. A reduced version of the model was developed by Hansen et al. [33], where the effects of leading edge separation (because of using relatively thick airfoils on wind turbines) and compressibility were ignored; thus, reducing the number of tunning parameters. However, the development of bigger wind turbines with active pitch control (for damping tower fore-aft vibrations) has pushed the blades to endure higher pitch rates and larger deformations due to increased flexibility. Therefore, leading edge separation has become probable on thick wind turbine airfoils and should be included in the modeling [43].

The B-L model simulates the governing physical mechanisms of dynamic stall in four separate modules and the results are then combined in a linear fashion to obtain the total unsteady lift. The different modules are depicted as a flow chart in figure 2.11; the forcing input is in the form of AoA variation in time. An indicial formulation of the B-L is particularly suited for obtaining a transient solution in a time marching fashion. Each of the constituent modules of the model are discussed as follows, using [46] and [30] as reference.

1. **Attached Flow Module:** Theodorsen's theory [89] for unsteady flow over a flat plate is the basis behind this module. A rational function approximation of the Theodorsen's function is used to model the lag in

lift build-up due to a sudden change (step) in angle of attack. The indicial lift responses obtained from this function are superimposed using Duhamel integral over time. This gives the circulatory part of the lift, which comes from the wake behind the airfoil. The non-circulatory part of lift has an impulsive and added mass contribution. The impulsive contribution comes from compressibility effects related to piston theory, as mentioned by Leishman and Beddoes [46], and are also modeled using indicial function approximation. The mathematical formulations for the circulatory and non-ciculatory lift are

(a) Ciculatory lift: The ciculatory normal force is given by

$$C^C_{N,n} = C_{N_\alpha}(\alpha_{E,n} - \alpha_0) = C_{N_\alpha}(\alpha_n - X_n - Y_n - \alpha_0) \tag{2.28}$$

where α_E is the effective angle of attack at the airfoil section. The subscript n denotes the current time sample. The time difference between time samples is given by $\Delta t = t_n - t_{n-1}$. X_n and Y_n are the deficiency functions representing the effects of shed wake vortices and are expressed as

$$X_n = X_{n-1}\exp\big(-b_1\Delta S\big) + A_1\Delta\alpha_n\exp\big(-b_1\Delta S/2\big) \tag{2.29}$$
$$Y_n = Y_{n-1}\exp\big(-b_2\Delta S\big) + A_2\Delta\alpha_n\exp\big(-b_2\Delta S/2\big) \tag{2.30}$$

where $\Delta S = \frac{2V\Delta t}{c}$ is the non-dimensional incremental time with V being the local free-stream velocity at the airfoil section. $1/b_1$, and $1/b_2$ are time constants of the lag (deficiency) equations 2.29 and 2.30, respectively, with A_1 and A_2 being their corresponding coefficients.

(b) Non-ciculatory lift: The non-circulatory normal force is given by

$$C^I_{N,n} = \frac{4K_\alpha c}{V}\Big(\frac{\Delta\alpha_n}{\Delta t} - D_n\Big) \tag{2.31}$$

and the deficiency function is obtained from

$$D_n = D_{n-1}\exp\left(\frac{-\Delta t}{K_\alpha T_I}\right) + \left(\frac{\Delta\alpha_n - \Delta\alpha_{n-1}}{\Delta t}\right)\exp\left(\frac{-\Delta t}{2K_\alpha T_I}\right) \tag{2.32}$$

The above deficiency function, like equation 2.29 and 2.30, has a decaying first part and an incremental second part. Although, unlike equation 2.29 and 2.30, it models the accretion of pressure disturbances over time. $T_I = c/a$ is the non-circulatory time constant which gives an indication of propagation time for pressure disturbances over the airfoil; hence, characterizing the decay of impulsive loads. This time constant after being multiplied with a K_α factor gives the time constants for equation 2.32. As described in [46], K_α factor depends on Mach number and is nearly constant for incompressible flow regime ($M < 0.3$, typical for wind turbines).

The total normal force coefficient for attached flow (potential flow lift) is expressed as the sum of the circulatory and non-circulatory components.

$$C^P_{N,n} = C^C_{N,n} + C^I_{N,n} \tag{2.33}$$

The pitching moment coefficient and chordwise force coefficient can be derived in a similar manner.

2. **Trailing Edge Separation Module:** Non-linear effects of trailing edge flow separation are included in this module through a dimensionless separation point parameter 'f', using Kirchhoff's theory. Moreover, a lag in flow separation is also incorporated in the form of a pressure lag and boundary layer (viscous) lag. According to Kirchhoff's theory, the non-linear static normal force can be obtained from

$$C_N = C_{N_\alpha}\left(\frac{1+\sqrt{f}}{2}\right)^2(\alpha - \alpha_0) \tag{2.34}$$

On re-arranging, the above expression, f can be expressed as a function of angle of attack. C_N and α values are used from the static airfoil data and a piece-wise exponential function is fitted to obtain a smooth variation of f with α. As f would correspond to a static flow behaviour, it needs to be modified for unsteady flows. In unsteady flow trailing edge separation also experiences lag due to leading edge

pressure and boundary layer development. The pressure lag is incorporated through the following equation

$$C'_{N,n} = C^p_{N,n} - D_{p,n} \tag{2.35}$$

$$D_{p,n} = D_{p,n-1}\exp\left(-\frac{\Delta S}{T_p}\right) + \left(C^p_{N,n} - C^p_{N,n-1}\right)\exp\left(-\frac{\Delta S}{2T_p}\right) \tag{2.36}$$

The time constant T_p depends on Mach number and is mainly independent of airfoil shape. It can be obtained from unsteady airfoil data. From C'_N, another effective angle of attack α_f is determined, which is used to determine an effective separation point $f' = f(\alpha_f)$

$$\alpha_{f,n} = \frac{C'_{N,n}}{C_{N_\alpha}} + \alpha_0 \tag{2.37}$$

Another first order filter is used on the effective separation point for boundary layer lag effects

$$f''_n = f'_n - D_{f,n} \tag{2.38}$$

$$D_{f,n} = D_{f,n-1}\exp\left(-\frac{\Delta S}{T_f}\right) + \left(f'_n - f'_{n-1}\right)\exp\left(-\frac{\Delta S}{2T_f}\right) \tag{2.39}$$

T_f is a time constant dependent upon Mach number. However, unlike T_p, it is dependent on airfoil shape. It can be determined from unsteady airfoil data or unsteady boundary layer code. Finally, the unsteady normal force coefficient representing trailing edge separation is calculated as

$$C^f_{N,n} = C_{N_\alpha}\left(\frac{1+\sqrt{f''_n}}{2}\right)^2(\alpha_{E,n} - \alpha_0) + C^I_{N,n} \tag{2.40}$$

3. **Leading Edge Separation Module:** For static conditions, onset of leading edge separation occurs when a critical leading edge pressure is achieved. As leading edge pressure is directly proportional to the normal force coefficient C_N; therefore, it is easy to define a criteria based on a critical value of C_N, called critical normal force coefficient C_{N_1}. This criteria is used to update a non-dimensional vortex time parameter[2] (τ_v), which keeps track of the location of the concentrated vorticity. It is to be noted that in unsteady conditions there is a lag is leading edge pressure, meaning that the critical condition will be obtained at a higher AoA than static conditions. This effect can be included by comparing C'_N with C_{N_1}. The vortex time parameter, for each time iteration, is updated in the following manner

$$\tau_{v,n} = \begin{cases} \tau_{v,n-1} + \frac{(0.45V)2\Delta t}{c} & \text{if } C'_N > C_{N_1} \\ 0 & \text{if } C'_N < C_{N_1} \;\&\; \Delta\alpha_n > 0 \end{cases} \tag{2.41}$$

The above equation only updates the vortex time parameter if the critical conditions has been met. Otherwise, the parameter is set to zero at the start of an upstroke cycle. Furthermore, it is assumed that the vortex convects at a velocity less than half of the free-stream [21, 46].

4. **Vortex Lift Module:** As described in section 2.1.2, the LEV augments the lift (normal force coefficient) as long as it stays over the upper surface of the airfoil. This physical mechanism of dynamic stall is imitated by the Vortex Lift Module. The induced lift contribution from the LEV, also called vortex lift, is computed and added to the lift from the trailing edge separation module to get the total unsteady lift. The vortex lift contribution is only incremented if the vortex stays over the airfoil surface. Once the vortex passes the trailing edge the vortex contribution decays and does not get incremented. The vortex time parameter is used to determine when the vortex has passed the airfoil trailing edge. The increment in vortex lift is obtained from

$$C_{v,n} = C^C_{N,n}\left(1 - K_{N,n}\right) \tag{2.42}$$

$$K_{N,n} = \left(\frac{1+\sqrt{f''_n}}{2}\right)^2 \tag{2.43}$$

[2] τ_v is a measure of how many semi-chords a concentrated vorticiy (or LEV) has traveled over the airfoil. $\tau_v = 0$ means the vortex is at the leading edge while $\tau_v = T_{vl}$ indicates its position to be at the trailing edge.

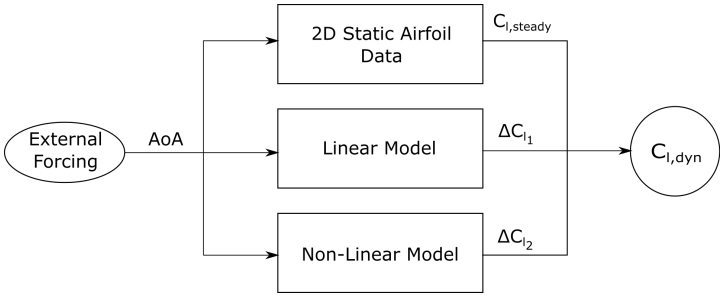

Figure 2.12: Block diagram representation of Snel's dynamic stall model.

while total accumulated vortex lift is computed from

$$C^{v}_{N,n} = \begin{cases} C^{v}_{N,n-1}\exp\left(-\frac{\Delta S}{T_v}\right) + \left(C_{v,n} - C_{v,n-1}\right)\exp\left(-\frac{\Delta S}{2T_v}\right) & \text{if } 0 < \tau_{v,n} < T_{vl} \\ C^{v}_{N,n-1}\exp\left(-\frac{\Delta S}{T_v}\right) & \text{else} \end{cases} \tag{2.44}$$

The above equation increments the vortex lift only when the LEV starts convecting over the upper surface (i.e. $0 < \tau_{v,n} < T_{vl}$). As long as it remains attached and grows at the leading edge it does not largely effect the lift; hence, in this condition the total accumulated vortex lift only decays exponentially with a vortex decay constant T_v. T_{vl} is the non-dimensional time taken by the vortex to traverse the chord. T_v and T_{vl} are independent of Mach number and loosely dependent on airfoil shape; they can be determined from unsteady airfoil data.

Finally, to get the total unsteady normal force at each time sample, the normal force from equation 2.40 and 2.44 is combined as a linear sum as shown in equation 2.45.

$$C_{N,n} = C^{f}_{N,n} + C^{v}_{N,n} \tag{2.45}$$

2.3.2. Snel's Model

This model was formulated out of the need to reproduce the effects of periodic vortex shedding in deep stall regime, as was first modeled by Truong [94]. It requires very small number of tunning parameters and mainly relies on mathematical reasoning to reproduce dynamic stall effects. The model consists of two main parts: the linear part modeled by a first order ordinary differential equation and a non-linear part modeled by a second order non-linear differential equation. Therefore, the total dynamic lift is expressed as:

$$C_{l_{dyn}} = C_{l_{steady}} + \Delta C_{l_1} + \Delta C_{l_2} \tag{2.46}$$

where ΔC_{l_1} is the change in steady lift that comes from the linear part of the model. It goes to zero when there is no forced excitation. On the other hand, ΔC_{l_2} represents the change in lift from the non-linear part of the model. It also decays to zero; however, only for attached flow regime of the lift curve. In stall regime, it introduces high frequency fluctuations to the steady lift. A block representation of the model can be seen in figure 2.12.

Part 1 - Conventional Linear Model
The conventional linear part is represented by the following differential equation:

$$\tau\frac{d\Delta C_{l_1}}{dt} + cf_{10}\Delta C_{l_1} = ft_1 \tag{2.47}$$

τ is a time constant describing time taken by flow to travel across one semi-chord ($\tau = \frac{c}{2U}$). The coefficients ft_1 and cf_{10} are time-dependent. ft_1 represents the external forcing given to the system and is expressed as a non-dimensional derivative of $\Delta C_{l,pot}$, that is

$$ft_1 = \tau\frac{d\Delta C_{l,pot}}{dt} \tag{2.48}$$

where,

$$\Delta C_{l,pot} = 2\pi \sin(\alpha - \alpha_0) - C_{l,steady} \tag{2.49}$$

While the coefficient cf_{10} represents the stiffness of the restoring behaviour of this first order differential equation, as given by:

$$cf_{10} = \frac{1 + 0.5\Delta C_{l,pot}}{8(1 + E\tau(d\alpha/dt))} \tag{2.50}$$

Where, $E = 80$ in upstroke and $E = 60$ in downstroke. Equation 2.50 shows that when the AoA is increasing, the denominator would be high; hence, resulting in a lower stiffness and vice versa when the AoA is decreasing.

Part 2 - Non Linear Model
The non-linear part of the model is represented by the following differential equation:

$$\tau^2 \frac{d^2\Delta C_{l_2}}{dt^2} + cf_{21}\frac{d\Delta C_{l_2}}{dt} + cf_{20}\Delta C_{l_2} = ft_2 \tag{2.51}$$

As the equation is non-linear; therefore, it contains contributions from ΔC_{l_2} in the coefficients cf_{20} and cf_{21}, which represent stiffness and damping coefficients, respectively.

$$cf_{20} = k_s^2\left[1 + 3(\Delta C_{l_2})^2\right]\left[1 + 3\left(\frac{d\alpha}{dt}\right)^2\right] \tag{2.52}$$

$$cf_{21} = \begin{cases} 60\tau k_s\left[-0.01(\Delta C_{l,pot} - 0.5) + 2(\Delta C_{l_2})^2\right] & \text{if } \frac{d\alpha}{dt} \geq 0 \\ 2\tau k_s & \text{if } \frac{d\alpha}{dt} < 0 \end{cases} \tag{2.53}$$

While forcing is introduced through the term ft_2 as

$$ft_2 = 0.1k_s\left(-0.15\Delta C_{l,pot} + 0.05\frac{d\Delta C_{l,pot}}{dt}\right) \tag{2.54}$$

It is to be noted that coefficients cf_{20} and cf_{21} contain contributions from the AoA (external) forcing as well. k_s represents the Strouhal frequency of vortex shedding in a uniform flow and has a typical values ranging between 0.17 and 0.2. In this way, Snel's Model is able to account for high frequency dynamics observed in wind tunnel data along with modeling dynamic stall hysteresis from forced excitations, all requiring virtually no tunning of parameters.

2.3.3. ONERA Model

The ONERA Model was developed in the early 1980s by Tran and Petot [93]. The model was formulated based on simplifying assumptions of linearization. While in wind turbine applications these linearization assumptions might not be realistic because of the large changes in AoA incurred during their operation. Nevertheless, the model is still very useful because of its ability of being coupled with structural equations (as it is formulated by differential equations) to yield a complete dynamic stability analysis. The model was modified by Peters [67] to cater for large AoA and reversed flow, where the original model became unstable. Peters also incorporated plunging degree of freedom as forcing input into the model equations, previously pitching was the only forcing input, and he determined plunging coefficients without resorting to additional parameter identification. The early versions of the model only gave the dynamic lift coefficient, which was improved by Petot [68] to give dynamic drag and moment as well. The model is comprised of a 1^{st} order linear differential equation modeling the attached flow region of the lift curve, and a 2^{nd} order non-linear differential equation modeling the stall regime. One of drawbacks of this method is the large number of tunning parameters required for these differential equations. The tunning parameters are determined through a identification procedure involving oscillating airfoil wind tunnel tests [53, 93]. The equations of the ONERA model, taken from [40], are

$$\dot{C_{l_1}} + \lambda_L C_{l_1} = \lambda_L C_{l_{pot}} + (\lambda_L s_L + \sigma_L)\dot{\alpha} + s_L\ddot{\alpha} \tag{2.55}$$

$$\ddot{C_{l_2}} + a_L\dot{C_{l_2}} + r_L C_{l_2} = -(r_L\Delta C_l + e_L\Delta\dot{C}_l) \tag{2.56}$$

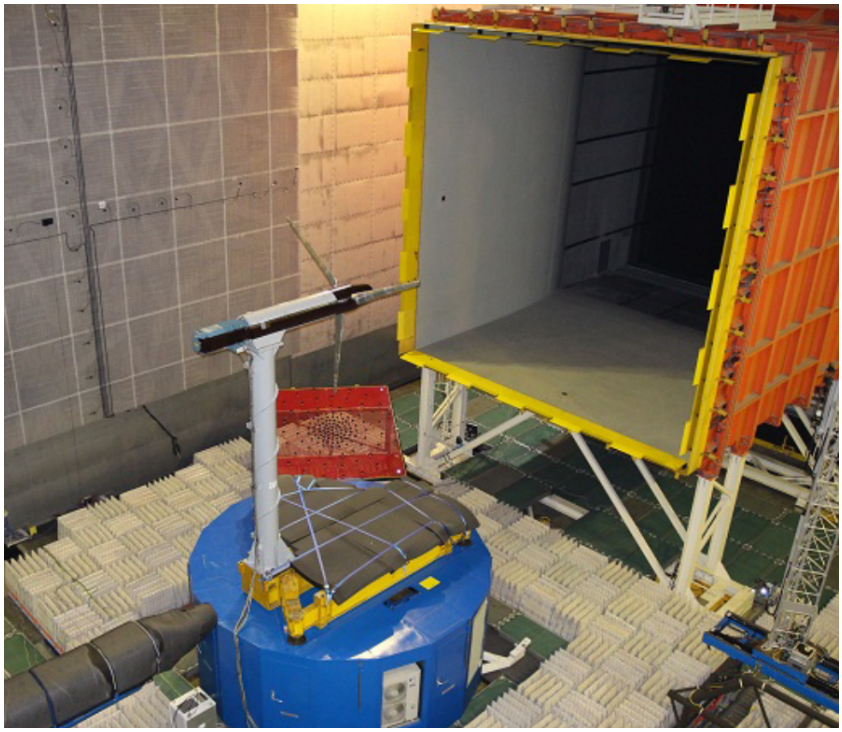

Figure 2.13: An image of the MEXICO wind tunnel model from the rear. The nozzle of the open jet test section can be viewed upstream of the rotor. Image taken from [9].

$$C_{l_{dyn}} = C_{l_1} + C_{l_2} \tag{2.57}$$

equation 2.55 and 2.56 are differentiated with respect to non-dimensional time: $s = \frac{2Ut}{c}$. The parameters λ, s_L, and σ_L depend on AoA and can be obtained from unsteady experimental data or flat plate values can be also be used. On the other hand, the coefficients a_L, r_L, and e_L are functions of the difference between potential flow lift and static lift from steady airfoil polars, mathematically

$$\Delta C_l = C_{l_{pot}} - C_{l_{stat}} \tag{2.58}$$

where,

$$r_L = \left[r_0 + r_2 (\Delta C_l)^2 \right]^2 \tag{2.59}$$

$$a_L = a_0 + a_2 (\Delta C_l)^2 \tag{2.60}$$

$$e_L = e_2 (\Delta C_l)^2 \tag{2.61}$$

The coefficients a_0, a_2, r_0, r_2, and e_2 are acquired from wind tunnel test. However, if wind tunnel data is not available then values of 'mean airfoil' can be used instead [4, 40].

2.4. Wind Tunnel Investigations

There is a lack of reliable wind tunnel measurements, performed on a complete wind turbine model, in the literature. To the knowledge of the author, there have been two main wind tunnel measurement campaigns on large scale wind turbine models. One of them is the NREL Unsteady Aerodynamic Experiment (UAE) [80] in the NASA Ames wind tunnel on a 10 meter diameter rotor carried out in 2001. The other one is the Model Rotor Experiments under Controlled Conditions (MEXICO) [76] in the German-Dutch Wind Tunnel (DNW) on a 4.5 meter diameter rotor carried out in 2006. Other wind tunnel tests have been performed, but they either lack extensive measuring equipment (like, pressure sensors) or are scaled down versions of MEXICO or NREL-UAE wind tunnel models [15, 16, 99]. The MEXICO measurement had issues with the pressure measurement quality at standstill conditions, along with some other issues as presented in [9]. Hence, a second round of MEXICO experiments were undertaken and were labeled as New MEXICO experiments [9]. It is to

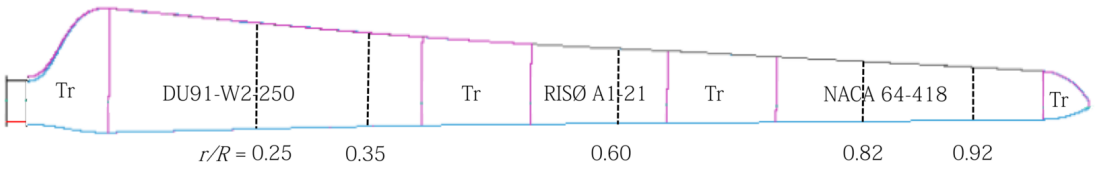

Figure 2.14: A schematic showing the layout of the MEXICO blade. The vertical dashed lines represent the locations of the pressure sensors along the span of the blade. 'Tr' denotes transfer zones between the airfoil sections, root and the tip. Taken from [27].

Table 2.2: A brief summary of a few important parameters of the New MEXICO experiments. The values are taken from [9, 11, 75, 76, 83]

Number of blades	3
Rotation	clockwise, viewed from upstream
Rotor diameter	4.5 m
Blade length	2.05 m
Tilt angle	0 ^{o}
Cone angle	0 ^{o}
Design pitch angle	-2.3 ^{o}
Design tip speed ratio	6.67 @ 15 m/s with 424.5 rpm
Rotor speed	0, 324, 424 rpm
Max. tunnel speed	30 m/s
Test section	9.5 x 9.5 x 20 m^3
Rotor model location	7 m downstream of nozzle
Measurement time	5 s per data point

be mentioned that there have been numerous studies trying to benchmark the performance of standalone dynamic stall models [30, 33, 40, 43, 46, 53, 60, 81]. However, there is a scarcity of studies where dynamic stall models are used in conjunction with a wind turbine aerodynamic solver, either a Blade Element Momentum (BEM) based model or a free vortex wake model, to study the effect of yawed flow or standstill conditions [21, 66, 100]. Mainly, because of the lack of experimental data for validation, as already mentioned. The current study aims to fill this gap by exploiting the recently available New MEXICO data for validation of the models.

2.4.1. New MEXICO Wind Tunnel Tests

The original MEXICO experiments were conducted in December 2006 at the Large Scale Low Speed facility (LLF) of DNW. Overall, the experiments were a success but there were some questions that were left unanswered. Therefore, a proposal for a second MEXICO experiment was forwarded. This New MEXICO experiment was performed in 2014 [9]. The New MEXICO experiments used the same 3 blade rotor with 4.5 diameter wind tunnel model as the original MEXICO experiments. The wind tunnel model is shown in figure 2.13. The MEXICO rotor is completely stiff, and it is sufficiently instrumented with pressure sensors at various locations along the span. In addition, a six component balance is mounted at the base of the turbine to acquire total forces and moments. The blade cross-section is composed of a 'DU 91-W2-250' airfoil near the root, a 'RISO-A1-21' airfoil at the mid span, and a 'NACA 64(3)-418' near the tip, as shown in figure 2.14. 148 Kulite® pressure sensors[3] are distributed over five different blade sections. To measure the blade root bending moments strain gauges are mounted at the root of each blade. In the original MEXICO experiments a zig zag tap was added at 5 percent chord both on the suction and pressure side to promote turbulent transition of boundary layer and avoid laminar separation. However, a concern was raised that the zig zag tapes might be de-cambering the blade sections by thickening the boundary layer (due to its own thickness) [9], in addition to transitioning to turbulent flow. Therefore, in the New MEXICO experiments the zig zag tape was removed from the outboard part ($\frac{r}{R} > 0.7$) of the blades for comparison. PIV measurements (sampling frequency 2.4 Hertz) were also performed to determine the velocity field upstream and down stream of the rotor. For further information regarding the New MEXICO model the report by Borsma and Schepers [9] can be consulted. A brief summary of some important parameters of the New MEXICO experiment, mainly taken

[3] Pressure sensors have a sampling frequency of 5.515 kHz after filtering [75, 83].

from Boorsma [11], are presented in table.

3

New MEXICO: Preliminary Data Analysis

This chapter mainly discusses the pressure data of the New MEXICO rotor at a few selected cases representative of axial flow, yawed flow, and standstill conditions. The chapter starts by describing the data acquisition and instrumentation system, followed by calibration and data reduction of the pressure sensor signals. A few representative cases are discussed. Along the way, comments about the quality of data and its suitability for validation are made. In the end, a spectral analysis of normal and tangential force obtained from integration of the pressure data is carried out.

3.1. Instrumentation and Data Storage

New MEXICO is particularly attractive for validating engineering models because it offers a controlled environment with the least possible turbulence levels between 0.2% to 0.4% [11]. This enables to readily analyze and calibrate dynamic stall models. Therefore, selection of appropriate cases for validating dynamic stall models is crucial. Particular emphasis will be given to the quality of data from pressure sensors i.e they shouldn't have kinks in the measurements. As pressure sensor data will be later used to calculate tangential and normal force coefficients for validation.

The New MEXICO blades were instrumented with 148 Kulite®pressure sensors which measure the absolute pressure. The sensors were distributed at 25%, 35%, 60%, 82%, and 92% span (Spanwise location is defined from the rotor center normalized by the rotor radius i.e. $\frac{r}{R}$. While the blade span, in meters, is measured from the root flange of the blade, which is situated at $0.210\,m$ from rotor center [11]) across the three different blades as shown in table 3.1. A large number of different measurement were collected at various experimental conditions. For further information regarding the New MEXICO experimental setup and test matrix, the reader is advised to read Boorsma & Schepers [11].

Table 3.1: Location of pressure sensors on the three blades and the relative azimuthal definition for the three blades. Note: the zero rotor azimuth is defined as the position when blade 1 is at 12 o' clock position.

Blade	Pressure Sensors	Relative Azimuth	Airfoil at Sensor Location
1	25% & 35% span	0^o	DU91-W2-250
2	60% span	-120^o	RISOE A2-21
3	82% & 92% span	120^o	NACA-64418

The pressure data was sampled at a frequency of $5.514\,kHz$, which gives approximately 27600 sample points for 5 seconds of a tunnel run. The measurements are assorted according to run, polar, and data point number. Their description can be found on MexNext portal [56]. Spurious sensor data was removed during data reduction. The completely faulty sensors were removed from the the data points, as indicated by red circles in figure A.1. Also, there were some spurious sensor signals in particular data points which were also removed, a summary of which is given by Parra [61]. A convention for flow angles and velocities for the New MEXICO rotor is presented in figure 3.1.

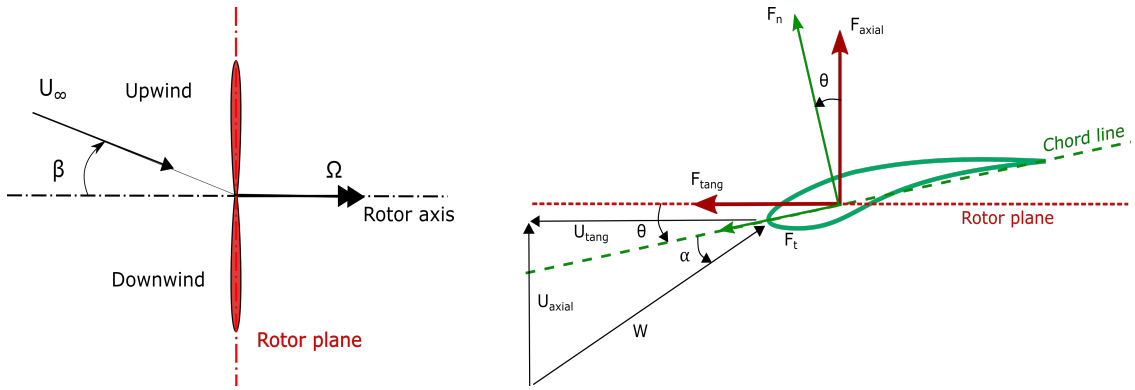

(a) Top view Schematic.

(b) Blade section velocity triangle and loads.

Figure 3.1: Depiction of the convention of angles, velocities, and sectional loads for the New MEXICO rotor.

3.2. Data Processing and Case Selection

The data was corrected for sensor drift by taking zero measurements prior to and after a set of runs with a particular measurement configuration. The corrected or reduced pressure is also the differential (or gauge) pressure. The resulting pressures were then bin averaged to convert from a time series to a function of azimuthal locations. For further information regarding data reduction and calibration the reader is referred to Parra [61]. In the present analysis bin averaged reduced pressure data is used and all pressures are in Pascals.

The pressures are expressed in non-dimensional form as pressure coefficients using the relation:

$$C_p = \frac{p - p_\infty}{\frac{1}{2}\rho_\infty V_\infty^2} = \frac{p - p_\infty}{p_0 - p_\infty} = \frac{p_{corr}}{p_{stag}} \tag{3.1}$$

where, p is the measured pressure, p_0 is the stagnation pressure, p_{corr} is the reduced pressure, and p_{stag} is the reduced stagnation pressure. The reduced stagnation pressure can be approximated to be equal to the maximum reduced pressure on the pressure side [11]. The acquired pressure coefficients are plotted versus the normalized chord-wise location (x/c). Area enclosed by the pressure coefficient curves is directly proportional to the resultant force coefficient as given by

$$C_R = \frac{1}{c}\int_{LE}^{TE} (C_p(l) - C_p(u))\, dx \tag{3.2}$$

C_R is the resultant aerodynamic force, $C_p(l)$ is for lower surface while $C_p(u)$ is for the upper surface pressure coefficients. The set of cases selected for a preliminary analysis are summarized in table 3.2. The selections are made to cover the extreme ends of the test envelope. All the cases selected are for a pitch angle of −2.3 degrees as it is the design pitch.

Table 3.2: A summary of selected cases. "clean" configuration implies that for $\frac{r}{R} > 70\%$ roughness strips were removed. While "rough" configuration implies that roughness strips were used throughout the blade span. *Each standstill case is run three times with each blade being at the 12 o' clock (zero azimuth) position once.

Case Type		Data Point	U_∞ [m/s]	β [deg.]	θ [deg.]	Ω [rpm]	λ [−]
Axial Flow (clean)	**High RPM**	429	6.95	0	-2.3	425.1	14.41
		447	23.97	0	-2.3	425.1	4.18
		965	29.93	0.01	-2.3	425.1	3.35
	Low RPM	490	5.17	0	-2.3	324.9	14.81
		508	18.37	0	-2.3	324.9	4.17
		961	30.06	0.01	-2.3	324.9	2.55
Standstill*(rough)		423, 424, 425	~ 30	30.01	90	0	0
		405, 406, 407	~ 30	-90	90	0	0
Yawed Flow (clean)		948	9.89	45.01	-2.3	425.1	10.03
		951	24.04	45.01	-2.3	425.1	4.16
		957	24.04	-30	-2.3	425.1	4.17

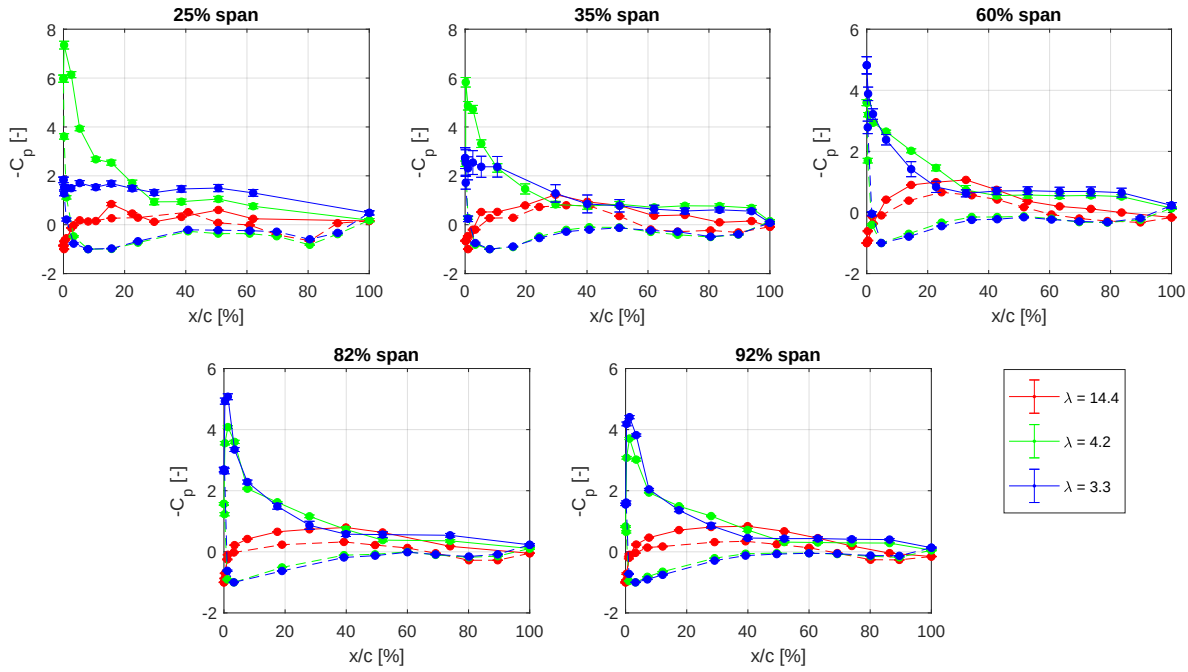

Figure 3.2: Mean pressure coefficient versus normalized chord-wise position. The error bars indicate the standard deviation of pressure coefficients. Dashed lines represent the lower surface while solid lines represent the upper surface of the blade section. For this figure: $\beta \approx 0^o$, $\theta = -2.3^o$, and $\Omega = 424.5\,rpm$.

3.3. Pressure Sensor Data

In this section reduced pressure sensor data results for selected cases will be presented and discussed.

3.3.1. Axial Flow Results

The blades experience steady conditions in axial flow; therefore, azimuthal variation of all the cases are not included in this report. Moreover, examination of the azimuthal variation did not show large changes in the C_p distribution for axial flow conditions. This fact is also corroborated by small error bars in figures 3.2 and 3.3 for high tip speed ratios. The slightly larger error bars observed in figures 3.2 and 3.3 for 25% and 35% span at low tip speed ratios might be due to some transient vortex shedding phenomena at high AoA, corresponding to data point 956 and 961 in table 3.2. In these figures, locations where $C_p = -1$ are stagnation points. It is seen that for lower tunnel wind speeds, or higher tip speed ratio, location of the stagnation point is closer to the leading edge suggesting that lower AoAs are experienced by the blade sections. In contrast, cases with higher tunnel speeds, or lower tip speed ratio, show that higher AoAs are experienced by the blade sections because stagnation points are further aft of leading edge. Moreover, the suction pressure at the upper surface for these low tip speed ratio test cases is also higher.

Overall, the results for axial flow look encouraging. However, cases with very low tunnel velocities or high tip speed ratios, like the pressure coefficients for 25% and 35% span, seem to have kinks in the data. The differential pressure in these cases is below 1000 Pascals, which might be causing the sensors to experience a high signal to noise ratio resulting in those kinks in the measurements or some sensors might be malfunctioning during the test runs. Further investigation might be necessary to identify the exact cause but that is out of scope for the current research.

3.3.2. Standstill Results

Usually in standstill operation, the blades of a turbine are pitched 90 degrees to prevent high loads on the structure. This load reduction will only happen if turbine is experiencing axial flow. However, in storm conditions, yawed flow with high AoA is a possibility. These are the conditions that the results in figures 3.4 and 3.5 are trying to reproduce in the New MEXICO experiment. These cases result in extremely large AoA on the blade sections.

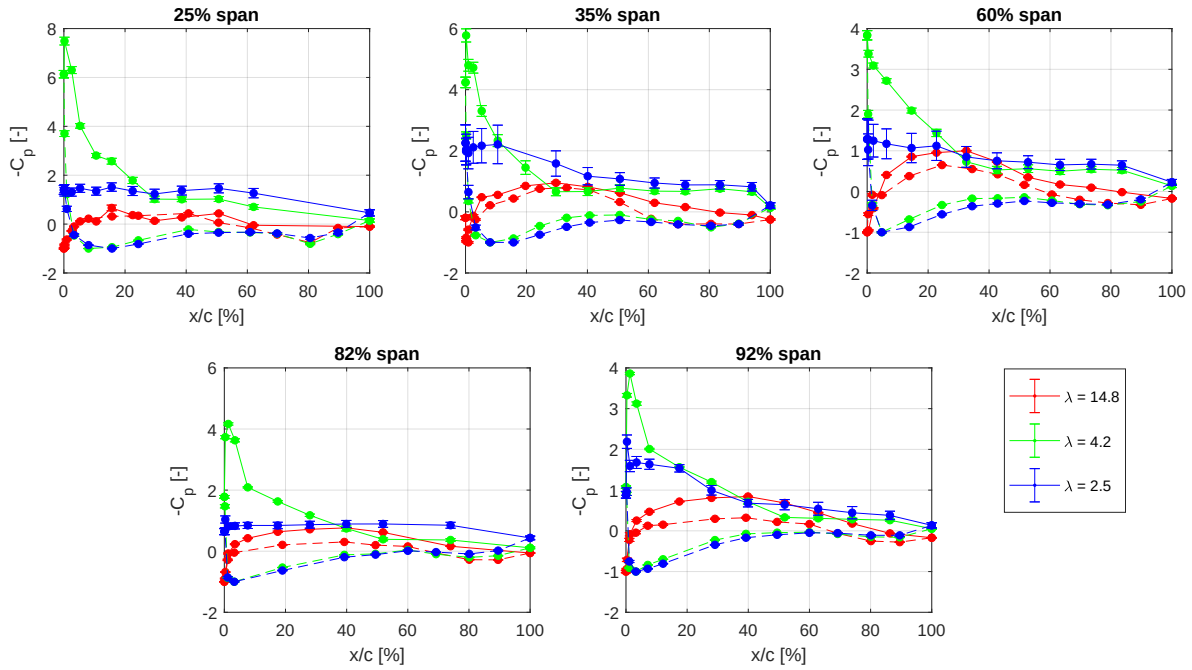

Figure 3.3: Mean pressure coefficient versus normalized chord-wise position. The error bars indicate the standard deviation of pressure coefficients. Dashed lines represent the lower surface while solid lines represent the upper surface of the blade section. For this figure: $\beta \approx 0^o$, $\theta = -2.3^o$, and $\Omega = 324.9\,rpm$.

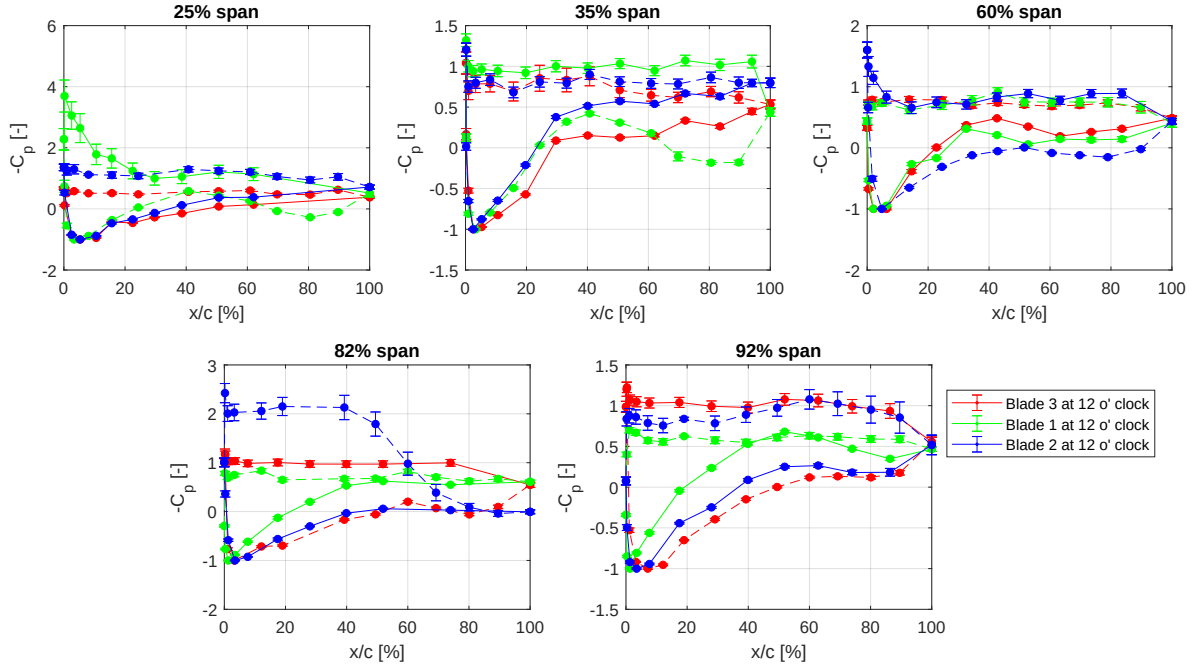

Figure 3.4: Mean pressure coefficient versus normalized chord-wise position. The error bars indicate the standard deviation of pressure coefficients. Dashed lines represent the lower surface while solid lines represent the upper surface of the blade section. For this figure: $\beta = 30^o$, $\theta = 90^o$, and $\Omega = 0\,rpm$.

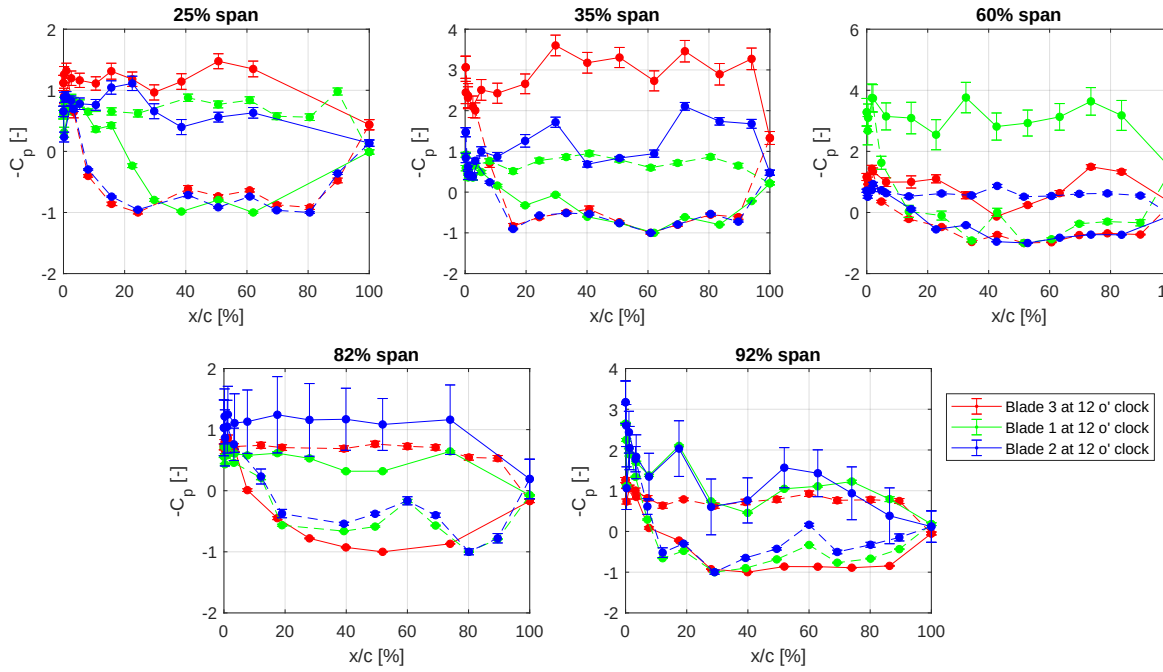

Figure 3.5: Mean pressure coefficient versus normalized chord-wise position. The error bars indicate the standard deviation of pressure coefficients. Dashed lines represent the lower surface while solid lines represent the upper surface of the blade section. For this figure: $\beta = -90^o$, $\theta = 90^o$, and $\Omega = 0\,rpm$.

In figure 3.4, for blade 3 at the 12 o' clock position, the pressure distributions at 82% and 92% span have stagnations points on the lower surface (meaning a positive AoA) while pressure distributions at 25%, 35%, and 60% span experience negative AoA. Furthermore, for 82% and 92% span, pressure distributions at upper surface are nearly flat meaning that these sections are in a state of stall. This is consistent as the NACA-64418 airfoil used on these sections, stalls at approximately 14 degrees, where quasi AoA is close to 30 degrees in these locations. For blade 1 at 12 o' clock position, 60%, 82%, and 92% span experience negative AoA while 25%, and 35% span experience positive AoA. It can be seen that 35% span is in stall while 25% span is not. The DU91 airfoil section at both these spans are operating close to stall, but the 25% section is encountering a lower AoA than 35% section due to twist of the blade. A similar set of explanation can be extended to understand the results when blade 2 is at 12 o' clock azimuthal location. However, 82% section shows a peculiar pressure distribution when blade 2 is at 12 o' clock position. It seems that a low pressure separation bubble exists on the lower surface of this section from 0% to 40% chordwise position.

The results in figure 3.5 are seen to have large number of kinks in pressure distributions. It could be because of -90 degrees yaw angle which gives extremely high AoA, both positive and negative. For blade 3 at 12 o' clock, 82% and 92% span show massive separation at the lower surface while the stagnation point is far aft on the upper surface, emphasizing a large negative AoA. On the other hand, C_p distribution at 25% and 35% span show separation on the upper surface with stagnation point being less aft from leading edge than 82% and 92% span due to twist of blade. The RISO airfoil at 60% span shows a strange dip in suction pressure on upper surface at 40% chord. A similar set of reasoning can explain the results when blade 1 and 2 are at 12 o' clock location. An interesting observation is when blade 2 is at 12 'o clock position, where large magnitudes of standard deviation in the pressure distribution at the upper surface are observed for 82% and 92% span. Suggesting that vortex shedding phenomenon might be causing some transients in the data.

3.3.3. Yawed Flow Results

In yawed flow, the rotor experiences a cyclic variation of AoA. The cyclic variation could be dominated by either the advancing and retreating blade effect or the skewed wake effect. At higher tip speed ratios, the skew wake effect is dominant due to higher induction and higher tangential velocity components compared to axial velocity component, vice verse is true for low tip speed ratios where advancing/retreating blade effect is dominant. In the case where advancing and retreating blade effect is dominant, a positive yaw angle will

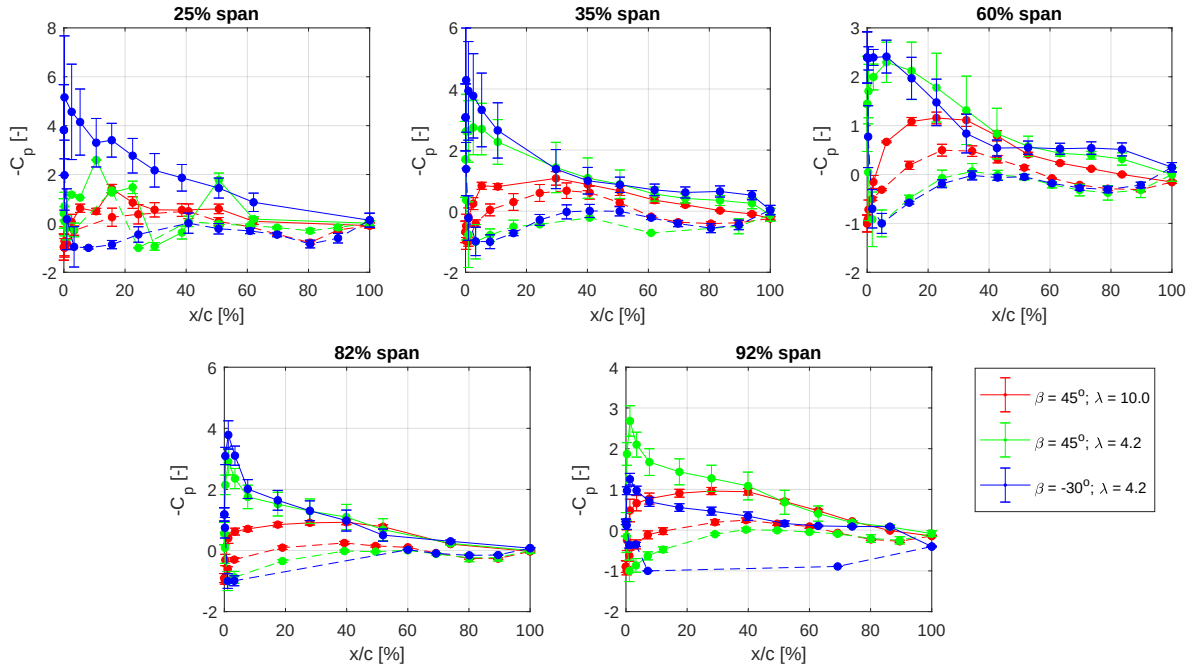

Figure 3.6: Mean pressure coefficient versus normalized chord-wise position. The error bars indicate the standard deviation of pressure coefficients. Dashed lines represent the lower surface while solid lines represent the upper surface of the blade section. For this figure: $\theta = -2.3^o$, and $\Omega = 425.1\,rpm$.

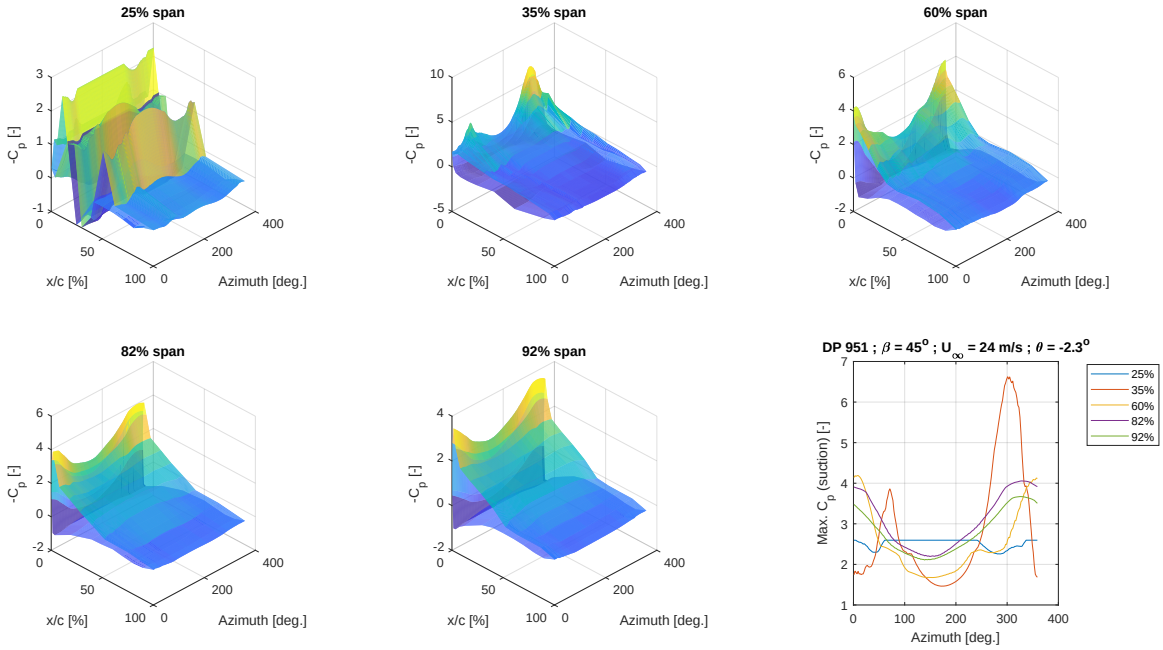

Figure 3.7: Surface plot of pressure coefficient versus normalized chord-wise position and azimuthal angle. For this figure: $U_\infty = 24.04\,m/s$, $\beta = 45^o$, $\theta = -2.3^o$, $\Omega = 425.1\,rpm$, and $\lambda = 4.2$.

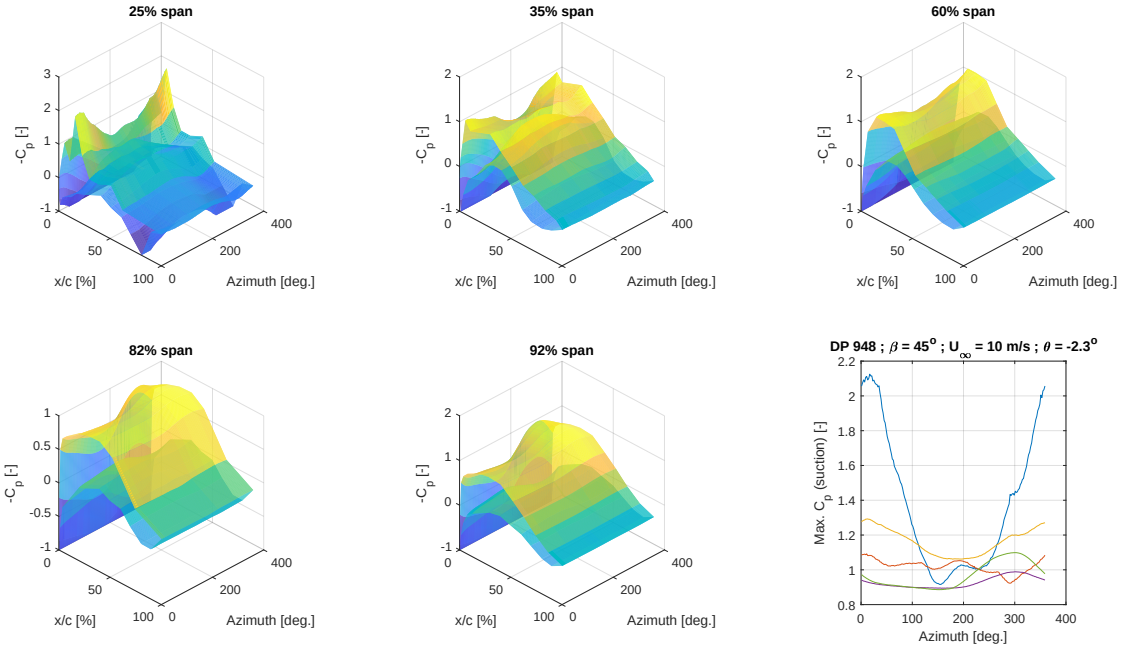

Figure 3.8: Surface plot of pressure coefficient versus normalized chord-wise position and azimuthal angle. For this figure: $U_\infty = 9.89\,m/s$, $\beta = 45^o$, $\theta = -2.3^o$, $\Omega = 425.1\,rpm$, and $\lambda = 10$.

give high AoA at zero azimuth and low AoA at 180 degree azimuth. This variation is more pronounced for inboard sections due to the smaller tangential velocity component, as is substantiated by figure 3.7.

Figures 3.6 and 3.7 show that the data at 25% span for test case with 45 degrees yaw and $\lambda = 4.2$ is absurd and should be discarded. In figure 3.7, the data at 35% span for this particular test case clearly shows the presence of dynamic stall phenomenon characterized by a sharp rise in max suction C_p on upper surface followed by a steep drop. From figure 3.6, it can be seen that dynamic stall is indicated by a large standard deviation in the pressure coefficient at the upper surface. This seems to happen for cases with lower tip speed ratios and mostly at the inboard sections of the blade. As this test case is dominated by the advancing/retreating blade effect; therefore, peaks in suction pressure are seen near the zero azimuth position. It should be noticed that a large chunk of pressure data from the lower surface of 82% and 92% span, for test case with 45 degree yaw at $\lambda = 4.2$, was discarded during data reduction.

An example of a test case where the skewed wake effect is dominant can be seen in figure 3.8. Here, clearly, the peak in suction pressure does not occur at the zero azimuth but close to an azimuth of 270 degrees. As the induction due to the wake behind the rotor is higher at 90 degrees for a positive yaw angle, the 270 degree azimuth has a higher AoA due to lower induction. Thus, resulting in the observed suction peak close to 270 degrees.

3.4. Computing Forces

The forces acting on a blade section can be computed through integrating the pressure distributions along the chord using trapezoidal rule of integration. The pressure taps along the blade surface are numbered in a clockwise sense (to preserve consistency with New MEXICO data), as illustrated in figure 3.9. Here the red point denotes a fictitious pressure tap created at the trailing edge of the blade to prevent discontinuity in the integration process. The value of differential pressure for this fictitious pressure tap is calculated to be the average of the 2^{nd} and N^{th} pressure tap.

$$F_n = \sum_{i=1}^{N} \frac{1}{2}\left(p_i + p_{i+1}\right)\left(x_i - x_{i+1}\right) \tag{3.3}$$

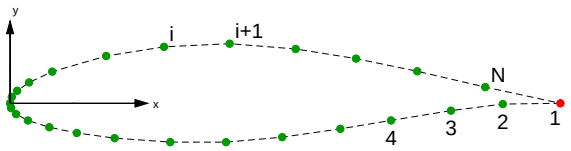

Figure 3.9: New MEXICO blade NACA 64-418 airfoil section with pressure taps highlighted as green points. The red point at the trailing edge is a fictitious pressure tap.

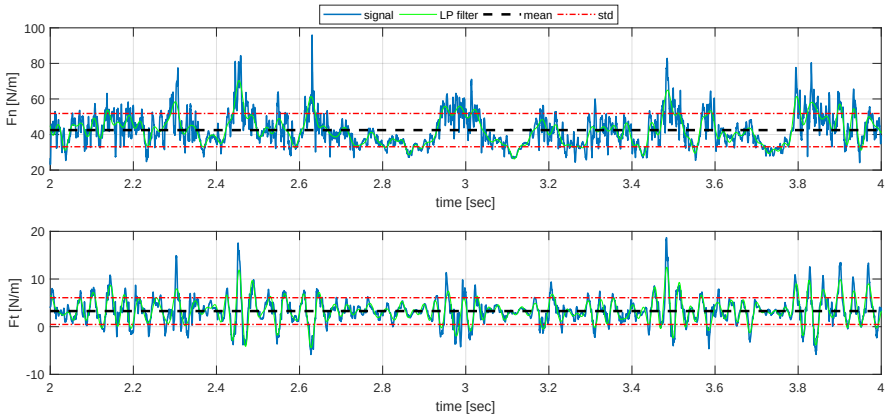

Figure 3.10: Normal and tangential force variation with time for 82% spanwise section. A low pass IIR filter (denoted LP filter) is appled to remove high frequency fluctuations from the signals. Test condition details: Data point 407 ; $\beta = -90^o$; $U_\infty = 30 m/s$; $\theta = 90.0^o$; $\Omega = 0.0\, rpm$.

$$F_t = \sum_{i=1}^{N} \frac{1}{2}(p_i + p_{i+1})(y_i - y_{i+1}) \tag{3.4}$$

In the above equation, values of variables for $(N+1)^{th}$ subscript are taken to be equal to the fictitious pressure tap with subscript 1. As an example, a result of this procedure is depicted in the left plot of figure 3.15 in the form of normal force coefficient variation with azimuthal angle and AoA. The AoA is determined through an inverse BEM approach discussed in section 3.6. While the normal force coefficient is calculated according to the following relation:

$$C_n = \frac{F_n}{\frac{1}{2}\rho W^2 c} = \frac{F_n}{c p_{stag}} \tag{3.5}$$

3.5. Frequency Domain Analysis

In this section frequency domain analysis of the New MEXICO measurements in standstill conditions is presented. The main purpose of undertaking this campaign was to unmask vortex shedding of self-excited nature, previously, Snel [81] had hypothesized its existence and tried to include it in his dynamic stall model. Before performing frequency domain analysis, time series data was inspected. In this case, times series of normal and tangential force is obtained from integrating differential pressures from pressure ports, discussed in section 3.4. A time series of such a data for a particular spanwise location and test condition is presented in figure 3.10. Here the time series has also been filtered, using a low pass infinite impulse response (IIR) filter with a passband frequency of 40 Hertz, to visualize any cyclic behavior in the signal. The time signal shows repetition of peaks in time, but it is hard to imply anything about the periodicity of signal or its frequency content. Therefore, a Fourier analysis is justified.

3.5.1. Signal Processing and Spectral Analysis

In New MEXICO test runs, pressure data was acquired for approximately 5 seconds at a frequency of 5514 Hertz, giving a total of 27610 sample points for each run. This gives a frequency resolution of $\frac{5514}{27610} \approx 0.2$ Hertz in spectral analysis. Before performing spectral analysis some pre-processing of the signal was carried out.

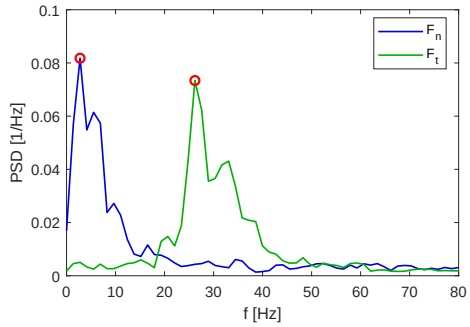

(a) Hanning window with 4000 samples

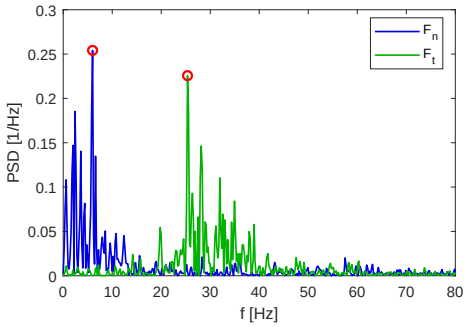

(b) Hanning window with 27610 samples

Figure 3.11: Power spectral density plot showing the frequency content of normal force and tangential force time signal for two different window sizes. The spectra is show for 82% spanwise section with the following test conditions: Data point 407 ; $\beta = -90^o$; $U_\infty = 30 m/s$; $\theta = 90.0^o$; $\Omega = 0.0\, rpm$.

The normal and tangential force signals were subtracted from their mean values (here, assuming stationary time series or assuming mean does not change in time as test conditions don't change) to remove power of DC frequency. Otherwise, spectrum would give huge peaks at zero frequency as it contains most of the signal energy. Additionally, signals were divided by their standard deviation to standardize the spectrum output and facilitate comparison between normal and tangential force spectrum on the same plot, as they are different orders of magnitude. The standardization process in mathematical notation is expressed as

$$Z(t) = \frac{X(t) - \bar{X}}{\sigma_X} \tag{3.6}$$

where, $X(t)$ is time series signal, $\bar{X}$ is mean and σ_X is standard deviation of that signal. $Z(t)$ is the standardized signal. After standardization Welch's method was used in MATLAB to estimate the power spectral density of signals. Windowing function or shaping of signal was also performed to mitigate noise in the spectrum by averaging segments (windows) of time series and also reducing spectral leakage in the process. It is to be noted that a smaller window size results in more averaging of segments. A comparison of its effects is presented in figure 3.11 for a 'hanning' window function with 50% overlap. A window size of 4000 implies that the signal has been divided into approximately 6 segments containing 4000 samples each. In figure 3.11a, windowing has reduced noise in the spectrum but at the cost of increasing frequency bin resolution to approximately 1.38 Hz. Moreover, the windowing function does not uncover or unmask dominant frequency peaks which are not visible from a spectrum with a window size equal to total number of signal samples (27610), as shown in figure 3.11b, which has a better frequency resolution of 0.2 Hz. Hence, the latter windowing function setting was chosen for subsequent analysis.

In order to identify erroneous frequency components, spectra of test runs with zero tunnel speed before and after axial and yawed flow standstill runs was analyzed. Certain peaks in power spectral density (PSD) were observed at frequencies to which no definite cause could be associated, as highlighted by red circles in figure 3.12b corresponding to 0.1997 Hz and 12.78 Hz. Figure 3.12a shows that there are fluctuation in all pressure sensor signals at zero tunnel speed. The erroneous frequencies are either due to malfunctioning pressure sensors or some external disturbance. However, further investigation of other data points at zero tunnel speed revealed that they are most likely from pressure sensors. Most of these erroneous frequencies are also observed for cases with tunnel speed of 30 m/s. Suggesting that the power of these frequencies is increased with tunnel speed, which could only be possible if they are from malfunctioning pressure sensors. Because, if they were from an external source of disturbance then their power content would have been relatively lower than other flow mechanisms at higher tunnel speeds. A summary of all observed erroneous frequencies in test runs at zero tunnel speed is complied in table 3.3.

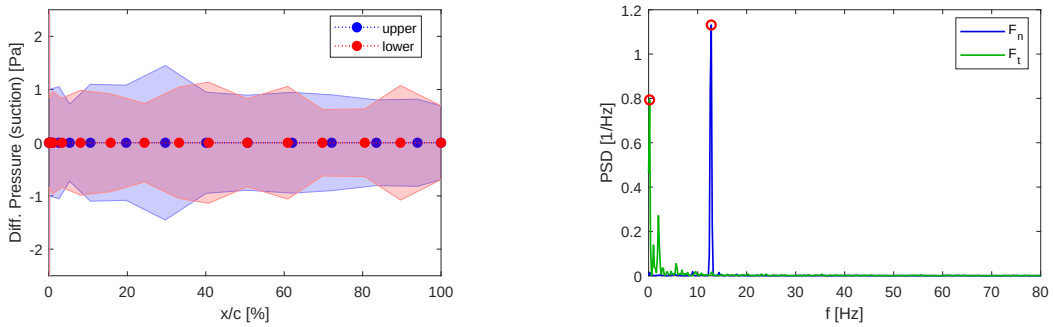

(a) Standard deviation of pressure port signals.

(b) PSD of normal and tangential force signal

Figure 3.12: Pressure port signals and PSD of normal and tangential force signal for test case at zero tunnel speed. The results are shown for 35% spanwise section with the following test conditions: Data point 371 ; $\beta = 0^o$; $U_\infty = 0 m/s$; $\theta = 0^o$; $\Omega = 0.0\, rpm$.

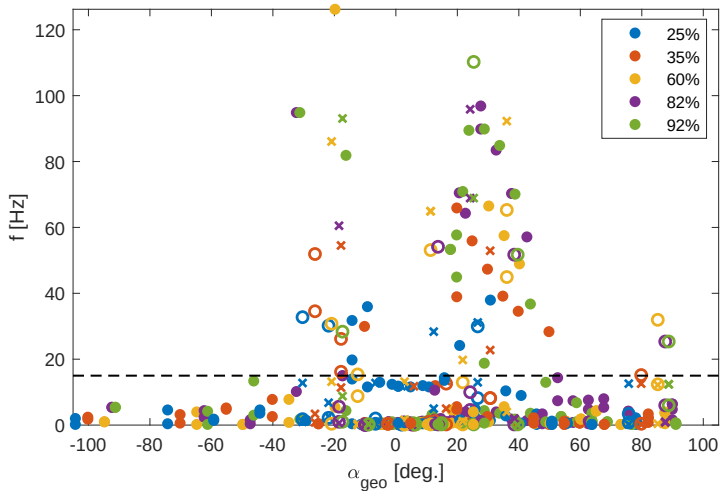

Figure 3.13: Scatter plot showing dominant frequencies observed in all standstill cases versus the corresponding geometric AoA at a particular test condition and spanwise location. The cross markers (**x**) denote presence of spawise flow from tip to root, hollow circle markers (**o**) denotes presence of spanwise flow from root to tip while filled circle markers (•) represent no spanwise flow. The dashed black line denotes the 15 Hz frequency level.

Table 3.3: A compilation of erroneous frequencies observed in standstill runs at zero tunnel speed ($U_\infty = 0\, m/s$).

Case Type	Data Point	$\beta\,[deg.]$	$\theta\,[deg.]$	Erroneous Frequencies [Hz]
Standstill axial flow (rough)	371	0	0	0.1997, 0.3994, 12.58, 12.78
	396	0	25	0.1997, 0.7988, 3.195, 11.58
	402	0	-2.3	0.1997, 0.9986, 12.78
Standstill yawed flow (rough)	404	-90	90	0.1997
	426	0	90	0.1997, 0.3994

3.5.2. Strouhal Frequencies

The process of dominant frequency extraction was automated in MATLAB environment to get a holistic picture of frequency content across all the varied standstill test conditions. A scatter plot of dominant frequencies extracted from all standstill runs and spanwise sections is presented in figure 3.13; it is plotted against corresponding geometric AoA. The figure contains dominant frequencies from both normal and tangential force time signals in one plot. Most of the frequencies observed below the 15 Hz level (shown by dashed black line in figure 3.13) will be discarded while computing Strouhal number due to two main reasons: firstly, frequencies below this level correspond to erroneous frequencies listed in table 3.3 and, secondly, these frequencies would results in very low Strouhal numbers that cannot be associated with any flow mechanism.

Therefore, with an aim to avoid ambiguity, frequencies below 15 Hz level have been filtered out while computing the Strouhal frequency. The Strouhal frequency is computed according to the following formula:

$$St = \frac{f L_{char}}{V} \tag{3.7}$$

where, L_{char} is the characteristic length based on the projected chord length or airfoil section thickness t perpendicular to the incoming flow and is equal to

$$L_{char} = \max \begin{cases} c \sin \alpha \\ t \end{cases} \tag{3.8}$$

V is the local inflow velocity in the plane of a blade section and f is the principle shedding frequency. A scatter plot of Strouhal frequencies observed in standstill conditions is presented in figure 3.14. Firstly, only the solid filled circle markers are observed. This figure shows two distinct clusters of data points. One in the positive AoA range from approximately 16 to 42 degrees, and other cluster from −9 to −32 degrees. A denser clustering of data points highlighted by the solid black curve lies in the Strouhal frequency range of 0.12 to 0.20, which is typical for bluff body vortex shedding in deep stall as was mentioned by Schreck [79]. These Strouhal numbers occur between 20 to 50 degrees in deep stall regime for New MEXICO blade. It can be seen, depending on blade section, that the Strouhal number remains almost constant for a small range of AoA within this region, especially prominent for 35% blade section. In the literature, there have been numerous experimental and computational studies to determine bluff body vortex shedding Strouhal number. Yang et al. [101] mention experiments conducted by Fage and Johansen [22] on inclined flat plates where they found an approximately constant Strouhal frequency of 0.148 for 30 to 90 degrees AoA (Reynolds number in this study is not explicitly mentioned but according to a rough estimation it is about 0.17 million). Yang et al. them-self did a DNS simulation but it is for very low Re and AoA is up till 30 degrees. Another important aspect of the effect of shape of bluff body on Strouhal frequency was highlighted by Radi et al. [69]. Although their study was also at very low Reynolds number but they did show that the Strouhal frequency changed from 0.2 to 0.155 for a perfect circular cross-section to a flat plate cross-section, respectively. Signifying the effect of cross-sectional shape on Strouhal frequency. Analysis of wind tunnel tests on wind turbine airfoil section (S809 airfoil) at high AoA, by Swalwell [88], revealed Strouhal numbers from 0.15 to 0.18. Pellegrino and Meskell [63] conducted a computational study on the same airfoil section at very high AoA revealing Strouhal numbers from 0.11 to 0.15, close to that of a flat plate. Lastly to mention, Boorsma [6] performed a wind tunnel investigation on the DU91-W2-250 profile at large AoA, same as inboard airfoil section on MEXICO blade, and found the Strouhal numbers from 0.16 to 0.17.

Another important aspect in figure 3.14 is highlighted by the dashed black curve. Here, the points represent post-stall periodic flow regime. This 'low frequency' (low Strouhal frequency) oscillatory flow regime near stall has been observed in the past by Schreck [79], Bragg et al. [12], Yon and Katz [102], Zaman et al. [104], and Mabey [52]. Zaman et al. [103] first documented this low frequency flow oscillation with a Strouhal frequency of 0.02 ($Re = 4 \times 10^4 - 1.4 \times 10^5$) on a LRN (1)-1007 airfoil. They later conducted experimental and computational studies [104] to further investigate the phenomena. There, they traced the origin of these 'low frequency' oscillations near leading edge on upper airfoil surface due to "periodic switching between stalled and unstalled states". Bragg et al. [12] conducted further experiments on LRN(1)-1007 airfoil at various Reynolds number and AoA. They found, in general, the Strouhal number in 'low frequency regime' increases with AoA and Reynolds number. Through laser sheet and surface oil flow visualization they were able to relate the cause of these oscillations to a leading edge separation bubble. They concluded that formation and bursting of the leading edge separation bubble is what causes the 'low frequency' oscillations. A summary of Strouhal numbers, associated with 'low frequency' oscillations near stall, observed in various studies is presented in table 3.4. For New MEXICO blade, 'low frequency' region lies between approximately 15 and 22 degrees AoA, which is infact close to near stall or post stall region of the airfoil sections. The Strouhal numbers within this region range from 0.05 to 0.09.

In figure 3.14, hollow circle markers represent spanwise flow from root to tip while cross markers represent spanwise flow from tip to root at a blade section. These markers are more dispersed over the domain of interest. It is hard to associate any peculiar trend to these marker points. A 3D CFD simulation is needed to accurately predict and verify the behavior at these marker points.

Generally, for the New MEXICO blade periodic bluff body vortex shedding is seen for a small AoA range in deep stall regime. It is nearly non-existent for AoA beyond 50 degrees. This behavior could be due to finite aspect ratio effects. Lindenburg [50] mentioned that an infinitely long rectangular flat plate is more probable

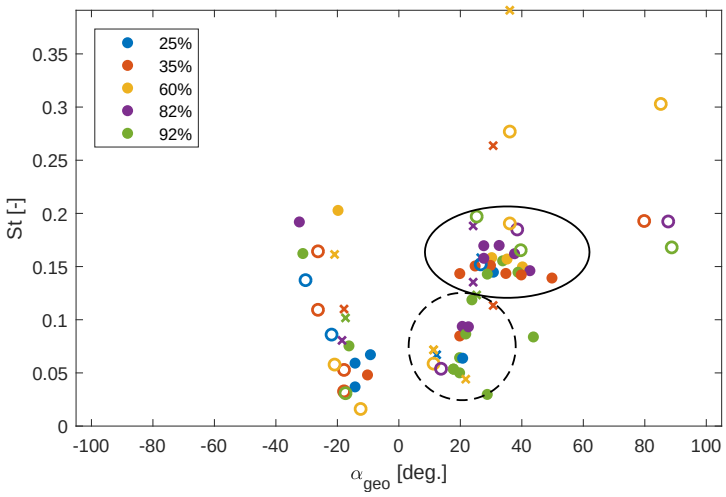

Figure 3.14: Scatter plot showing Strouhal numbers observed in all standstill cases versus the corresponding geometric AoA at a particular test condition and spanwise location. The cross markers (**x**) denote presence of spawise flow from tip to root, hollow circle markers (**o**) denotes presence of spanwise flow from root to tip while filled circle markers (•) represent no spanwise flow.

Table 3.4: A summary of Strouhal frequencies observed for near stall flow oscillations on airfoils in the literature.

Source	**Strouhal Frequency** [-]
Zamman et al. (1987 & 1989) [103, 104]	~0.02
Mabey (1992) [52]	0.076
Bragg et al. (1995) [12]	0.017 – 0.032
Yon and Katz (1997) [102]	0.04 – 0.06
Schreck (2007) [79]	0.01 – 0.08

to have structured vortex shedding. Therefore, a finite aspect ratio blade (New MEXICO blade has an aspect ratio of 14) will have partially structured vortex shedding due to early break-up of shed vortices caused by suction of air into the vortex core. Lindenburg [50] also associated the absence of periodic vortex shedding in a finite aspect ratio blade to the lower drag coefficient at close to 90 degrees AoA. In case of New MEXICO blade, this effect is clearly visible from 3D airfoil polars in figure 5.3, 5.4, and 5.5.

3.6. Determination of AoA using Inverse BEM

Determining the local AoA at a blade section of a rotating blade is a daunting task. There are a handful of methods to extract local AoA information from experimental data. One of the techniques is inverse BEM method. Inverse BEM method [26, 70] is mainly used in the literature to determine the AoA from sectional loads obtained from wind tunnel measurements or CFD. The inverse BEM method calculates the induction factors and thus the local AoA at a particular blade section by employing the same basic principle and equations as classical BEM model. This method works well in axially aligned flow. It also needs corrections for tip losses and turbulent wake state (i.e. when a>0.4). BEM models are normally improved and validated using CFD, wind tunnel, or field test measurements. Therefore, using inverse BEM to calculate AoA from wind tunnel measurement data should be avoided if the BEM model has to be validated with that data [70]. In inverse BEM method, the resultant velocity is calculated, using equations 3.9 to 3.11, taking into account the advancing and retreating blade effect.

$$W = \sqrt{U_{axial}^2 + U_{tang}^2} \tag{3.9}$$

where,

$$U_{axial} = U_\infty (1 - a) \cos\beta \tag{3.10}$$

$$U_{tang} = \left[r\Omega - U_\infty \sin\beta \cos\psi \right] (1 + a') \tag{3.11}$$

β is the yaw angle defined positive when coming from the right side as seen by the rotor while ψ is the azimuthal angle defined from the 12 o' clock position. This method gives reasonable results for axial flow condi-

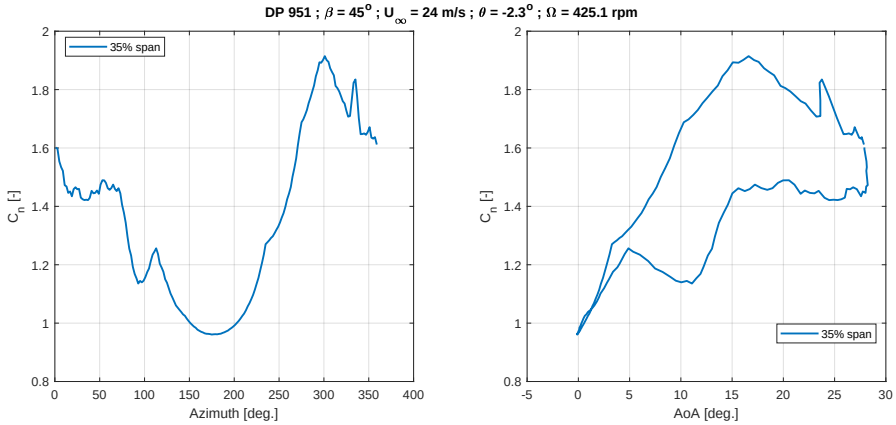

Figure 3.15: Variation of normal force coefficient with azimuthal angle (left plot) and local AoA (right plot) for New MEXICO experiment in yawed conditions. The normal force is normalized with the product of differential stagnation pressure and chord.

tions; however, reservations have been expressed by researchers regarding its application to yawed flow cases [70]. Furthermore, corrections applied to classical BEM, like tip correction and Glauert correction for heavily loaded rotor, should also be applied to inverse BEM. A stepwise implementation of this method, adapted from [26], is presented in a step-wise manner as follows:

1. Initialization of the axial and tangential induction factors.

2. Computing axial and tangential velocity from 3.10 and 3.11, respectively, to obtain inflow angle and AoA using

$$\phi = \tan^{-1}\left(\frac{U_{axial}}{U_{tang}}\right) \tag{3.12}$$

$$\alpha = \phi - \theta \tag{3.13}$$

   where, θ is the sum of the pitch angle and local twist of the blade section.

3. Extract sectional forces per unit span from New MEXICO data. These sectional forces are normal (F_n) and tangential (F_t) to chord of blade section, as shown in figure 3.1b. Therefore, they are transformed in the normal and tangential direction corresponding to the rotor plane.

$$F_{axial} = F_n \cos\theta - F_t \sin\theta \tag{3.14}$$

$$F_{tang} = F_n \sin\theta + F_t \cos\theta \tag{3.15}$$

4. Calculating new induction values using:

$$a_{new} = \frac{1}{\frac{4\pi r \rho W^2 F \sin^2\phi}{BF_{axial}} + 1} \tag{3.16}$$

$$a'_{new} = \frac{1}{\frac{4\pi r \rho W^2 F \sin\phi\cos\phi}{BF_{tang}} - 1} \tag{3.17}$$

5. Compute the difference between the new and old induction values. If the difference is above tolerance then update old values and go to step 2, else terminate loop.

It is to be noted that both Prandtl tip loss and Glauert correction are implemented in the above described model in step 4. Formulations for Glauert correction and Prandtl tip loss factor (F) were taken from Burton [13]. Again, it is reiterated, the purpose of using inverse BEM is just to give a physical sense of AoA and induction variation; it will not be used in validating engineering models in BEM to avoid any bias. An example of results from an inverse BEM are presented in figure 3.15, where a dynamic stall hysteresis loop can be clearly visualized for the New MEXICO rotor operating in yaw.

3.7. Chapter Conclusion

The following conclusions about the New MEXICO measurements were drawn from this chapter:

- In axial flow conditions, low tip speed ratio (or high tunnel speed) pressure distributions show a reasonable trend without any large kinks. The same statement also holds for yawed flow measurements. Mainly, the cases with high tip speed ratio show large kinks in pressure measurements especially for 25% and 35% section. However, this might not be a problem for current research as the focus would be on cases with low tip speed ratios where dynamic stall is more probable.
- Standstill pressure distribution for very large AoA show kinks in pressure distribution. On the contrary, at somewhat lower AoA, but still in deep stall regime, there are lesser kinks in measurements. Hence, it can be said that the quality of standstill measurements deteriorates at extremely large AoA. Nonetheless, a further analysis of the standstill measurements needs to be performed to establish there credibility.
- Dynamic stall is observed at the inboard sections for yawed flow measurements at large yaw angles and low tip speed ratios (or high tunnel velocity). Care must be taken while using yawed flow measurements for validation as some measurements show completely absurd pressure distributions.
- Structured bluff body vortex shedding was observed in a limited range of AoA from 20 to 50 degree in deep stall on the New MEXICO blade. Low Strouhal frequency shedding behavior was seen in the post stall regime, and it was seen to increase with increasing AoA. The absence of structured vortex shedding is due to finite aspect ratio of the MEXICO blade, which destabilizes the vortex core causing early break-up of shed vortices.

4

Computational Set-up and Code Description

This chapter formally introduces the computational tool, Aero-Module, used in this study. A detailed overview is presented of the various aerodynamic models and engineering add-ons incorporated in this tool. Thereafter, the computational grid and various settings used for simulation are discussed. The chapter ends with validation of standalone dynamic stall models and Aero-BEM model with available experiments.

4.1. ECN Aero-Module

ECN Aero-Module code is used in this study to simulate the new MEXICO measurements. Aero-Module is a sophisticated numerical tool developed to solve the aerodynamics of a wind turbine. It has the capability to solve the flow around a conventional horizontal axis wind turbine or a vertical axis wind turbine. Over the years, the code has been updated to include the latest engineering models. The code is written in object oriented FORTRAN in a modular format. This enables easy modification or inclusion of more advanced models into the source code. Primarily, Aero-Module was developed to be coupled with a structural solver for aeroelastic computations; however, it can also operate standalone for aerodynamic computations on a rigid wind turbine, figure 4.1.

Two aerodynamic models, namely a BEM model and a free vortex wake model, are programmed in Aero-Module. The BEM model is adapted from another aeroelastic code called PHATAS [49]. While the free wake model is based on the Aerodynamic Windturbine Simulation Module (AWSM) [96]. These two models share the same input file, meaning that the same set of tower effect modeling, wind inputs, rotational correction, and dynamic stall models can be used in conjunction with either a BEM model or AWSM. The steady airfoil

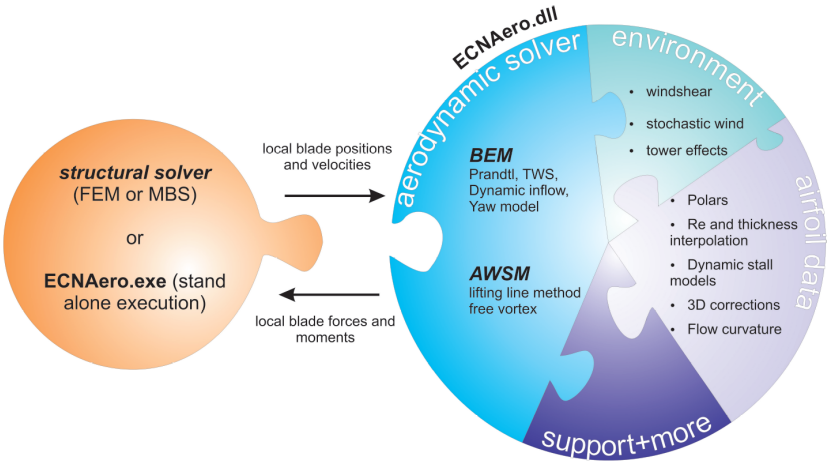

Figure 4.1: An overview of ECN Aero-Module. Taken from [8].

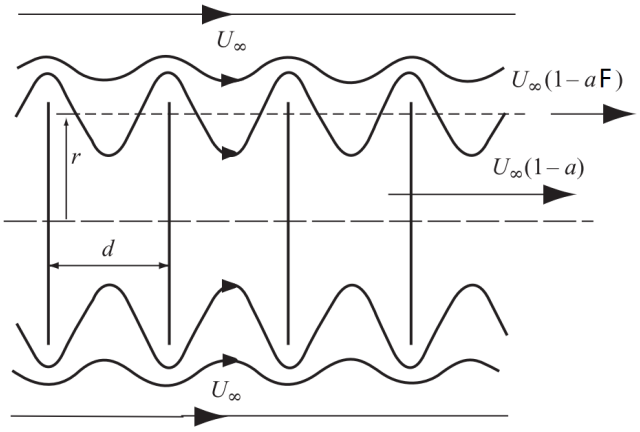

Figure 4.2: Illustration of Prandtl's wake-disc model. Adapted from [13].

polars are used in both models to predict the non-linear aerodynamics over the rotor. The airfoil characteristics are interpolated between blade airfoil sections according to the thickness distribution along the span. Furthermore, an airfoil polar for multiple Reynolds number can be included to get interpolated airfoil characteristics for a specific Reynolds number. In subsequent section, both aerodynamic models will be discussed in detail using information from the user manual [8].

4.1.1. Aero-BEM

An unsteady BEM formulation is programmed in Aero-Module, which follows the same basic principle as the classical BEM theory discussed in section 2.2.1. This BEM code iteratively solves for a solution using annulus averaged axial induction as the main criteria to determine convergence. The solution can either be based on an element based approach or a annulus based approach. In elemental approach, axial induction is calculated for each element separately using momentum equations, which is then used to obtain annulus averaged axial induction. On the contrary, in case of annulus based approach, the variables in the momentum equation are averaged over the annulus before solving. This procedure directly gives the annulus averaged axial induction after solution of the momentum equations. The latter approach is more suitable for non-uniform inflow and is the default option for most simulations.

Prandtl Correction

The actuator disk theory assumes a solid rotor disk. However, in reality a rotor has finite number of blades which present losses due to shedding of vortices from the tip and root of the blade. Prandtl [13] proposed a correction to account for these losses by dividing the annulus average induction with a Prandtl tip or root factor F to acquire local induction at every element.

$$F = \frac{2}{\pi} cos^{-1}\Big(\exp\frac{-\pi(R-r)}{d}\Big) \tag{4.1}$$

where, d represents the distance between trailing vortex sheets as shown in figure 4.2. A larger distance between these consecutive vortex sheets would result in more flow from the free-stream, outside the wake, to enter between these vortex sheets resulting in more losses. d is inversely proportional to tip speed ratio. A higher tip speed ratio would reduce the distance between trailing vortex sheets; thus, diminishing tip or root losses. Due to the controversy surrounding the location of root vortex, Aero-BEM has provided a variable called "AEROROOT" in its input file to specify the location of root vortex. If the user does not specify this then the location is calculated from blade geometry.

Correction for Heavily Loaded Rotor

For axial induction greater than 0.5 the momentum theory becomes invalid and rotor enters the turbulent wake state. Momentum thoery predicts reversed flow in the far wake for this state which is not possible. Therefore, this condition is corrected by using turbulent wake state equations (TWS) above a certain threshold value of annulus average axial induction, typically $a_T = 0.38$. Above this threshold, the quadratic expres-

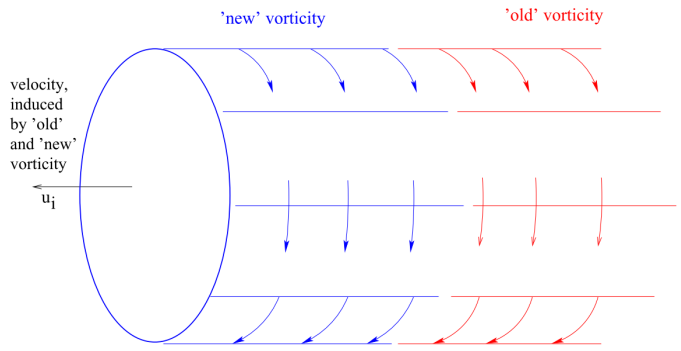

Figure 4.3: Depiction of a mixed wake after a sudden change in rotor loading. Reproduced from [77].

sion for thrust coefficient, equation 2.10, is replaced by a linear relation, given by equation 4.2, that is tangent to the quadratic expression at the threshold value.

$$C_T = 4(a_T^2 + a(1-2a_T)) \quad \text{for } a > a_T \tag{4.2}$$

Dynamic Inflow Correction
Dynamic inflow is an unsteady aerodynamic effect, often labeled "aerodynamic inertia", experienced by a rotor whenever there is a change in pitch angle, rotor speed, or wind speed. This change in rotor loading causes a mixed wake downstream of the rotor as shown in figure 4.3. The old vorticity in the wake influences induction at the rotor causing a delay in build-up of induction to its steady state value. For more details on the phenomenon, the reader is referred to section 2.1.1. In Aero-BEM this effect is modeled by adding a first order term containing the time derivative of annulus average induction, as shown in equation 4.3, called ECN Dynamic Inflow model [86]. The coefficient of this term is a function of radial location through a factor $f(r)$. It is to be noted that this form of equation 4.3 is identical to the first order filter equation 2.3.

$$C_T = 4a(1-a) + \frac{4Rf(r)}{U_\infty}\frac{\partial \bar{a}}{\partial t} \tag{4.3}$$

Yawed Flow Correction
Incoming wind is not always axially aligned with the rotor; therefore, there is a need to accurately simulate aerodynamics in oblique inflow. As already discussed in section 2.1, yawed inflow is governed by two different phenomenon, namely, the advancing/retreating blade effect and skewed wake effect. The advancing/retreating blade effect is intrinsically included in the formulation of Aero-BEM; however, to model the skewed wake effect it needs a correction model. For that purpose, Aero-BEM has a provision for using either Glauert yaw correction [25] or ECN yaw correction. Glauert correction uses a sinusoidal function given by equation 2.2 to account for azimuthal variation of induction due to a skewed wake downstream. While ECN yaw correction uses a more accurate approach employing equation 4.4 by Schepers [73]. This particular correction includes the effect of trailing root vorticity on the induction, in addition to trailing tip vorticity.

$$a = \bar{a}\left[1 - A_1\cos(\phi_r - \psi_1) - A_2\cos(2\phi_r - \psi_2)\right] \tag{4.4}$$

In the above equation, A_1, A_2, ψ_1, and ψ_2 are functions of radial location and yaw angle; these parameters are determined from a second order Fourier curve fitting on experimental data.

4.1.2. Aero-AWSM

Aero-AWSM is an implementation of a free vortex wake model; therefore, it follow the same set of principles described in detail in section 2.2.2. Aero-AWSM models the flow field around a blade section with a bound vortex on the airfoil quarter chord and shed vorticity in the wake as illustrated in figure 4.4a. The bound vorticity and shed vorticity extend in three dimensional space using discrete vortex filaments, represented in figure 4.4b. More specifically, bound vorticity extends along the span passing through quarter chord points of every blade section; consequently, forming a lifting line. This representation of blade with a single lifting line

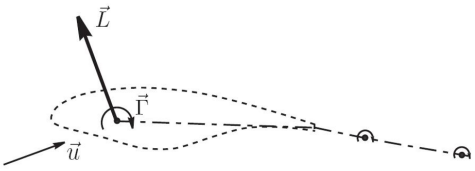

(a) AWSM flow field model around a blade section.

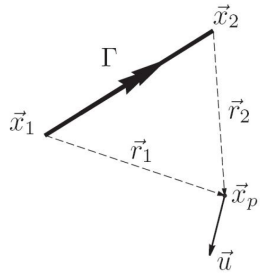

(b) Position vectors describing a vortex filament.

Figure 4.4: The lifting line and free vortex wake modeling fundamentals. Taken from Van Garrel [96].

is because of one main assumption in AWSM. According to this assumption, due to larger size of a blade in spanwise dimension as compared to chordwise and thickness dimension, the flow field can be concentrated along the quarter chord and assumed to vary predominately along the spanwise dimension. This lifting line formulation is combined with a free vortex wake model to give Aero-AWSM.

Lifting Line Model

This model is formulated on the generalized lifting line theory [42]. As already explained, the main assumption of this model dictates that vorticity is concentrated at the quarter chord location resulting in a lift force at that point determined by the local incoming flow, figure 4.4a, which is in plane of blade cross-section. Consequently, restricting the applicability of this model to slender and planar blades where spanwise flow is small [96]. The non-linear viscous effects are included in this model through the use of steady 2D airfoil polars. The aerodynamic coefficients computed from these polars are used to determine a new value of circulation based on Kutta-Joukowski theorem according to the following relation:

$$d\vec{L} = \rho\Gamma\vec{u} \times d\vec{l} \tag{4.5}$$

where, $d\vec{l}$ is the length of the vortex filament element shown in figure 4.4b. The velocity induced by such a filament at point P is calculated using the following relation derived from Biot-Savart Law [96]:

$$\vec{u}_\Gamma(x_p) = \frac{\Gamma}{4\pi} \frac{(r_1 + r_2)(\vec{r}_1 + \vec{r}_2)}{r_1 r_2 (r_1 r_2 + \vec{r}_1 \cdot \vec{r}_2) + (\delta l_0)^2} \tag{4.6}$$

The position vectors $\vec{r}_1$ and $\vec{r}_2$ are used to locate point P relative to the end points of the filament. The parameter δ is the cut-off radius parameter and l_0 is the length of the filament. The core of a vortex filament is a singularity, meaning that induced velocity would go to infinity at the vortex core; hence, to overcome this problem a rankine vortex assumption is used. Here, core of the vortex is assumed to be in solid body rotation. The cut-off radius parameter determines the extent of viscous core.

Vortex Wake Model

The wake from a wind turbine rotor is modeled with discrete vortex rings. The rotor has a bound vortex at the quarter chord with trailing vortices and shed vortices convecting in the wake, as shown in figure 4.5, to form a lattice of discrete vortex rings (vortex lattice). The generation of shed vorticity follows Kevlin's ciculation theorem describing conservation of circulation around a closed curve. According to this theorem, vorticity is shed into the wake when there is a change in bound vorticity on the airfoil.

$$\frac{D\Gamma}{Dt} = \frac{1}{\Delta t}\left(\Gamma_{airfoil} + \Gamma_{wake}\right) = 0 \tag{4.7}$$

From above expression, it can be seen that the shed vorticity should have an opposite direction to that of bound vorticity. Each new shed vortex is created at a location 25% chord distance downstream of trailing edge. The vortex ring upstream of this location has a strength Γ at current time step. While the strength of newly created vortex ring is equal to the change in circulation from previous time to current time instant. Vortex rings for four previous time steps are shown in figure 4.5. Position and shape of the wake in time is determined through two separate mechanisms. First, the effect of onset wind velocity is applied to each vortex

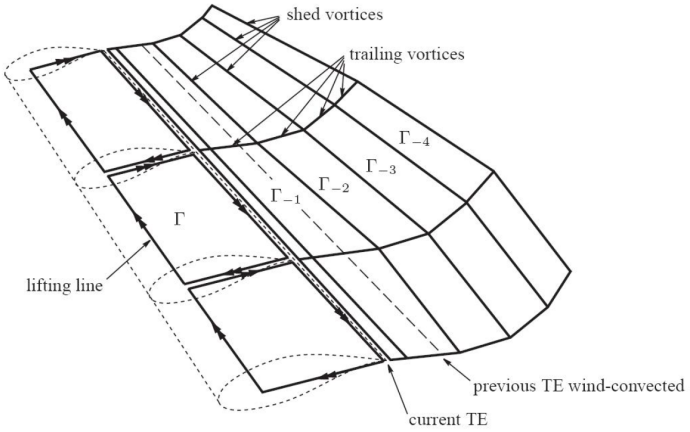

Figure 4.5: Illustration of wake geometry in AWSM. Taken from Van Garrel [96].

lattice node to compute convection. Secondly, convection of each vortex lattice node due to induced velocities from all bound vortices, trailing vortices, and other shed vortices is computed. This technique where vortex self-induction and induction due to other vortices is considered is called a free wake model approach. The AWSM code has the capability to perform a full free-wake simulation, a prescribed wake simulation, or a hybrid wake simulation. In case of a hybrid wake, wake convection is modelled using free-wake approach up till a certain distance downstream of rotor. After which a precribed wake approach is utilized. The hybrid approach reduces computational time in comparison to a full free wake approach while , simultaneously, avoiding shortcomings of a full prescribed wake approach.

4.2. Common Engineering Models

An advantage of incorporating BEM and AWSM in one code is the ability to use same add-on engineering models for both in an easy way. AWSM models most of the aerodynamic effects intrinsically; however, it still needs certain engineering models that are also common to a BEM based model. These common engineering models include dynamic stall models, 3D rotational correction models, structural models, and models for incorporating tower effects. Here, only dynamic stall model and 3D rotational correction model used in Aero-Module will be discussed further.

4.2.1. Dynamic Stall Models

Aerodynamic flow around an airfoil section does not respond to changes in flow conditions instantaneously but there is a delay in the aerodynamic response. These models add a correction to the steady airfoil polars for unsteady dynamic stall effects to account for that delay in aerodynamic response. For that purpose following dynamic stall models are already implemented in Aero-Module:

1. **Snel 1st order model:**

   It only simulates the lag in flow separation due to dynamic stall effects. It takes the difference between potential lift and steady lift from airfoil polar as a forcing input. One of the main advantages of this model is that it does not require any airfoil specific tunning parameters. The model has been discussed in detail in section 2.3.2. The implementation in Aero-Module is based on the work of Herman Snel [81].

2. **Snel 2nd order model:**

   This model builds on top of Snel's 1st order model. It uses a second order Van Der Pol type non-linear differential equation to simulate the effects of vortex shedding. The model is designed to give high frequency fluctuations in lift response at high AoA without external excitation.

Table 4.2: Overview of values used for Beddoes-Leishman model parameters for wind turbine applications.

Source	T_p	T_f	T_v	T_{vl}
Leishman [47]	1.7	3	6	7
FFA [5, 55]	0.8	5	2	8
Gupta et al. [30]	1.7	3	6	11
Pereira et al. [65]	1.5	5	6	5
Holierhoek et al. [40]	2.5	3	6	-

3. **Beddoes-Leishman model:**

This model tries to simulate the primary physical mechanisms that govern dynamic stall. It does so in form of an open loop system with four modules. These modules simulate effects of shed vorticity, trailing edge separation, leading edge separation, and vortex lift. There are numerous implementations of this model in the literature; its implementation in Aero-Module follows the work of Bjorck [5], Holierhoek et al. [40], and Pereira et al. [64]. A detailed description of the model following from the afore-mentioned literature is presented in section 2.3.1. Some modifications, specific to Aero-Module, are not discussed in section 2.3.1; hence, are described below:

- Wind Reference Frame
  The original model [46] was formulated in a body fixed reference frame (i.e. normal and tangential direction). Bjorck [5] changed the model equations to wind reference frame with the exception of vortex lift equations, which were still computed in body fixed frame.
- AoA Modification
  In order to make the model workable at complete range of AoA from 0^o to 360^o the following modifcations are made to the AoA:

$$\alpha_{mod} = \alpha - 180 \quad \text{if } \alpha > +90 \tag{4.8}$$

$$\alpha_{mod} = \alpha + 180 \quad \text{if } \alpha < -90 \tag{4.9}$$

  Additionally, to prevent absurd solutions due to application of linear theory in deep stall, a fade factor is applied to the change in AoA.

$$fade = \cos^2 \alpha \tag{4.10}$$

- Model Parameters
  The model uses several empirical parameters. Most of these parameters are time constants non-dimensionalized with time taken for flow to travel half chord distance. The parameters associated with modeling effect of shed vorticity (A_1, A_2, b_1, and b_2) and impulsive component (K_α) of lift are independent of airfoil shape and are taken from Leishman [46, 47]. Mainly, time constant parameters associated with pressure lag (T_p), boundary layer lag (T_f), and vortex decay time (T_v) have different values used in various literature. Typical values of these parameters used in literature for wind turbines applications are presented in table 4.2. Pereira et al. [64] did a quantitative comparison of the Beddoes-Leishman model with old MEXICO measurements. In the current study, a sensitivity analysis was performed on B-L parameters; Pereira et al.'s parameters were found to give reasonable results, see appendix D. Therefore, for this study parameters used in their model will be adopted unless otherwise stated. An additional parameter 'A_{cd}' introduced by Montgomerie [58] for modeling separation drag is also implemented in the current model. Bjorck [5] suggested an optimal value for this parameter to be close to 0.1. Table 4.1 shows values for all parameters used in the current study.

Table 4.1: Implemented semi-empirical parameters for the Beddoes-Leishman dynamic stall model. Taken from [64].

A_1	A_2	b_1	b_2	K_α	T_p	T_f	T_v	T_{vl}	A_{cd}
0.3	0.7	0.14	0.53	0.75	1.5	5	6	5	0.13

- Shed Vorticity Modification
  The attached flow module of the Beddoes-Leishman model accounts for the effect of shed vorticity by using deficiency functions given by equation 2.29 and 2.30. This can be seen as an improvement to BEM model which does not intrinsically account for effects of shed vorticity. However, for AWSM these deficiency functions are switched off to prevent modeling of the same effect twice, because AWSM intrinsically models effect of shed vorticity.
- Lift Curve Slope
  By default, Aero-Module uses a lift curve slope of 2π for non-cylindrical sections (i.e. t/c < 0.8) [7]. However, capability to include calculation of lift curve slope from linear regression using 2D airfoil polar was also implemented in this study.
- Leading Edge Stall Criteria
  In order to determine the onset of leading edge separation and trigger the vortex lift module, the original Beddoes-Lesihman model [46] uses a leading edge stall criteria based on a normal force coefficient corresponding to break in pitching moment coefficient. However, for wind turbine airfoils the break in pitching moment is not always clearly defined [65]. Therefore, maximum lift force coefficient is used as a criteria to determine leading edge separation. This criteria has been documented by Pereira [65] to work well for wind turbine applications.

4. **ONERA model:**

   This model makes use of a first order linear differential equation to model the effects of shed vorticity in inviscid attached flow regime. Furthermore, a second order non-linear differential equation is also included to model non-linear viscous effects in stall regime. For a detailed description of the model, the reader is referred to section 2.3.3. The model implemented in Aero-Module follows the implementation discussed in [40]. The ONERA model requires a large number of tunning parameters that need to be determined from unsteady experimental data. In case of non-availability of such data, the parameters for flat plate and 'mean airfoil' are used [4].

Table 4.3: Parameters used for the ONERA dynamic stall model. Taken from [40].

λ_L	σ_L	r_0	r_2	a_0	a_2	e_2	π
0.17	$2\,\pi$	0.2	0.2	0.3	0.2	0.53	π

4.2.2. 3D Rotational Augmentation Model

In order to account for stall delay due to rotational augmentation at the inboard sections of the blade, Snel's 3D rotational correction [82] with Lindenburg's [51] 'centrifugal pumping' model based on local speed ratio dependency is implemented. The correction has the formulation presented in equation 2.4, here it is repeated for convenience:

$$C_{l_{3D}} = 3.1\left(\frac{c}{r}\right)^2\left(\frac{\Omega r}{U_{eff}}\right)^2\left(C_{l_{pot}} - C_{l_{2D}}\right) \tag{4.11}$$

where,

$$C_{l_{pot}} = 2\pi(\alpha - \alpha_0) \tag{4.12}$$

U_{eff} is the effective local velocity at a blade section, $C_{l_{pot}}$ is the potential lift coefficient, and α_0 is zero lift AoA. The correction is only applied up till 50 degree AoA. From 30 to 50 degrees it is linearly decreased to zero. For further information on rotational augmentation the reader is referred to section 2.1.3.

4.3. Computational Set-up

BEM and AWSM models need a backbone airfoil polar to model the non-linear aerodynamic effects. As New MEXICO blade has three different airfoil sections distributed along its span. The 2D airfoil polars used in this study are taken from different sources. The airfoil polar for DU91-W2-250 airfoil was taken from measurement in Delft Low Speed Tunnel (LST) [91]. The airfoil polar for RISO-A2-21 airfoil section was unavailable; therefore, wind tunnel data for RISO-A1-21 airfoil section [23] was used instead. Like, DU91-W2-250 airfoil,

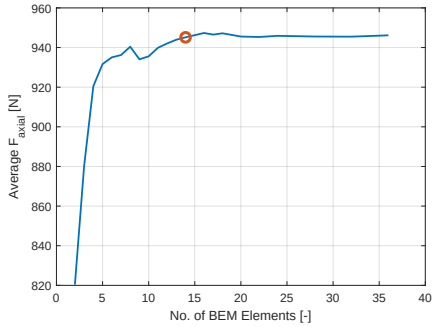

Figure 4.6: Convergence of axial force averaged over one revolution with increasing number of spanwise elements. The current results are show for the following test conditions: $\beta = 0^o$; $U_\infty = 10\ m/s$; $\theta = -2.3^o$; $\Omega = 425.1\ rpm$

measurements on NACA 64418 were also taken from Delft LST [11]. It is worth mentioning that Aero-Module requires aerodynamic coefficients for each profile from −180 to 180 degree AoA range. The data in deep stall AoA range was not available in the literature; consequently, deep stall data for DU96-W-180 airfoil section was used [11, 92] for all three airfoil sections of the MEXICO blade.

In the current work, following correction models were enabled for all BEM computations in Aero-Module, unless otherwise stated:

1. Prandtl tip and root correction.
2. Turbulent wake state equation for thrust.
3. ECN dynamic inflow model [86].
4. ECN yaw model [73].
5. Snel's rotational correction [82]

In order to aid in visualization of results, the same sign convention is used for New MEXICO measurements and Aero-Module simulations, as indicated in figure 3.1. In ECN Aero-BEM the blade span needs to be discretized into elements. A convergence study was performed for this purpose, where the BEM simulation was run for different number of blade elements. Result of the study is presented in figure 4.6. A discretization of 14 elements was considered sufficient for the present analysis as highlighted by red circular marker in figure 4.6. The time step size was determined from a rule of thumb given in Aero-Module training presentation slides [10]. According to this rule, for yawed flow cases a minimum of 10 degrees of azimuthal discretization is necessary. Based on this criteria the time step size should be less than 0.0078 seconds for New MEXICO simulation cases. Hence, a time step size of 0.00393 seconds was selected. A steady uniform free-stream wind velocity is used for all simulations to match the new MEXICO experimental conditions. Tower effects are excluded from the analysis due to large distance between the tower and rotor for the new MEXICO experiment. This was intentionally incorporated in the design of this experiment to isolate tower effects from the rotor. The tower is approximately half a rotor diameter downwind of the rotor [11].

4.4. Validation of Standalone Dynamic Stall Models

It is important to validate dynamic stall models before using them in conjunction with a BEM model. However, dynamic wind tunnel data for airfoil sections used on the new MEXICO blade is currently not available in the literature. Therefore, dynamic wind tunnel data on S814 airfoil section from Ohio State University (OSU) will be used as it is publicly available [41]. The reason for choosing this airfoil section is its high thickness to chord ratio ($\frac{t}{c} = 24\%$) and tailored design for wind turbine applications. The OSU dynamic test were done with a sinusoidal pitch oscillation. Aero-Module, by default, does not have a provision for simulating pitch oscillation of a 2D airfoil section. Hence, for this purpose, a modification was made in Aero-Module source code to incorporate input of pitch oscillation frequency and amplitude through a separate input file "pitch_motion.txt". Furthermore, to model the 2D airfoil section, a single blade of uniform chord and thickness with a span of approximately 200 times the chord was modeled in Aero-Module. Sectional lift and drag

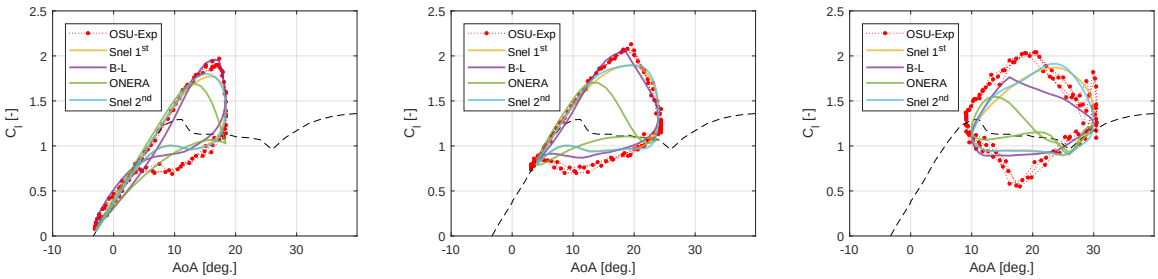

(a) Light dynamic stall ($\alpha_{mean} = 8^o$) (b) Deep dynamic stall ($\alpha_{mean} = 14^o$) (c) Deep dynamic stall ($\alpha_{mean} = 20^o$)

Figure 4.7: Dynamic stall hysteresis simulated with different dynamic stall models and compared with experimental data on S814 airfoil conducted at Ohio State University wind tunnel (OSU-Exp) [41]. The reduced frequency is approximately 0.09 and pitch amplitude is 10 degrees. Note: the dashed black line represents the steady airfoil polar.

coefficients were then extracted from the mid-span of the modeled blade. It is to be noted that during standalone simulations rotational corrections, Prandtl tip and root correction, dynamic inflow model, and yaw model were switched off.

The OSU dynamic tests were performed at a reduced frequency of approximately 0.09 for S814 airfoil section. The simulated results are compared with experimental results in figure 4.7 for different mean AoA. The pitch oscillation amplitude for all these cases is roughly 10 degrees. For light dynamic stall, it is seen that the lift coefficient switches between attached and stalled flow regime. In attached flow regime a counter-clockwise hysteresis loop is observed while in separated flow regime the hysteresis is clockwise. All dynamic stall models predict a clockwise hysteresis loop in the separated flow regime. While, in the attached flow regime only Beddoes-Leishman model is able to capture a counter-clockwise hysteresis loop due to modeling of Theodorsen's effect [89] associated with shed vorticity. The attainment of maximum lift coefficient and subsequent abrupt forced stall, due to end of oscillation half-cycle, is well captured by Beddoes-Leishman model and Snel's model in comparison to ONERA model.

Deep dynamic stall results are presented in figures 4.7b and 4.7c. Here again, Beddoes-Leishman and Snel's model seem to outperform ONERA model, not only in capturing the trend but also in more closely predicting the magnitude of the lift coefficient. In figure 4.7c, at a high mean AoA, even Beddoes-Lesihman and Snel's model are having a hard time predicting the maximum lift coefficient and trend in the down-stroke. Previously, dynamic stall models have been documented to under-perform in deep stall, as was indicated by Holierhoek et al. [40]. For further investigations into performance of standalone dynamic stall models the reader is referred to the afore mentioned literature by Holierhoek et al.. It should also be kept in mind while making deductions that there are certain uncertainties associated with experimental data, for example, OSU measurements have an uncertainty of approximately $+/-0.25$ degrees in AoA [41].

4.5. Validation of Axial Flow Simulations

Generally, the axial flow simulations seem to follow the experimental trend nicely as shown by figure 4.8a and 4.8b, and 4.8c. A peculiar hump can be seen in figure 4.8a and 4.8b, more pronounced in figure 4.8b. This peculiar hump in simulations near the 60% section has also been observed by Schepers et al. [76]. In figure 4.8c, Aero-BEM seems to slightly under-predict the experimental results at the inboard sections while over-predicting at the outboard stations. The results in figure 4.8c are for a higher tunnel speed of 24 m/s, meaning that the turbine is experiencing high AoA, probably near the non-linear stall regime of the blade sections. It is also the reason for a slightly higher standard deviation in the normal force indicated by error bars in figure 4.8c. The under-prediction of normal force in the inboard sections of the blade could be due to strong rotational effects causing a delay in stall in experimental results. This behavior has been previously documented for the original MEXICO experiment [76]. Although, rotational augmentation correction is included in Aero-BEM but it does not seem to sufficiently account for this pronounced effect in experiments. Overall, the results in figure 4.8 give an average relative error close to 10% from the new MEXICO measurements.

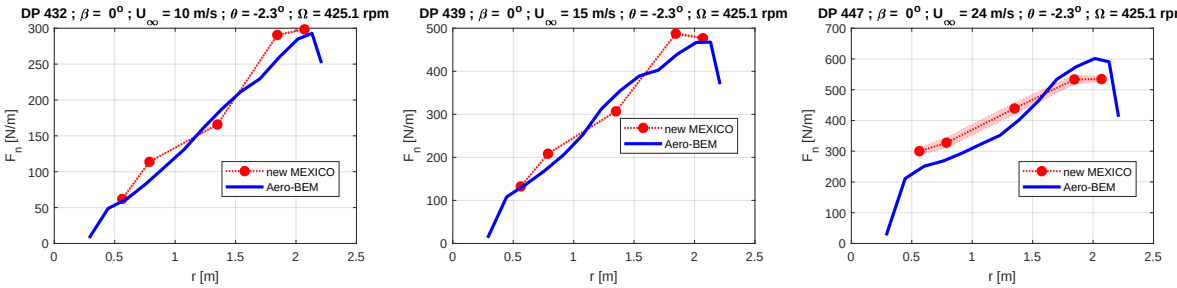

(a) $U_\infty = 10\ m/s$ (b) $U_\infty = 15\ m/s$ (c) $U_\infty = 24\ m/s$

Figure 4.8: Comparison of average normal force variation along the span between Aero-BEM and new MEXICO measurement in axial flow conditions. The simulations are performed without dynamic stall models. Note: the shaded regions indicate standard deviation of normal force.

5

Analysis of Standstill Conditions

This chapter presents a thorough analysis of New MEXICO measurements in standstill conditions along with validation of BEM simulations with dynamic stall models. The chapter starts by giving an overview of test cases that are analyzed, followed by presentation of 3D airfoil polars extracted from New MEXICO standstill measurements. The 3D polars are compared with trends in the literature to establish their credibility. After that, validation and statistical error analysis of simulated test cases is reported. Additionally, validation of simple cross-flow principle and a recently developed cross-flow model by Guanaa et al. [24] is performed. The chapter concludes with implementation of improvements to Beddoes-Lesihman and ONERA model.

5.1. Overview of Standstill Conditions

Generally, above the cut-off wind speed a wind turbine will initiate a shut down phase. During this phase, the rotor blades are pitched into the wind and parked; hence, the wind turbine is in standstill. In standstill a wind turbine does not have yaw control. Therefore, a change in wind direction can result in extremely high AoA, blade loads, and possibly vortex-induced vibrations. In order to shed light on the aerodynamics of a blade in standstill conditions the New MEXICO measurements are a valuable resource. New MEXICO measurements in standstill were performed for axially aligned flow with and without outboard roughness (see section 2.4.1 for details) and yawed flow with outboard roughness. An overview of all New MEXICO standstill test cases is reported in table 5.1. For standstill cases in yawed flow, the aerodynamic flow over all three blades will not be identical. Hence, to capture the flow over all three blades for each test condition, three runs were performed with each blade being at 12 o' clock location once. This procedure was required as the pressure sensors at five spanwise sections were distributed among the three blades, as was described in table 3.1.

Table 5.1: A concise summary of all the standstill data points in the New MEXICO measurement campaign.

Case Type	Data Point	U_∞ $[m/s]$	β $[deg.]$	θ $[deg.]$	Ω $[rpm]$
Standstill axial flow (rough)	372 – 394 397 – 401	~30	0	-2.3 – 90	0
Standstill yawed flow (rough)	405 – 425	~30	-90, -60, -45, -30, -15 +15, +30	90	0
Standstill axial flow (clean)	905 – 925	~30	0	60 – 90	0

5.2. 3D Airfoil Polars

In this section standstill measurements in the New MEXICO database are used to recreate the steady 3D airfoil polars. The purpose of doing this exercise is to compare the results with 2D airfoils polars and the trends observed in literature to establish a holistic credibility of standstill measurements. A summary of all the standstill data points used for this recreation are outlined in table 5.1. Each data point would correspond to one point on the C_l versus α and C_d versus α curve for a particular span-wise section. The AoA corresponding to each C_l and C_d value is computed through geometric considerations as presented in figure 5.2. Standstill cases with yaw where the blade section is either at 8 o' clock or 4 o' clock position have been excluded in this

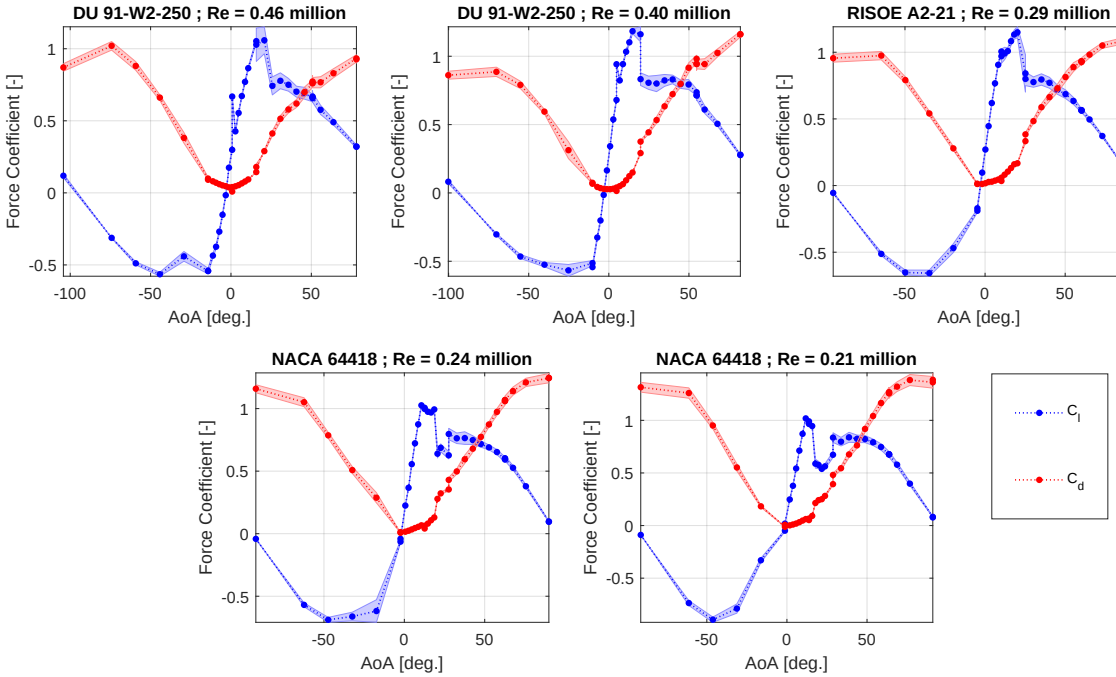

Figure 5.1: Airfoil polars reconstructed from Standstill measurements in axial and yawed conditions with roughness installed on outboard blade sections ($\frac{r}{R} > 70\%$). The AoA on the x-axis is the geometric AoA and the tunnel velocity in all these test runs was approximately 30 m/s. Note: the shaded regions denote the standard deviation of the measurements.

extraction process due to strong span-wise flow components in those blade positions. However, standstill cases with yaw where the blade is at 12 o' clock position are part of the extracted airfoil polars.

The standstill case in axial flow and yawed flow with roughness installed covered a wider range of AoA in comparison to axial flow with roughness removed; therefore, it is presented in figure 5.1. In this figure, there is an increase in unsteadiness after stall indicated by the increasing standard deviation in the lift force coefficient. Furthermore, an increase in standard deviation of the drag coefficient with a subsequent decrease in the standard deviation of lift coefficient is observed in the deep stall regime beyond, approximately, 50 degrees AoA. This is expected as the airflow nearly becomes perpendicular to the airfoil and lift coefficient approaches almost zero. A similar sort of trend in standard deviation is also observed for deep stall with negative AoA. However, in this case the location of stall is not clearly indicated due to scarcity of sufficient data points.

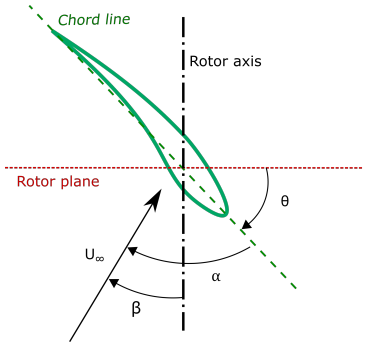

Figure 5.2: Schematic showing the calculation of geometric AoA for standstill cases with yaw. Note: the geometric AoA is only calculated for 12 o' clock blade position.

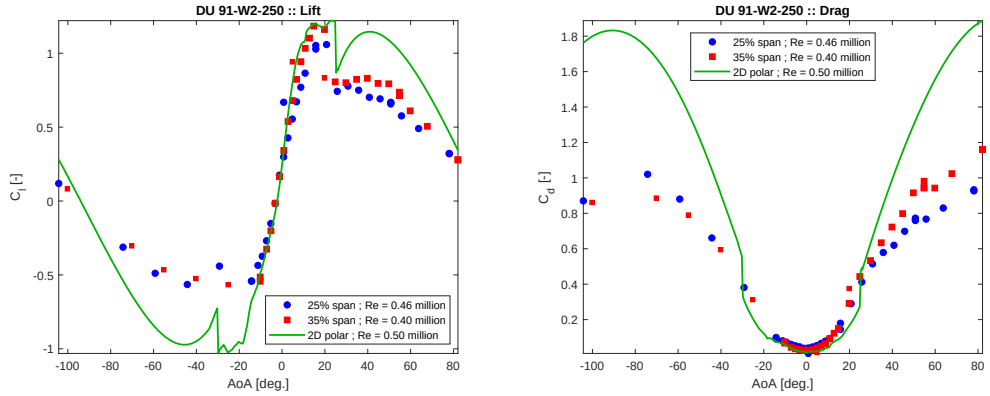

Figure 5.3: Comparison between airfoil polars extracted from standstill measurements (shown as red or blue points) with the ones used in Aero-Module simulations (green curve). The deep stall airfoil characteristics in the negative AoA range were extracted from Standstill runs in yawed conditions and are distinguished by either an upward facing or inverted triangular data point.

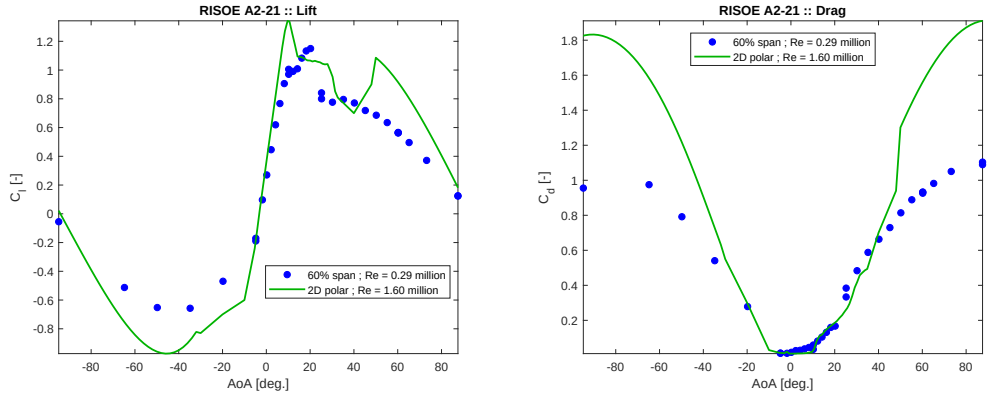

Figure 5.4: Comparison between airfoil polars extracted from standstill measurements (shown as blue points) with the ones used in Aero-Module simulations (green curve). The deep stall airfoil characteristics in the negative AoA range were extracted from Standstill runs in yawed conditions and are distinguished by either an upward facing or inverted triangular data point.

5.2.1. Comparison with 2D Airfoil Polars

The agreement of these polars with the 2D airfoil polars, which are used in Aero-Module simulations, is reasonable good within attached flow regime and up until stall. However, in the deep stall regime there is a large difference between the airfoil polars. This is realistic as a 2D section has more base drag. It is to be noted that the 2D airfoil polars in deep stall regime, for all three airfoil sections, are taken from deep stall measurements on DU96-W-180 airfoil conducted by TU Delft [92]. This was done due to non-availability of wind tunnel data for those airfoils. Lindenburg [49] assumed the influence of Reynolds number in the deep stall regime to be minimal for wind turbine applications. This assumption is somewhat true as, typically, high Reynolds number delays separation by transitioning the boundary layer to turbulent or by energizing the boundary layer. However, for complete separation in deep stall regime this might not be the case. The Reynolds number for the DU 91-W2-250 airfoil section in figure 5.3 is almost similar between the 2D and 3D airfoil polars. While in case of RISO A2-21 section, the 2D airfoil polar is for a very high Reynolds number compared to the 3D polar, which could be the reason for the higher $C_{l_{max}}$ observed for 2D airfoil polar in figure 5.4. Finally, for the NACA 64418 section, the Reynolds number between 2D and 3D airfoil polars are comparable. However, it is to be noted that this blade section, containing NACA airfoil sections, would only experience these low Reynolds number in standstill conditions. In normal operation, this section would experience Reynolds number close to 0.7 million.

Observing figure 5.3, it can be seen that the lift coefficient for the section closer to the root is lower than 35% section and 2D airfoil polar. This is due to induction effects from the root of a finite aspect ratio MEXICO blade. A similar behavior was reported by Timmer [90] for the NREL UAE phase VI measurements in NASA Ames wind tunnel. There, he also observed that these end effects due to induction were more visible for

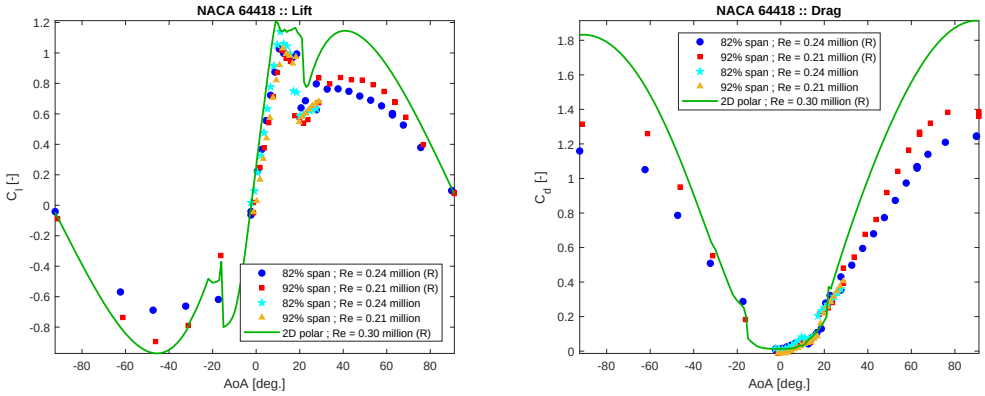

Figure 5.5: Comparison between airfoil polars extracted from standstill measurements (shown as red or blue points) with the ones used in Aero-Module simulations (green curve). The deep stall airfoil characteristics in the negative AoA range were extracted from Standstill runs in yawed conditions and are distinguished by either an upward facing or inverted triangular data point. Note: (R) denotes outboard roughness installed or outboard roughness effects are included.

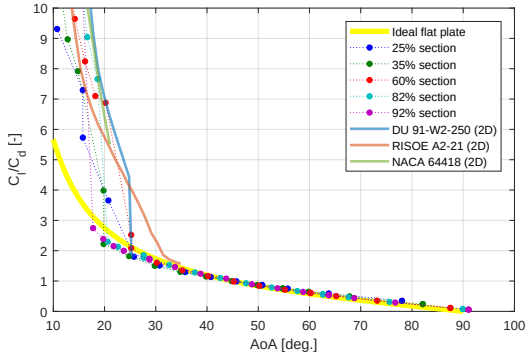

(a) A comparison of lift to drag ratio of 3D polars from five different sections of New MEXICO blade with the ideal flat plate theory and 2D airfoil polars.

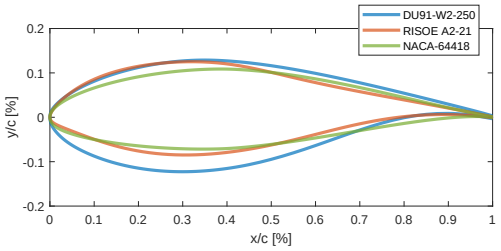

(b) Comparison of New MEXICO airfoil profiles.

Figure 5.6: Lift to drag ratio versus AoA and airfoil section geometry of New MEXICO blade sections.

section closer to the root. On the other hand, in figure 5.5, the 3D polars indeed have a lower lift coefficient than the 2D polars. In the attached flow regime, 82% section with rough and clean configuration has a slightly higher lift curve slope than 92% section with rough and clean configuration. However, in deep stall regime the 82% section has a lower lift and drag coefficient unlike figure 5.3, where the section near the edge of blade (25% section) seems to have lower lift and drag coefficient, supposedly, due to more pronounced end effects.

5.2.2. Comparison with Flat Plate Theory in Deep Stall

In deep stall regime, flow over the upper airfoil surface is completely separated. In such a situation the influence of upper surface thickness on pressure distribution can be neglected, for airfoils with moderate lower surface thickness, as was pointed out by Timmer [90] and Lindenburg [50]. Based on this, it can be assumed that the lift to drag ratio in the deep stall regime would closely resemble that of a flat plate as the upper surface pressure distribution is independent of upper surface thickness. The lift and drag coefficient can be computed from the following equation based on ideal flat plate theory, taken from Timmer [90]:

$$C_l = 2\sin\alpha\cos\alpha \tag{5.1}$$

$$C_d = 2\sin^2\alpha \tag{5.2}$$

Using the above equations, lift to drag ratio for an ideal flat plate was computed and plotted against the lift to drag ratio obtained from 3D and 2D airfoil polars in figure 5.6a. In this figure, it is seen that all curves coalesce to follow the trend predicted by flat plate theory above 30 degrees AoA, characterizing deep stall regime.

Table 5.2: Summary of selected standstill cases for analysis.

Case no.	Case Type	Data Point	$U_\infty\,[m/s]$	$\beta\,[deg.]$	$\theta\,[deg.]$	$\Omega\,[rpm]$
1	**Standstill axial flow (rough)**	372	~30	0	90	0
2		382	~30	0	75	0
3		373	~30	0	45	0
4		386	~30	0	30	0
5		400	~30	0	12	0
6		375	~30	0	-2.3	0
7	**Standstill yawed flow (rough)**	405, 406, 407	~30	-90	90	0
8		408, 409, 410	~30	-60	90	0
9		411, 412, 413	~30	-45	90	0
10		414, 415, 416	~30	-30	90	0
11		420, 421, 422	~30	15	90	0
12		423, 424, 425	~30	30	90	0

However, below this AoA, lift to drag ratio differ depending upon airfoil section and spanwise location. It is to be mentioned here that although 2D airfoil polars in the deep stall regime are taken from DU-96-W180 profile [92], but data at moderate AoA is still obtained from experimental measurements on respective airfoils and in figure 5.6a 2D polars are shown up till these AoA (excluding DU-96-W180 data in deep stall). Therefore, 2D polars are included in figure 5.6a and can be considered valuable for analysis below deep stall AoA. For 2D polars, the deep stall regime starts above 30 degree for RISOE airfoil section while for DU it starts above 25 degrees. Due to lack of data for NACA airfoil in deep stall it is hard to pinpoint at which AoA the deep stall regime would start; however, based on visual inspection it seems to be lower than 25 degrees. For 3D polars, 25% and 35% DU profile sections and 60% RISO profile section have a higher relative thickness than the NACA profile at 82% and 92% sections, as illustrated by figure 5.6b. It appears that 3D polars for DU and RISO profile sections (i.e. 25%, 35%, and 60% sections) seem to enter deep stall regime at a relatively higher angle of attack than NACA profile sections (i.e. 82% and 92% section). This behavior could be because relatively thinner airfoils show a tendency of leading edge separation with large separation over the complete upper surface, often referred to as "thin airfoil stall" [1]. Similar to a flat plate where onset of leading edge separation causes an abrupt stall. Due to this tendency relatively thin airfoils seem to enter deep stall at lower AoA. A peculiar behavior of RISOE profile section is that despite having a lower maximum relative thickness of 21% compared to DU profile section's 25% maximum relative thickness, it seems to enter deep stall (or, in other words, onset of leading edge separation) at a relatively higher AoA for both 2D and 3D airfoil polars. Compared to DU profile, RISO profile has a large camber due to a comparatively lower lower surface thickness as seen in figure 5.6b. To sum it all up, figure 5.6a further establishes an already know fact, presented by Timmer [90], that lift to drag ratio for a finite or infinite (2D) blade section is identical to a flat plate. Thus, strengthening the credibility of New MEXICO measurements in Standstill.

5.3. Validation of Aerodynamic Simulations

In this section, a comprehensive analysis and simulation of selected standstill measurements from the New MEXICO database is presented. The selected standstill measurements are summarized in table 5.2. Standstill experimental runs in yawed flow conditions were performed three times each (thus, three Data Points), as can be seen from the table 5.2, so that every blade is positioned at 12 o' clock once. This way the five span-wise pressure sensor locations, which are distributed among the three blades, are able to capture the asymmetric flow conditions on the three blades in standstill yawed flow. The selected cases in table 5.2 covered a diverse spectrum of test conditions. Preference was given to cases where extremely large AoA are expected, like case 6 and case 7 in table 5.2. The simulations were performed using the BEM model in Aero-Module. Dynamic stall models were included to evaluate their performance in such an adverse condition for which they were not originally designed. As mentioned, standstill cases where the rotor is expected to incur extremely high AoA were considered for the analysis in the hope to observe self-excited vortex shedding oscillations. Four different dynamic stall models were investigated in this analysis campaign, namely:

1. Snel's 1^{st} order model
2. Beddoes-Leishman model

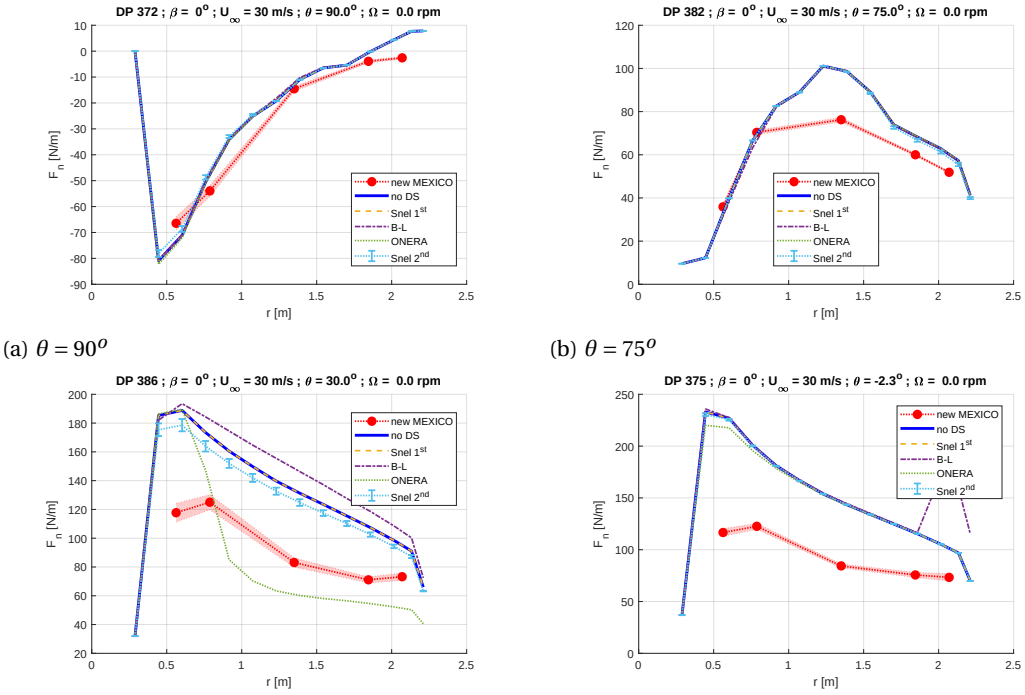

(a) $\theta = 90^o$ (b) $\theta = 75^o$

(c) $\theta = 30^o$ (d) $\theta = -2.3^o$

Figure 5.7: Normal force variation along span of the New MEXICO blades in standstill with axial flow. Four different dynamic stall models: Snel's first order model, Beddoes-Lesihman model (B-L), ONERA model, and Snel's second order model along with a simulation without dynamic stall model (no DS) are compared with New MEXICO measurements. All simulations are performed using a BEM model. Test condition for axial results: $\beta = 0^o$; $U_\infty = 30 m/s$; $\Omega = 0.0\, rpm$

3. ONERA model
4. Snel's 2^{nd} order model

For simulations, the rotational augmentation effects were turned off as the turbine is no longer rotating in standstill conditions. It is to be noted that Prandtl tip and root correction were also turned off. Principally, these corrections were developed to be used for a rotating finite bladed rotor; hence, its use in standstill simulations is questionable. Number of blade elements along the span were kept at 14. A time step size of 0.00393 seconds was chosen for the analysis. The total simulation time was approximately 2.12 seconds. For simplicity, tower effects were turned off, also these effects are assumed to be small for New MEXICO rotor as there is a distance of roughly one rotor radius from the tower to the rotor center.

5.3.1. Standstill in Axial Flow

Each standstill test case in axial flow is performed with a particular pitch setting. Figure 5.7 shows the spanwise normal force variation for different pitch settings in axial flow. For a high pitch setting, like 90 degrees in figure 5.7a and 75 degrees in figure 5.7b, the AoA variation along the blade span is roughly within -15 – 0 degrees and 0 – 15 degrees, respectively. For these pitch settings, the AoA are roughly within the attached flow regimes of airfoil sections. Which is why, simulated trends from all dynamic stall model simulations show a good match with experimental results. However, reducing the pitch setting to 30 degrees and -2.3 degrees, figure 5.7c and figure 5.7d, respectively, shows a larger deviation of simulations from experimental results. In fact, there are also deviations among simulations with different dynamic stall models. In these pitch settings the blade is expected to experience large AoA along span, in range of approximately 45 – 60 degrees for 30 degree pitch setting and roughly in range of 75 – 90 degrees in case of -2.3 degree pitch setting. The standard deviation in experimental results is seen to be larger for 30 degree pitch setting than at -2.3 degree pitch setting, which is much clearly seen from figure 5.12 corresponding to case 4 and case 6, respectively. Only Snel's second order model seems to simulate some unsteadiness for 30 degree pitch setting, indicated by larger error-bars in figure 5.7c. However, this same model captures negligible unsteadiness for -2.3 degree pitch setting, probably because it is being artificially switched off using fader functions. On the other hand,

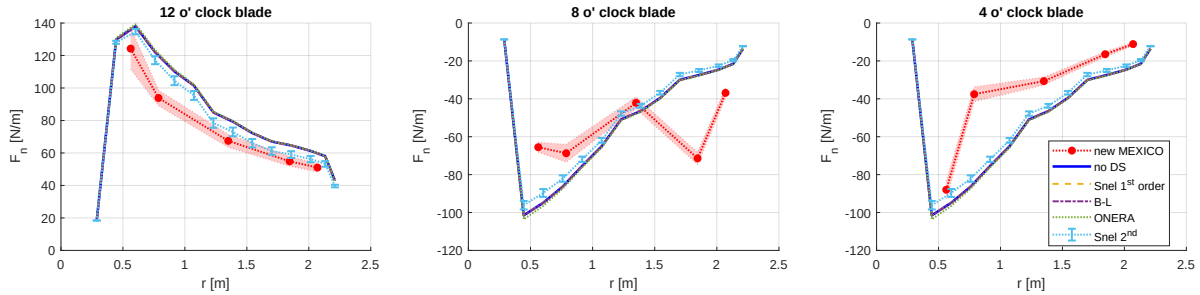

Figure 5.8: Normal force variation along span of the New MEXICO blades in standstill with +30 degrees yaw. Four different dynamic stall models: Snel's first order model, Beddoes-Lesihman model (B-L), ONERA model, and Snel's second order model along with a simulation without dynamic stall model (no DS) are compared with New MEXICO measurements. All simulations are performed using a BEM model. Test condition for current results: $\beta = +30^o$; $U_\infty = 30 m/s$; $\theta = 90.0^o$; $\Omega = 0.0\, rpm$

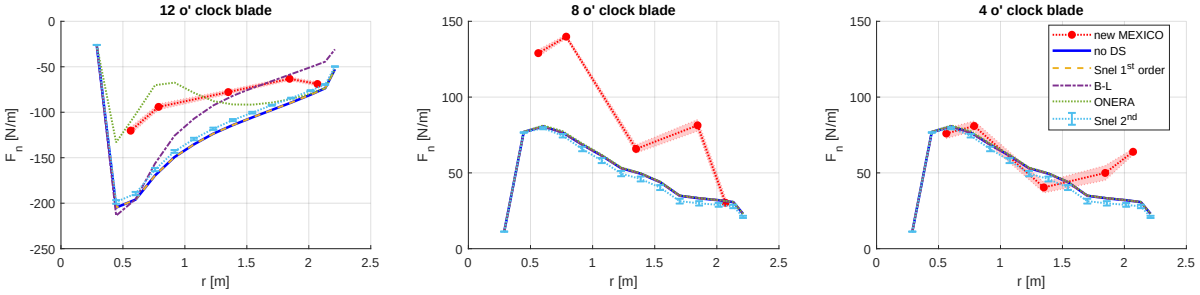

Figure 5.9: Normal force variation along span of the New MEXICO blades in standstill with -45 degrees yaw. Four different dynamic stall models: Snel's first order model, Beddoes-Lesihman model (B-L), ONERA model, and Snel's second order model along with a simulation without dynamic stall model (no DS) are compared with New MEXICO measurements. All simulations are performed using a BEM model. Test condition for current results: $\beta = -45^o$; $U_\infty = 30 m/s$; $\theta = 90.0^o$; $\Omega = 0.0\, rpm$

Snel's first order model gives exactly the same results as BEM without using dynamic stall model. Beddoes-Leishman and ONERA model seem to show very strange behaviour. Especially, the trend predicted by ONERA model in figure 5.7c and the sudden peak in normal force near the tip predicted by Beddoes-Leishman model in figure 5.7d seem erroneous.

5.3.2. Standstill in Yawed Flow

In case of standstill in yawed flow, for positive yaw angles, simulations give reasonably good results which are in agreement with New MEXICO measurements , as seen in figure 5.8. Here, again, Snel's second order model seems to capture some unsteadiness in experimental results. For negative yaw angles the simulations seem to largely over-predict the normal force for the blade at 12 o' clock position, as observed in figure 5.10. The large over-prediction in normal force is actually contributed from the large difference between 2D airfoil polars used in simulation and 3D airfoil polars extracted from standstill measurements, as showcased by figures 5.3, 5.4, and 5.5. It can be clearly seen from these figures that 2D airfoil polars used in simulation give a higher magnitude of lift coefficient and drag coefficient for negative and positive AoA in deep stall regime. Using standstill data from three data points at the same conditions, the force distribution along the blade span for the three blades is reconstructed, as depicted by figure 5.8,5.10, and 5.9. In these figures, all the blades are pitched at 90 degrees. In all the standstill cases, a common trend of increasing normal force from tip to root is observed for all three blades. Despite the fact that twist of the blade might be reducing the geometric AoA near the root, the afore-mentioned common trend still seems to persist. Mainly, because the increase in normal force from the larger chord near the root is more pronounced than an increase or decrease in normal force due to change in AoA from twist of blade. The blades at 4 o' clock and 8 o' clock for standstill in yawed flow exhibit spanwise flow. In figure 5.10 and 5.9, 8 o' clock blade will have spanwise flow from root to tip and vise verse for 4 o' clock blade. The opposite will be true for figure 5.8 due to the positive yaw angle.

Generally, for standstill in yawed flow, all dynamic stall models seem to show similar results with the exception of results for 12 o' clock blade from figure 5.9. Here, the normal force predicted by ONERA model seems to be close to measurements; however, the trend looks erroneous. On the other hand, in this particular figure, Beddoes-Leishman model deviates from other dynamic stall models by predicting a lower normal

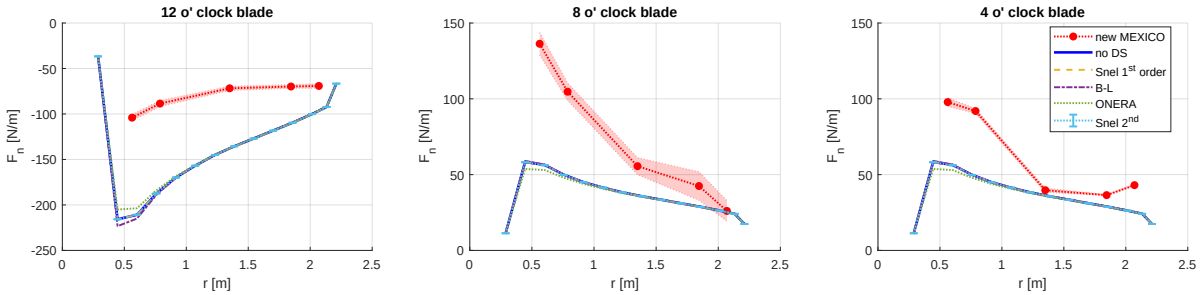

Figure 5.10: Normal force variation along span of the New MEXICO blades in standstill with -90 degrees yaw. Four different dynamic stall models: Snel's first order model, Beddoes-Lesihman model (B-L), ONERA model, and Snel's second order model along with a simulation without dynamic stall model (no DS) are compared with New MEXICO measurements. All simulations are performed using a BEM model. Test condition for current results: $\beta = -90^o$; $U_\infty = 30 m/s$; $\theta = 90.0^o$; $\Omega = 0.0\, rpm$

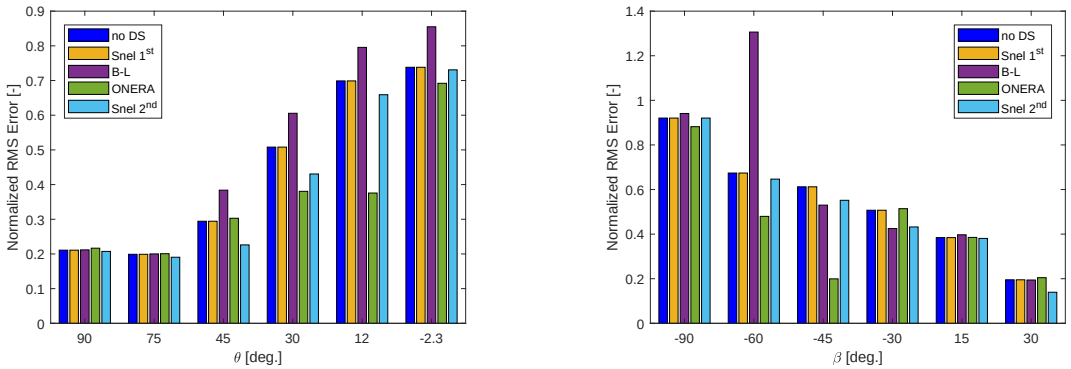

(a) Axial flow in standstill

(b) Yawed flow in standstill

Figure 5.11: A summary of normalized root mean square (RMS) errors with respect to the New MEXICO measurements and their variation with changing test conditions in standstill. Note: RMS error is normalized with mean load along the span from New MEXICO measurements.

force trend near the tip region. In terms of predicting unsteadiness, only Snel's second order model is showing some promise. Nevertheless, for 8 o' clock blade in figure 5.10, the model fails to capture large unsteadiness in experimental results. Here, the 8 o' clock blade section is almost perpendicular to the incoming flow and in the wake of 4 o' clock blade. Thus, this blade must be experiencing a complicated deep stall flow regime which the model is not able to replicate.

5.3.3. Statistical Error Analysis

In order to quantify the performance of different dynamic stall models, normalized root mean square error was used. An average relative error estimate was also considered; however, it suffers from the problem of division by zero in denominator. As in some test cases the normal force is close to zero, so a root mean square estimate is more robust. The root mean square error (RMS) was computed according to the following relation:

$$\text{RMS Error} = \sqrt{\frac{\sum_{i=1}^{N_{span}} \left(F_{n,meas}(i) - F_{n,pred}(i)\right)^2}{N_{span}}} \tag{5.3}$$

where, N_{span} is the number of spanwise stations, which is equal to five. $F_{n,meas}(i)$ is time averaged value of experimental normal force and $F_{n,pred}(i)$ is time averaged value of simulated normal force at a particular spanwise section. The RMS error is normalized with mean value of time averaged normal force along span.

$$\text{NRMS Error} = \frac{\text{RMS Error}}{\frac{1}{N_{span}} \sum_{j=1}^{N_{span}} F_{n,meas}(j)} \tag{5.4}$$

The normalized RMS error facilitates the comparison between various test cases which is presented in the bar graphs of figure 5.11 for axial and yawed flow in standstill conditions. In figure 5.11a, the NRMS error

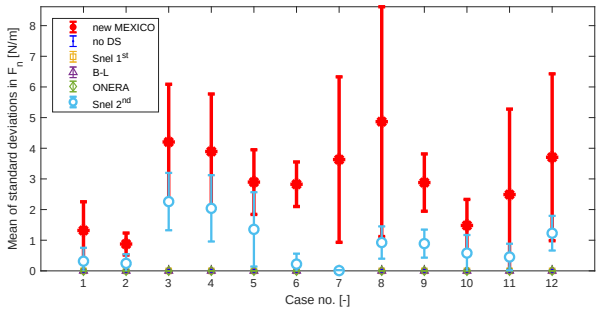

Figure 5.12: Scatter plot representing mean of all standard deviation values in normal force obtained from a particular test case number indicated on the x-axis corresponding to the test cases listed in table. Note: the error bars in the scatter plot indicated the standard deviation of standard deviation values in normal force fora particular case number.

trend increases with reducing the pitch setting of the blade, implying that a large discrepancy exists between simulations and experiments for very high AoA. It might seem at first glance that ONERA model is the best performing among the tested dynamics stall models. However, closer inspection of results in figure 5.7c show that it completely misrepresents the experimental trend. Standstill in yaw shows large NRMS errors for larger yaw angles. In fact, larger yaw angles again imply very large AoA. Here, ONERA model again seems to show lower errors as compared to other dynamic stall models, especially for -45 degrees yaw. Nonetheless, closer inspection of results in figure 5.9 reveal an erroneous trend.

In conclusion, caution should be exercised while using dynamic stall models in standstill situations with very large AoA. Mainly because these models were originally designed to work up until moderate AoA. Validity of these models in deep stall regime is questionable. Say for instance, in case of the Beddoes-Lieshman model, it uses Kirchoff's law to determine the location of separation point, as described in section 2.1.2. However, Kirchoff's law itself is based on a small angle approximation. Similarly, for the ONERA model a linearization assumption is used where it is assumed that the changes in AoA are small. This is again violated in deep stall with extremely large AoA. Only, Snel's model does not explicitly require any restriction on AoA.

From the scatter plot in figure 5.12, it is seen that there is a lot of unsteadiness present in the New MEXICO measurements in standstill. However, majority of the analyzed dynamic stall models do not seem to show any unsteadiness in simulations, which is, of course, expected as none of these models have a provision for self-excitation except Snel's second order model. As discussed in section 2.1.2, Snel's model uses a non-linear second order Van Der Pol type equation to simulate oscillations in loads due to self-excited vortex shedding. It is seen from figure 5.12 that Snel's second order model is more active for cases 3, 4, and 5 corresponding to pitch settings of 45, 30, and 12 degrees, respectively, in axial flow. The model seems to show negligible activity for case 7 (with -90 degrees yaw), whereas experiments show large fluctuations in normal force. On the whole, the model seems to be more active for large positive AoA related to cases 3, 4, and 5.

5.4. Cross-Flow Principle

Cross-flow principle is among the main underlying principles used in strip theory. It was first proposed by Hoerner [37, 38] to predict aerodynamic loads on a circular cross-section of a cylindrical rod in cross-flow. The main underlying assumptions of this principle is that the 2D cross-sectional shape does not change along the span and induced velocities are neglected. However, both these assumptions are not completely true in the case of a wind turbine blade. Despite this, the cross-flow principle is extensively used in the prediction of standstill loads on a wind turbine blade. Originally the cross-flow principle states:

The aerodynamic loads on a cross-section of a cylinder placed in oblique flow can be determined from the normal component of inflow velocity by neglecting the spanwise component.

In standstill conditions with yawed flow the flow over all three blades is no longer identical. In fact in such conditions, a blade will not experience cross-flow only if it is at 12 o' clock or 6 o' clock position. In case of New MEXICO rotor in standstill conditions with yaw, one blade is always at 12 o' clock. Meaning that the blade at 8 o' clock and 4 o' clock will experience spanwise flow. Here, the cross-flow principle offers itself as a valuable tool for predicting the aerodynamic loads. The Aero-BEM and Aero-AWSM models in Aero-Module

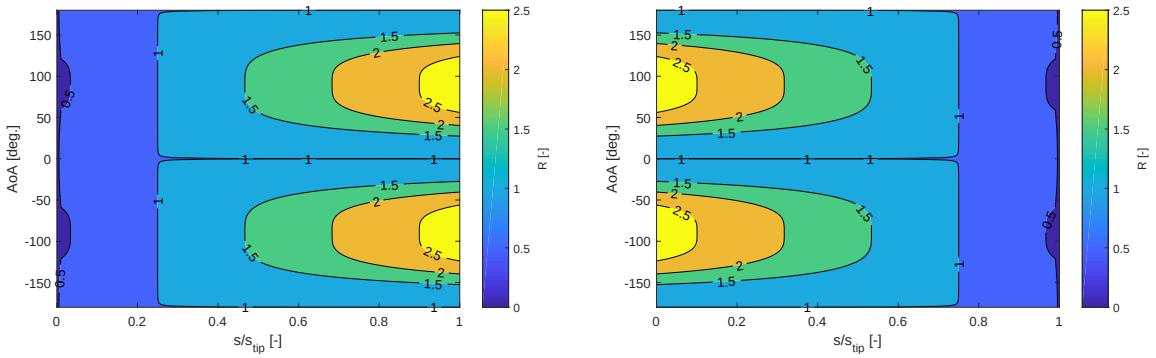

(a) $\theta_{cf} = 60^o$ (b) $\theta_{cf} = -60^o$

Figure 5.13: Variation of cross-flow error ratio, predicted by equation 5.8, with AoA, spanwise location, and cross-flow angle.

both make use of this principle to predict standstill loads on a wind turbine rotor.

5.4.1. Cross-Flow Model

Recently, Gaunaa et al. [24] conducted an extensive validation of the cross-flow principle on the DTU 10 MW reference blade [2]. They used DTU's in-house CFD code EllipSys3D to perform Detached Eddy Simulations (DES) with k-ω Shear Stress Transport (SST) turbulence model of a single blade. The simulations were performed for five different cross-flow angles from -60 to +60 degrees. With each cross-flow angle, the simulation was repeated at 52 different pitch angle settings at an inflow velocity of 12 meters per second. The sectional lift and drag force was computed in accordance with cross-flow principle using

$$C_{l_{cf}} = \frac{L_{cf}}{\frac{1}{2}\rho U_\infty^2 \cos^2\theta_{cf} c} \tag{5.5}$$

$$C_{d_{cf}} = \frac{D_{cf}}{\frac{1}{2}\rho U_\infty^2 \cos^2\theta_{cf} c} \tag{5.6}$$

where, θ_{cf} is the cross-flow angle of incoming velocity with respect to the blade quarter chord line. θ_{cf} is defined positive when spanwise flow is coming from tip towards root. Gaunaa et al. [24] proposed a cross-flow error ratio on lift, drag, and resultant force coefficients to determine the effectiveness of cross-flow principle. For brevity, only cross-flow error ratio on resultant force coefficient is presented as follows

$$R(s,\alpha,\theta_{cf}) = \frac{C_{f_{cf}}(s,\alpha,\theta_{cf})}{C_{f_{unyawed}}(s,\alpha)} \tag{5.7}$$

In the above equation, the resultant force coefficient is expressed as $C_f = \sqrt{C_l^2 + C_d^2}$ and s is the coordinate of spanwise blade section. Here, α is defined in-plane of the blade section without the spanwise flow component. The cross-flow error ratios for lift and drag coefficient are also defined in a similar fashion. From equation 5.7, an error ratio of 1 would imply that the sectional force coefficient obtained in cross-flow (nominator) is equal to the one obtained through neglecting spanwise flow component or assuming an unyawed flow (denominator). In order words meaning that the cross-flow is giving appreciable results. However, Gaunaa et al. [24] found that this is only true for a small range of AoA for the simulated cross-flow angles. Therefore, they applied a first order correction model as an add-on to the cross-flow principle. The correction model is based on replicating the cross-flow error ratio through a mathematical equation of the form

$$R(k_{cf},\alpha,\theta_{cf}) = \frac{2}{\pi}\arctan\left(40k_{cf}\left(1+1000\,\mathrm{sech}\left(\frac{\theta_{cf}}{2}\right)\right)\right)\left[1+|\sin\theta_{cf}|\left(k_{cf}-\frac{1}{4}\right)\left(\frac{8}{3}\sin^2\alpha+\frac{2}{3}|\sin\alpha|\sin^2 2\alpha\right)\right] \tag{5.8}$$

where,

$$k_{cf} = \begin{cases} \frac{s}{s_{tip}} & \text{if } \theta_{cf} > 0 \\ 1-\frac{s}{s_{tip}} & \text{else} \end{cases} \tag{5.9}$$

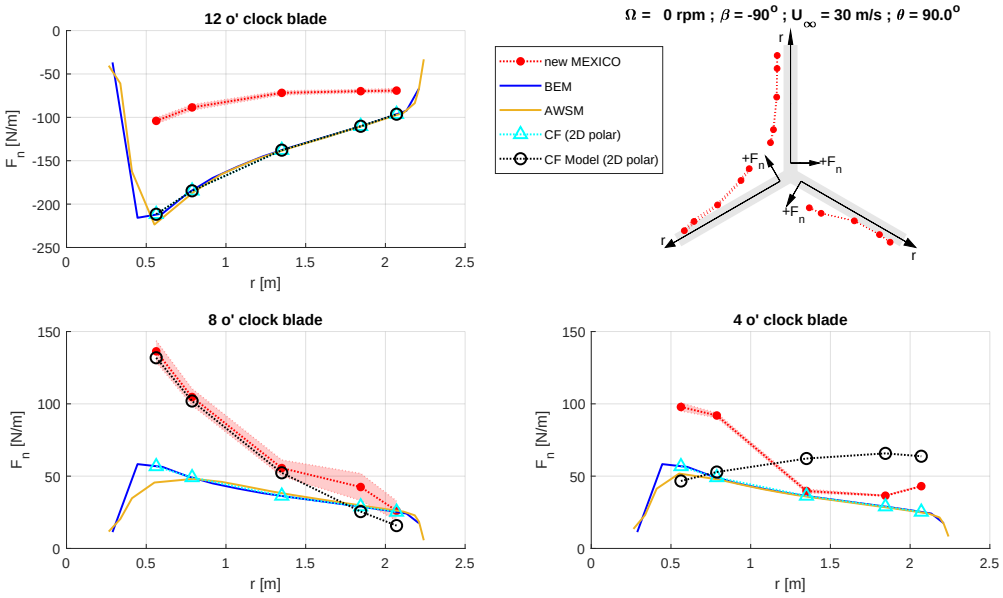

Figure 5.14: Normal force variation along blade span for the three blades of New MEXICO rotor in standstill conditions with -90 degrees yaw. The experimental normal force variation is compared with four different set of simulations: BEM, AWSM, Cross Flow (CF) principle using 2D airfoil polars, and Cross Flow (CF) model. Note: The normal force in the top right figure has been scaled down by a factor of 400 to compare it on the same scale as rotor blade dimensions.

The above equation tries to imitate the cross-flow error ratio trends observed in CFD simulations. Generally, it tries to increase the loads for upwind side of a blade in cross-flow as can be seen from figure 5.13, where $\theta_{cf} = -60^o$ implies root of blade is upwind (i.e. flow from root to tip) and vice versa for $\theta_{cf} = 60^o$. It was also observed in this work that cross-flow error ratios for lift, drag, and total force were identical (i.e. $R_l \approx R_d \approx R$). Therefore, a single error ration correction given by equation 5.8 can be applied to lift, drag, or total force coefficients.

5.4.2. Validation

The first order cross-flow model, described above, has been applied as an add-on to simple cross-flow principle to predict the normal force coefficients on the New MEXICO rotor blades in standstill conditions with yawed flow. Additionally, BEM and AWSM simulations (without dynamic stall model) were also performed. The reason for performing AWSM simulation was to access the significance of finite blade induction effects, as AWSM intrinsically models this effect through trailing vorticity. In this way, the assumption of neglecting induced velocities in standstill, as was also made by Gaunaa et al. [24] in deriving their cross-flow model, can be reinforced. For the sake of simplicity, results for -90, -60, and +30 degrees yaw will be presented in this section.

Figure 5.14 and 5.15 show results for standstill in -90 and -60 degrees yaw, respectively. In such conditions large cross-flow is expected over the 8 o' clock blade from root to tip ($\theta_{cf} = -60^o$) and vice versa ($\theta_{cf} = +60^o$) for 4 o' clock blade. On the other hand, in case of figure 5.16 with +30 degrees yaw, spanwise flow is expected from tip to root ($\theta_{cf} = +60^o$) over 8 o' clock blade and vise versa ($\theta_{cf} = -60^o$) for 4 o' clock blade. Both BEM and AWSM rely on cross-flow principle to compute sectional forces, which is the reason why the simple computations using cross-flow principle and 2D airfoil polars (shown in cyan colored triangles) mostly lie on top of BEM and AWSM simulations with a few exceptions near the root. Observing the results of AWSM in these three figures it can be clearly seen that AWSM is predicting induction effects to be more prominent near root as opposed to tip. It might be due to generally higher loads near the root from increased chord length of blade sections. However, the difference is not large. In figure 5.14, the cross-flow model seems to show promising results for the 8 o' clock blade; nonetheless, it misrepresents the trend completely in case of 4 o' clock blade where the tip of the blade is upwind. While, as expected, the cross-flow model does not change the loads for 12 o' clock blade as it is not experiencing cross-flow. For 12 o' clock blade the difference with measurements are still large for larger yaw angles, which has been already discussed in section 5.3. On the whole, the cross-flow model tries to capture the reality in some instances, but it is far from being a complete correction model

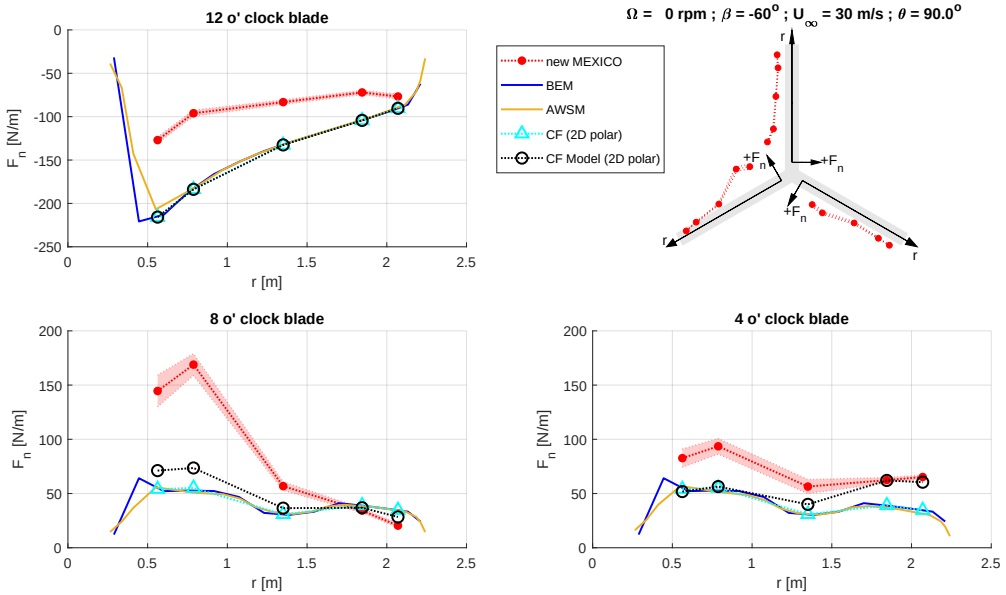

Figure 5.15: Normal force variation along blade span for the three blades of New MEXICO rotor in standstill conditions with -60 degrees yaw. The experimental normal force variation is compared with four different set of simulations: BEM, AWSM, Cross Flow (CF) principle using 2D airfoil polars, and Cross Flow (CF) model. Note: The normal force in the top right figure has been scaled down by a factor of 400 to compare it on the same scale as rotor blade dimensions.

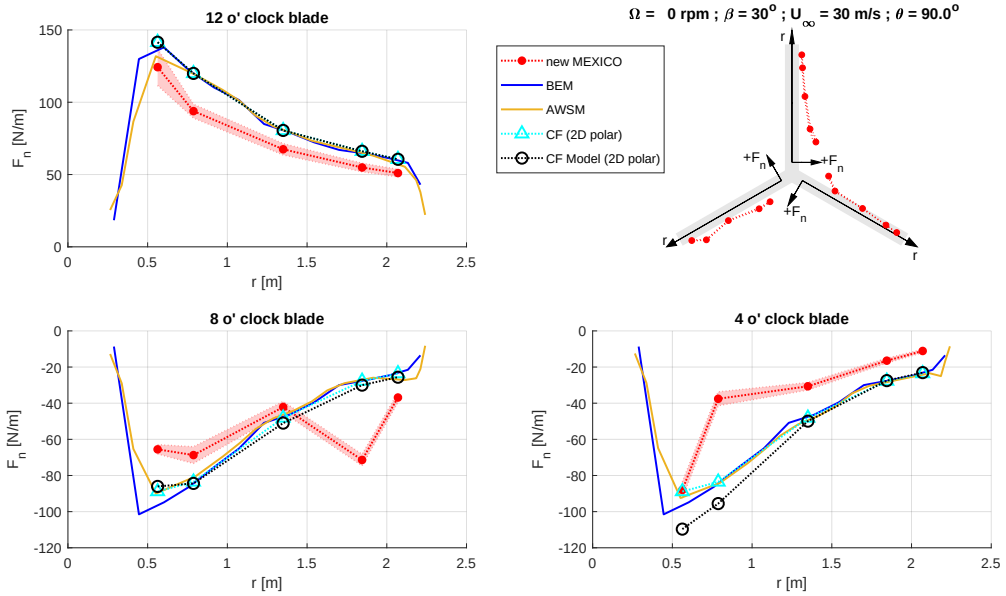

Figure 5.16: Normal force variation along blade span for the three blades of New MEXICO rotor in standstill conditions with +30 degrees yaw. The experimental normal force variation is compared with four different set of simulations: BEM, AWSM, Cross Flow (CF) principle using 2D airfoil polars, and Cross Flow (CF) model. Note: The normal force in the top right figure has been scaled down by a factor of 400 to compare it on the same scale as rotor blade dimensions.

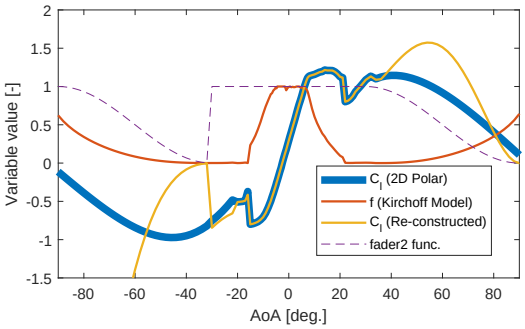

Figure 5.17: Comparison between lift coefficient from 2D polar and its reconstruction using B-L dynamic stall model. Additionally, variation of separation point parameter f and fader2 function with AoA is shown. The DU 91-W2-250 2D airfoil polar is used in this figure.

for the cross-flow principle. It still needs to be optimized for generic blades as it was originally developed based on DTU 10 MW reference blade CFD simulations. As far as New MEXICO measurements in standstill with yawed flow are concerned, there is a general trend of larger normal force for the blade with spanwise flow from root to tip in comparison to the blade having spanwise flow from tip to root, as observed in figure 5.14, 5.15, and 5.16.

5.5. Improving the B-L Trailing Edge Separation Model

In section 5.3, it was seen that the B-L model showed erroneous results for very large AoA. This problem was investigated further and the trailing edge separation model was improved. The cause of this problem was found to be mainly associated with the Kirchoff flow separation model. This model is based on small angle approximation, and it fails at large AoA. As described in section 2.3.1, the Kirchoff model uses a flow separation parameter f to describe the location of the separation point with respect to chord length. The values for this parameter starts increasing after 40 degrees AoA, as shown in figure 5.17. Implying that the separation point starts moving towards the trailing edge at very large AoA, which is wrong. As at very large AoA there is massive separation on the airfoil upper surface. In order to remedy this problem, Aero-Module (by default), uses a fader2 function of the form:

$$\text{fader2} = \cos^2\left(1.5(\alpha - 30)\right) \tag{5.10}$$

This function is applied beyond +/- 30 degrees. However, there was a problem in the implementation of this function which resulted in poor results for negative AoA beyond -30 degrees, as seen from figure 5.17. In fact, the strange jump in normal force near the tip predicted by the B-L model in figure 5.7d is due to this problem. It happens when the B-L model loops back to -90 degree AoA for AoA larger than +90 (reason for this implementation is discussed in section 4.2.1). This problem can be fixed by using the following form of the function for AoA below -30 degrees.

$$\text{fader2} = \cos^2\left(1.5(\alpha + 30)\right) \tag{5.11}$$

Despite this minor fix, the re-constructed C_l poorly matches the actual 2D airfoil polar used in the simulations. Therefore, to address this issue three different models proposed by Øye [60], Bjørck [5], and Larsen [43] were assessed.

Øye's model [33, 60] uses a linear interpolation between the fully separated and attached flow lift coefficient to re-construct the steady lift polars as shown by equation 5.12.

$$C_{l_{steady}} = f \cdot C_{l_\alpha}(\alpha - \alpha_0) + (1 - f) \cdot C_{l_{sep}} \tag{5.12}$$

and,

$$C_{l_{sep}} = \frac{C_{l_{2D}} - f \cdot C_{l_\alpha}(\alpha - \alpha_0)}{1 - f} \tag{5.13}$$

where, $C_{l_{sep}}$ is the fully separated lift coefficient. The model uses Kirchoff's law, equation 2.34, to calculate the separation point location within the AoA range from -30 to +30 degrees. Beyond this range the separation

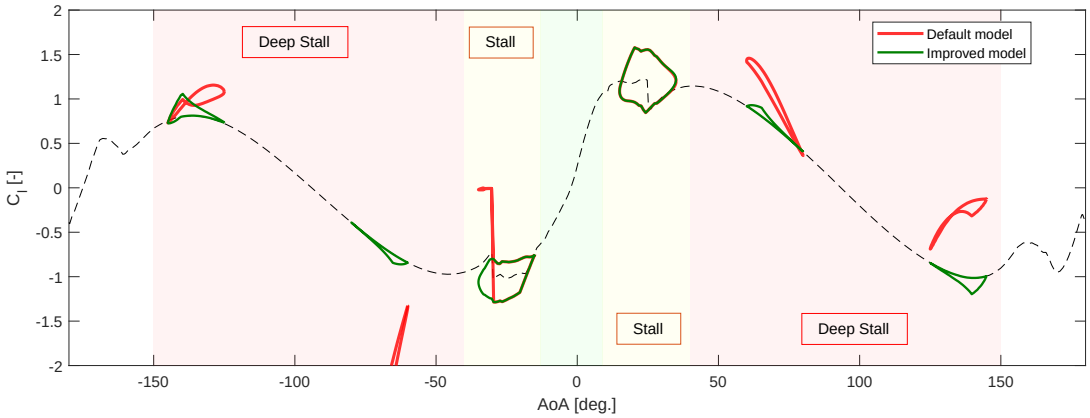

Figure 5.18: Comparison between default and improved separation model (Bjørck's model) in the B-L subroutine in Aero-Module. The lift hysteresis loops are simulated for various mean AoA according to the following pitching oscillation input: $\alpha = \alpha_{mean} + 10^0 \sin\omega t$, with a reduced frequency of 0.09. The dashed lines (- - -) denote the static lift curve for the DU 91-W2-250 airfoil.

point location is set to zero. The main drawback of this model is that equation 5.13 poses a singularity in attached flow ($f = 1$), when calculating $C_{l_{sep}}$ from 2D airfoil polars.

Bjørck's model [5] is based on the same idea but with slightly different implementation. Instead of using equation 5.13 to compute $C_{l_{sep}}$, it approximates $C_{l_{sep}}$ in the partially separated and attached flow regime ($0 < f <= 1$) as:

$$C_{l_{sep}} = \frac{C_{l_\alpha}(\alpha - \alpha_0)}{4} \quad \text{for } C_{l_{2D}} > \frac{1}{4} C_{l_\alpha}(\alpha - \alpha_0) \tag{5.14}$$

while in the fully separated regime ($f = 0$) it is made equal to the 2D polar.

$$C_{l_{sep}} = C_{l_{2D}} \quad \text{for } C_{l_{2D}} < \frac{1}{4} C_{l_\alpha}(\alpha - \alpha_0) \tag{5.15}$$

The steady lift coefficient is then re-constructed using Taylor's approximation on Kirchoff's law:

$$C_{l_{steady}} = C_{l_{sep}} + \frac{1}{4} C_{l_\alpha}(\alpha - \alpha_0)\left(f + 2\sqrt{f}\right) \tag{5.16}$$

Again, the separation point location is computed using approximate Kirchoff model given by equation 2.34 for $C_{l_{2D}} > \frac{1}{4} C_{l_\alpha}(\alpha - \alpha_0)$. It is set to zero in the fully separated regime determined by the criteria: $C_{l_{2D}} < \frac{1}{4} C_{l_\alpha}(\alpha - \alpha_0)$

Larsen's model [43] determines the location of the separation point using conformal mapping, where the separation point location is projected onto a circle in the complex plane. A new separation parameter Θ is defined as:

$$f = \frac{1 + \cos\Theta}{2} \tag{5.17}$$

Here, flow is fully separated for $\Theta = \pi$ and fully attached for $\Theta = 0$. The following set of equation is used to determined the separation point location by rearranging for Θ.

$$C_l = \begin{cases} \cos^4\left(\frac{\Theta}{4}\right) C_{l_\alpha}(\alpha - \alpha_0) & \text{if } 0 < f \leq 1 \\ 4\cos^4\left(\frac{\Theta}{4}\right) C_{l_{2D}} & \text{if } f = 0 \end{cases} \tag{5.18}$$

The main advantage of using Larsen's model over all the other models is that it avoids a singularity that is intrinsic in Kirchoff's flow model for values of f close to zero. The singularity reveals itself by differentiating equation 2.34 with respect to f.

$$dC_l = \frac{C_{l_\alpha}(\alpha - \alpha_0)}{4}\left(\frac{1}{\sqrt{f}} + 1\right) df \tag{5.19}$$

From above equation, it is clear that at very small values of f a small change in f would results in a very large change in C_l. Larsen's model avoids this particular singularity.

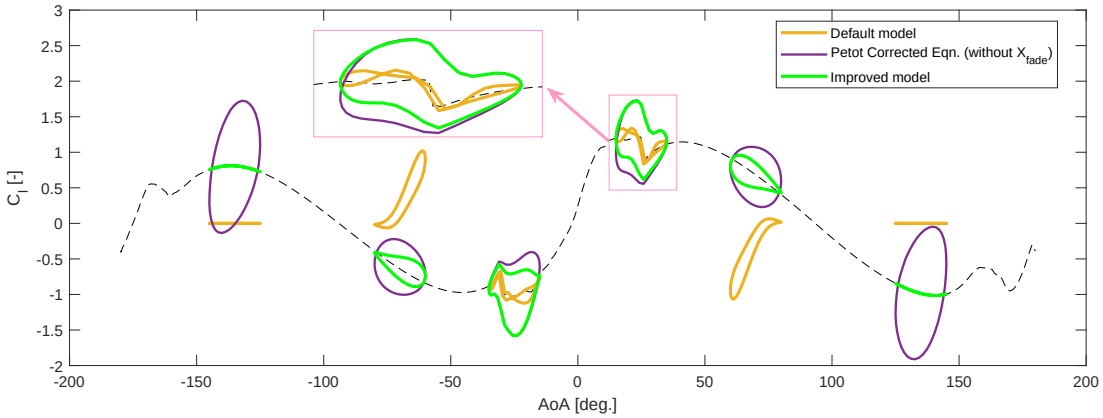

Figure 5.19: Comparison between default and improved ONERA model implementation in Aero-Module. The lift hysteresis loops are simulated for various mean AoA according to the following pitching oscillation input: $\alpha = \alpha_{mean} + 10^0 \sin \omega t$, with a reduced frequency of 0.09. The dashed lines (- - -) denote the static lift curve for the DU 91-W2-250 airfoil.

5.5.1. Results and Discussion

Bjørck's and Øye's model both rely on the Kirchoff model to compute the separation point location in the partially separated and attached flow regime. However, they use different formulations than used in the original Beddoes-Leishman model [46] to re-construct the lift coefficient once the separation point location has been determined. On the other hand, Larsen's model uses a different separation parameter Θ based on conformal mapping. Unlike, Bjørck's and Øye's model, Larsen's model does not clearly define the AoA criteria beyond which full separation should be assumed. Therefore, Bjørck's criteria was used while implementing Larsen's model in Aero-Module. All three models described above were implemented in Aero-Module in such a way that an easy switch between the models could be possible to facilitate easy comparison. The models were programmed in Aero-Module as a FORTRAN function to be used inside the 'BeddoesLeishmanDynamicStall' subroutine. The 'BeddoesLeishmanDynamicStall' subroutine and separation model functions are included in appendix E.

On comparing the results from the different implemented models in figures E.1 and E.2, it was seen that Bjørck's model gave the exact same results as the Kirchoff flow model in the attached flow and partially separated flow regime. Larsen's model showed slight differences from the Kirchoff flow model and Bjørck's model. On the other hand, Øye's model showed more difference from other models. However, in the deep stall regime (when $f = 0$) all the models give similar results as the trailing edge separation module is no longer operational. The hysteresis seen at these AoA is mainly simulated by the vortex lift module. As far as, improvement of the model as compared to the original implementation in Aero-Module is concerned, a large improvement can be seen from figure 5.18 by using Bjørck's model.

5.6. Improvement of the ONERA Model

Like the B-L model, ONERA model did not yield appreciable results in the high AoA range. The source code of the model was thoroughly analyzed and two main problems were spotted with the implementation. Firstly, a fader function "cdelPot()" (denoted here by X_{fade}) was used beyond 45 degree AoA to prevent queer results at large AoA, the function had the following form:

$$X'_{fade} = 2.0 - \frac{|\alpha|}{45} \tag{5.20}$$

$$X_{fade} = X'^2_{fade}(3.0 - 2X'_{fade}) \tag{5.21}$$

The function was applied to equation 2.58; the output of equations 2.55 and 2.56 (i.e. C_{l_1} and C_{l_2}), which produced incorrect results. Because of this implementation the lift coefficient predicted by ONERA model was decreased below the static lift curve. The correction eventually decreased the lift coefficient to zero instead of decreasing the dynamic lift coefficient to zero. To circumvent this problem and prevent queer results at large AoA the "cdelPot()" function was only applied to the change in lift given by:

$$\Delta C_{l_{dyn}} = C_{l_1} + C_{l_2} - C_{l_{static}} \tag{5.22}$$

The second main problem was identified in the second order differential equation of the model i.e. equation 2.56. The second term on the RHS of equation 2.56 is similar to the one presented in the original paper [53]. However, this term was later modified by Petot [68] to time rate of change of AoA as shown below:

$$\ddot{C_{l_2}} + a_L \dot{C_{l_2}} + r_L C_{l_2} = -(r_L \Delta C_l + e_L \dot{\alpha}) \tag{5.23}$$

As was seen in figures 4.7b and 4.7c, ONERA model wasn't capturing the experimental trends properly. Using the above equation, with a value of -2.86 for parameter e_2 in equation 2.61, this problem was resolved. Usually, dynamic stall models have a hard time capturing the reattachment phase of the hysteresis loop. Therefore, as a further improvement, to accurately capture the experimental trend during the down-stroke cycle the stiffness term of equation 5.23 was modified such that the stiffness was higher during the downstroke in comparison to the upstoke.

$$r_L = \begin{cases} \left[r_0 + r_2 \left(\Delta C_l\right)^2 \right]^2 & \text{if } \frac{d\alpha}{dt} \geq 0 \\ \left[K \cdot r_0 + r_2 \left(\Delta C_l\right)^2 \right]^2 & \text{if } \frac{d\alpha}{dt} < 0 \end{cases} \tag{5.24}$$

where, K is the newly introduced factor which controls the stiffness increase in downstroke cycle. Typical values for this factor were observed to lie between 1.5 to 3. For an overview of the performance of this improved model the reader is advised to refer to figures F.1, F.2, and F.3 in appendix F.

5.6.1. Results and Discussion

Figure 5.19 shows a comparison between the default and improved implementation of ONERA model over a range of different dynamic stall loops, mainly at large AoA. From the figure it is clear that the default implementation was not valid for AoA larger than 20 degrees. Even for AoA between 15 and 35 degree, shown by the zoomed plot in figure 5.19, the default model was not giving good results. With the implementation of improved equation suggested by Petot [68] (shown by purple curve) the hysteresis loops show large improvement. Nonetheless, the model still gives unrealistic results are extremely large AoA as these are outside the domain of the model. The increase in the size of the hysteresis loops is caused due to the first forcing term on the RHS in equation 5.23 becoming extremely large due to large increase in ΔC_l (difference between potential lift and static lift curve). Therefore, the fading function given by equation 5.21 was necessary. Finally, the effect of incorporating equation 5.24 can also be observed in the zoomed plot in figure 5.19 through the difference between the green and purple curve.

5.7. Chapter Conclusion

The following conclusion are drawn from this chapter:

- There is reasonable agreement between the 2D and 3D airfoil polars in attached flow regime up until stall. However, in deep stall the 3D airfoil polars show lower lift and drag coefficients than 2D airfoil polars. The lift to drag ratio versus AoA trend obtained from 3D airfoil polars matches extremely well with the trend predicted by 2D flat plate theory in the deep stall regime. This is because in deep stall, flow is completely separated over upper surface and effect of upper surface thickness can be neglected. The relatively thin NACA airfoil profile enters deep stall earlier than DU and RISO airfoil profile due to higher tendency towards leading edge separation because of its lower thickness.
- Large difference between simulations and New MEXICO measurements is observed in Standstill conditions at large AoA. The cause of this discrepancy is associated with the difference between 2D airfoil polars, used as backbone curves for simulations, and extracted 3D airfoil polars from New MEXICO standstill measurements. Furthermore, ONERA and B-L model give absurd results at large AoA, mainly because their underlying assumptions fail at large AoA, while Snel's model gives results similar to a BEM model without dynamic stall. As expected, none of the tested dynamic stall models simulate unsteadiness at large AoA except Snel's second order model. This is because Snel's model uses a second order non-linear Van Der Pol equation to model dynamic stall of self-excited nature at large AoA.
- The cross-flow principle is not completely valid at large AoA with substantial spanwise flow. A first order correction proposed by Gaunaa et al. [24] was tested; it wrongly predicted the trend in some cases or did not make a large difference in other cases. Therefore, the correction model still needs improvement for applicability to different wind turbine blades as it was originally developed for DTU 10 MW reference turbine.

- The Kirchoff flow separation model implemented in Aero-Module was giving erroneous results for large AoA. Therefore, a new separation model proposed by Larsen [43] was implemented that circumvents the deficiencies of Kirchoff flow separation model.
- The ONERA model was improved by modifying the second forcing term of the second order non-linear equation with time rate of change of AoA, as proposed by Petot [68]. Furthermore, a new piecewise function was proposed in the current study to better model the re-attachment phase of dynamic stall hysteresis loop.

6

Case Study: AVATAR Rotor in Standstill Conditions

The chapter discusses an aeroelastic case study performed on the AVATAR rotor blade using PHATAS-Aero: aeroelastic coupling between Aero-Module and PHATAS. The aim of the study was to address the differences in aerodynamic damping predicted by different dynamic stall models. Specific cases from the AVATAR Aeroelastic Workout (October 2015, Polimi) [62] were investigated.

6.1. Overview of the AVATAR Rotor

The AVATAR Reference Wind turbine is based on the INNWIND.EU 10 MW research wind turbine [72]. The main differences lie in rotor design of the two turbines. AVATAR wind turbine has a larger rotor diameter than INNWIND.EU wind turbine, and it is designed for lower inductions. A summary of some important properties of the AVATAR wind turbine is presented in table 6.1.

Table 6.1: A summary of important properties of the AVATAR 10 MW reference wind turbine. Taken from [72].

Rated Power	10 MW
Rotor Configuration	3 bladed, upwind
Control Type	variable speed, pitch regulated
Rotor Diameter	205.8 m
Blade Length	100.08 m
Hub height	132.7 m
Cut-in Wind Speed	4 m/s
Cut-out Wind Speed	25 m/s
Rated Wind Speed	10.75 m/s
Rated Rotor Speed	9.6 rpm
Shaft Tilt Angle	5^o
Rotor Precone Angle	-2.5^o

The main purpose of designing the AVATAR rotor was to challenge current state-of-the-art aeroelastic tools to assess their validity for future 10 – 20 MW wind turbines. For the current study, the AVATAR rotor will be used to conduct a comparison between dynamic stall models in Aero-Module at standstill conditions. The comparison will be performed for Case 2 of the text matrix from the AVATAR Aeroelastic Workshop [62]. This aeroelastic workout was mainly performed to assess the discrepancy between participating partner simulations of storm load cases (DLC 6.2) that was previously observed in AVATAR WP-1 of Deliverable 1.3 [72]. Following this workout, participating partners of the AVATAR project performed comparison of aeroelastic simulations in standstill conditions for storm load cases as part of AVATAR WP4 Deliverable 4.5 [35]. In this deliverable, B-L model, RISO model, and ONERA model were compared, and it was found that BEM-based simulations predict instabilities at yaw angle ranges: $30^o \leq \beta \leq 80^o$ and $-30^o \leq \beta \leq -70^o$. Moreover, including turbulent inflow reduced the instabilities as it decreases the correlation between forces along the blade span.

Table 6.2: A summary of natural modes for an isolated non-rotating AVATAR blade. Reproduced from AVATAR Work Package 4 [17].

Mode	Frequency [Hz]	Logarithmic Damping [%]
1^{st} flap	0.682	3.030
1^{st} edge	0.903	3.006
2^{nd} flap	1.870	8.298
2^{nd} edge	2.594	8.645
3^{rd} flap	3.818	16.959
3^{rd} edge	5.486	18.306
1^{st} torsion	6.055	9.916

Stettner et al. [87] found that dynamic stall models (also, their airfoil dependent parameters) play a significant role in determining the aerodynamic damping and instabilities; they associate this to be the main cause of discrepancies observed in Deliverable 1.3. In order to perform any aeroelastic analysis, it is of paramount importance to have knowledge of the natural frequencies of the blade; therefore, a table summarizing the natural frequencies and logarithmic damping of the first seven natural modes of the AVATAR blade is presented in table 6.2.

6.2. B-L Model: Modeling Effect of Time-Varying Incoming Velocity

Before proceeding with analyzing AVATAR test cases, the B-L model was improved to include the effect of time-varying incoming velocity, because this effect is important for correctly modeling blade lead-lag vibrations. The original B-L model was based on Theodorsen's theory to model the unsteady effects in attached flow. This theory assumes a harmonic wake with a constant free-stream velocity. It is applicable to pitching and plunging motion of airfoils; however, it does not show any unsteadiness for cases where the airfoil undergoes a streamwise variation of the incoming velocity in time. For practical application in an aeroelastic code this is a drawback as the blade lead-lag motion might not be simulated properly. Van der Wall and Leishman [95] conducted an investigation of this effect on a flat plate airfoil using different theories and compared the results with CFD simulations. They found that this effect is mainly dominant for high reduced frequencies. In the literature two different attempts to incorporate this effect in the B-L model were made by Bjørck [5] (FFA Model) and Hansen et al. [33] (Risø Model). These two approaches were implemented in Aero-Module and their performance was compared with the results from Van der Wall and Leishman [95].

FFA model: This model employs a relatively simple modification to incorporate the effects of time-varying flow velocity into the attached flow module of B-L model. It uses the downwash instead of AoA at the three quarter chord location in the deficiency functions to model the effect of shed vorticity in the wake. The downwash is approximated using:

$$w_{\frac{3}{4}} = W \sin \alpha_{\frac{3}{4}} \tag{6.1}$$

The deficiency functions of equation 2.29 and 2.30 are modified as

$$X_n = X_{n-1} \exp\big(-b_1 \Delta S\big) + A_1 \Delta w_{\frac{3}{4},n} \exp\big(-b_1 \Delta S/2\big) \tag{6.2}$$

$$Y_n = Y_{n-1} \exp\big(-b_2 \Delta S\big) + A_2 \Delta w_{\frac{3}{4},n} \exp\big(-b_2 \Delta S/2\big) \tag{6.3}$$

Finally, the effective AoA can be computed using:

$$\alpha_{E,n} = \alpha_{\frac{3}{4},n} - \frac{X_n + Y_n}{W} \tag{6.4}$$

Risø model: This model introduces a time-varying velocity in the Duhamel's integral formulation, which results in non-linear first order differential equations to model the hysteresis effects in attached flow. The indicial formulation of these equations is presented below:

$$X_n = X_{n-1} \exp\big(-P_1 \Delta t\big) + \frac{Q_1}{P_1}\Big(1 - \exp\big(-P_1 \Delta t\big)\Big) \tag{6.5}$$

$$Y_n = Y_{n-1} \exp\big(-P_2 \Delta t\big) + \frac{Q_2}{P_2}\Big(1 - \exp\big(-P_2 \Delta t\big)\Big) \tag{6.6}$$

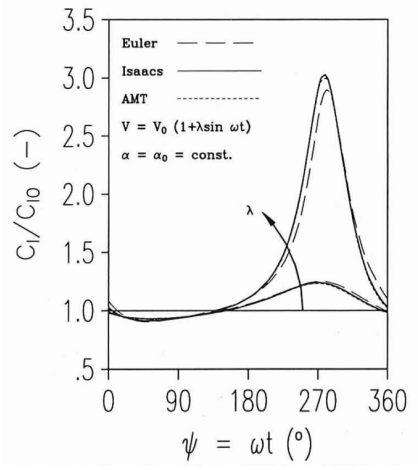

(a) Results taken from van der Wall and Leishman [95].

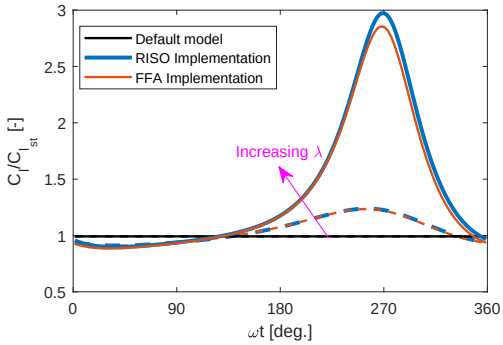

(b) Simulated Results from Aero-Module simulations using B-L model.

Figure 6.1: Unsteady variation of lift coefficient for a flat plate oscillating in streamwise direction. The velocity at the plate oscillates according to the relation: $U = U_m(1 + \lambda \sin \omega t)$ with a reduced frequency of $k = 0.2$ and a constant AoA of 5 degrees. Results are shown for two different values of λ i.e. 0.4 and 0.8.

where P_i and Q_i are computed using the following relations:

$$P_i = b_i \frac{W_n + W_{n-1}}{c} + \frac{W_n - W_{n-2}}{\Delta t(W_n + W_{n-1})} \tag{6.7}$$

$$Q_i = \frac{b_i A_i}{c}\left(W_n \alpha_{\frac{3}{4},n} + W_{n-1}\alpha_{\frac{3}{4},n-1}\right) \tag{6.8}$$

Eventually, the effective AoA is computed as

$$\alpha_{E,n} = \alpha_{\frac{3}{4},n}(1 - A_1 - A_2) + X_n + Y_n \tag{6.9}$$

6.2.1. Validation of Improved Model

The simulated results from the implemented models are presented in figure 6.1b for a flat plate oscillating in streamwise direction. The default model without the above mentioned improvements does not capture any unsteadiness for fore-aft motion of an airfoil with constant AoA. However, Van der Wall and Leishman [95] had showed through flat plate CFD simulations (Euler Code) in figure 6.1a that the unsteadiness increases with increasing amplitude of fluctuating velocities, dictated by the factor λ in this case. Overall, both implemented models in Aero-Module show appreciable results in comparison to results taken from Van der Wall and Leishman [95].

6.3. Computational Set-up

The aeroelastic coupling between Aero-Module and PHATAS will be used to simulate AVATAR rotor in standstill conditions. Aero-Module will compute aerodynamic forces and moments which will be transfered to PHATAS structural solver to compute blade deformations and rate of deformation. This information is then fed back into Aero-Module to re-compute aerodynamics; this process is repeated until convergence. Both PHATAS input file and Aero-Module input file are required for such simulations. 'phatAero.exe' is called in Windows command line followed by name of the PHATAS input file to start the simulations. This process of writing input files and running simulations through command line is automated using MATLAB environment.

The analysis will be restricted to simulating the blade only structural response in the presence of aerodynamic forces. Therefore, flapwise, lagwise, and torsional deformations were modeled in the aeroelastic simulations. While, modeling of tower dynamics, shaft torsion, and yaw dynamics was switched off in PHATAS input file. Furthermore, 3D rotational correction, Prandtl tip and root correction, and dynamic inflow correction was switched off in the Aero-Module input file. 22 BEM elements were used in all aeroelastic simulations. A maximum simulation time of 120 seconds was used to keep computational cost at a minimum. The AoA

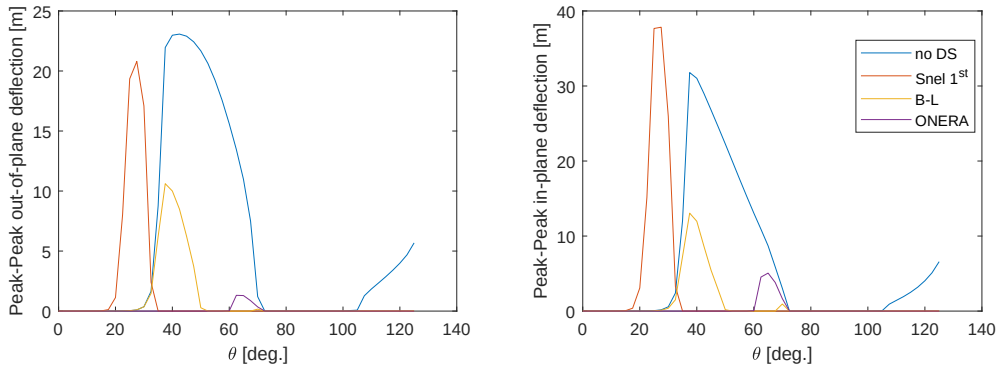

Figure 6.2: Peak to peak flapwise (out-of-plane) and lagwise (in-plane) tip deflections, in undeformed rotor plane reference system, versus different pitch setting for different dynamic stall models. The results are shown for blade 1 which is fixed at 90 degree azimuth. While a uniform steady wind of 42 m/s is used.

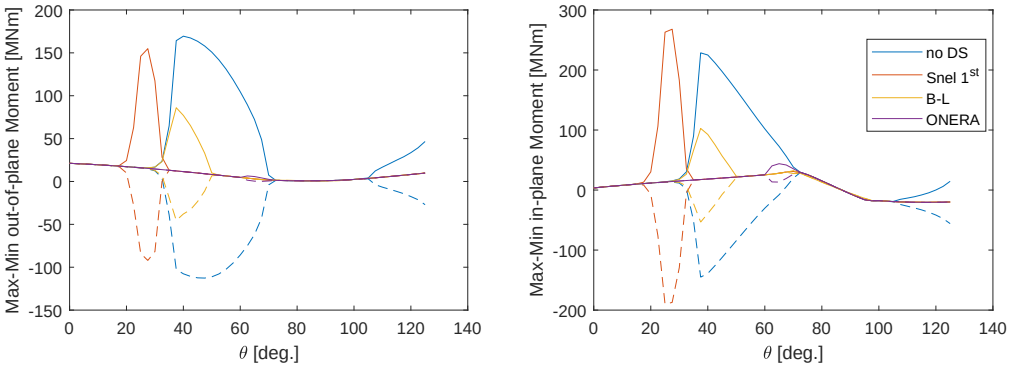

Figure 6.3: Maximum and minimum flapwise (out-of-plane) and lagwise (in-plane) root bending moments, in undeformed rotor plane reference system, versus different pitch setting for different dynamic stall models. The results are shown for blade 1 which is fixed at 90 degree azimuth. While a uniform steady wind of 42 m/s is used.

was evaluated at the three quarter chord point while flapwise and lagwise tip deformations (in undeformed rotor plane reference system) are shown for blade section at 94.94 meters from blade root. Lastly, steady inflow velocity was used without vertical shear gradient.

In order to excite the natural modes of the blade structure an initial excitation is necessary. This excitation was given through a sharp rise in inflow velocity from 1% to 100% of the given inflow velocity in a time interval of 0.1 seconds. After this excitation the blade is in a state of free vibration and the effect of aerodynamic modeling on the damping of these free vibrations can be assessed.

6.4. Fixed Rotor with Different Pitch Settings

Case 2 of the text matrix from the AVATAR Aeroelastic Workshop [62] was simulated and the results are discussed in this section. For these simulations, blade 1 was fixed at 90 degree azimuth angle. Shaft tilt angle, rotor cone angle, and gravity was set to zero, and the simulations were performed for pitch angles from 0 – 125 degrees with steps of 2.5 degree. A steady uniform wind speed of 42 meter per second was used. The simulations were performed with the following aerodynamic models:

1. Quasi-steady (no DS)
2. Snel 1^{st} order model
3. B-L model
4. ONERA model

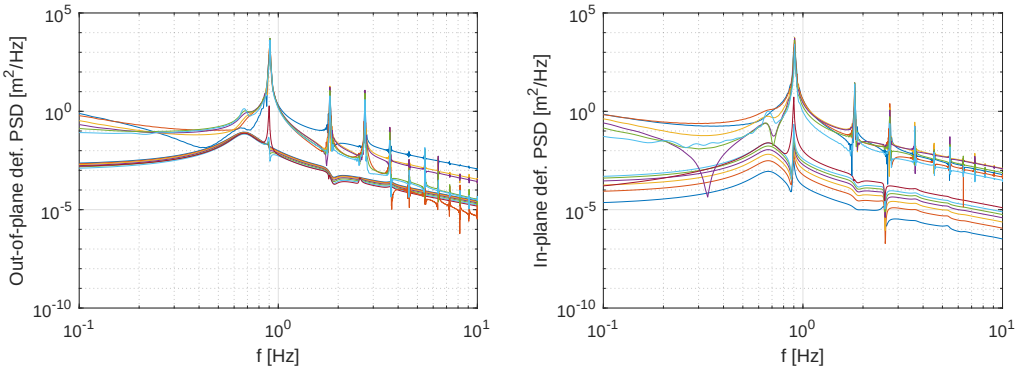

Figure 6.4: PSD of flapwise (out-of-plane) and lagwise (in-plane) deflections, in undeformed rotor plane reference system, near the tip for different pitch setting from 0 to 125 degrees with a step of 5 degrees. The results are shown for blade 1 which is fixed at 90 degree azimuth. Quasi-steady aerodynamics was used to populate the results at a uniform steady wind of 42 m/s.

6.4.1. Effect of Time Step Size

Selection of a suitable time step size is very important for aeroelastic simulations. A very large time step size may add numerical damping to the system. On the other hand, a very small time step size, in addition to large computational time, may result in problems with convergence due to division by a very small number when higher order numerical derivatives are approximated. Therefore, a sensitivity of the time step size on the simulation results was performed as a priori. Four different time step sizes were evaluated using quasi-steady aerodynamic models. The computed peak-peak tip deformations and max-min root bending moments are shown in figure H.1 and H.3, respectively, for different pitch settings. These figures indicate two important things. Firstly, the results depend on the chosen time step size and no clear monotonic trend can be observed with reducing time step size. Secondly, despite the dependency on time step size, the different time step sizes show very large values in roughly the same range of pitch settings. These very large values of deformations and bending moments suggest onset of an aerodynamic instability which is adding energy to the blade structure and increasing the vibration amplitude till failure occurs. In reality, the blade would have incurred catastrophic failure well before it reaches the high peak-peak amplitudes observed in figure H.1 and high max-min bending moments observed in figure H.3. Based on this analysis, further simulations with dynamic stall models in this section were performed for time step size of 0.05 and 0.02 second. However, for brevity, only simulation results for 0.05 second step size will be presented in this chapter (unless otherwise stated) as no substantial difference in the range of pitch settings giving instabilities was observed between the two time step sizes.

6.4.2. Tip Deflections and Bending Moments

Using Dynamic stall models seem to have a large impact on the instabilities observed in simulations at various pitch settings. Generally, dynamic stall models tend to reduce the range of pitch settings where instabilities are observed, as seen in figures 6.2 and 6.3. The reason why large amplitudes in figure 6.2 and figure 6.3 indicate instability and not resonance is due to the fact that there is no external forcing frequency being applied to the blades. The blades are given an initial transient jump in velocity to excite the modes, after which the blades are in a state of free vibration. Therefore, purely aerodynamic and structural damping are at play to damp the structural vibrations of the blade. In cases where aerodynamic forces do positive work on the structure the vibrations increase in amplitude and give instability due to negative aerodynamic damping. All three dynamic stall models predict different ranges of pitch settings for instabilities. The ONERA model predicts instability to happen between 60 to 70 degree pitch setting. B-L model predicts instability between 25 to 50 degree pitch setting. While Snel's model predicts an instability between 20 to 35 degree, which is outside the range of instability predicted by quasi-steady aerodynamics. In order to identify the mode of vibration causing the observed instabilities a Discrete Fourier Transform of all time response simulations at various pitch settings with quasi-steady aerodynamics is presented in figure 6.4. The PSD of tip deformations clearly shows a dominant peak at a frequency of 0.9 Hertz, corresponding to the first edgewise mode as indicated by table 6.2. The first edgewise mode vibration has the most energy content over the entire range of pitch settings considered in the present analysis. Therefore, edgewise instability is mainly prevalent in the current case study. This is expected as edgewise vibrations are typically less damped in comparison to flapwise

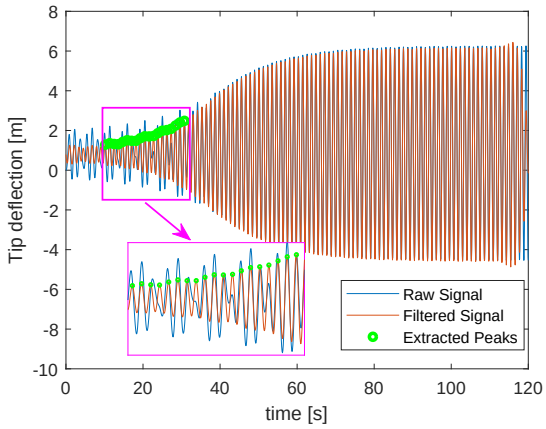

(a) Tip displacement time signal for out-of-plane deformation in the undeformed rotor plane reference system for a pitch setting of 65 degrees.

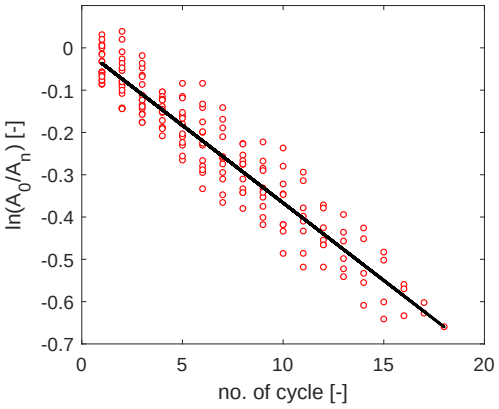

(b) Linear Regression fit to natural log of amplitude ratios versus number of cycles n between peaks.

Figure 6.5: The figure depicts the filtering of tip displacement signal to extract peak values. These peak values are used to compute natural log of amplitude ratios and plotted against the number of cycles between amplitudes to find a regression fit.

vibrations.

6.4.3. Determination of Damping Ratio

Determination of aerodynamic damping from a non-linear time response simulation is a challenging task. In the current section a methodology that was used to approximate the overall damping ratio from time series of tip deformations will be presented. The method employs filtering the signal to isolate the 1^{st} edgewise frequency. The filtered signal is then used to extract peak amplitudes. Eventually, the peak amplitudes are used to compute logarithmic decrement and, subsequently, damping ratio.

Filtering Signal

As the time signal is a constitution of various frequency components, as shown in figure 6.4; therefore, filtering the signal to extract behavior of desired frequency component is justified. This is achieved through the use of bandpass butter worth filter (4^{th} order). Before signal filtering, the signal is de-trended by subtracting the mean. Then, zero-phase filtering is performed to eliminate any phase difference that the process of filtering could have brought about in the filtered signal. The passband frequency is set to be around +/- 15% of the 1^{st} edgewise frequency. Finally, the mean is added back to the filtered signal. An example of a filtered signal is shown in figure 6.5a. In this way 1^{st} edgewise frequency can be isolated from the non-linear time response and the free vibration decay of the first edgewise mode can be analyzed.

Logarithmic Decrement

Logarithmic decrement δ is related to damping ratio ζ of a second order system through the following expression:

$$\delta = \frac{2\pi\zeta}{\sqrt{1-\zeta^2}} \tag{6.10}$$

On rearranging for ζ, the above equation can be written as

$$\zeta = \frac{\delta}{\sqrt{\delta^2 + (2\pi)^2}} \tag{6.11}$$

On isolating one natural frequency (edgewise mode) from the non-linear time response, through signal filtering, we can assume the time response of the filtered signal to follow a behavior similar to a second order system given by:

$$x(t) = A_0 e^{-\zeta\omega_n t}\cos(\omega_d t - \phi) \tag{6.12}$$

where, $\omega_d = \omega_n\sqrt{1-\zeta^2}$ is the damped natural frequency, A_0 is the initial peak amplitude, and ϕ is the phase lag. The above equation models the time response of an under-damped and unforced second order system.

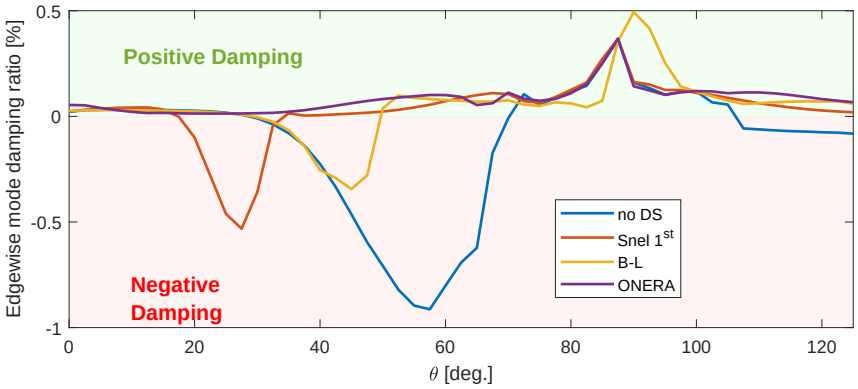

Figure 6.6: Edgewise mode damping ratio versus pitch angle for different dynamic stall models. The results are shown for blade 1 which is fixed at 90 degree azimuth. Quasi-steady aerodynamics was used to populate the results at a uniform steady wind of 42 m/s.

The important thing to note from equation 6.12 is the exponential decay term which is a direct function of damping ratio and natural frequency ω_n. The decayed amplitude of successive peaks can be written as

$$A_{n+1} = A_n e^{-\zeta\omega_n(t_{n+1}-t_n)n} \tag{6.13}$$

where, $t_{n+1} - t_n = \frac{2\pi}{\omega_d}$ is the time period between successive peaks. Taking the natural log on both sides of equation 6.13 gives a linear relation between number of successive peaks (or number of cycles) and the natural log of amplitude ratios between those peaks, where the slope gives the value of the logarithmic decrement.

$$\ln\left[\frac{A_n}{A_{n+1}}\right] = \left[\frac{2\pi\zeta}{\sqrt{1-\zeta^2}}\right] n \tag{6.14}$$

As an example, the extraction of peaks from filtered time response signal is shown in figure 6.5a. The extracted peaks are then used to compute the natural log of amplitude ratios and plotted versus the number of cycles between amplitudes as depicted by figure 6.5b. A linear regression line is fit to the data, the slope of which is the logarithmic decrement. The damping ratio can be easily calculated using equation 6.11. The described method is only valid for conditions where the system is under-damped i.e. $0 < \zeta < 1$ and the decay is exponential (meaning system has linear damping).

6.4.4. Damping Ratio

A graph of the approximated damping ratio for different dynamic stall models is presented in figure 6.6. Overall, the dynamic stall models substantially increase the damping in the stall regime. Nonetheless, there are differences among models in certain ranges of pitch settings. With the ONERA model, no instability is observed over the entire range of pitch settings. Snel's model shows instability due to negative damping in the range from 18 to 35 degree pitch setting. While B-L model gives negative damping from 35 to 50 degree pitch setting. The damping ratios in the attached flow regime, between 75 to 100 degree pitch angle, predicted by ONERA model and Snel model are similar to quasi-steady aerodynamic model. However, B-L model shows a different trend in that regime.

Of particular interest is the case with 30 degree pitch setting. Here, the Snel's model predicts negative aerodynamic damping and an edgewise instability. A closer look at the tip displacement and lift hysteresis, for a subset of the complete simulation time which is shown in figure H.13, reveals an increase in edgewise vibration over time and a counter-clockwise lift hysteresis for the Snel's model. While dynamic stall models, typically, give a clockwise lift hysteresis that tends to increase aerodynamic damping. From figure H.13, it can be seen that the blade mainly vibrates in the edgewise direction. When the blade oscillates backward towards trailing edge direction (lag motion) the AoA increases; a subsequent decrease in lift coefficient would make the amplitude of the lag motion larger, as in case of Snel's model. On the contrary, a subsequent increase in lift coefficient would make the amplitude of the lag motion smaller, as in case of ONERA model. The cause of this peculiar behaviour from Snel model was further investigated and the 'cdelpot()' function was found to be causing the problem. The 'cdelpot()' function of the form similar to equation 5.21 is used in the Snel's model implemented in Aero-Module to reduce dynamic stall effects for large AoA. However, this function seems to

be causing the edgewise instability, as was observed in figure H.13. Removing this function results in positive aerodynamic damping from Snel's model in the pitch angle range from 18 to 35 degree.

Another important thing to note from figure 6.6 is the fact that B-L model predicts instability for pitch settings lower than 50 degrees. This is in the deep stall regime where the trailing edge separation module of B-L model is switched-off (i.e. $f = 0$). Implying that hysteresis effects seen is simulations is only due to vortex lift module. In figure H.16 (60^o pitch angle) and H.17 (110^o pitch angle), the B-L model shows a near elliptical hysteresis loop about the static lift curve and gives positive aerodynamic damping. On the contrary, in figure H.15 (50^o pitch angle), the trailing edge separation module is being switched off beyond 35 degree AoA resulting in a sort of half hysteresis loop. This hysteresis loop gives positive aerodynamic damping for upper half cycle of vibration when the AoA is increasing while giving negative aerodynamic damping for downstroke cycle when AoA is decreasing. A similar sort of behaviour is also observed for a pitch setting of 40 degree in figure H.14.

In appendix H.2, PSD of tip deformations for different dynamic stall models is compared with quasi-steady aerodynamics. Generally, the results in this section show that the dynamic stall models tend to reduce energy content of the 1^{st} edgewise frequency component in comparison to quasi-steady aerodynamics. Thus, corroborating previous discussion on increased aerodynamic damping offered by dynamic stall models. However, in appendix H.2, a few cases are presented where some of the dynamic stall models are not able to reduce the energy content of 1^{st} edgewise frequency component; eventually leading to instability as shown in figure H.6 and figure H.7 for Snel and B-L model, respectively.

6.5. Chapter Conclusion

The following conclusions are drawn from this chapter:

- The time step size of aeroelastic simulations was shown to have an important influence on simulation results. Despite this finding, the range of pitch settings where aeroelastic instabilities were observed was roughly similar for different time step sizes. A very large time step size may add numerical damping to the system. On the other hand, a very small time step size, in addition to large computational time, may result in problems with convergence due to division by a very small number when higher order numerical derivatives are approximated. The latter problem was encountered with some ONERA model simulations where second order time derivatives are approximated.

- Different dynamic stall models predict different ranges of pitch settings for instabilities. The ONERA model predicts instability to happen between 60 to 70 degree pitch setting. B-L model predicts instability between 25 to 50 degree pitch setting. While Snel's model predicts an instability between 20 to 35 degree, which is outside the range of instability predicted by quasi-steady aerodynamics.

- A method to extract damping ratio from non-linear time response simulations was presented. The method uses a band pass filter to isolate 1^{st} edgewise frequency time response. It extracts peaks from filtered time series to determine the logarithmic decrement and damping ratio. This method is only applicable for under-damped system which has linear damping (or in other words an exponential term for decay/growth).

- The shape of dynamic stall hysteresis loop has a large effect on aerodynamic damping. A clockwise circular or elliptical hysteresis loop gives positive aerodynamic damping. Generally, all three dynamic stall models showed increased aerodynamic damping in comparison to quasi-steady aerodynamic model. Nonetheless, Snel's model and B-L model showed negative damping ratio in certain pitch angle ranges while ONERA model showed positive damping ratio for the entire range of pitch settings. The negative damping ratio predicted by Snel's model was mainly caused by a fader function called "cdelpot()" (implemented in Aero-Module) which had changed the direction of hysteresis loop to counter-clockwise. On the other hand, B-L model usually showed negative damping ratio for cases where the trailing edge separation module was switched off (i.e. $f = 0$). This resulted in sort of half hysteresis loop giving negative damping in lower half cycle.

7

Analysis of Yawed Conditions

The chapter discusses one of the most important and complex conditions encountered in the operation of wind turbines. It starts by giving an overview of yawed conditions and measurements available from New MEXICO experiments. Attention is focused on measurements where dynamic stall is expected. Influence of rotational augmentation in simulating dynamic stall conditions is presented and an optimum model is selected. Following that, simulations of MEXICO rotor in yawed conditions are performed with different dynamic stall models and compared with experimental data.

7.1. Overview of Yawed Conditions

Wind turbines are prone to yaw misalignment during most of their life cycle. Despite the fact that most modern wind turbines have a yawing mechanism to align the rotor with the incoming wind direction. The reason is the slow response time of the yawing mechanism in moving the massive rotor assembly as compared to sudden changes in wind direction [57]. Yawed flow not only restricts the power output of a wind turbine but it also exposes it to increased cyclic loads due to unsteady aerodynamics. Hence, accurate prediction of these unsteady loads is paramount for an optimum blade design. New MEXICO database has a wide set of measurements performed in yawed conditions. It is a valuable asset for validating the performance of aerodynamic models. An overview of all new MEXICO tests runs with yawed condition is presented in table 7.1.

Table 7.1: Overview of all yawed flow test cases in the New MEXICO measurement campaign. Taken from [11].

Case Type	Data Points	$U_\infty\,[m/s]$	$\beta\,[deg.]$	$\theta\,[deg.]$	$\Omega\,[rpm]$
Yawed flow (clean)	929 – 932	10, 15, 18, 24	8	-2.3	425.1
	933 – 938	10, 15, 18, 24	15	-2.3	425.1
	939 – 947, 703 – 738	10, 15, 18, 24	30	-2.3, 0.7	425.1
	948 – 952	10, 15, 18, 24	45	-2.3	425.1
	953 – 957, 663 – 699, 742 – 753	10, 15, 18, 24	-30	-2.3	425.1

It is already mentioned that MEXICO rotor has pressure sensors mounted on three different blades at five different spanwise sections, table 3.1. This arrangement of pressure sensors would introduce a phase shift of +/- 120 degrees between the normal force variation with azimuthal angle. This phase shift was eliminated in the data reduction performed by Parra [61]. Hence, the five spanwise measurements of normal force variation with azimuth are assumed to be taken from Blade 1. For consistency, the simulation results shown in this chapter will also be for Blade 1. It is speculated that Blade 2 and Blade 3 will go through similar load variation but with phase shift of +/- 120 degrees.

Depending on yaw angle and tip speed ratio the rotor will experience a periodic change in AoA. These periodic changes in AoA give rise to hysteresis in the C_l vs α curve due to dynamic stall. The hysteresis gives larger lift coefficient than would be experienced in steady conditions. These periodic changes will occur at a frequency of 1P. The reduced frequency associated with this unsteadiness can be approximated using equation 2.1. Here, assuming effective velocity to be mainly dominated by tangential velocity component

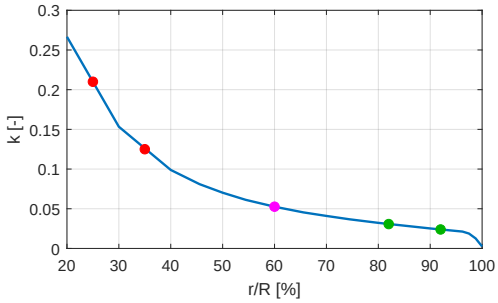

Figure 7.1: Approximated reduced frequency variation with radial position. The highlighted points denote the location of pressure sensors along the span on the MEXICO blade.

given by $r\Omega$ gives the following approximation:

$$k \approx \frac{\Omega c}{2r\Omega} = \frac{c}{2r} \tag{7.1}$$

The above equation is plotted in figure 7.1. It can be seen from this figure that the 25% and 35% spanwise section experience a highly unsteady flow. 82% and 92% spanwise sections are below the reduced frequency limit of 0.05 for unsteady flow [48]; hence, belong to quasi-steady flow regime.

Dynamic stall happens when the blade sections experience high AoA variations in vicinity of stall. For wind turbines, it typically occurs for low tip speed ratios. In case of MEXICO experiment this would happen for cases with high tunnel speeds i.e. 24 m/s. At these low tip speed ratios the advancing and retreating blade effect (section 2.1) is dominant, because of two reasons: (1) component of incoming velocity in tangential direction becomes comparable to $r\Omega$ velocity (2) a lesser skewed wake effect due to faster convection of wake. In this chapter, focus would be on cases with high tunnel speed where dynamic stall is most probable. For a positive yaw angle, according to the convention in figure 3.1, a zero azimuthal angle would correspond to a retreating blade situation with a maximum AoA. On the other hand, the blade is advancing into the in-plane component of incoming velocity at 180 degree azimuth, giving a minimum AoA. From 0 to 180 degree, the AoA reduces from maximum to minimum value often referred to as the downstroke cycle. While upstroke cycle is from 180 degrees to 360 degrees, where the AoA increases from minimum to maximum. At the start of upstroke the rotor experiences maximum velocity and load; vice versa for start of downstroke.

7.2. Influence of Rotational Augmentation

Rotational augmentation or stall delay directly influences the unsteady loads predicted by a dynamic stall model near the inboard parts of a rotating blade. Therefore, it is important to establish an accurate model for predicting stall delay before proceeding with simulating dynamic stall in yawed conditions. A brief introduction of this phenomenon has been presented in section 2.1.3. Due to this phenomenon an increase in lift coefficient is observed for inboard stations of a rotating blade while stall is postponed to a higher AoA; hence, the name "stall delay". The effect is mainly associated with three different mechanisms, adapted from Lindenburg [51]:

- A spanwise gradient of suction peaks near the leading edge of the blade section exists. The suction peaks are directly proportional to dynamic pressure which in turn is directly proportional to squared radial position. Therefore, the suction peaks are stronger at the outboard sections of the blade (with the exception of tip region). This gradient warrants a radially outward directed flow due to this radial pressure gradient.
- The air in the boundary layer surrounding a rotating blade is subject to centrifugal forces irrespective of flow being separated or attached. This "centrifugal pumping" is cause of spanwise flow from root to tip.
- Coriolis forces act in the direction of trailing edge (opposing the adverse pressure gradient) on the stalled flow region with radial flow. This pushes the separation point towards the trailing edge and reduces the size of trailing edge separation bubble. Thus, effectively, increasing suction on the blade section.

Table 7.2: A summary of correction factors used in the literature to model the effect of rotational augmentation.

Source	Correction Factor
Snel et al. (1994) [82]	$f_{C_l} = 3\left(\frac{c}{r}\right)^2$
Chaviaropouloa and Hansen (2000) [14]	$f_{C_l} = 2.2\left(\frac{c}{r}\right)\cos^4\theta$
Lindenburg (2004) [51]	$f_{C_l} = 3.1\left(\frac{\Omega r}{U_{eff}}\right)^2\left(\frac{c}{r}\right)^2$
Dumitrescu et al. (2007) [19, 20]	$f_{C_l} = 1 - \exp\left(-\frac{1.25}{\frac{r}{c}-1}\right)$
Schepers (2012) [77]	$f_{C_l} = 3.8\left(\frac{c}{r}\right)^{1.4}\cos^6\theta$

Rotational Augmentation was first documented by Himmelskamp [36]. Thereafter, there have been numerous studies in the literature to understand this phenomenon in more detail. Of particular interest are two separate CFD studies conducted by Guntur et al. [28] and, more recently, by Bangga et al. [3] on the MEXICO rotor. Guntur et al. found an aft movement of the separation point due to rotational augmentation. They also measured thickness of the trailing edge separation bubble and found that it was suppressed due to rotation. Lastly, they documented presence of rotational augmentation when there is no separation. Bangga et al. also did a similar study; however, unlike Guntur et al. they used azimuthal averaging technique of Hansen et al. [32] instead of inverse BEM to determine effective AoA from CFD computations. They presented a strong spanwise flow in the inboard regions of the blade up until 60% section, corresponding to $\frac{c}{r} = 0.1$. According to the authors, rotational augmentation was not observed for $\frac{c}{r} > 0.1$; they recommend to apply 3D correction models within this limit. Centrifugal force was identified as the main cause of radial flow. Furthermore, in contrast to the observation of Guntur et al., they found rotational augmentation to be only significant if there is separated flow.

7.2.1. Stall Delay Models

Numerous attempts have been made in the literature to model rotational augmentation. Most of these attempts add its effect as a correction to the 2D steady lift curve. The correction is calculated through a correction factor f_{C_l} that is multiplied by the difference between potential lift and steady lift coefficient. The basic form of these correction models follow the equation:

$$C_{l_{3D}} = C_{l_{2D}} + f_{C_l} \cdot \Delta C_l \tag{7.2}$$

where,

$$\Delta C_l = 2\pi \sin(\alpha - \alpha_0) - C_{l_{2D}} \tag{7.3}$$

A summary of various correction factors used in the literature is presented in table 7.2. One of the earliest attempts in the wind turbine community to model this effect was made by Snel et al. [82]. He used comparison with measurements to find an empirical fit: suggesting rotational effects are proportional to $(c/r)^2$. However, previously, Banks and Gadd [98] showed these effects are theoretically proportional to $(c/r)^{\frac{2}{3}}$. Lindenburg [51] improved on Snel's model by adding a local speed ratio dependency. Chaviaropouloa and Hansen [14] studied rotational augmentation using a quasi-3D Navier-Stokes model. They found strong dependency of (c/r) ratio and twist angle with rotational augmentation, which they included in their model as seen in table 7.2. An improvement to their model was made by Schepers [77], he compared numerical simulations with NREL Phase IV field measurements and improved the (c/r) ratio and twist angle dependencies. A model which is comparatively different from other correction models was derived by Dumitrescu [19, 20], which used an exponential function to model the (c/r) dependency. An important thing to note regarding these empirical models is that they do not intrinsically model the after stall dependency of rotational effects on AoA. Instead, they rely on conditional statements to model this after stall dependency. For example, Snel's

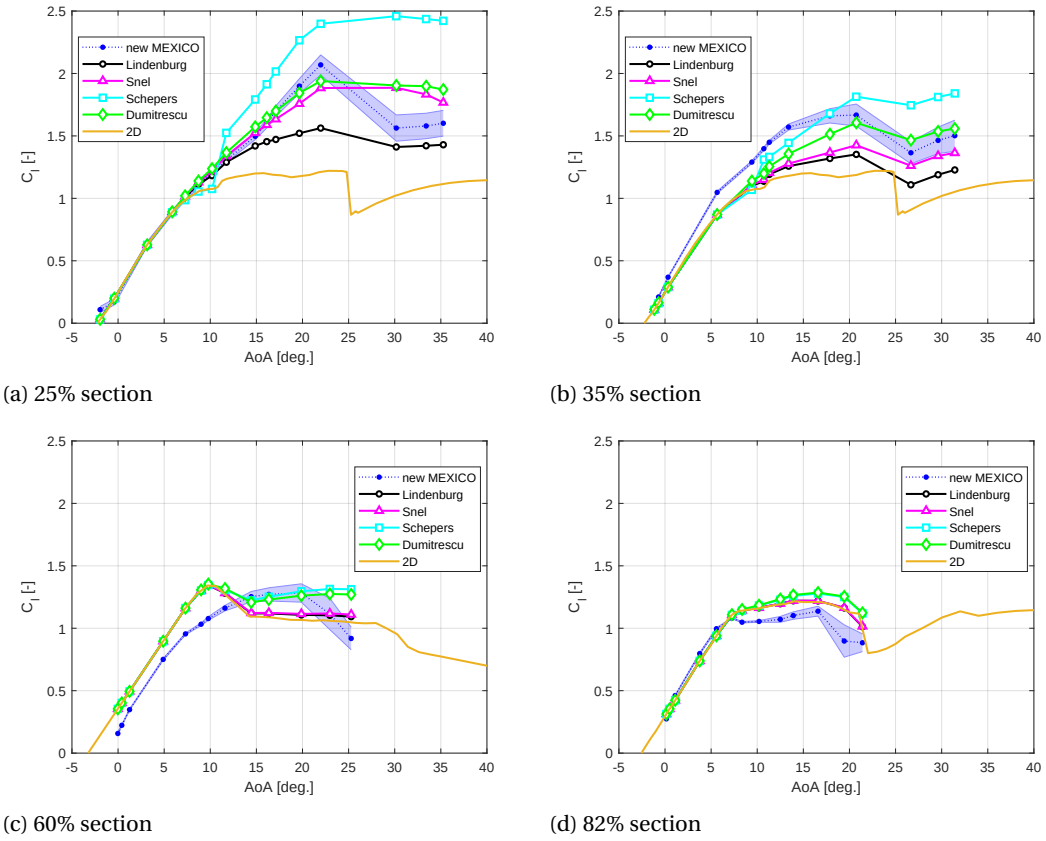

(a) 25% section

(b) 35% section

(c) 60% section

(d) 82% section

Figure 7.2: Lift coefficient versus effective AoA predicted by various stall delay engineering models. The experimental data has been extracted from new MEXICO measurements in axially aligned flow with rotational speed of 425 rpm. The shaded area represents standard deviation in measurements. Note: the effective AoA is determined for experimental data using inverse BEM approach.

model applies the correction up until an AoA of 30 degrees after which the correction is linearly decreased to zero till an AoA of 50 degrees.

7.2.2. Comparison with Measurements

In order to select the optimum model for simulating the effects of rotational augmentation, 3D airfoil polars from axial conditions on the new MEXICO experiment were extracted and compared with 2D airfoil polars. The effective AoA was estimated using inverse BEM algorithm described in section 3.6. The method has been documented to work well in the literature for axial flow conditions and has been used to extract 3D airfoil polars before [28, 29, 64]. Here again, the author would like to emphasize that inverse BEM is used for selecting the optimum 3D correction model in conjunction with recommendations from literature, and not for validating or tunning the 3D correction model itself.

A comparison between the various correction models of table 7.2 has been presented in figure 7.2 for four different spanwise section of the MEXICO blade. Here, the results are also compared with 2D and 3D rotationally augmented measurement data. Lindenburg model underpredicts lift coefficient. He presented a "centrifugal pumping" model based on local speed ratio. The model showed good agreement with NASA-Ames NREL wind tunnel measurements [51]; however, according to Lindenburg the model could not explain the strong increase in lift coefficient near the root. Which is also observed here in figure 7.2a. Snel's model works well for 25% section. Nonetheless, it slightly under predicts for outward radial positions; this same behavior was also documented by Guntur [29] for the old MEXICO measurements. Schepers's model largely overpredicts the lift coefficient for 25% section. For 60% and 82% span, Scheper's model converges with the results from Dumitrescu's model. Dumitrescu's model seems to be performing well among all other models, but it seems to augment lift even for 82% span. 60% section has a (c/r) of 0.1052 which is within the limit for rotational augmentation effect established by Bangga et al. [3]. Also, in the results it can be clearly seen that 60% section shows stall delay. Dumitrescu's model captures this effect while Snel's model does not, Guntur

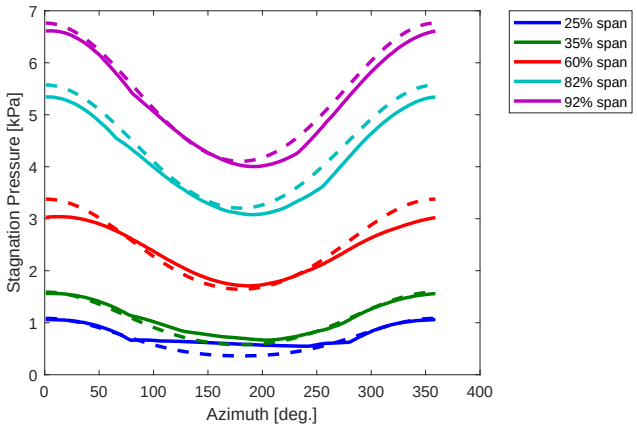

Figure 7.3: Variation of stagnation pressure with azimuthal angle for five different spanwise sections of the MEXICO blade. The solid lines (—) denote stagnation pressure estimated from pressure taps while dashed lines (- - -) denote stagnation pressure estimated through kinematic consideration. The results in this figure are shown for DP 693 with the following conditions: $\beta = -30^o$, $\theta = -2.3^o$, and $\Omega = 425.1\,rpm$..

[29] documented the same observation in his study. Despite this shortcoming of Snel's model, it was seen to give appreciable results for the MEXICO rotor in the study of Pereira et al. [64].

Regarding modeling effect on rotational augmentation on drag coefficient there is a divide between the scientific community [51]. The scientfic community has mixed reviews for modeling this effect, particularly because some literatures document an increase of drag due to rotational augmentation [14, 36, 78] while others warrant a decrease in drag coefficent [3, 18, 97]. Therefore, applying a drag correction was excluded; also because the 3D drag coefficients did not show large difference from the 2D polars as shown in figure C.1. It should be kept in mind that estimation of drag coefficient in this figure is expected to be inaccurate as it was obtained from integrating pressure distribution from pressure taps [51].

7.3. Validation of Aerodynamic Simulations

For the validation of aerodynamic simulations, attention would be focused on New MEXICO test cases where dynamic stall is most probable, as discussed in section 7.1, this corresponds to cases with high tunnel velocity. Emphasis will be given on comparison with normal force as it directly translates to loads experience by a rotor blade. A summary of New MEXICO data points analyzed in the current section are presented in table:

Table 7.3: Selected New MEXICO data points for validation of aerodynamic simulations.

Case Type	Data Points	$U_\infty\,[m/s]$	$\beta\,[deg.]$	$\theta\,[deg.]$	$\Omega\,[rpm]$
Yawed flow (clean)	932	24	8	-2.3	425.1
	938	24	15	-2.3	425.1
	942	24	30	-2.3	425.1
	951	24	45	-2.3	425.1
	693	24	-30	-2.3	425.1

The simulations were performed with the following dynamic stall models:

1. Snel's 1^{st} order model
2. Beddoes-Leishman model
3. ONERA model
4. Snel's 2^{nd} order model

Additionally, Snel's 3D correction was utilized as it was seen, in section 7.2, to perform well for the New MEXICO rotor. ECN's yaw model was also switched on, although at the conditions selected in table 7.3 this model has a negligible contribution. Dynamic inflow model was also turned on but, again, its effect will also

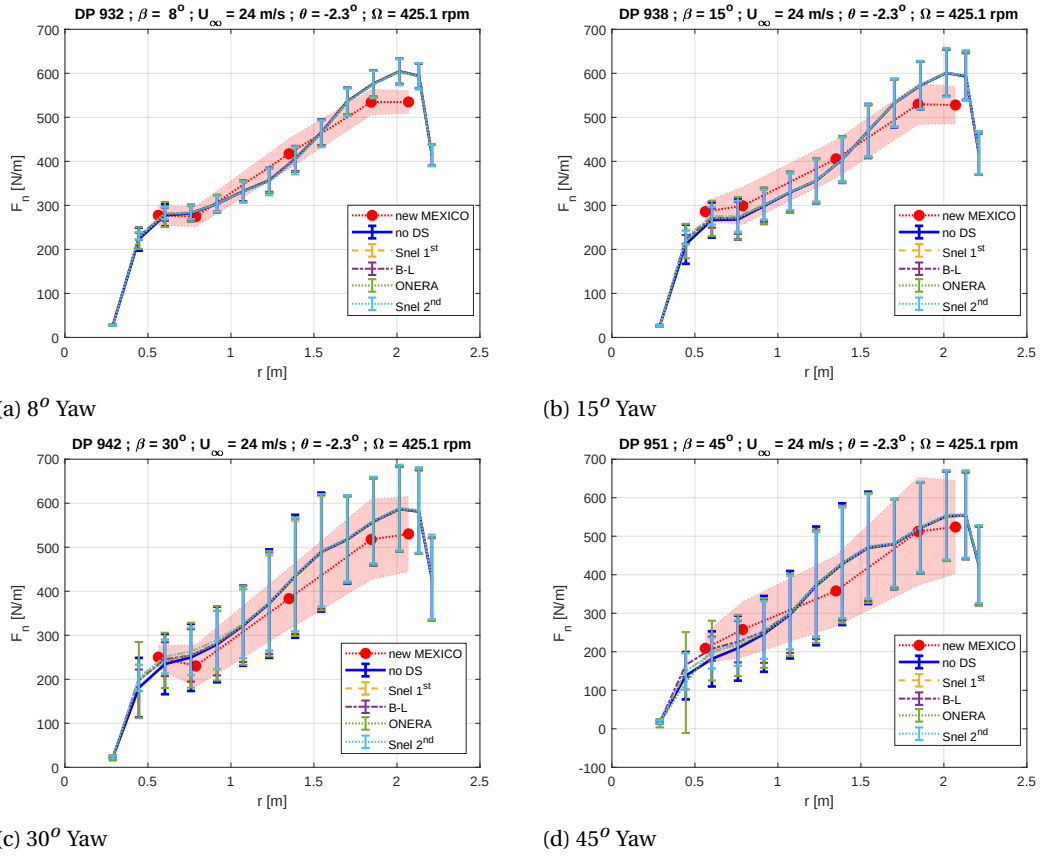

(a) 8^o Yaw

(b) 15^o Yaw

(c) 30^o Yaw

(d) 45^o Yaw

Figure 7.4: Spanwise variation of mean normal force simulated with different dynamic stall models and compared with New MEXICO measurements. The shaded region denotes the standard deviation of measurements while error bars denote standard deviation of simulations in an oscillation cycle.

be negligible due to different orders of magnitude between the time scales for dynamic stall and dynamic inflow effects, i.e $\frac{c}{U_\infty} << \frac{D}{U_\infty}$. Both Prandtl tip and root correction were include while performing simulations. Approximately, 15 revolutions of the rotor were simulated and results were extracted from the second last simulation cycle.

Normalization of aerodynamic loads obtained from New MEXICO measurements is a challenging task. The difficulty lies in obtaining an accurate estimation of local dynamic pressure at a blade section. Taking the local stagnation pressure might seem like a possible way to go; however, local stagnation pressure is prone to uncertainties. The local stagnation pressure is estimated as the maximum pressure obtained from the pressure taps. A drawback of this approach is that it does not yield accurate results if the stagnation point lies between the pressure taps. As an example stagnation pressure is plotted against azimuthal angle in figure 7.3 for yawed conditions. It was observed that the afore mentioned method of obtaining stagnation pressure, denoted by solid lines in the figure, gives large uncertainty for inboard sections due to higher AoA and lower stagnation pressures. As the blade sections are only heavily instrumented near the leading edge (LE); therefore, higher AoA may result in a stagnation point location away from the LE where distance between pressure taps is large. Thus, using local stagnation pressure could introduce further error into the normal force coefficient. Another option could be to use the dynamic pressure determined through kinematic consideration by neglecting induction effects, denoted by dashed lines in figure 7.3. This approach is more realistic for inboard blade sections where induction is lower compared to outboard blade sections. Moreover, using this normalization has the advantage that same normalization can be used for simulation and measurements; thus, preventing introduction of any addition normalization errors.

7.3.1. Spanwise Load Variation

The normal force generally increases from the root towards the tip for a rotating rotor. Mainly because outboard radial positions experience a higher effective flow velocity due to rotation. This effect is seen for a

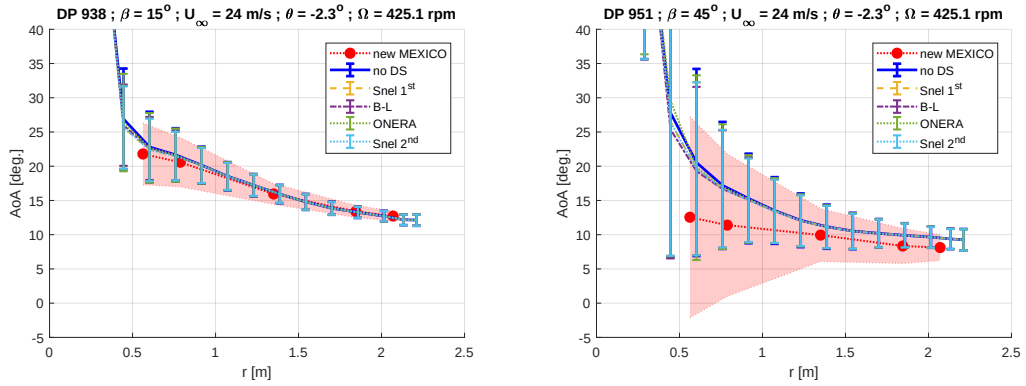

(a) 15^o Yaw (b) Comparing 45^o & -30^o Yaw

Figure 7.5: Spanwise variation of AoA for different dynamic stall models. The AoA for the measurements has been determined using inverse BEM. The shaded region denotes the standard deviation of measurements while error bars denote standard deviation of simulations in an oscillation cycle.

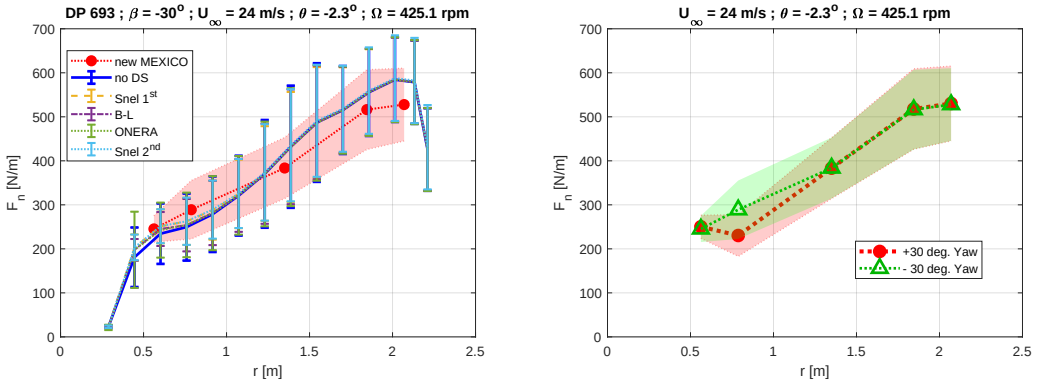

(a) -30^o Yaw (b) Comparing $+30^o$ & -30^o Yaw

Figure 7.6: Spanwise variation of mean normal force simulated with different dynamic stall models and compared with New MEXICO measurements. The shaded region denotes the standard deviation of measurements while error bars denote standard deviation of simulations in an oscillation cycle.

rotor rotating in yawed flow in figure 7.4. The higher effective flow velocity results in higher loads at outboard sections despite the fact that at outboard sections the AoA is comparatively lower. Meaning that at high free-stream velocities, or tunnel speeds, inboards sections of the blade are more prone to operating near the stall regime. The latter is corroborated by figure 7.5. Here, inboard sections not only have a higher mean AoA but also higher amplitude of AoA fluctuations during a revolution of the blade. Comparatively, the outboard sections have lower AoA and a lower amplitude of AoA fluctuations. This results in a smaller dynamic stall hysteresis loop for the outboard sections. Also, as reduced frequency is lower at outboard sections in comparison to inboard sections, figure 7.1. Hence, one can say dynamic stall effects are more prominent for the inboard sections, especially, 25% and 35% section of the MEXICO blade.

Generally, the spanwise variation of normal force agrees reasonable well with experimental data. In figure 7.4, the mean normal force trend is within 10% of the experimental results. However, the standard deviation of normal force seems to deviate from experiments especially for cases with higher yaw angles. Despite that the simulations do capture the trend of increasing standard deviation with increasing yaw angle. The reason for increased standard deviation can be explained through the advancing and retreating blade effect. With increasing yaw angle the component of incoming free-stream in the direction of tangential velocity component becomes larger. Thus, giving a larger variation between dynamic pressure at the 0 degree and 180 degree azimuth. A prominent thing to note in figure 7.4a and figure 7.4b is the over-prediction of normal force at the far outboard sections of the blade. Implying that the tip correction is not sufficiently accounting for tip losses. The dynamic stall models only seem to kick in for the inboard section of the blade as can be seen from increasing difference between error bars near the root.

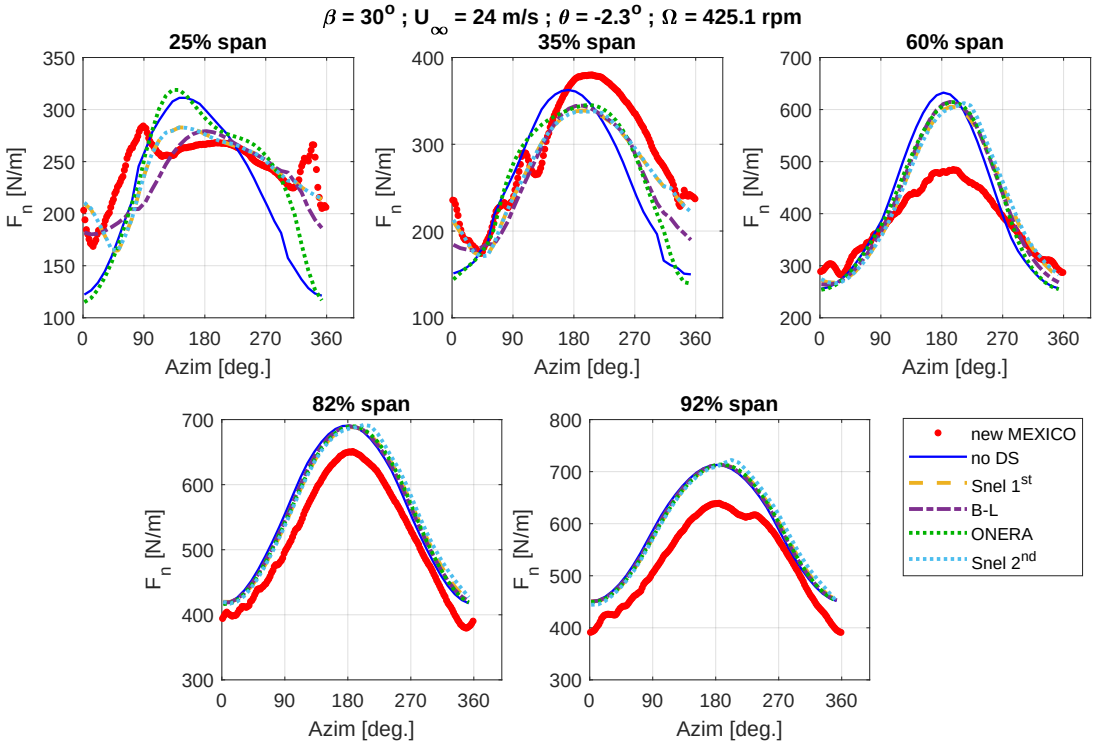

Figure 7.7: Azimuthal variation of normal force at five different spanwise sections on the MEXICO blade.

Strangely enough a hump in normal force is observed near the 60% section, figure 7.4d. This hump was also previously observed in figure 4.8b with axial flow conditions at a tunnel speed of 15 meter per second. It is speculated that the bell shaped peak in 2D lift coefficient curve (figure 7.2c and 5.4) near the stall AoA of 10 degree for the RISOE airfoil section is the cause for this peculiarity as this 2D polar is fed as the backbone curve for simulations. This speculation is further confirmed by observing figure 7.5, which shows the spanwise variation of AoA. Here, the mean AoA around the 60% section reduces from roughly 16 degrees for 15 degrees yaw angle to 11 degrees for 45 degrees yaw angle. As the the yaw angle increase from 15 degrees in figure 7.4b to 45 degrees in figure 7.4d the hump starts appearing in the mean normal force trend. The reason that this effect is prominent is because none of the other airfoils have a peak in 2D lift curve like RISOE airfoil as can be seen from figures 5.3 and 5.5.

Figure 7.6a shows spanwise variation of normal force for a −30 degree yaw angle. The tower effects are negligible on the MEXICO rotor due to the rotor being half a diameter aft of the tower. Hence, it is expected that mean loads and standard deviation of loads for −30 degree yaw and +30 degree yaw would be identical. In fact, for −30 degree yaw case the +30 degree azimuthal load variation is phase shifted by 180 degrees because of in-plane component of wind coming from the opposite side. A comparison between New MEXICO measurements for −30 degree and +30 degree yaw is depicted in figure 7.6b. Here, the results are very identical except for the 35% section. On closer inspection of pressure distributions it was revealed that pressure distributions at 35% section for +30 degree yaw case have large kinks in measurements, figure B.1. Therefore, in the following sections measurements for −30 degree yaw at 35% section will be phase shifted 180 degrees to replace erroneous results for 35% section in +30 degree yaw.

7.3.2. Azimuthal Load Variation

For a positive yaw angle the azimuthal load variation shows a peak value close to 180 degree azimuth because at this location the resultant flow velocity is highest. This is observed in figures 7.7. On comparing dynamic stall simulations with simulation without dynamic stall model (denoted by 'no DS' in figures), it is seen that dynamic stall models are mainly active for 25% and 35% section. Thus, corroborating the assumptions made in section 7.1. Furthermore, the dynamic stall simulations seem to capture the experimental trend with reasonable accuracy. An exception can be made for the 60% section where simulations show a higher peak and mean value of normal force. This deviation can be traced back to the hump in mean normal force observed in

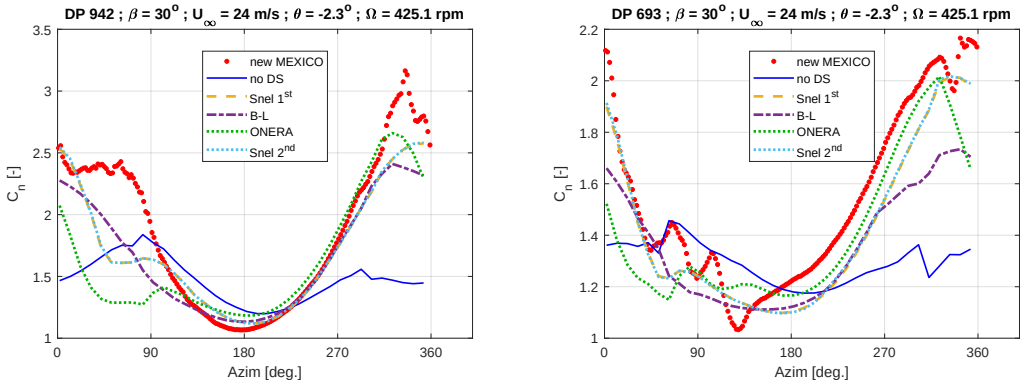

(a) 25% section ; 30^o Yaw

(b) 35% section ; 30^o Yaw

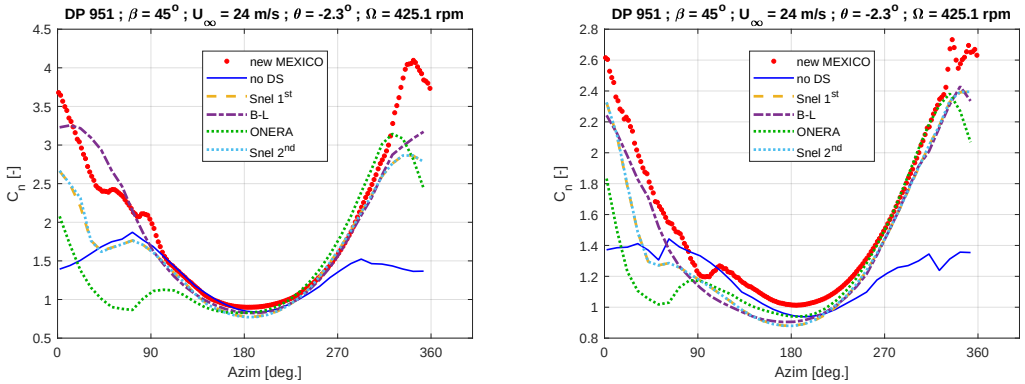

(c) 25% section ; 45^o Yaw

(d) 35% section ; 45^o Yaw

Figure 7.8: Normal force coefficient variation with azimuth angle simulated from different dynamic stall models and compared with New MEXICO measurements. Note: normal force has been normalized with dynamic pressure calculated through kinematic considerations to calculate normal force coefficient.

figures 7.4c and 7.4d. Here again, the accuracy of backbone airfoil polars plays a significant role in prediction of dynamic loads.

Among the different dynamic stall models, results for Snel's 1^{st} order and 2^{nd} order model are mostly on top of each other. Suggesting that Snel's 2^{nd} order correction does not have a large effect on loads in yawed flow conditions. On the other hand, Beddoes-Lesihman model seems to be giving results similar to Snel's model with larger differences mainly observed near 0 degree azimuth. Because at 0 degrees azimuth the AoA is higher than at 180 degree azimuth and dynamic stall hysteresis is at the end of upstroke or start of downstroke cycle. This is where most models are expected to differ owing to their different modeling approaches. Lastly, ONERA model seems to under perform among the models being tested. Generally, without dynamic stall models the simulations under predict the loads at 0 degree azimuth because of entering into static stall. This effect can be clearly observed by normalization of normal forces.

Normalization of normal forces were performed using the following relation:

$$C_n = \frac{F_n}{\frac{1}{2}\rho W^2 c} \tag{7.4}$$

where, W is obtained through kinematic considerations. The results for normalized normal force is presented in figures 7.8. Observing the solid blue lines for simulations without dynamic stall models, it can be seen that the blade section enters static stall from 230 degree azimuth. While the experiments show an increase in normal force coefficient beyond static stall limits. All dynamic stall models seem to capture this phenomenon differently. Again, Snel's model and Bedddoes-Leishman model are performing better than the ONERA model. Even these models mainly have difficulty capturing the peak in normal force coefficient and the subsequent flow reattachment phase. The results in figure 7.8b are phase shifted 180 degrees for DP 693 with -30 degree yaw to give results for $+30$ degree yaw. This was done because pressure distributions at this spanwise section for DP 942 with $+30$ degree yaw had large kinks in measurements.

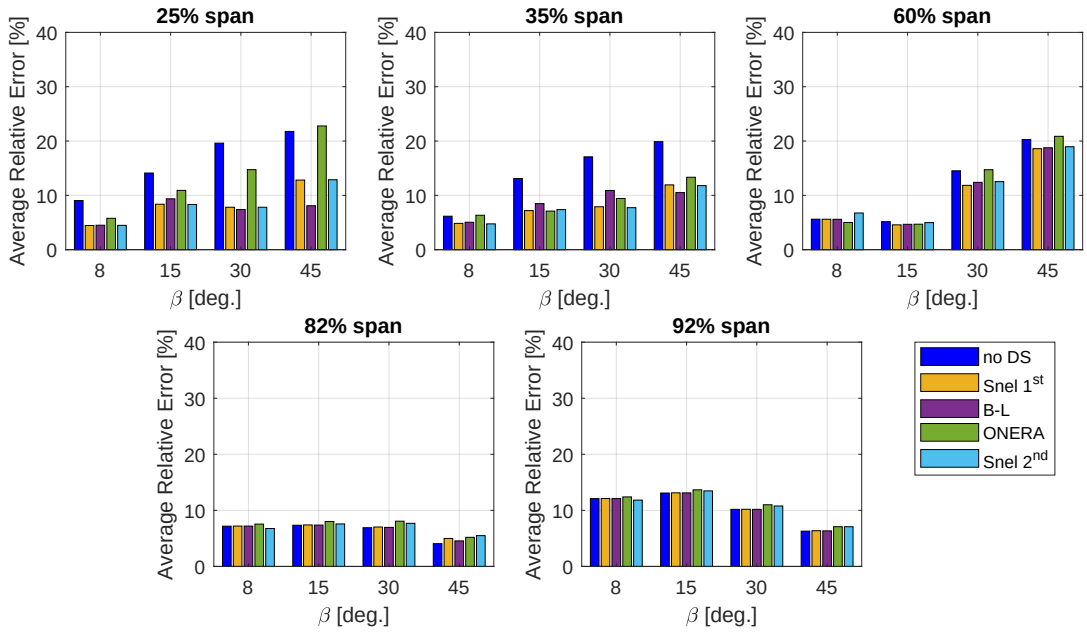

Figure 7.9: Variation of average relative error in normal force with yaw angle for different dynamic stall models. The average relative error is calculated with respect to the New MEXICO measurements.

7.3.3. Error Analysis

To assess the performance and differences between different dynamic stall models a quantitative error analysis was performed on the test cases of table 7.3. Average Relative Error (ARE) of normal force variation with azimuth was used as a measure to quantify the difference between New MEXICO measurements and simulations. The error was computed according to the following formula:

$$\text{ARE} = \sum_{\psi=0}^{360} \left| \frac{F_{n,meas}(i) - F_{n,pred}(i)}{F_{n,meas}(i)} \right| \tag{7.5}$$

A bar graph showing the variation of average relative error for different yaw angles and spanwise locations is presented in figure 7.9. An important observation from this figure is that for 60%, 82%, and 92% section the errors associated with different dynamic stall models are almost similar to simulations without using dynamic stall models. This is expected as at outboard spanwise locations dynamic stall effects are not prominent. The added value of using a dynamic stall model is only realized in the 25% and 35% section. At these sections, Snel's model and Beddoes-Leishman model seem to perform well while ONERA model shows errors comparable to simulations without dynamic stall models. Generally, for inboard sections, the error seems to increases with increasing yaw angle as the hysteresis loop extends into deep stall regime. On the other hand, 60% section shows substantially large errors for yaw angles of 30 and 45 degrees. This is infact because of the same reason why a hump was observed in figures 7.4c and 7.4d; it has to do with 2D backbone polar for the RISO airfoil. Lastly, the 92% section seems to show a different trend in error for increasing yaw angles. The error for this section is larger for smaller yaw angles and vice versa. It is mainly due to the fact that at smaller yaw angles the mean AoA is large; thus, giving more pronounced tip effects which were not captured by simulations as can be seen in figures 7.4a and 7.4b.

7.4. Mapping of Optimum Parameters for Beddoes-Leishman Model

Starting right away with the optimization of parameters using an algorithm might yield unrealistic solution because the optimization algorithm might tap into unrealistic or unphysical solution space. Therefore, prior knowledge of the solution space is paramount to help in understanding the results from an optimization study. Therefore, the solution space was explored for a few representative cases which have been proven to have least amount of experimental uncertainty and represent the dynamic stall phenomenon realistically. For this purpose, New MEXICO test cases with $+/-30$ degree yaw and 45 degree yaw were selected. It is to be noted that cases with -30 degree yaw were performed multiple times in the DNW wind tunnel and have good

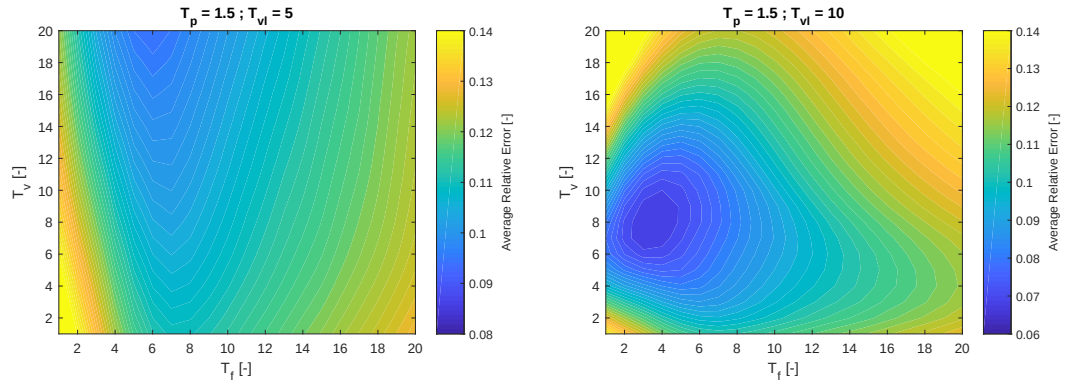

(a) $T_{vl} = 5$ (b) $T_{vl} = 10$

Figure 7.10: Contour plot showing the variation of average relative error between measurements and simulations with B-L model for different values of T_f and T_v. The results in this figure are shown for 35% section with the following test conditions: DP 693 ; $\beta = -30^o$, $\theta = -2.3^o$, and $\Omega = 425.1\,rpm$

reproducibility [8, 61]. Furthermore, experimental measurements for 25% and 35% section will be considered for this study.

The Beddoes-Leishman model parameters associated with attached flow will not be changed in the current analysis as they have been extensively validated previously by Leishman [47]. Here, only the parameters associated with separated flow and vortex lift will be considered, namely, pressure lag (T_p), boundary layer lag (T_f), vortex decay time constant (T_v), and vortex travel time (T_{vl}). According to Leishman [46], T_p is mainly independent of airfoil shape but depends on Mach number. Hence, this parameter was fixed to the value of 1.5, taken from Pereira et al. [65]. T_f is strongly dependent on airfoil shape while T_v and T_{vl} loosely depend on airfoil shape. These parameters will be adjusted to find an optimum solution. An objective function was created to access the average relative error for different inputs of the selected B-L parameters. The results from this objective function are plotted in figure 7.10.

In figure 7.10a, the optimum solution seems to be at a very high value of T_v which seems unrealistic. In figure 7.10b, it can be seen the optimum solution has shifted to a lower value of T_v for a T_{vl} value of 10. It is speculated that compensating for the less loads, due to smaller time it takes for vortex to travel across airfoil upper surface (T_{vl}), the lag in separation (T_f) or lag in vortex lift (T_v) need to be higher to compensate for that effect. Which is the reason why the minimum region shifts to higher T_f and T_v values for a lower T_{vl} value. From figure 7.10b, it can be noted that the error stays well below 8% for approximately $2 < T_p < 5$ and $6 < T_v < 10$. In fact the same analysis was extended to DP 951 and DP 942 and roughly the same range for T_p and T_v with $T_{vl} = 10$ was found to give optimal agreement with experiment. An example of results with optimum parameters is shown in figure 7.11.

7.5. Chapter Conclusion

The following conclusions are drawn from this chapter:

- Snel's 3D rotational correction model was found to give good results for the New MEXICO rotor. This particular model was selected to be used in conjunction with dynamic stall models for yawed flow simulations.
- Estimating stagnation pressure as the maximum pressure obtained from pressure taps on New MEXICO blade yields large uncertainties, especially for 25% spanwise section and large AoA. Therefore, dynamic pressure determined through kinematic considerations was used for normalization of normal force.
- Spanwise variation of normal force was within 10% of the experimental results. A small hump in normal force was observed near the 60% section (figure 7.4d and 7.4c) which was associated with the near stall aerodynamic characteristics of RISOE airfoil section.
- Generally, it was observed that dynamic stall models reduce the error by 8-10% compared to quasi-steady aerodynamic model. This observation holds for inboard regions of the New MEXICO blade where dynamic stall effects are more pronounced. An exception to this trend comes from the ONERA

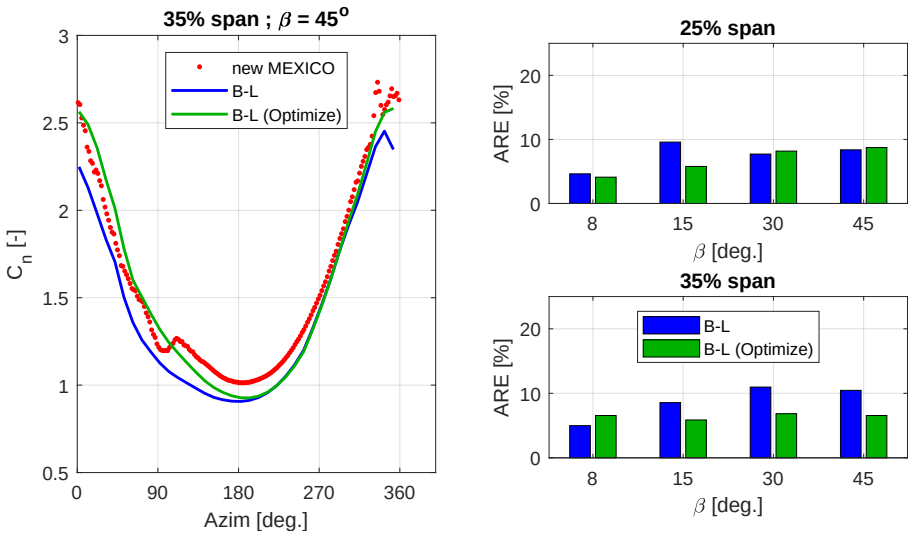

Figure 7.11: Comparison of variation of normal force versus azimuth with Optimized parameters of B-L model. Also, improvement of average relative error is presented in the right figures with the optimized parameters. The following parameters are used for B-L (Optimize) results, shown in green: $T_p = 1.5$; $T_f = 4$; $T_v = 8$; $T_{vl} = 10$.

model which was seen to give less improvement in errors for large yaw angles, especially for the 25% blade section of New MEXICO blade.

- The 60% section of New MEXICO blade at large yaw angles showed larger errors for quasi-steady and dynamic stall models alike. This behavior again pointed to the difference between stall characteristics of steady 2D and 3D polars (extracted from New MEXICO blade 60% section) of the RISOE airfoil, figure 5.4.

8

Conclusions and Recommendations

This chapter summarizes the conclusions and recommendations that were derived during the course of this project.

8.1. Conclusions

The main conclusions derived from the study have been grouped together in the following subsections:

8.1.1. New MEXICO Data Analysis

A detailed analysis of New MEXICO experiment pressure measurements over five different spanwise locations was carried out. It was revealed that cases with high tip speed ratio showed large kinks in pressure measurements especially for 25% and 35% section. However, this was not seen as a problem for the current research as the focus was on cases with low tip speed ratios where probability of dynamic stall occurrence is high. The quality of standstill pressure distribution was observed to deteriorate for very large AoA. Furthermore, large standard deviations were observed for some standstill test cases; thus, suggesting existence of vortex shedding phenomenon in standstill measurements at very large AoA. The latter observation led to a spectral analysis of normal and tangential force time series obtained through integration of pressure distribution data. Structured bluff body vortex shedding was observed in a limited range of AoA from 20 to 50 degree in deep stall regime on the New MEXICO blade. Low Strouhal frequency shedding behavior was seen in the post stall regime, and it was seen to increase with increasing AoA. The absence of structured vortex shedding at very large AoA was attributed to finite aspect ratio of the MEXICO blade, which destabilizes the vortex core causing early break-up of shed vortices.

3D airfoil polars were extracted from New MEXICO standstill measurements. A reasonable agreement was found between the 2D and 3D airfoil polars in attached flow regime up until stall. An exception to this rule was the RISOE airfoil at 60% spanwise section which showed different stall behavior than its 2D airfoil polar. However, in deep stall the 3D airfoil polars showed lower lift and drag coefficients than 2D airfoil polars. The lift to drag ratio versus AoA trend obtained from 3D airfoil polars matches extremely well with the trend predicted by 2D flat plate theory in the deep stall regime. This is because in deep stall, flow is completely separated over upper surface and effect of upper surface thickness can be neglected. The relatively thin NACA airfoil profile enters deep stall earlier than DU and RISO airfoil profile due to higher tendency towards leading edge separation because of its lower thickness.

8.1.2. Standstill Conditions for Rigid New MEXICO Rotor

Large difference between simulations and New MEXICO measurements was observed in Standstill conditions at large AoA, using a BEM based aerodynamic model. The cause of this discrepancy was associated with the difference between 2D airfoil polars, used as backbone curves for simulations, and extracted 3D airfoil polars from New MEXICO standstill measurements. Furthermore, ONERA and B-L model gave absurd results at large AoA, mainly because their underlying assumptions fail at large AoA, while Snel's model gives results similar to a quasi-steady aerodynamic model. As expected, none of the tested dynamic stall models simulate unsteadiness at large AoA except Snel's second order model. This is because Snel's model uses a second order non-linear Van Der Pol equation to model dynamic stall of self-excited nature at large AoA. Validity of the

cross-flow principle was also investigated as BEM models are based on this principle. It was found that the cross-flow principle is not completely valid at large AoA with substantial spanwise flow. A first order correction proposed by Gaunaa et al. [24] was tested; it wrongly predicted the trend in some cases or did not make a large difference in other cases. Therefore, the correction model still needs improvement for applicability to different wind turbine blades as it was originally developed for DTU 10 MW reference turbine.

8.1.3. Improvement of Dynamic Stall Models

Beddoes-Leishman model and ONERA model implementation in Aero-Module showed some problems in reproducing static airfoil polars and simulating dynamic stall at very large AoA. Therefore, different numerical and theoretical improvements were proposed and implemented. Beddoes-Leishman model relies on Kirchoff model to mathematically represent lag in separation over airfoil suction side. The Kirchoff flow separation model implemented in Aero-Module was giving erroneous results for very large AoA. Therefore, a new separation model proposed by Larsen [43] was implemented that circumvents the deficiencies of Kirchoff flow separation model. On the other hand, ONERA model had some problems with numerical implementation which were sorted out. Mathematically, the ONERA model was improved by modifying the second forcing term of the second order non-linear equation with time rate of change of AoA, as proposed by Petot [68]. Furthermore, a new piecewise function was proposed in the current study to better model the re-attachment phase of dynamic stall hysteresis loop in the ONERA model.

8.1.4. Standstill Conditions for Flexible AVATAR Rotor

An aeroelastic analysis of the AVATAR rotor was performed to characterize the effect of dynamic stall models on aerodynamic damping. The time step size of aeroelastic simulations was shown to have an important influence on simulation results. Despite this finding, the range of pitch settings where aeroelastic instabilities were observed was roughly similar for different time step sizes. A very large time step size may add numerical damping to the system. On the other hand, a very small time step size, in addition to large computational time, may result in problems with convergence due to division by a very small number when higher order numerical derivatives are approximated. The latter problem was encountered with some ONERA model simulations where second order time derivatives are approximated. The results for peak-peak tip displacements and max-min bending moments revealed different dynamic stall models to predict different ranges of pitch settings for instabilities. The ONERA model predicted instabilities to happen between 60 to 70 degree pitch setting. B-L model predicted instabilities between 25 to 50 degree pitch setting. While Snel's model predicted instabilities between 20 to 35 degree. In order to extract damping ratio from non-linear time series a methodology was proposed. The method used a band pass filter to isolate 1^{st} edgewise frequency time response. It then extracted peaks from filtered time series to determine the logarithmic decrement and damping ratio. This method is only applicable for an under-damped system which has linear damping (or in other words an exponential term for decay/growth). Detailed analysis of spectral plots, time trace of tip displacement and lift coefficient hysteresis loops revealed that the shape of dynamic stall hysteresis loop has a large effect on aerodynamic damping. A clockwise circular or elliptical hysteresis loop gives positive aerodynamic damping. Generally, all three dynamic stall models showed increased aerodynamic damping in comparison to quasi-steady aerodynamic model, especially in the stall regime. Nonetheless, Snel's model and B-L model showed negative damping ratio in certain pitch angle ranges while ONERA model showed positive damping ratio for the entire range of pitch settings. The negative damping ratio predicted by Snel's model was mainly caused by a fader function called "cdelpot()" which had changed the direction of hysteresis loop to counter-clockwise. On the other hand, B-L model usually showed negative damping ratio for cases where the trailing edge separation module was switched off (i.e. $f = 0$). This resulted in a sort of half hysteresis loop giving negative damping in lower half cycle.

8.1.5. Rotating Yawed Conditions for Rigid New MEXICO Rotor

Performance of dynamic stall models was evaluated in yawed flow conditions using New MEXICO data. Before simulating yawed conditions a suitable rotational augmentation correction was determined. Snel's 3D rotational correction was found to give good results for the New MEXICO rotor. This particular model was selected to be used in conjunction with dynamic stall models for yawed flow simulations. A difficulty was encountered in estimating stagnation pressure as the maximum pressure obtained from pressure taps on New MEXICO blade yields large uncertainties, especially for 25% spanwise section and large AoA. Therefore, dynamic pressure determined through kinematic considerations was used for normalization of normal force. Error analysis of the results revealed that spanwise variation of normal force was within 10% of the experi-

mental results. A small hump in normal force was observed near the 60% section (figure 7.4d and 7.4c) which was associated with the peculiar near stall aerodynamic characteristics of RISOE airfoil section. Generally, it was observed that dynamic stall models reduce the error in azimuthal variation of normal force by 8-10% compared to quasi-steady aerodynamic model. This observation holds for inboard regions of the New MEXICO blade where dynamic stall effects are more pronounced. An exception to this trend comes from the ONERA model which was seen to give less improvement in errors for large yaw angles, especially for the 25% blade section of New MEXICO blade. The 60% section of New MEXICO blade at large yaw angles showed larger errors for quasi-steady and dynamic stall models alike. This behavior again pointed to the difference between stall characteristics of steady 2D and 3D polars (extracted from New MEXICO blade 60% section) of the RISOE airfoil, figure 5.4.

8.2. Recommendations

The following recommendations are suggested for a future project:

- Inverse BEM was used to determine AoA and aerodynamic coefficients from experimental data in this study. It is recommended to compare the results with other methods like, inverse free vortex wake method.
- An unsteady aerodynamic experiment with pitch oscillations with mean AoA in deep stall regime is very important to validate dynamic stall model behavior in deep stall. This experiment is crucial to shed light on how realistic are aeroelastic instabilities predicted by some dynamic stall models in standstill conditions.
- In case of spanwise flow in standstill conditions with yawed flow, a higher order cross-flow model needs to be developed. Developing such a model with New MEXICO data might not be feasible due to limited number of data points. Therefore, an extensive CFD or wind tunnel campaign needs to be carried out on similar grounds as Gaunaa et al's work [24].
- Bluff body vortex shedding was observed for a limited range of AoA in deep stall regime from New MEXICO experiments. In order to fully establish the underlying reason for not observing vortex shedding for very large AoA a detailed CFD analysis of New MEXICO blade at a few representative AoA say 40, 70, and 90 degrees is justified. It will give valuable insight into the flow mechanisms hindering vortex shedding phenomenon at these large AoA.
- Among the different dynamic stall models analysed in this study, only Snel's second order model has a special provision, in the form of a Van der Pol type equation, to simulate vortex shedding. Tunning of Snel's second order model to accurately reproduce unsteady fluctuations in loads for a 2D airfoil section in deep stall regime and then using the tunned model for comparison with New MEXICO results in deep stall is another possible direction to pursue in a future project.
- In the current research AVATAR rotor was analysed for one specific case, where only blade torsion, flapwise, and edgewise DOFs were considered. Effect of including complete turbine dynamics say drive train torsion, tower stiffness, and turbulent inflow should also be investigated.
- In chapter 6, damping ratio was estimated using a logrithmic decrement approach, as discussed in section 6.4.3. This approach is only valid for cases where system is underdamped and damping is linear. Furthermore, for a multiple DOF system like a wind turbine blade the simulation results are highly nonlinear and the use of such a simplified method may not yield quantitatively accurate results. Therefore, it is recommended to use system identification methods to determine aerodynamic damping in a future follow-up work.

A

Pressure Sensor Location on MEXICO Rotor Blades

In total 148 Kulite®pressure sensors are used on the MEXICO blade [11]. Most of the pressure sensors are distributed among the blade section locations mentioned in table 3.1 and are represented by blue markers in figure A.1. However, a few of the 148 sensors were mounted on similar blade section locations to assess reproducibility of pressure measurements on different blades. Some of the pressure sensors malfunctioned during the complete test campaign for all data points; they are highlighted by red circles in figure A.1. Also, some sensors malfunctioned for some particular set of data points. For information regarding those sensors the reader is referred to [11].

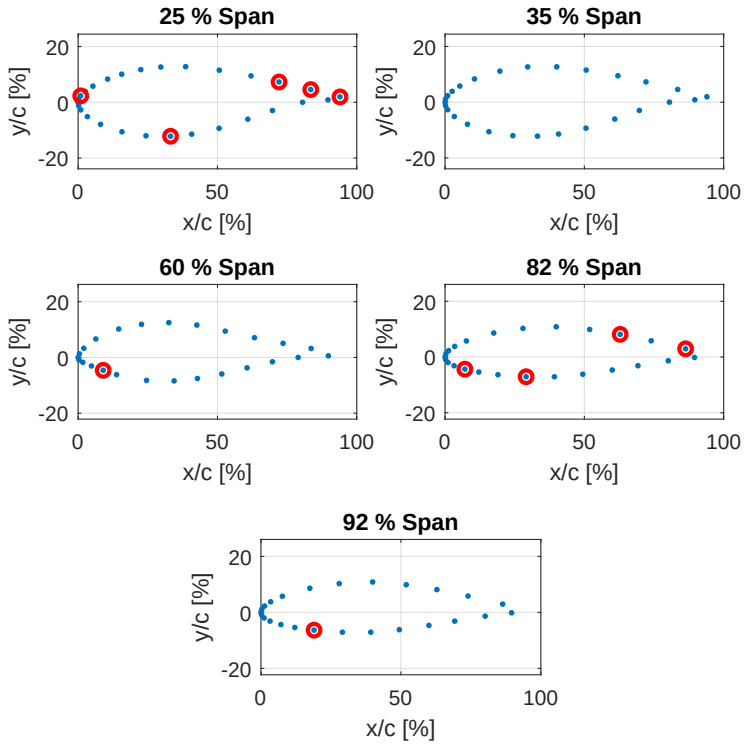

Figure A.1: Pressure sensor locations along five different blade sections on New MEXICO blade. The sensors that were malfunctioning in all measurements are highlighted by red circles. Data taken from [11].

B

Pressure Distribution on New MEXICO Rotor

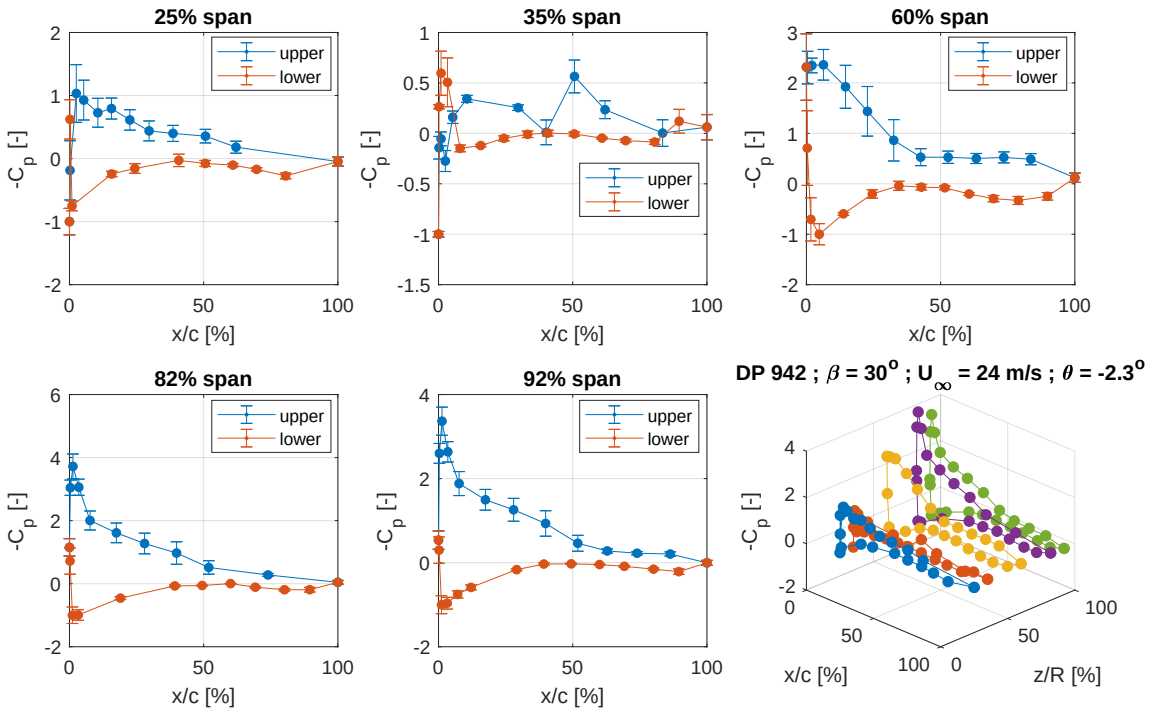

Figure B.1: Mean pressure coefficient versus normalized chord-wise position. The error bars indicate the standard deviation of pressure coefficients.

C

Rotational Effects on Drag Coefficient

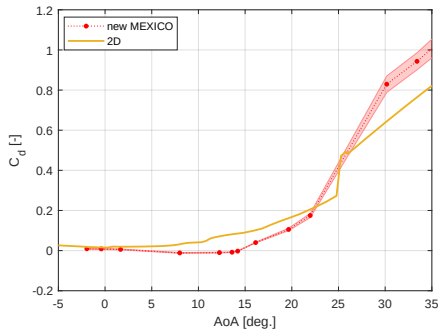

(a) 25% section

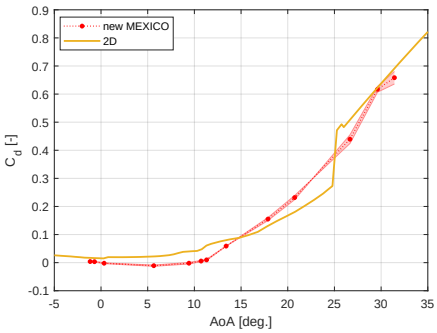

(b) 35% section

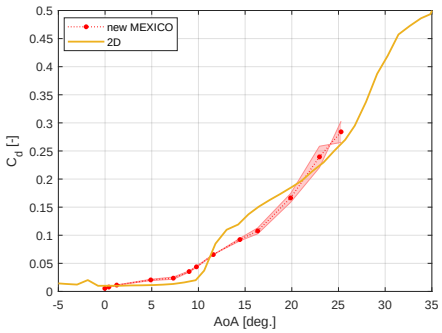

(c) 60% section

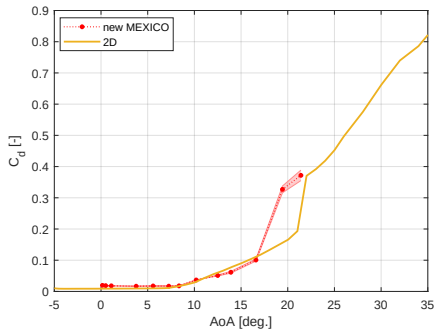

(d) 82% section

Figure C.1: Drag coefficient versus effective AoA. The 3D rotational experimental data has been extracted from new MEXICO measurements in axially aligned flow with rotational speed of 425 rpm. The shaded area represents standard deviation in measurements. Note: the effective AoA is determined using inverse BEM approach.

D

Sensitivity of Beddoes-Leishman Model Parameters

The Beddoes-Leishman model parameters associated with attached flow will not be changed in the current sensitivity analysis as they have been extensively validated previously by Leishman [47]. Here, only the parameters associated with separated flow and vortex lift will be adjusted to see their effect on the hysteresis loops for light and deep stall of figure 4.7.

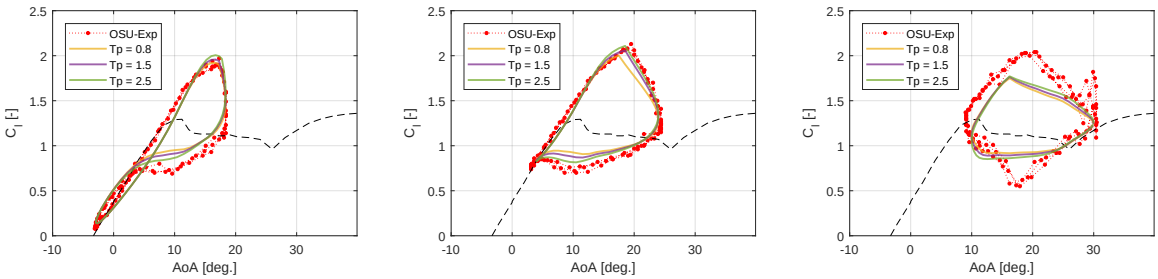

(a) Light dynamic stall ($\alpha_{mean} = 8^o$) (b) Deep dynamic stall ($\alpha_{mean} = 14^o$) (c) Deep dynamic stall ($\alpha_{mean} = 20^o$)

Figure D.1: Dynamic stall hysteresis simulated with B-L dynamic stall model and compared with experimental data on S814 airfoil conducted at Ohio State University wind tunnel (OSU-Exp) [41]. The reduced frequency is approximately 0.09 and pitch amplitude is 10 degrees. Note: the dashed black line represents the steady airfoil polar.

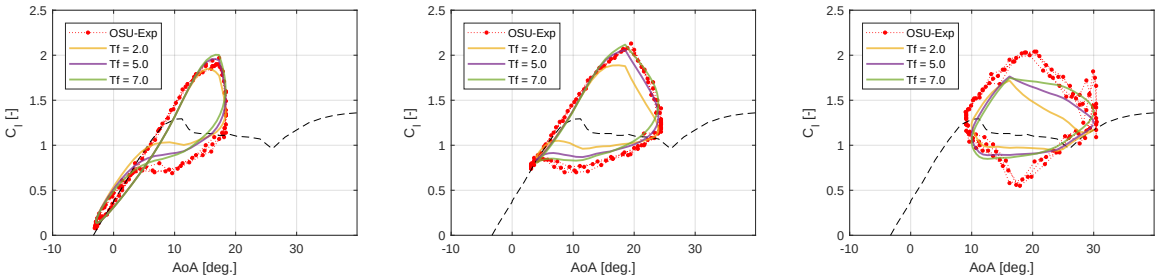

(a) Light dynamic stall ($\alpha_{mean} = 8^o$) (b) Deep dynamic stall ($\alpha_{mean} = 14^o$) (c) Deep dynamic stall ($\alpha_{mean} = 20^o$)

Figure D.2: Dynamic stall hysteresis simulated with B-L dynamic stall model and compared with experimental data on S814 airfoil conducted at Ohio State University wind tunnel (OSU-Exp) [41]. The reduced frequency is approximately 0.09 and pitch amplitude is 10 degrees. Note: the dashed black line represents the steady airfoil polar.

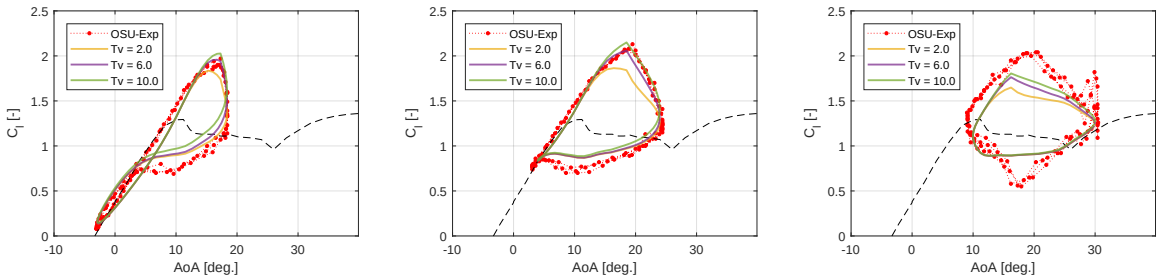

(a) Light dynamic stall ($\alpha_{mean} = 8^o$) (b) Deep dynamic stall ($\alpha_{mean} = 14^o$) (c) Deep dynamic stall ($\alpha_{mean} = 20^o$)

Figure D.3: Dynamic stall hysteresis simulated with B-L dynamic stall model and compared with experimental data on S814 airfoil conducted at Ohio State University wind tunnel (OSU-Exp) [41]. The reduced frequency is approximately 0.09 and pitch amplitude is 10 degrees. Note: the dashed black line represents the steady airfoil polar.

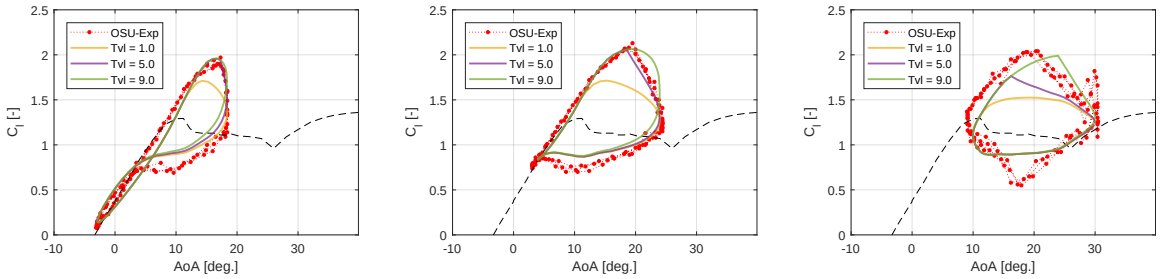

(a) Light dynamic stall ($\alpha_{mean} = 8^o$) (b) Deep dynamic stall ($\alpha_{mean} = 14^o$) (c) Deep dynamic stall ($\alpha_{mean} = 20^o$)

Figure D.4: Dynamic stall hysteresis simulated with B-L dynamic stall model and compared with experimental data on S814 airfoil conducted at Ohio State University wind tunnel (OSU-Exp) [41]. The reduced frequency is approximately 0.09 and pitch amplitude is 10 degrees. Note: the dashed black line represents the steady airfoil polar.

E

Implementation of Flow Separation Models in Beddoes-Leishman Model

E.1. Implementation in FORTRAN Subroutine

```
!#########################################################################
!
SUBROUTINE BeddoesLeishmanDynamicStall(this,dCl,dCd,dCm)
!*************************************************************************
!* SUBROUTINE BeddoesLeishmanDynamicStall
!*
!* DESCRIPTION:
!*     Routine that is called from an Element Airfoil
!*     It calculates the Beddoes Leishman dynamic stall correction to the lift
!*     coefficient and as output assign the corrected lift coefficient to the Element
!*     Airfoil
!*
!* LOGIC:
!*     Step 1: get timestep and initialise values
!*     Step 2: CIRCULATORY ATTACHED FLOW LIFT
!*     Step 3: NON-CIRCULATORY ATTACHED FLOW LIFT
!*     Step 4: LEADING EDGE SEPARATION LAG
!*     Step 5: NON LINEAR TRAILING EDGE SEPARATION
!*     Step 6: VORTEX LIFT

 ...........
 ...........

REAL(DP)                    :: Clsep , fE , Cl_Lar , theta2bar   ! new variables

FSMETHOD = general%FSMETHOD      ! Switching between different Flow Separation Models

 ...........
 ...........
 ...........
 ...........

! ----- Step 5. : NON LINEAR TRAILING EDGE SEPARATION
alphaF            = ClBar/dClda + aCl0
thisAlfF%alpha    = alphaF * RAD_TO_DEG
```

```
CALL static_force(thisAlfF)


IF (FSMETHOD .EQ. 0) THEN

this%fbar         = fSeparation(alphaF,thisAlfF%cl,dClda,aCl0)

ELSE IF (FSMETHOD .EQ. 1) THEN

thisAlfE%alpha    = alphaE * RAD_TO_DEG

CALL static_force(thisAlfE)

this%fbar         = fSeparation_Oye(alphaF,thisAlfF%cl,dClda,aCl0)
fE                = fSeparation_Oye(alphaE,thisAlfE%cl,dClda,aCl0)

ELSE IF (FSMETHOD .EQ. 2) THEN

this%fbar         = fSeparation_FFA(alphaF,thisAlfF%cl,dClda,aCl0)

thisAlfE%alpha    = alphaE * RAD_TO_DEG

CALL static_force(thisAlfE)

IF ( (ABS(thisAlfE%cl)) .LT. (ABS(0.25_dp*dClda*(alphaE - aCl0))) ) THEN

Clsep = thisAlfE%cl

ELSE

Clsep = 0.25_dp*dClda*(alphaE - aCl0)

END IF

ELSE IF (FSMETHOD .EQ. 3) THEN

this%fbar         = fSeparation_Larsen(alphaF,thisAlfF%cl,dClda,aCl0)

thisAlfE%alpha    = alphaE * RAD_TO_DEG

CALL static_force(thisAlfE)

IF ( (ABS(thisAlfE%cl)) .LT. (ABS(0.25_dp*dClda*(alphaE - aCl0))) ) THEN

Cl_Lar = 4.0_dp*thisAlfE%cl

ELSE

Cl_Lar = dClda*(alphaE - aCl0)

END IF

END IF

exponf  = DEXP(-delS/Tf)
this%Df = this%previous%Df*exponf + (this%fbar - this%previous%fbar)*DSQRT(exponf)
```

```
f2bar    = this%fbar - this%Df

IF (FSMETHOD .EQ. 0) THEN

Clf              = dClda*((1.0_dp + DSQRT(f2bar))/2.0_dp)**2.0_dp * &
(alphaE - this%aCl0 * DEG_TO_RAD)*fade2 + ClImp  !?KB Fading function for AOA>45deg

ELSE IF (FSMETHOD .EQ. 1) THEN

Clsep = (thisAlfE%cl - dClda*(alphaE - aCl0)*fE)/( 1 - fE )
Clf   = dClda*(alphaE - this%aCl0 * DEG_TO_RAD)*f2bar + Clsep*(1-f2bar) + ClImp

ELSE IF (FSMETHOD .EQ. 2) THEN

Clf = 0.25_dp*dClda*(alphaE - this%aCl0 * DEG_TO_RAD)*(f2bar + 2*DSQRT(f2bar) )  &
       + Clsep + ClImp

ELSE IF (FSMETHOD .EQ. 3) THEN

theta2bar = ACOS( 2.0_dp*f2bar - 1 )

Clf              = ((DCOS(theta2bar/4))**4)*Cl_Lar

END IF

.....
.....
.....
.....

END SUBROUTINE BeddoesLeishmanDynamicStall
!
!#############################################################################
```

E.2. Implementation in FORTRAN Functions

```
!#############################################################################
!
FUNCTION fSeparation_Oye(alpha,Cl,dClda,alpha0) RESULT(f)
IMPLICIT NONE
REAL(DP) :: alpha,cl,dClda,alpha0,f,alpha_plus,alpha_minus
!REAL(DP), PARAMETER    :: tol = 1e-3

alpha_plus = 30 * DEG_TO_RAD
alpha_minus = -30 * DEG_TO_RAD

IF (alpha.EQ.alpha0) alpha0 = alpha0 + EPS6

IF ( (alpha .LT. alpha_minus) .OR. (alpha .GT. alpha_plus) ) THEN

f = 0

ELSE

f = (2.0_dp*DSQRT(Cl/(dClda*(alpha - alpha0))) - 1.0_dp)**2

END IF
```

```
IF (f > 1.0_dp) f = 1.0_dp

END FUNCTION fSeparation_Oye
!
!#########################################################################
!
FUNCTION fSeparation_FFA(alpha,Cl,dClda,alpha0) RESULT(f)
IMPLICIT NONE
REAL(DP) :: alpha,cl,dClda,alpha0,f
!REAL(DP), PARAMETER    :: tol = 1e-3


IF (alpha.EQ.alpha0) alpha0 = alpha0 + EPS6

IF ( ABS(Cl) .LT. ABS(0.25_dp*dClda*(alpha - alpha0))  ) THEN

f = 0

ELSE

f = (2.0_dp*DSQRT(ABS(Cl/(dClda*(alpha - alpha0)))) - 1.0_dp)**2

END IF

IF (f > 1.0_dp) f = 1.0_dp

END FUNCTION fSeparation_FFA
!
!#########################################################################
!
FUNCTION fSeparation_Larsen(alpha,Cl,dClda,alpha0) RESULT(f)
IMPLICIT NONE
REAL(DP) :: alpha,cl,dClda,alpha0,f,theta,temp
!REAL(DP), PARAMETER    :: tol = 1e-3


IF (alpha.EQ.alpha0) alpha0 = alpha0 + EPS6

IF ( ABS(Cl) .LT. ABS(0.25_dp*dClda*(alpha - alpha0))  ) THEN

theta = PI_D

f = ( 1 + DCOS(theta) )/2.0_dp

ELSE

temp = ABS(Cl/(dClda*(alpha - alpha0)))

IF (temp > 1.0_dp) temp = 1.0_dp

theta = 4.0_dp*ACOS(temp**0.25_dp)

f = ( 1 + DCOS(theta) )/2.0_dp

END IF
```

```
IF (f > 1.0_dp) f = 1.0_dp

END FUNCTION fSeparation_Larsen
!
!##########################################################################
```

E.3. Results

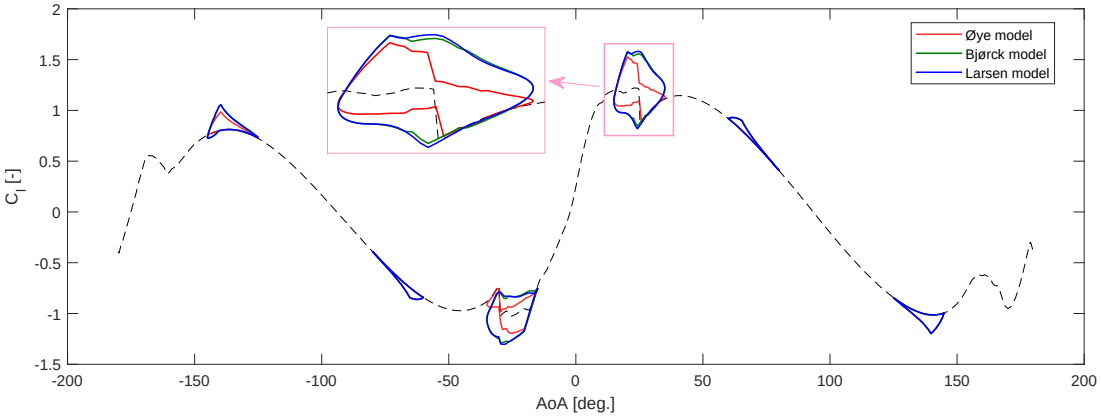

Figure E.1: Comparison between three different trailing edge separation models implemented in the B-L subroutine in Aero-Module. The lift hysteresis loops are simulated for various mean AoA according to the following pitching oscillation input: $\alpha = \alpha_{mean} + 10^0 \sin\omega t$, with a reduced frequency of 0.09. The dashed lines (- - -) denote the static lift curve for the DU 91-W2-250 airfoil.

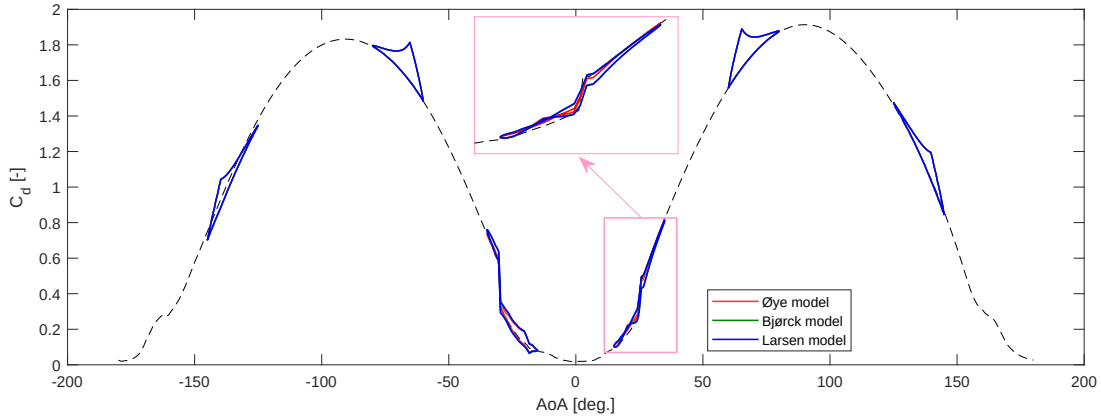

Figure E.2: Comparison between three different trailing edge separation models implemented in the B-L subroutine in Aero-Module. The drag hysteresis loops are simulated for various mean AoA according to the following pitching oscillation input: $\alpha = \alpha_{mean} + 10^0 \sin\omega t$, with a reduced frequency of 0.09. The dashed lines (- - -) denote the static drag curve for the DU 91-W2-250 airfoil.

F

Implementation of improved ONERA model

F.1. Implementation in FORTRAN subroutine

```
!#########################################################################
!
SUBROUTINE ONERADynamicStall(this,dcl)
!*************************************************************************
!* SUBROUTINE ONERADynamicStall
!*
!* DESCRIPTION:
!*     Routine that is called from an Element Airfoil
!*     It calculates the ONERA dynamic stall correction to the lift coefficient
!*     and as output assign the corrected lift coefficient to the Element Airfoil
!*
!* LOGIC:
!*     Step 1: get timestep and initialise values
!*     Step 2: Calculate time derivatives of alpha
!*     Step 3: Calculate parameter values
!*     Step 4: Determine 1st and 2nd order cl corrections

...........
...........

REAL(DP)                                :: K_fac

...........
...........

! ----- Step 3. :
!Correction to r0 to increase stiffness in downstroke
IF (this%clpot > 0.0_dp) THEN
        IF (dardt > 0.0_dp) THEN
                K_fac = 1.0_dp
        ELSE
                K_fac = general%ON_a0
        END IF
ELSE
        IF (dardt < 0.0_dp) THEN
                K_fac = 1.0_dp
```

```
        ELSE
                K_fac = general%ON_a0
        END IF
END IF

r0 = K_fac*r0
rL = (r0 + r2*this%delPot**2)**2
aL = a0 + a2*this%delPot**2
eL = e2*this%delPot**2

.....
.....
.....
.....

END SUBROUTINE ONERADynamicStall

!########################################################################
```

F.2. Results

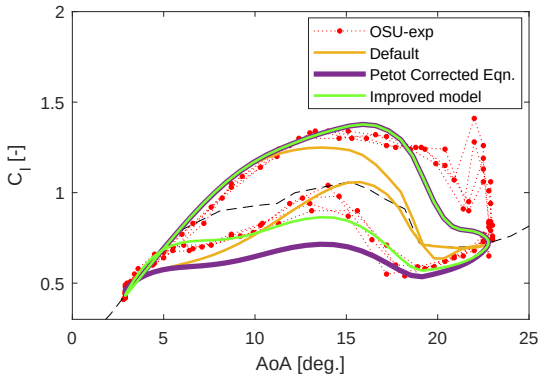

Figure F.1: Comparison of lift coefficient hyteresis between improved model and the model using Petot [68] corrected equations. The experimental results are shown for a S809 airfoil undergoing pitching oscillation with a reduced frequency of 0.042. The mean AoA for this case is 14 degrees.

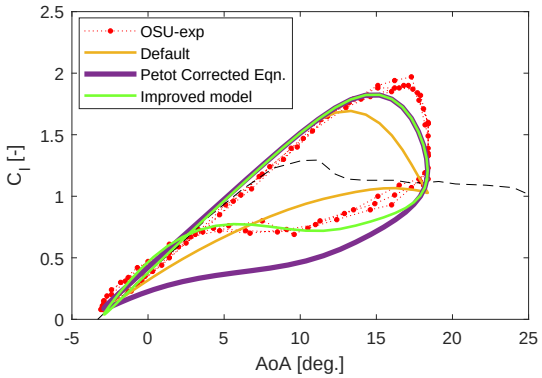

Figure F.2: Comparison of lift coefficient hyteresis between improved model and the model using Petot [68] corrected equations. The experimental results are shown for a S814 airfoil undergoing pitching oscillation with a reduced frequency of 0.089. The mean AoA for this case is 8 degrees.

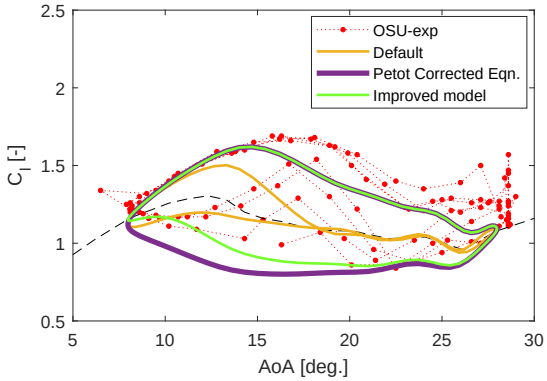

Figure F.3: Comparison of lift coefficient hyteresis between improved model and the model using Petot [68] corrected equations. The experimental results are shown for a NACA 4415 airfoil undergoing pitching oscillation with a reduced frequency of 0.047. The mean AoA for this case is 20 degrees.

G

Validation of Standalone Dynamic Stall Models

G.1. NACA 4415 Airfoil

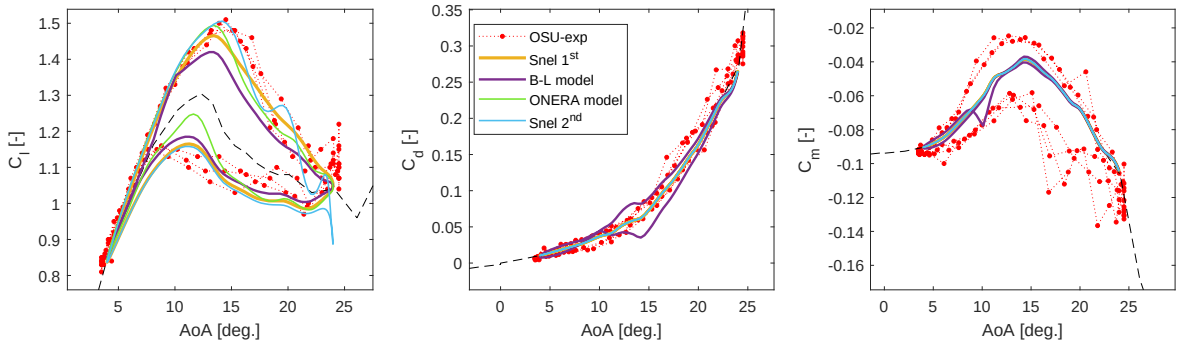

Figure G.1: Dynamic stall hysteresis simulated with different dynamic stall models and compared with experimental data on S814 airfoil conducted at Ohio State University wind tunnel (OSU-Exp) [39]. The reduced frequency is approximately 0.023 and pitch amplitude is 14 degrees. Note: the dashed black line represents the steady airfoil polar.

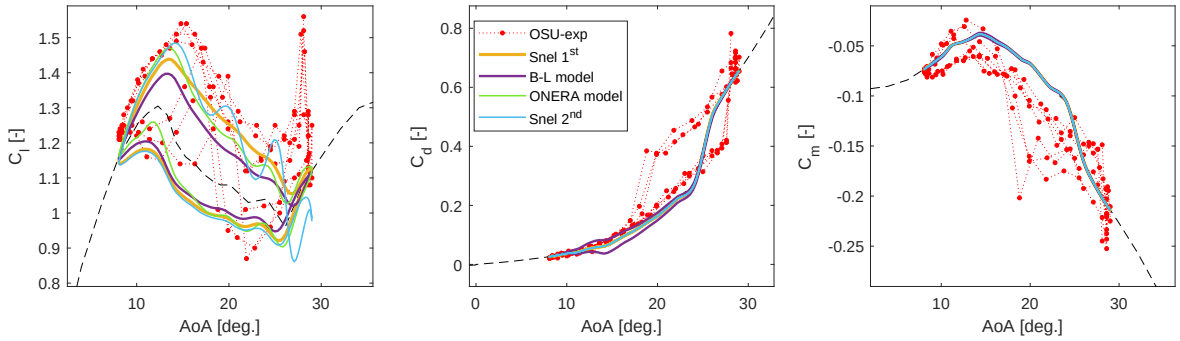

Figure G.2: Dynamic stall hysteresis simulated with different dynamic stall models and compared with experimental data on S814 airfoil conducted at Ohio State University wind tunnel (OSU-Exp) [39]. The reduced frequency is approximately 0.023 and pitch amplitude is 20 degrees. Note: the dashed black line represents the steady airfoil polar.

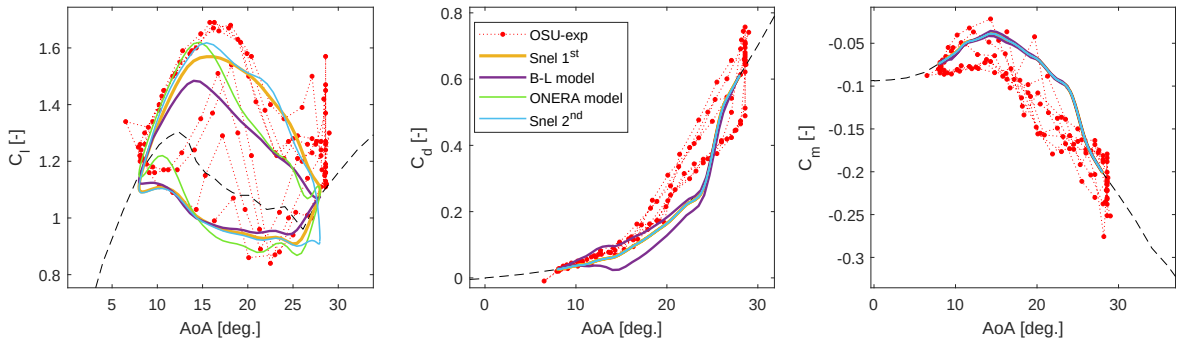

Figure G.3: Dynamic stall hysteresis simulated with different dynamic stall models and compared with experimental data on S814 airfoil conducted at Ohio State University wind tunnel (OSU-Exp) [39]. The reduced frequency is approximately 0.047 and pitch amplitude is 20 degrees. Note: the dashed black line represents the steady airfoil polar.

G.2. S814 Airfoil

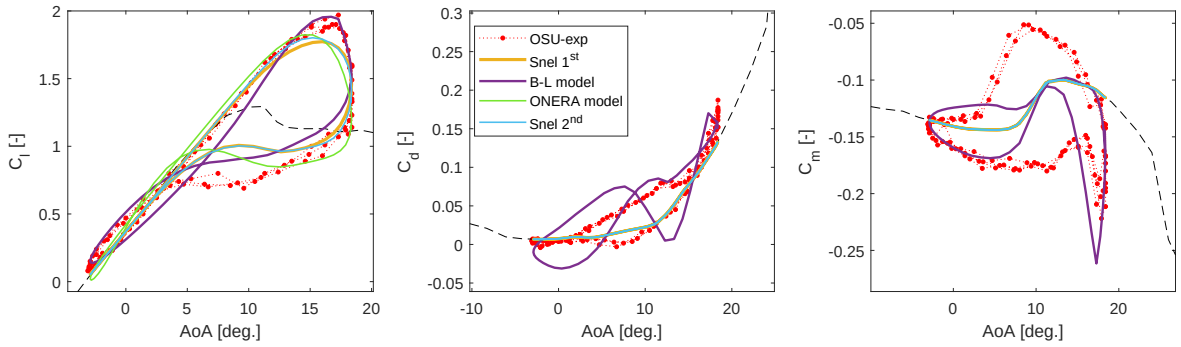

Figure G.4: Dynamic stall hysteresis simulated with different dynamic stall models and compared with experimental data on S814 airfoil conducted at Ohio State University wind tunnel (OSU-Exp) [41]. The reduced frequency is approximately 0.089 and pitch amplitude is 8 degrees. Note: the dashed black line represents the steady airfoil polar.

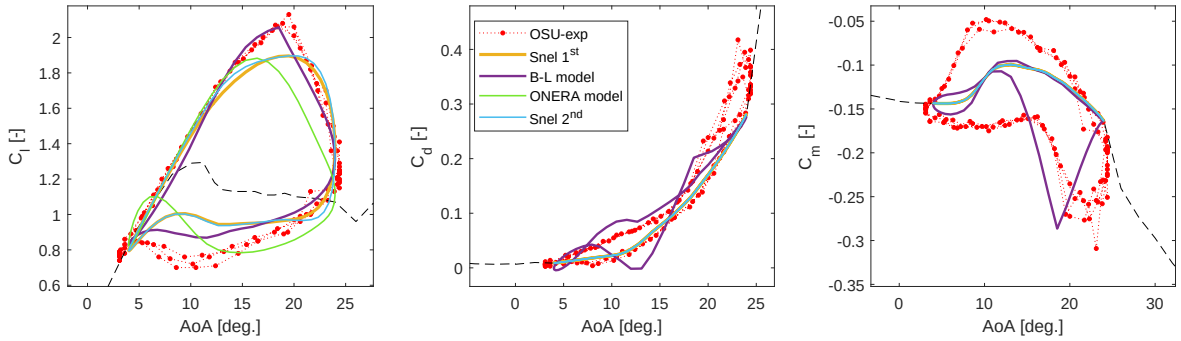

Figure G.5: Dynamic stall hysteresis simulated with different dynamic stall models and compared with experimental data on S814 airfoil conducted at Ohio State University wind tunnel (OSU-Exp) [41]. The reduced frequency is approximately 0.090 and pitch amplitude is 14 degrees. Note: the dashed black line represents the steady airfoil polar.

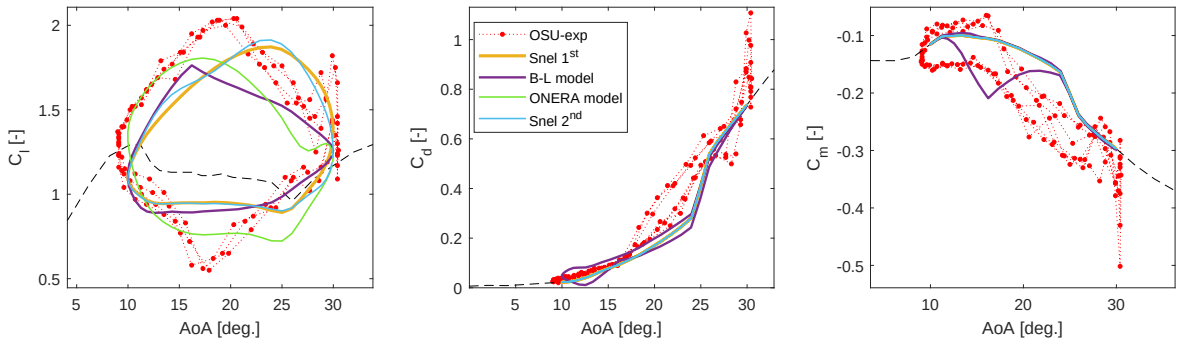

Figure G.6: Dynamic stall hysteresis simulated with different dynamic stall models and compared with experimental data on S814 airfoil conducted at Ohio State University wind tunnel (OSU-Exp) [41]. The reduced frequency is approximately 0.094 and pitch amplitude is 20 degrees. Note: the dashed black line represents the steady airfoil polar.

G.3. S809 Airfoil

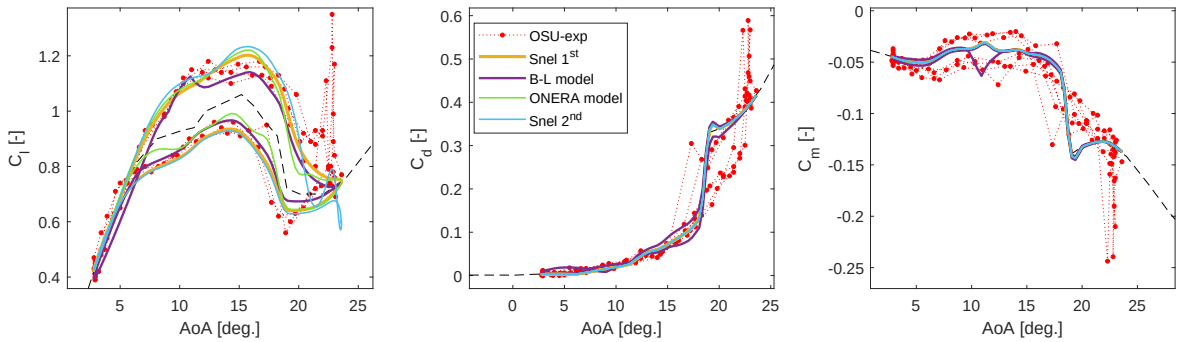

Figure G.7: Dynamic stall hysteresis simulated with different dynamic stall models and compared with experimental data on S809 airfoil conducted at Ohio State University wind tunnel (OSU-Exp) [71]. The reduced frequency is approximately 0.020 and pitch amplitude is 14 degrees. Note: the dashed black line represents the steady airfoil polar.

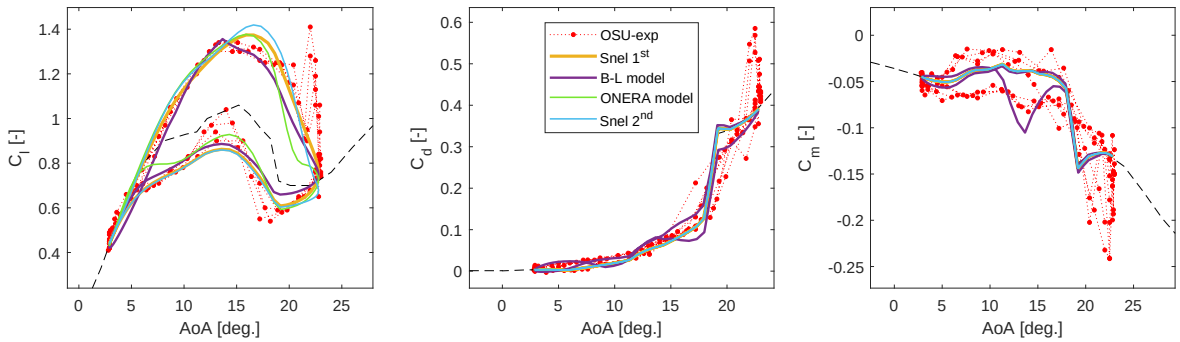

Figure G.8: Dynamic stall hysteresis simulated with different dynamic stall models and compared with experimental data on S809 airfoil conducted at Ohio State University wind tunnel (OSU-Exp) [71]. The reduced frequency is approximately 0.042 and pitch amplitude is 14 degrees. Note: the dashed black line represents the steady airfoil polar.

AVATAR Case Study: Miscellaneous Results

H.1. Effect of Time Step Size

The effect of time step size on the maximum and minimum root bending moments and peak-peak tip deformations in presented in this section.

H.1.1. Tip Deformations

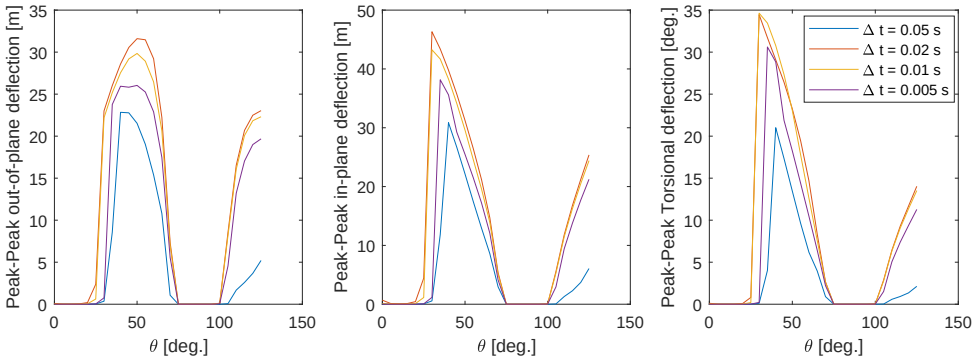

Figure H.1: Peak to peak tip deformations versus pitch setting for different time step sizes. Quasi-steady aerodynamics is used for simulation. The results are shown for blade 1 which is fixed at 90 degree azimuth angle. A uniform steady wind of 42 m/s is used for simulations.

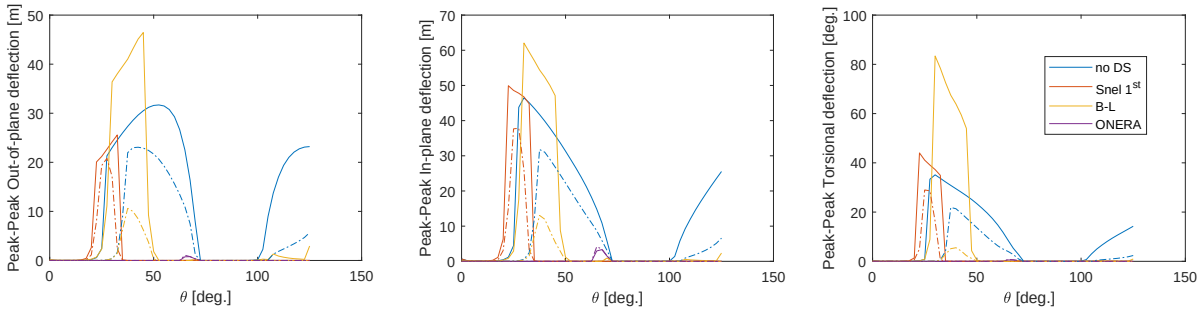

Figure H.2: Peak to peak tip deformations versus pitch setting for different dynamic stall models. ——— line shows results for time step size of 0.02 seconds while - · - · - · - line shows results for time step size of 0.05 seconds. Quasi-steady aerodynamics is used for simulation. The results are shown for blade 1 which is fixed at 90 degree azimuth angle. A uniform steady wind of 42 m/s is used for simulations.

H.1.2. Root Bending Moments

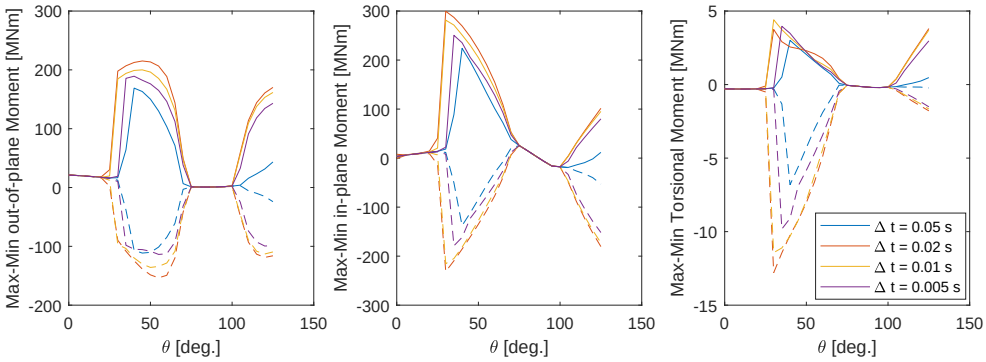

Figure H.3: Maximum and minimum blade root bending moments versus pitch setting for different time step sizes. Quasi-steady aerodynamics is used for simulation. The results are shown for blade 1 which is fixed at 90 degree azimuth angle. A uniform steady wind of 42 m/s is used for simulations.

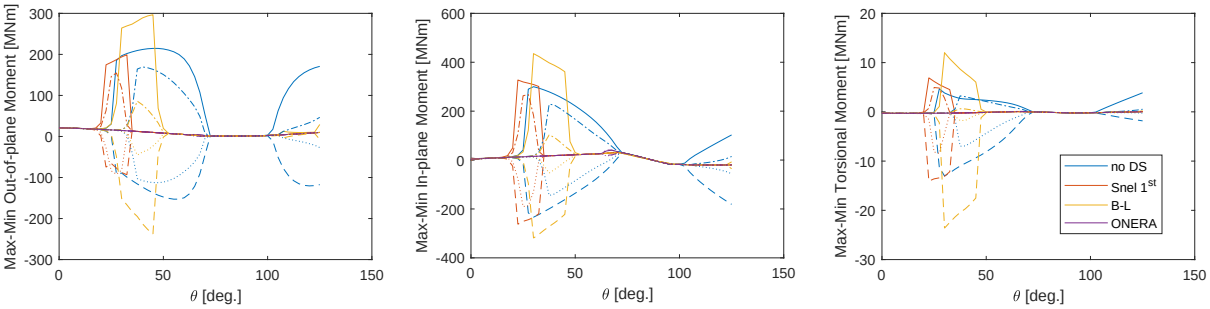

Figure H.4: Maximum and minimum blade root bending moments versus pitch setting for different dynamic stall models. ——— line shows results for time step size of 0.02 seconds while - · - · - · - line shows results for time step size of 0.05 seconds. Quasi-steady aerodynamics is used for simulation. The results are shown for blade 1 which is fixed at 90 degree azimuth angle. A uniform steady wind of 42 m/s is used for simulations.

H.2. PSD of Tip Deformation

The PSD of flapwise and lagwise tip deformation in undeformed rotor plane reference system is shown for different pitch settings in this section.

H.2.1. Pitch = 0^o

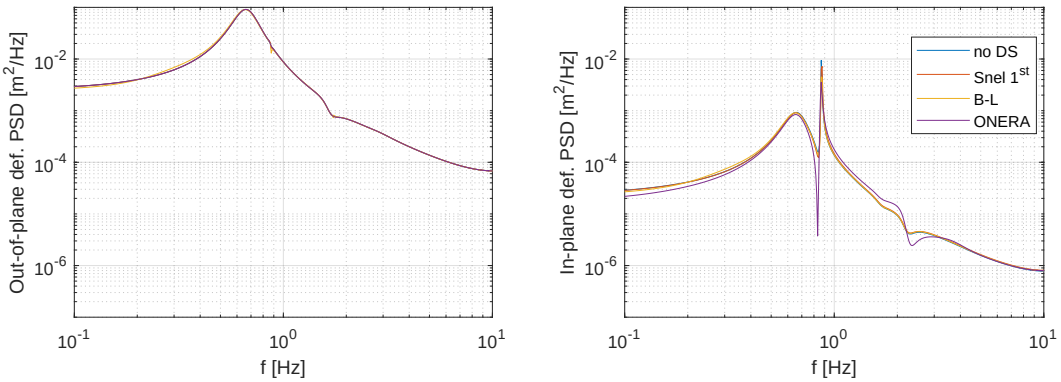

Figure H.5: PSD of flapwise (out-of-plane) and lagwise (in-plane) tip deformation, in undeformed rotor plane reference system, with a pitch setting of 0 degrees. The results are shown for blade 1 which is fixed at 90 degree azimuth angle. A uniform steady wind of 42 m/s is used.

H.2.2. Pitch = 30^o

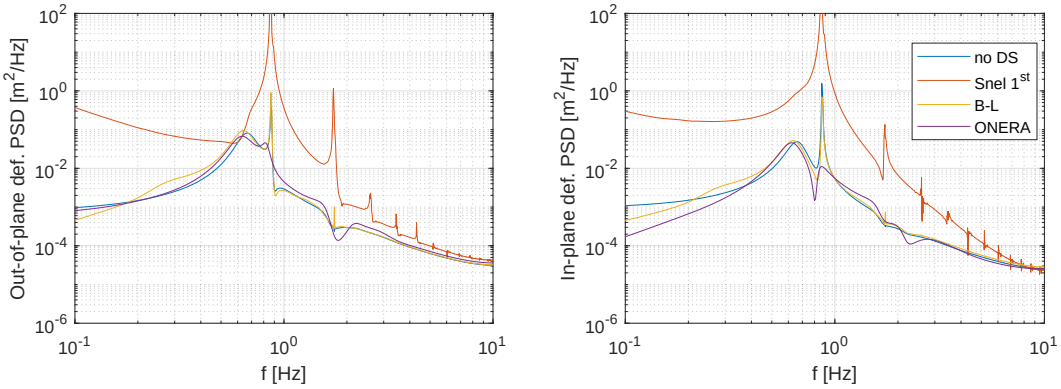

Figure H.6: PSD of flapwise (out-of-plane) and lagwise (in-plane) tip deformation, in undeformed rotor plane reference system, with a pitch setting of 30 degrees. The results are shown for blade 1 which is fixed at 90 degree azimuth angle. A uniform steady wind of 42 m/s is used.

H.2.3. Pitch = 40^o

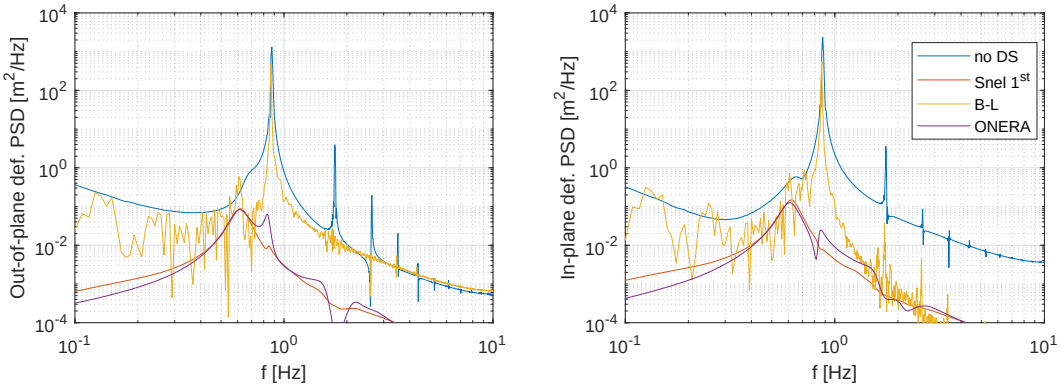

Figure H.7: PSD of flapwise (out-of-plane) and lagwise (in-plane) tip deformation, in undeformed rotor plane reference system, with a pitch setting of 40 degrees. The results are shown for blade 1 which is fixed at 90 degree azimuth angle. A uniform steady wind of 42 m/s is used.

H.2.4. Pitch = 50^o

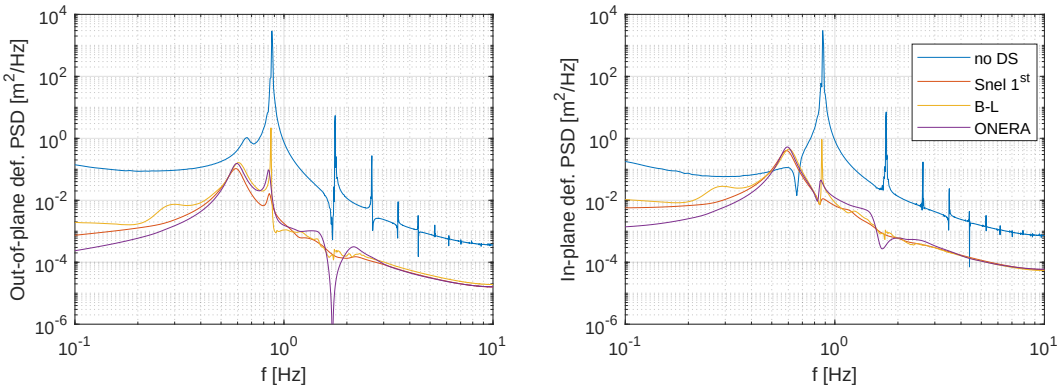

Figure H.8: PSD of flapwise (out-of-plane) and lagwise (in-plane) tip deformation, in undeformed rotor plane reference system, with a pitch setting of 50 degrees. The results are shown for blade 1 which is fixed at 90 degree azimuth angle. A uniform steady wind of 42 m/s is used.

H.2.5. Pitch = 60^o

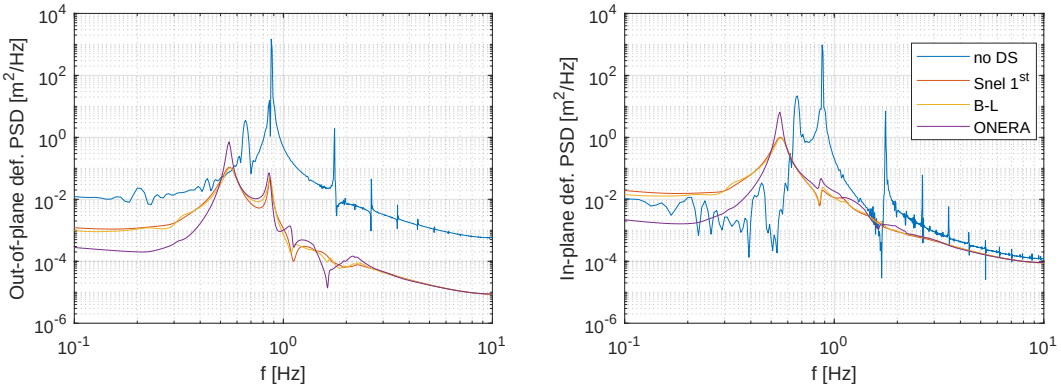

Figure H.9: PSD of flapwise (out-of-plane) and lagwise (in-plane) tip deformation, in undeformed rotor plane reference system, with a pitch setting of 60 degrees. The results are shown for blade 1 which is fixed at 90 degree azimuth angle. A uniform steady wind of 42 m/s is used.

H.2.6. Pitch = 110^o

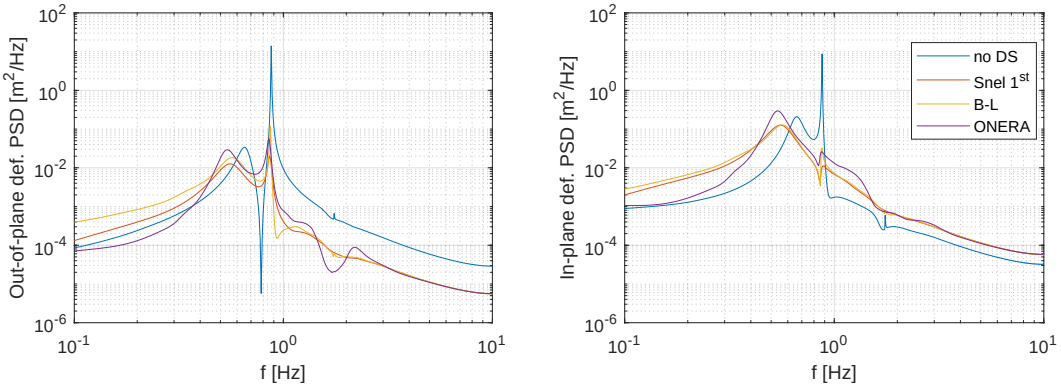

Figure H.10: PSD of flapwise (out-of-plane) and lagwise (in-plane) tip deformation, in undeformed rotor plane reference system, with a pitch setting of 110 degrees. The results are shown for blade 1 which is fixed at 90 degree azimuth angle. A uniform steady wind of 42 m/s is used.

H.2.7. Pitch = 125^o

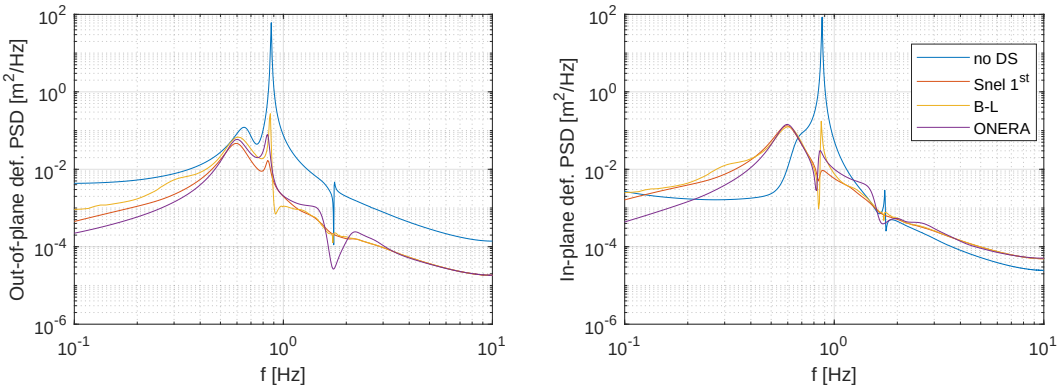

Figure H.11: PSD of flapwise (out-of-plane) and lagwise (in-plane) tip deformation, in undeformed rotor plane reference system, with a pitch setting of 125 degrees. The results are shown for blade 1 which is fixed at 90 degree azimuth angle. A uniform steady wind of 42 m/s is used.

H.3. Tip Deformation and Lift Hysteresis

H.3.1. Pitch = 0^o

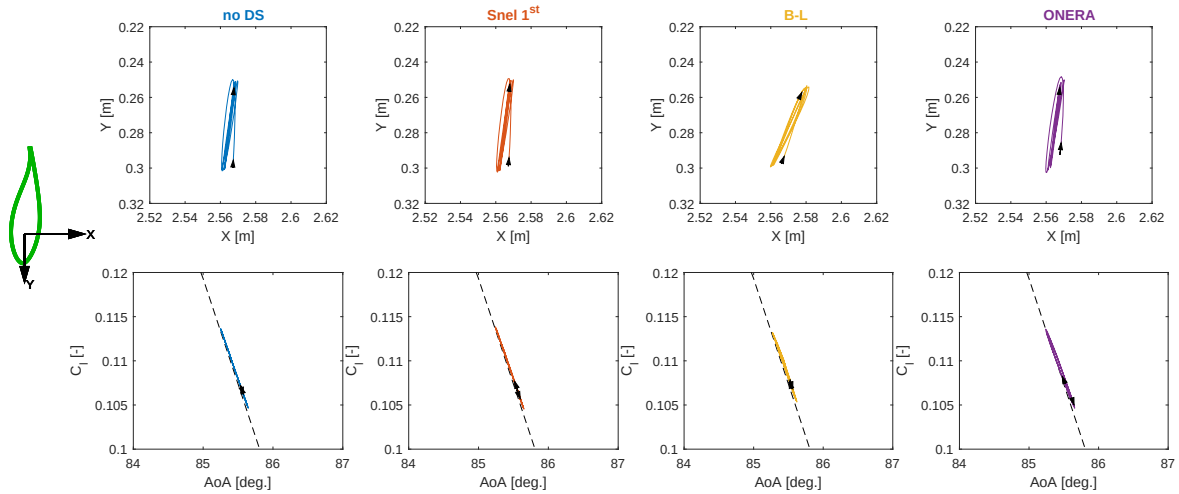

Figure H.12: A depiction of tip deformation in X and Y coordinate and lift coefficient hysteresis for a simulation time of 10 to 15 seconds with 0 degree pitch angle. The dashed line indicates the static lift coefficient in the lower row of plots. The results are shown for blade 1 which is fixed at 90 degree azimuth angle.

H.3.2. Pitch = 30^o

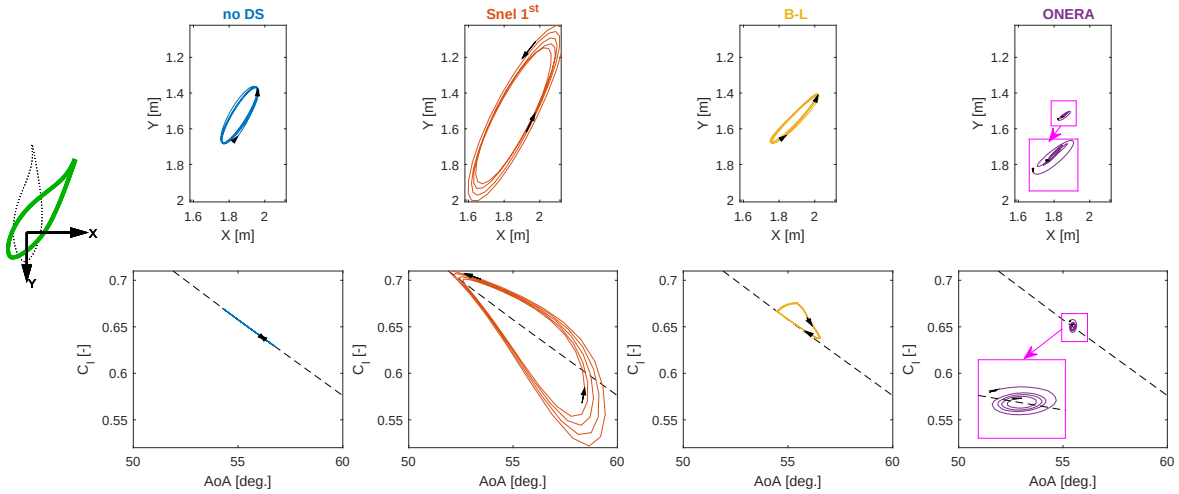

Figure H.13: A depiction of tip deformation in X and Y coordinate and lift coefficient hysteresis for a simulation time of 10 to 15 seconds with 30 degree pitch angle. The dashed line indicates the static lift coefficient in the lower row of plots. The results are shown for blade 1 which is fixed at 90 degree azimuth angle.

H.3.3. Pitch = 40^o

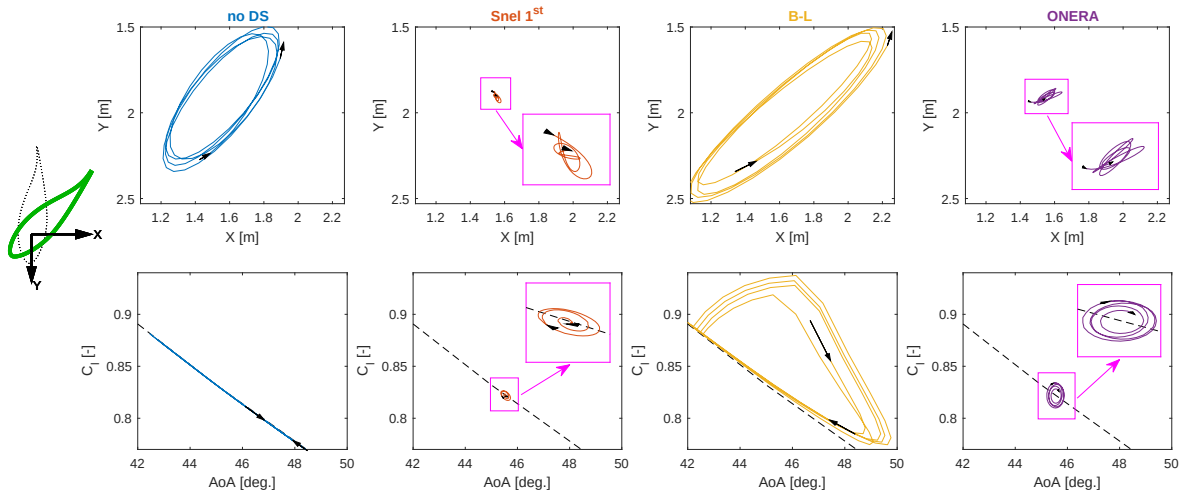

Figure H.14: A depiction of tip deformation in X and Y coordinate and lift coefficient hysteresis for a simulation time of 10 to 15 seconds with 40 degree pitch angle. The dashed line indicates the static lift coefficient in the lower row of plots. The results are shown for blade 1 which is fixed at 90 degree azimuth angle.

H.3.4. Pitch = 50^o

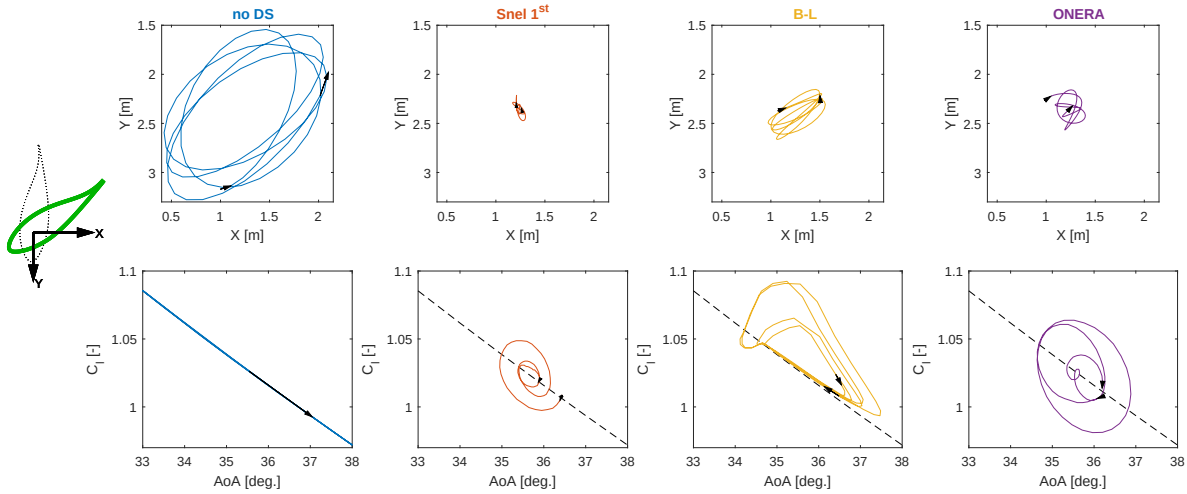

Figure H.15: A depiction of tip deformation in X and Y coordinate and lift coefficient hysteresis for a simulation time of 10 to 15 seconds with 50 degree pitch angle. The dashed line indicates the static lift coefficient in the lower row of plots. The results are shown for blade 1 which is fixed at 90 degree azimuth angle.

H.3.5. Pitch = 60^o

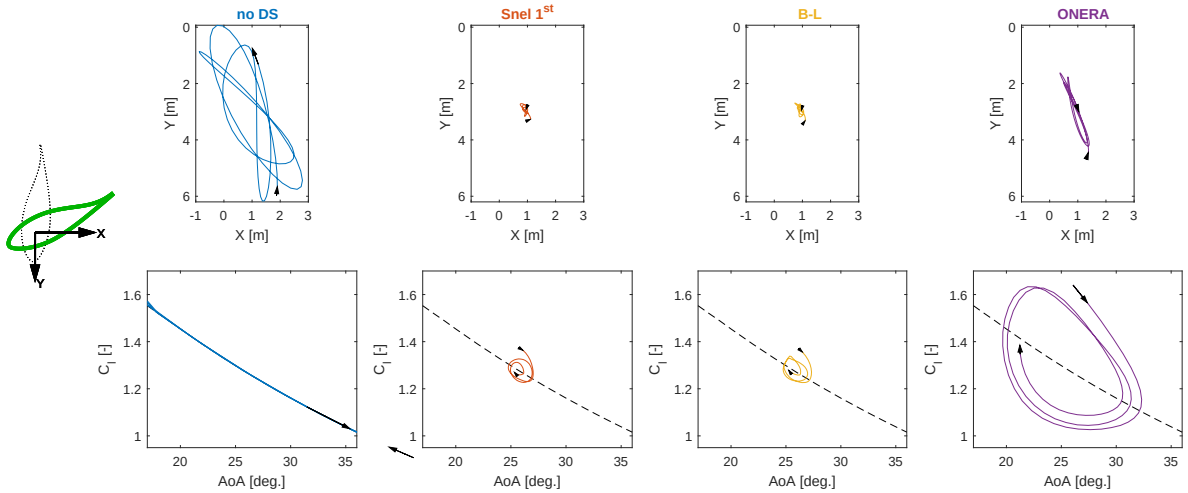

Figure H.16: A depiction of tip deformation in X and Y coordinate and lift coefficient hysteresis for a simulation time of 10 to 15 seconds with 60 degree pitch angle. The dashed line indicates the static lift coefficient in the lower row of plots. The results are shown for blade 1 which is fixed at 90 degree azimuth angle.

H.3.6. Pitch = 110^o

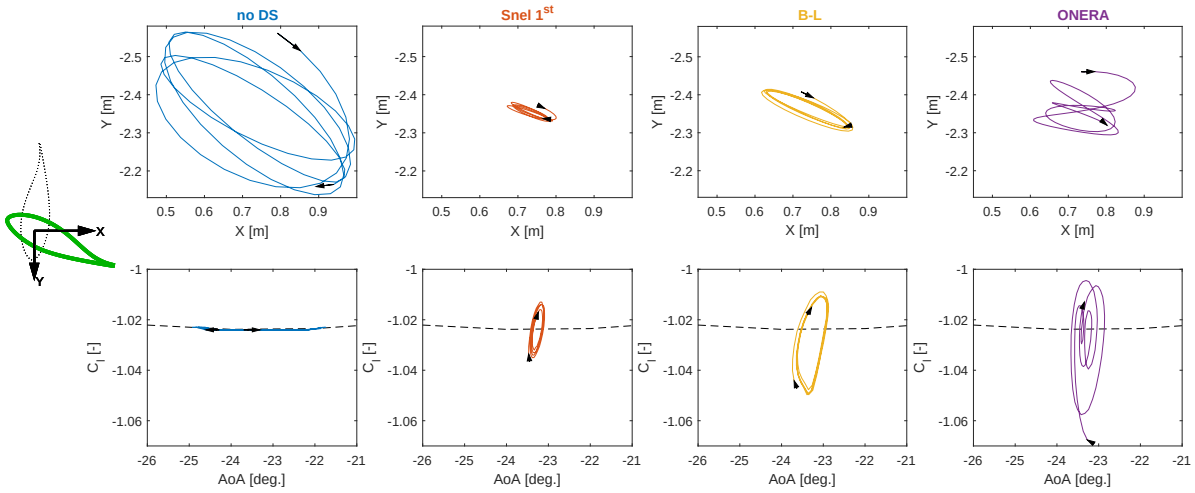

Figure H.17: A depiction of tip deformation in X and Y coordinate and lift coefficient hysteresis for a simulation time of 10 to 15 seconds with 110 degree pitch angle. The dashed line indicates the static lift coefficient in the lower row of plots. The results are shown for blade 1 which is fixed at 90 degree azimuth angle.

Bibliography

[1] J. D. Anderson Jr. *Fundamentals of Aerodynamics*, volume Fifth edit. Fifth edition, 2011. ISBN 0073398101. doi: 10.1036/0072373350.

[2] Christian Bak, Frederik Zahle, Robert Bitsche, Anders Yde, Lars Christian Henriksen, Anand Nata, and Morten Hartvig Hansen. Description of the DTU 10 MW Reference Wind Turbine. *DTU Wind Energy Report-I-0092*, (July):1–138, 2013. ISSN 1098-6596. doi: 10.1017/CBO9781107415324.004. URL https://dtu-10mw-rwt.vindenergi.dtu.dk.

[3] Galih Bangga, Thorsten Lutz, and Ewald Krämer. Root flow characteristics and 3D effects of an isolated wind turbine rotor. *Journal of Mechanical Science and Technology*, 31(8):3839–3844, 2017. ISSN 1738494X. doi: 10.1007/s12206-017-0728-6.

[4] W. A.A.M. Bierbooms. A comparison between unsteady aerodynamic models. *Journal of Wind Engineering and Industrial Aerodynamics*, 39(1-3):23–33, 1992. ISSN 01676105. doi: 10.1016/0167-6105(92)90529-J.

[5] Anders Björck. DYNSTALL: Subroutine Package with a Dynamic stall model. 2000.

[6] K. Boorsma. *Comparison of Experimental and Computational Aerodynamic Section Characteristics of DU91-W2-250 Profile*. PhD thesis, Delft University of Technology, 2003.

[7] K Boorsma. Power and loads for wind turbines in yawed conditions. Technical report, ECN, 2012.

[8] K. Boorsma and M. Caboni. ECN Aero-Module: User's manual, v238. Technical report, ECN, 2017.

[9] K. Boorsma and J. G. Schepers. New MEXICO experiment: Preliminary Overview with Inital Validation. Technical Report September, ECN, 2014.

[10] Koen Boorsma. ECN Aero-Module Training.

[11] Koen Boorsma and Gerard Schepers. Description of Experimental Setup: New MEXICO experiment. Technical Report May, ECN, 2017.

[12] B. M. Bragg, D. C. Heinrich, F. A. Balow, and K. B. M. Q. Zaman. Flow oscillation over an airfoil near stall. *AIAA Journal*, 34(1):199–201, 1996. ISSN 0001-1452. doi: 10.2514/3.13045. URL http://arc.aiaa.org/doi/10.2514/3.13045.

[13] Tony Burton, David Sharpe, Nick Jenkind, and Ervin Bossanyi. *Wind Energy Handbook*. 2011. ISBN 978-0-470-69975-1.

[14] P. K. Chaviaropoulos and M. O. L. Hansen. Investigating Three-Dimensional and Rotational Effects on Wind Turbine Blades by Means of a Quasi-3D Navier-Stokes Solver. *Journal of Fluids Engineering*, 122(2):330, 2000. ISSN 00982202. doi: 10.1115/1.483261. URL http://fluidsengineering.asmedigitalcollection.asme.org/article.aspx?articleid=1429176.

[15] Taehwan Cho and Cheolwan Kim. Wind tunnel test results for a 2/4.5 scale MEXICO rotor. *Renewable Energy*, 42:152–156, 2012. ISSN 09601481. doi: 10.1016/j.renene.2011.08.031. URL http://dx.doi.org/10.1016/j.renene.2011.08.031.

[16] Taehwan Cho and Cheolwan Kim. Wind tunnel test for the NREL phase VI rotor with 2m diameter. *Renewable Energy*, 65:265–274, 2014. ISSN 09601481. doi: 10.1016/j.renene.2013.10.009. URL http://dx.doi.org/10.1016/j.renene.2013.10.009.

[17] Alessandro Croce. Comparison of models with respect to stability analysis. Technical report, AVATAR Work Package 4: Task 4.1, 2015.

[18] Zhaohui Du. A 3-D stall-delay model for horizontal axis wind turbine performance prediction. *1998 Asme Wind Energy Symposium*, 1998.

[19] Horia Dumitrescu and Vladimir Cardos. Inboard Stall delay due to rotation. *INTECH*, 2011.

[20] Horia Dumitrescu, Vladimir Cardoş, and Alexandru Dumitrache. Modelling of inboard stall delay due to rotation. *Journal of Physics: Conference Series*, 75(1), 2007. ISSN 17426588. doi: 10.1088/1742-6596/75/1/012022.

[21] M. Elgammi and T. Sant. A Modified Beddoes-Leishman Model for Unsteady Aerodynamic Blade Load Computations on Wind Turbine Blades. *Journal of Solar Energy Engineering*, 138(October 2016): 1–18, 2016. ISSN 0199-6231. doi: 10.1115/1.4034241. URL http://solarenergyengineering.asmedigitalcollection.asme.org/article.aspx?doi=10.1115/1.4034241.

[22] A. Fage and F. C. Johansen. On the Flow of Air behind an Inclined Flat Plate of Infinite Span. *Proceedings of the Royal Society A: Mathematical, Physical and Engineering Sciences*, 116(773):170–197, 1927. ISSN 1364-5021. doi: 10.1098/rspa.1927.0130. URL http://rspa.royalsocietypublishing.org/cgi/doi/10.1098/rspa.1927.0130.

[23] Peter Fuglsang, Ks Dahl, and Ioannis Antoniou. *Wind tunnel tests of the Risø-A1-18, Risø-A1-21 and Risø-A1-24 airfoils*, volume 1112. 1999. ISBN 8755025382. URL http://orbit.dtu.dk/fedora/objects/orbit:88021/datastreams/file{_}7731506/content.

[24] Mac Gaunaa, Joachim Heinz, and Witold Skrzypiński. Toward an Engineering Model for the Aerodynamic Forces Acting on Wind Turbine Blades in Quasisteady Standstill and Blade Installation Situations. *Journal of Physics: Conference Series*, 753(2), 2016. ISSN 17426596. doi: 10.1088/1742-6596/753/2/022007.

[25] H. Glauert. A General Theory of the Autogyro. *Scientific Research Air Ministry - Reports and Memoranda No. 1111*, page 41, 1926.

[26] S. Guntur and N. N. Sørensen. An evaluation of several methods of determining the local angle of attack on wind turbine blades. *Journal of Physics: Conference Series*, 555(1), 2014. ISSN 17426596. doi: 10.1088/1742-6596/555/1/012045.

[27] Srinivas Guntur. *A Detailed Study of the Rotational Augmentation and Dynamic Stall Phenomena for Wind Turbines*. Phd thesis, Technical University of Denmark, 2013. URL https://findit.dtu.dk/en/catalog/2389472254.

[28] Srinivas Guntur and Niels N. Sørensen. A study on rotational augmentation using CFD analysis of flow in the inboard region of the MEXICO rotor blades. *Wind Energy*, 18(4):745–756, 2015. ISSN 10991824. doi: 10.1002/we.1726. URL http://onlinelibrary.wiley.com/doi/10.1002/we.1608/full.

[29] Srinivas K Guntur. A Detailed Study of the Rotational Augmentation and Dynamic Stall Phenomena for Wind Turbines DTU Vindenergi PhD Rapport 2013. *Forskningsbasen.Deff.Dk*, 0022(December):111, 2013. URL http://forskningsbasen.deff.dk/Share.external?sp=Sf1fb872b-712c-4e3e-97e0-c1a13e32428f{&}sp=Sdtu.

[30] Sandeep Gupta and J. Gordon Leishman. Dynamic stall modelling of the S809 aerofoil and comparison with experiments. *Wind Energy*, 2006. ISSN 10954244. doi: 10.1002/we.200.

[31] M. M. Hand, D. A. Simms, L. J. Fingersh, D. W. Jager, and J. R. Cotrell. Unsteady Aerodynamics Experiment Phase V: Test Configuration and Available Data Campaigns. Technical Report December, 2001. URL http://www.osti.gov/servlets/purl/787980-di45Yl/native/.

[32] M.O.L. Hansen, N.N. Sorensen, J. Norkaer, and Et al. Extraction of lift, drag and angle of attack from computed 3-D viscous flow around a rotating blade. *1997 European Wind Energy Conference*, 1997.

[33] Morten Hartvig Hansen, Mac Gaunaa, and Helge Aagaard Madsen. A Beddoes-Leishman type dynamic stall model in state-space and indicial formulations. Technical report, Technical University of Denmark, 2004. URL https://findit.dtu.dk/en/catalog/2389477433.

[34] S. Hauptmann, M. Bulk, L. Schon, S. Erbsloh, K. Boorsma, F. Grasso, M. Kuhn, and P. W. Cheng. Comparison of the lifting-line free vortex wake method and the blade-element-momentum theory regarding the simulated loads of multi-MW wind turbines. *Journal of Physics: Conference Series*, 555(1), 2014. ISSN 17426596. doi: 10.1088/1742-6596/555/1/012050.

[35] Joachim C Heinz, Niels N Sørensen, Vasilis Riziotis, Michael Schwarz, Sugoi Gomez-iradi, and Michael Stettner. Aerodynamics of Large Rotors. WP4. Deliverable 4.5. (August):80, 2016.

[36] H Himmelskamp. Profile investigations on a rotating airscrew. 1947.

[37] S. F. Hoerner. Fluid Dynamic Drag, 1965.

[38] S. F. Hoerner and H. V. Borst. Fluid-Dynamic Lift: Practical Information on Aerodynamic and Hydrodynamic Lift, 1985.

[39] M.J. Hoffmann, R. Reuss Ramsay, and G.M. Gregorek. Effects of grit roughness and pitch oscillations on the NACA 4415 airfoil. (July), 1996. doi: 10.2172/266691. URL http://www.osti.gov/servlets/purl/266691-Iy1spR/webviewable/.

[40] J. G. Holierhoek, J. B. De Vaal, A. H. Van Zuijlen, and H. Bijl. Comparing different dynamic stall models. *Wind Energy*, 2013. ISSN 10954244. doi: 10.1002/we.548.

[41] J. M. Janiszewska, M.J. Hoffmann, R. Reuss Ramsay, and G.M. Gregorek. Effects of grit roughness and pitch oscillations on the S814 airfoil. Technical Report May, 1996. URL https://wind.nrel.gov/airfoils/OSU{_}data/reports/3x5/s814.pdf.

[42] Joseph Katz and Allen Plotkin. *Low Speed Aerodynamics*. Cambridge University Press, Cambridge, New York, Melbourne, Madrid, Cape Town, Singapore, São Paulo, Delhi, Dubai, Tokyo, Mexico City, second edition, 2010. ISBN 0-521-66219-2.

[43] J. W. Larsen, S. R K Nielsen, and S. Krenk. Dynamic stall model for wind turbine airfoils. *Journal of Fluids and Structures*, 2007. ISSN 08899746. doi: 10.1016/j.jfluidstructs.2007.02.005.

[44] Gordon J. Leishman. *Principles of helicopter aerodynamics*. Cambridge University Press, 2nd edition, 2006. ISBN 0521858607. URL http://www.amazon.com/dp/0521858607.

[45] J. LEISHMAN. State-space model for unsteady airfoil behavior and dynamic stall. *30th Structures, Structural Dynamics and Materials Conference*, 1989. doi: 10.2514/6.1989-1319. URL http://arc.aiaa.org/doi/10.2514/6.1989-1319.

[46] J G Leishman and T S Bcddoes. A Semi-Empirical Model for Dynamic Stall. 1989.

[47] J G Leishman and T S Beddoes. A generalised model for airfoil unsteady aerodynamic behaviour and dynamic stall using the indicial method. In *Proceedings of the 42nd Annual forum of the American Helicopter Society*, pages 243–265. Washington DC, 1986.

[48] J. Gordon Leishman. Challenges in modelling the unsteady aerodynamics of wind turbines. *Wind Energy*, 5(2-3):85–132, apr 2002. ISSN 1095-4244. doi: 10.1002/we.62. URL http://doi.wiley.com/10.1002/we.62.

[49] C Lindenburg. Aerodynamic airfoil coefficients at large angles of attack. *Annual IEA Symposyum on the Aerodynamics of Wind Turbines*, (January):1–18, 2000.

[50] C Lindenburg. Investigation into Rotor Blade Aerodynamics Analysis of the stationary measurements on the UAE phase-VI rotor in the NASA-Ames wind tunnel. *Ecnnl*, (July):114, 2003. URL http://www.ecn.nl/docs/library/report/2003/c03025.pdf.

[51] C Lindenburg. Modelling of rotational augmentation based on engineering considerations and measurements. *European Wind Energy Conference*, (November):22–25, 2004.

[52] D. G. Mabey. Review of the normal force fluctuations on aerofoils with separated flow. *Progress in Aerospace Sciences*, 29(1):43–80, 1992. ISSN 03760421. doi: 10.1016/0376-0421(92)90003-Z.

[53] K W Mcalister, 0 Lambert, and D Petot. Application of the ONERA Model of Dynamic Stall. 1984.

[54] William J McCroskey. The phenomenon of dynamic stall. Technical report, 1981.

[55] Murat Mert. Optimization of Semi-Empirical Parameters in the FFA-Beddoes Dynamic Stall Model. 1999.

[56] MexNext. EPOS Portal. URL https://mexnext.ecn.nl/do/folder?id=12080-666f6c646572.

[57] Daniel Micallef and Tonio Sant. A Review of Wind Turbine Yaw Aerodynamics. *Wind Turbines - Design, Control and Applications*, 2016. ISSN 00796700. doi: 10.5772/63445. URL http://www.intechopen.com/books/wind-turbines-design-control-and-applications/a-review-of-wind-turbine-yaw-aerodynamics.

[58] Bjorn Montgomerie. Dynamic stall model called "SIMPLE". Technical report, Netherlands Energy Research Foundation ECN, 1996.

[59] Karen Mulleners and Markus Raffel. The onset of dynamic stall revisited. *Experiments in Fluids*, 52(3): 779–793, mar 2012. ISSN 0723-4864. doi: 10.1007/s00348-011-1118-y. URL http://link.springer.com/10.1007/s00348-011-1118-y.

[60] Stig Øye. Dynamic stall simulated as time lag of separation. In *Proceedings of the 4th IEA Symposium on the Aerodynamics of Wind Turbines*, Rome, 1991.

[61] E. A. Parra. Data Reduction and Analysis of New MEXICO Experiment. Technical Report February, 2016.

[62] Johan Peeringa, Alexander Lünenschloß, Marion Reijerkerk, Martin Stettner, Vasilis Riziotis, Alessandro Croce, Riccardo Riva, and Luca Sartori. AVATAR Aeroelastic Workout at PoliMi. Technical report, 2015.

[63] Alberto Pellegrino and Craig Meskell. Vortex shedding from a wind turbine blade section at high angles of attack. *Journal of Wind Engineering and Industrial Aerodynamics*, 121:131–137, 2013. ISSN 01676105. doi: 10.1016/j.jweia.2013.08.002. URL http://dx.doi.org/10.1016/j.jweia.2013.08.002.

[64] Ricardo Pereira, Gerard Schepers, and Marilena D Pavel. Validation of the Beddoes – Leishman Dynamic Stall Model for Horizontal Axis Wind Turbines using MEXICO Data. *49th AIAA Aerospace Sciences Meeting including the New Horizons Forum and Aerospace Exposition*, (January):207–219, 2011. ISSN 10954244. doi: 10.1002/we.

[65] Ricardo Pereira, Gerard Schepers, and Marilena D Pavel. Validation of the Beddoes – Leishman Dynamic Stall Model for Horizontal Axis Wind Turbines using MEXICO data. *49th AIAA Aerospace Sciences Meeting including the New Horizons Forum and Aerospace Exposition*, (January):207–219, 2011. ISSN 10954244. doi: 10.1002/we.

[66] Ricardo Pereira, Gerard Schepers, and Marilena D. Pavel. Validation of the Beddoes-Leishman dynamic stall model for horizontal axis wind turbines using MEXICO data. *Wind Energy*, 16(2):207–219, mar 2013. ISSN 10954244. doi: 10.1002/we.541. URL http://doi.wiley.com/10.1002/we.541.

[67] David A Peters. Toward a Unified Lift Model for Use in Rotor Blade Stability Analyses. *Journal of the American Helicopter Society*, 30(3):32–42, 1985. ISSN 00028711. doi: 10.4050/JAHS.30.32.

[68] D Petot. Differential equation modeling of dynamic stall. *Recherche Aerospatiale Technical Translation*, (5):59–72, 1989. ISSN 0379380x.

[69] Alexander Radi, Mark C. Thompson, John Sheridan, and Kerry Hourigan. From the circular cylinder to the flat plate wake: The variation of Strouhal number with Reynolds number for elliptical cylinders, 2013. ISSN 10706631.

[70] Hamid Rahimi, Gerard Schepers, Wen Zhong Shen, Néstor Ramos García, Marc Schneider, Daniel Micallef, Carlos Simao Ferreira, Eva Jost, Levin Klein, and Iván Herráez. Evaluation of different methods for determining the angle of attack on wind turbine blades with CFD results under axial inflow conditions. 2017. URL http://arxiv.org/abs/1709.04298.

[71] R. Reuss Ramsay, M.J. Hoffmann, and G.M. Gregorek. Effects of grit roughness and pitch oscillations on the S809 airfoil. Technical report, 1995. URL http://www.osti.gov/servlets/purl/266691-Iy1spR/webviewable/.

[72] Ainara Irisarri Ruiz Ruiz, Helge Aagaard Madsen, David Robert, Alessandro Croce, Luca Sartori, Marco Stefano Lunghini, Marion Reijerkerk, Henk-jan Kooijman, and Martin Stettner. Comparison of the INNWIND and AVATAR Research Wind Turbines. Technical Report November, 2015.

[73] Gerhard Schepers. An engineering model for yawed conditions, developed on basis of wind tunnel measurements. *American Institute of Aeronautics & Astronautics*, (c):164–174, 1999. doi: doi/10.2514/6.1999-39. URL http://arc.aiaa.org/doi/10.2514/6.1999-39.

[74] J G Schepers. *IEA Annex XX: Comparison between calculations and measurements on a wind turbine in yaw in the NASA-Ames windtunnel*. 2007. ISBN 2020021110. doi: ECN-E-07-072.

[75] J. G. Schepers and H. Snel. Model Experiments in Controlled Conditions - Final Report. *ECN Report: ECN-E-07-042*, page 54, 2007. doi: ECN-E-07-042.

[76] J G Schepers, K Boorsma, T Cho, Sugoi Gomez-iradi, P Schaffarczyk, A Jeromin, W Z Shen, T Lutz, K Meister, B Stoevesandt, S Schreck, D Micallef, R Pereira, T Sant, H a Madsen, and Niels N. Sorensen. Final report of IEA Task 29, Mexnext (Phase 1): Analysis of Mexico wind tunnel measurements. (Phase 1):312, 2012.

[77] J.G. Schepers. *Engineering models in wind energy aerodynamics*. PhD thesis, TU Delft, Delft, 2012. URL http://repository.tudelft.nl/assets/uuid:92123c07-cc12-4945-973f-103bd744ec87/PhD{_}Schepers.pdf.

[78] S. Schreck and M. Robinson. Rotational augmentation of horizontal axis wind turbine blade aerodynamic response. *Wind Energy*, 5(2-3):133–150, 2002. ISSN 1095-4244. doi: 10.1002/we.68. URL http://doi.wiley.com/10.1002/we.68.

[79] Scott Schreck. Spectral content and spatial scales in unsteady rotationally augmented flow fields. *Journal of Physics: Conference Series*, 75(1), 2007. ISSN 17426588. doi: 10.1088/1742-6596/75/1/012024.

[80] D. Simms, S.J. Schreck, M. Hand, and L.J. Fingersh. NREL Unsteady Aerodynamics Experiment in the NASA-Ames Wind Tunnel: A Comparison of Predictions to Measurements. *Nrel/Tp-500-29494*, (June):45, 2001. doi: NREL/TP-500-29494. URL https://www.nrel.gov/docs/fy01osti/29494.pdf{%}0Ahttp://arc.aiaa.org/doi/abs/10.2514/6.2001-35.

[81] H Snel. Heuristic modelling of dynamic stall characteristics. In *EWEC-CONFERENCE-*, pages 429–433. BOOKSHOP FOR SCIENTIFIC PUBLICATIONS, 1997.

[82] H Snel, R Houwink, and J Bosschers. Sectional prediction of lift coefficients on rotating wind turbine blades in stall. Technical report, ECN-C-93-052, 1994.

[83] H. Snel, J. G. Schepers, and B. Montgomerie. The MEXICO project (Model Experiments in Controlled Conditions): The database and first results of data processing and interpretation. *Journal of Physics: Conference Series*, 75(1), 2007. ISSN 17426588. doi: 10.1088/1742-6596/75/1/012014.

[84] Herman Snel. Review of aerodynamics for wind turbines. *Wind Energy*, 6(3):203–211, 2003. ISSN 10954244. doi: 10.1002/we.97.

[85] Herman Snel and Gerard Schepers. Engineering Models for Dynamic Inflow Phenomena. In *The European Wind Energy Conference*, Amsterdam, 1991.

[86] Herman Snel and Gerard Schepers. Joule 1: Joint investigation of dynamic inflow effects and implementation of an engineering model. Technical report, ECN, 1994.

[87] M. Stettner, M. J. Reijerkerk, A. Lünenschloß, V. Riziotis, A. Croce, L. Sartori, R. Riva, and J. M. Peeringa. Stall-Induced Vibrations of the AVATAR Rotor Blade. *Journal of Physics: Conference Series*, 753(4), 2016. ISSN 17426596. doi: 10.1088/1742-6596/753/4/042019.

[88] Katrina Elise Swalwell. The effect of turbulence on stall of horizontal axis wind turbines. pages 1–307, 2005. URL http://scholar.google.com/scholar?hl=en{&}btnG=Search{&}q=intitle:The+Effect+of+Turbulence+on+Stall+of+Horizontal+Axis+Wind+Turbines{#}8.

[89] Theodore Theodorsen. General theory of aerodynamic instability and the mechanism of flutter. Technical Report No. 496, 1935.

[90] W. A. Timmer. Aerodynamic characteristics of wind turbine blade airfoils at high angles-of-attack. *TORQUE 2010: The Science of Making Torque from Wind*, (1):71–78, 2010. doi: 10.1533/9780857097286.2.210.

[91] W. A. Timmer and R. P. J. O. M. van Rooij. Summary of the Delft University Wind Turbine Dedicated Airfoils. *Journal of Solar Energy Engineering*, 125(4):488, 2003. ISSN 01996231. doi: 10.1115/1.1626129. URL http://solarenergyengineering.asmedigitalcollection.asme.org/article.aspx?articleid=1456892.

[92] W.a. Timmer and R Van Rooij. Some aspects of high angle-of-attack flow on airfoils for wind turbine application. *EWEC 2001, Copenhagen, Denmark*, (July 2015):4–7, 2001. ISSN 01996231. doi: 10.1115/1.1626129. URL http://www.lr.tudelft.nl/fileadmin/Faculteit/LR/Organisatie/Afdelingen{_}en{_}Leerstoelen/Afdeling{_}AEWE/Wind{_}Energy/Research/Publications/Publications{_}2001/doc/TimmerEWEC2001.pdf.

[93] C T Tran and D Petot. Semi-empirical model for the dynamic stall of airfoils in view to the application to the calculation of responses of a helicopter blade in forward flight. *Vertica*, 5(1):35–53, 1980. ISSN 03605450.

[94] V. K. Truong. A 2-D Dynamic Stall Model Based on a Hopf Bifurcation. In *19th European Rotorcraft Forum*, number July, 1993.

[95] B. G. van der Wall and J. G. Leishman. On the Influence of Time-Varying Flow Velocity on Unsteady Aerodynamics. *Journal of the American Helicopter Society*, 39(4):25, 1994. ISSN 00028711. doi: 10.4050/JAHS.39.25.

[96] Arne Van Garrel. Development of a Wind Turbine Aerodynamics Simulation Module. *ECN Wind Energy*, (August):106, 2003. ISSN 0040-5736. doi: 10.13140/RG.2.1.2773.8000.

[97] Larry Viterna and Robert D Corrigan. Fixed pitch rotor performance of large horizontal axis wind turbines. *Annual Review of Fluid Mechanics*, 15(1):69–85, 1982. ISSN 00664189. doi: 10.1146/annurev.fl.15.010183.000453. URL http://naca.larc.nasa.gov/search.jsp?R=524871{&}id=2{&}as=false{&}or=false{&}qs=Ns=HarvestDate{%}7C1{&}N=4294871842.

[98] W.H.H. Banks. Delaying effect of rotation on laminar separation, 1963.

[99] Jing Ping Xiao, Jie Wu, Li Chen, and Zhe Yu Shi. Particle image velocimetry (PIV) measurements of tip vortex wake structure of wind turbine. *Applied Mathematics and Mechanics (English Edition)*, 32(6):729–738, 2011. ISSN 02534827. doi: 10.1007/s10483-011-1452-x.

[100] B F Xu, Y Yuan, and T G Wang. Development and application of a dynamic stall model for rotating wind turbine blades. *Journal of Physics: Conference Series*, 524(1):012133, 2014. ISSN 1742-6596. doi: 10.1088/1742-6596/524/1/012133. URL http://stacks.iop.org/1742-6596/524/i=1/a=012133.

[101] Dan Yang, Bjørnar Pettersen, Helge I Andersson, and Vagesh D Narasimhamurthy. Vortex shedding in flow past an inclined flat plate at high incidence. 2012. doi: 10.1063/1.4744982.

[102] Steven A. Yon and Joseph Katz. Study of the Unsteady Flow Features on a Stalled Wing. *AIAA Journal*, 36(3):305–312, 1998. ISSN 0001-1452. doi: 10.2514/2.372. URL http://arc.aiaa.org/doi/abs/10.2514/2.372.

[103] K. B. M. Q. Zaman. Effect of Acoustic Excitation on Stalled Flow Over a low-Re airfoil. *AIAA Journal*, 30 (6):1492–1499, 1987.

[104] K. B.M.Q. Zaman, D. J. McKinzie, and C. L. Rumsey. *A Natural Low-Frequency Oscillation of the Flow over an Airfoil Near Stalling Conditions*, volume 202. 1989. ISBN 0022112089001. doi: 10.1017/S0022112089001230.